EUROPEAN COMMISSION

Community research

Long-term Performance of Engineered Barrier Systems

PEBS

Long-term Performance of Engineered Barrier Systems PEBS

Extrapolation of the models developed to the repository long- term evolution and evaluation of uncertainties

(DELIVERABLE-N°: D3.5-4)

Contract (grant agreement) number: FP7 249681

Author(s): K. Wieczorek (Ed.), O. Czaikowski, I. Gaus, A. Gens, U. Kuhlmann, A. Mon, L. Montenegro, A. Naves, J. Samper, M. Sanchez, R. Senger, R. Vasconcelos

Reporting period: 01/03/10 – 28/02/14

Date of issue of this report: 27/08/14

Start date of project: 01/03/10 Duration: 48 Months

Project co-funded by the European Commission under the Seventh Euratom Framework Programme for Nuclear Research &Training Activities (2007-2011)		
Dissemination Level		
PU	Public	PU
RE	Restricted to a group specified by the partners of the [acronym] project	
CO	Confidential, only for partners of the [acronym] project	

EURATOM

Table of Contents

1 Introduction

The EC co-funded project PEBS (Long-term Performance of the Engineered Barrier System) aimed at the evaluation of the sealing and barrier performance of the EBS with time, through development of a comprehensive approach involving experiments, model development and consideration of the potential impacts on long-term safety functions.

The experiments and models cover the full range of conditions from initial emplacement of wastes (high heat generation and EBS resaturation) through to later stage establishment of near steady-state conditions, i.e. full resaturation and thermal equilibrium with the host rock. The idea was to integrate these aspects in a manner that would lead to a more convincing connection between the initial transient state of the EBS and its long-term state that provides the required isolation of the wastes.

The project work builds on existing knowledge and experience generated during recent years and supported by ongoing national and EC research programmes. The project intends to provide a more complete description of the THM and THM-C (thermal-hydraulic-mechanical-chemical) evolution of the EBS system, a more quantitative basis for relating the evolutionary behaviour to the safety functions of the system and a further clarification of the significance of residual uncertainties for long-term performance assessment.

The PEBS project is organized in four scientific work packages. All numerical modelling is performed within Work Package 3, which is structured in five tasks. While four of these tasks are devoted to numerical simulation of the various experiments performed in Work Package 2 of PEBS, Task 3.5 concentrates on long-term extrapolation aspects. This deliverable (D3.5-4) is presents the modelling work performed for Task 3.5.

Besides numerical modelling other activities were part of Task 3.5. These are reported in additional documents:

- Evaluation of the usefulness of natural analogues for providing support, testing and validation of long-term predictions of current THMC models. (PEBS Milestone 3.5-3 document)
- Integrated analysis of the hydrodynamic, thermal and chemical data from several space and time scales in terms of dimensionless variables (Deliverable D3.5-1)

- Review of thermomechanical continuum mixture theories potentially applicable for EBS materials and development of a concept of non-associative immiscibility and a respective schematical formulation of a material model (Deliverable D3.5-4a)

2 Objectives and Scope

The overall objectives of Work Package 3 are

- To perform coupled HM, THM, and THMC analyses to provide a sound basis for the interpretation of the various tests planned in the framework of Work Package 2;
- To develop new or improved models as demanded by the calibration of computational results with the measured data;
- To use the data and improved models for extrapolation to long-term evolution of the repository and to investigate model uncertainty and its impact on long-term prediction, thus providing input to Work Package 4.

The last of the above items is the objective of Task 3.5, “Extrapolation to repository long-term evolution”. It involves

- Critical assessment of the results of the other WP 3 tasks regarding their implications for different time and space scales including long-term conditions;
- Identification of the significant processes in the resaturation phase and after resaturation;
- Development or modification of the available HM, THM and THM-C formulations to incorporate phenomena and processes deemed to be relevant for long-term predictions;
- Performance of coupled numerical analyses for long-term evolution of the engineered barrier system in the repository, with different degrees of abstraction and different focuses according to the different modelling teams;
- Evaluation of the model uncertainty and its implications for long-term prediction and safety analysis.

One of the first exercises of Task 3.5 was to define a set of long-term simulation cases to be modelled. These should be relevant for the repository long-term evolution, build on the insights from the other PEBS tasks and provide input to Work Package 4, “Analysis of impact on long-term safety and guidance for repository design and construction”. In order to have a maximum benefit from the modelling exercise, it was concluded that

- The processes which exhibit uncertainties are the most relevant for the extrapolation consideration;
- Substantial data to improve their description should be provided within PEBS;
- The modelling cases to be considered should be of interest to more than one of the partners.

With these criteria in mind, the following long-term simulation cases were defined:

- Case 1 – Isothermal buffer evolution;
- Case 2 – Thermo-hydro-mechanical evolution of the buffer at temperatures up to 100 °C;
- Case 3 – Thermo-hydro-mechanical evolution of the buffer with temperatures temporarily exceeding 100 °C;
- Case 4 – Geochemical evolution at canister-bentonite and bentonite-concrete interfaces, including a long-term simulation of a repository in granite.

All of the cases are based on repository concepts in clay or crystalline rock, namely the Swiss and Spanish concepts, thus generating relevant output. In some of the cases (Cases 2 and 3) several partners performed simulations in parallel, with different codes and assumptions, providing complementing information. An overview of the cases with the teams involved and basic features of their simulations is given in Tab. 2.1. In the following Sections 3 – 6, the simulation cases and their results are described in detail.

Tab. 2.1 Overview of the modelling cases for long-term extrapolation

Case	Title	Modelling Team	Code	Process Classes Considered	Features
1	Isothermal buffer evolution	CIMNE	CODE_BRIGHT	THM	2D, advanced models
2	Thermo-Hydro-Mechanical Evolution of the Buffer (T <= 100 °C)	CIMNE	CODE_BRIGHT	THM	2D, advanced models
2	"	Nagra	TOUGH2	TH	2D, inverse parameter optimization
3	Thermo-Hydro-Mechanical Evolution of the Buffer (T > 100 °C)	Nagra	TOUGH2	TH	3D
3	"	GRS	CODE_BRIGHT	TH	3D, basic models
3	"	CIMNE	CODE_BRIGHT	THM	2D
4	Geochemical Evolution at Interfaces	UDC	Inverse FADES	THCm	2D, mechanic considered in terms of porosity change

3 Modelling Case 1: Isothermal Buffer Evolution

Isothermal barrier behaviour in the PEBS project has been mainly explored through reference to the large scale “Engineered Barrier” (EB) experiment performed in the Mont Terri underground laboratory. The EB experiment has been dismantled during the lifetime of the PEBS project providing valuable data concerning the hydration of an engineered barrier without thermal effects (Palacios et al., 2013).

The observations gathered from the samples retrieved during the dismantling operation showed that the barrier was either saturated or very close to saturation throughout. A significant degree of homogenization had occurred during the hydration phase but heterogeneities were still observed to persist at the end of the experiment. The modelling of the EB test performed by CIMNE concerning both the operational phase and the dismantling is described in Deliverable D3.1-1/D3.1-2. The distributions of dry densities/porosities computed by the coupled HM numerical analysis turned out to show a quite reasonable agreement with the dismantling results.

The availability of a numerical model capable of a satisfactory representation of the EB test provides the opportunity to explore further the engineered barrier behaviour under different conditions. Thus, it was decided to extend the analysis of the EB experiment to long times to examine the long-term state of the barrier. In particular, it should be interesting to check if the trend towards greater homogeneity continues and heterogeneities finally disappear.

3.1 Description of the case

The main features of the modelling performed (geometry, initial and boundary conditions, constitutive laws and material parameters) are presented in detail in Deliverable 3.1-1/3.1-2. Only some key aspects are presented here for completeness.

The basic THM formulation presented in Deliverable D3.5-2 (Gens & Sánchez, 2014) has been simplified by neglecting all the terms related to thermal effects, thus resulting in a coupled HM formulation. A 2-D plane strain mesh was chosen to represent the modelled domain which is 80 m wide and 80 m high. A central plane of symmetry was used which implies only the half portion of experiment was considered in the analysis. A constant value of 1.0 MPa was assumed as the initial water pressure in the host

rock. Furthermore the initial stress state in the rock was assumed to be anisotropic with vertical and horizontal stress values of 6.0 and 4.8 MPa, respectively. These values reproduce quite well the initial conditions in the EB experiment site before the tunnel opening. The external mechanical boundary conditions were 0-displacement on the vertical and the lower horizontal boundaries. A compressive vertical stress of 6.0 MPa was applied to the upper horizontal boundary. A liquid pressure of 1.0 MPa was prescribed along the upper and lower horizontal boundaries and on the right vertical boundary of the modelled domain. The modelled geometry and the initial and boundary conditions prior to the excavation are given in Fig. 3.1

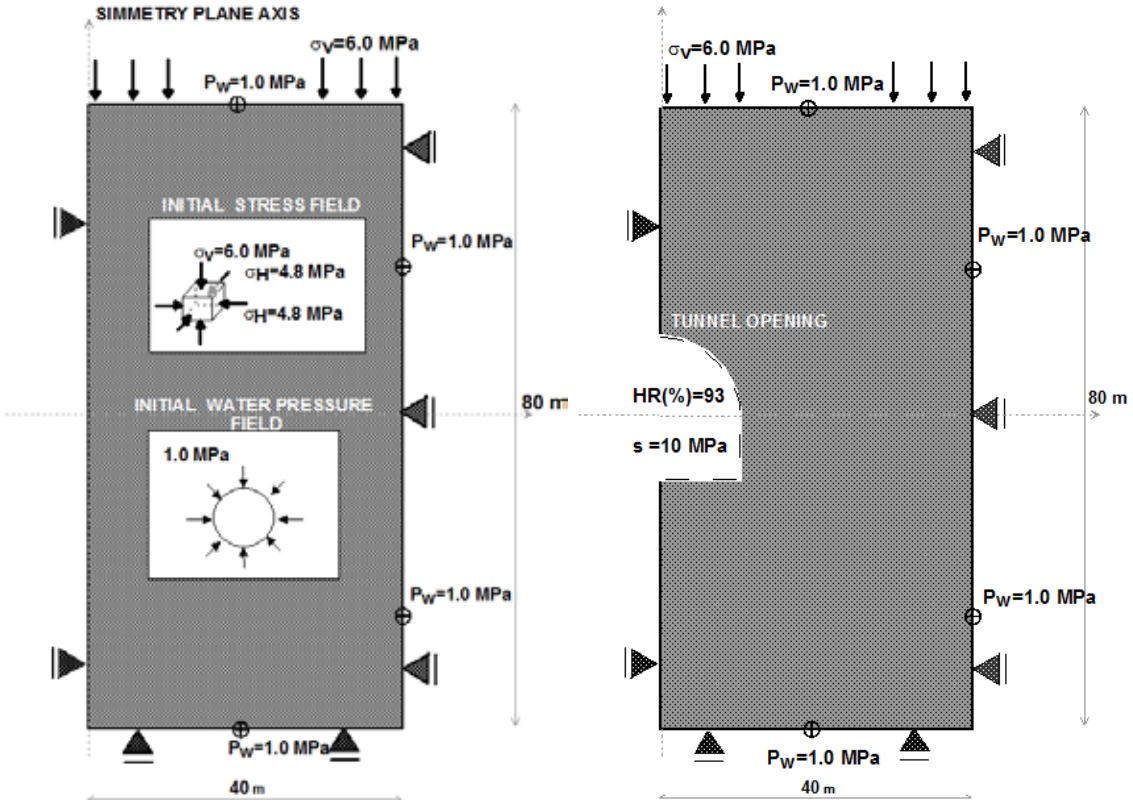

Fig. 3.1 Geometry, initial and boundary conditions prior to the excavation (left) and before the tunnel opening (right). The figure is not to scale.

The tunnel was excavated 160 days before the emplacement of the buffer materials. The excavation was modelled by a relaxation of the total stresses. A constant suction of 10.0 MPa was imposed on the tunnel surface that corresponds to a relative humidity of about 93%. Figure 3.1 also shows the geometry of the excavation and the boundary conditions for the tunnel construction. The tunnel has a horseshoe shaped cross section and its dimensions are about 3.00 m wide and 2.65 m height.

Once the tunnel has been constructed the buffer materials were emplaced. The canister diameter is about 0.97 m. The initial stress and water pressure fields in the host rock correspond to the end of the excavation period. The initial suction for the bentonite pellets and compacted blocks was set to 300 MPa and 150 MPa, respectively. The initial stress state for the bentonite based materials was assumed to be isotropic with a confining stress of 0.3 MPa. In Fig. 3.2, a detailed view of the buffer materials distribution inside the EB niche site is given. A period of 5 days was left before the hydration phase starts.

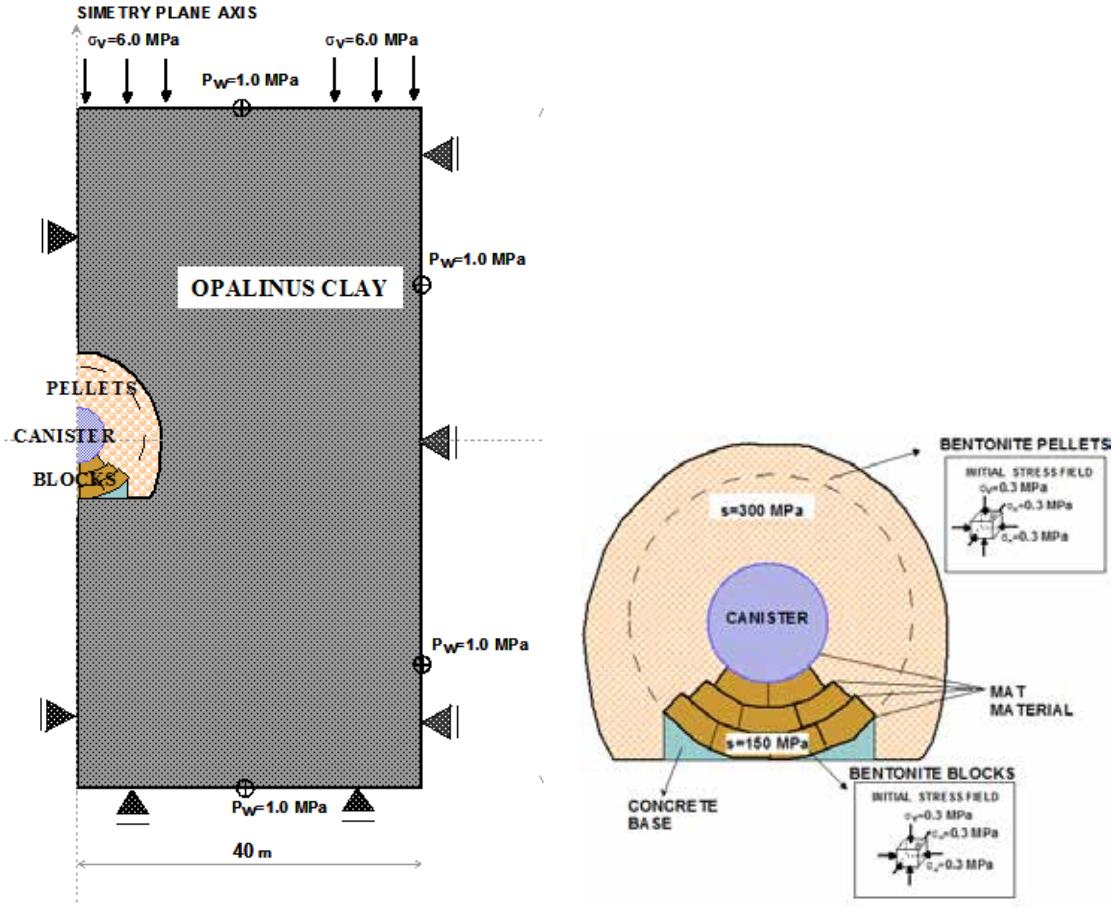

Fig. 3.2 View of the clay barrier emplacement, the material configuration and its initial state inside the barrier.

The modelling of the hydration involved a number of phases with different boundary conditions in order to simulate as closely as possible the protocol of the real experiment. In the final hydration phase, water was no longer injected in the bentonite barrier; only hydration from the rock occurred. In the long-term analysis reported here, this hydration condition was kept unchanged until time reached 100 years from the beginning of hydration.

The mechanical behaviour of the host rock and the concrete bed on which the bentonite blocks lie was modelled by elastic constitutive laws. Because of the special characteristics of granular bentonite, a double structure elastoplastic model has been adopted. In contrast, bentonite blocks are modelled by the conventional Barcelona Basic Model (BBM). Constitutive laws are described and material parameters are listed in Deliverable D3.1-1/D3.1-2.

3.2 Results

The model computations for the evolution of relative humidity in the buffer and inside the rock are plotted in Fig. 3.3. Since the end of the forced hydration of the barrier (on June 18, 2007 that corresponds to the day 1869 since the start of the hydration test) all the sensors have recorded a 100% value for relative humidity and no changes of this variable should be expected from that time on. However, the pore water pressure in the near field keeps increasing over time until it reaches values close to the pore pressure state prior to the tunnel excavation. This can be observed in Fig. 3.4 in which the evolution of liquid pressure inside the rock is depicted and also in Fig. 3.5a, where some pore pressure profiles at different times at the elevation of the EB experiment site are given. Furthermore, the pore pressure state inside the buffer tends to equalize with the liquid pressure of the rock (see Fig. 3.5a) as a consequence of the water flow from the rock towards the saturated barrier. Figure 3.5b shows the spatial distribution of the stress field in the rock at several times at the elevation of the experiment site. A gradual recovery of stresses towards the initial stress state of the rock mass before tunnel construction can be observed.

As Fig. 3.6 shows, no significant vertical movements of the canister are computed in the long-term modelling after the end of the real EB experiment (on January 14, 2013 corresponding to the end of the data collection period). Porosity inside the buffer remains unchanged since the bentonite barrier reached a saturated condition (about the day 1850 of the hydration experiment). As a consequence, the dry density distribution in the barrier keeps the same spatial configuration and the same degree of heterogeneity as observed at dismantling (see Fig. 3.7). Model computations do not show any tendency towards a higher degree of homogenisation in the long term.

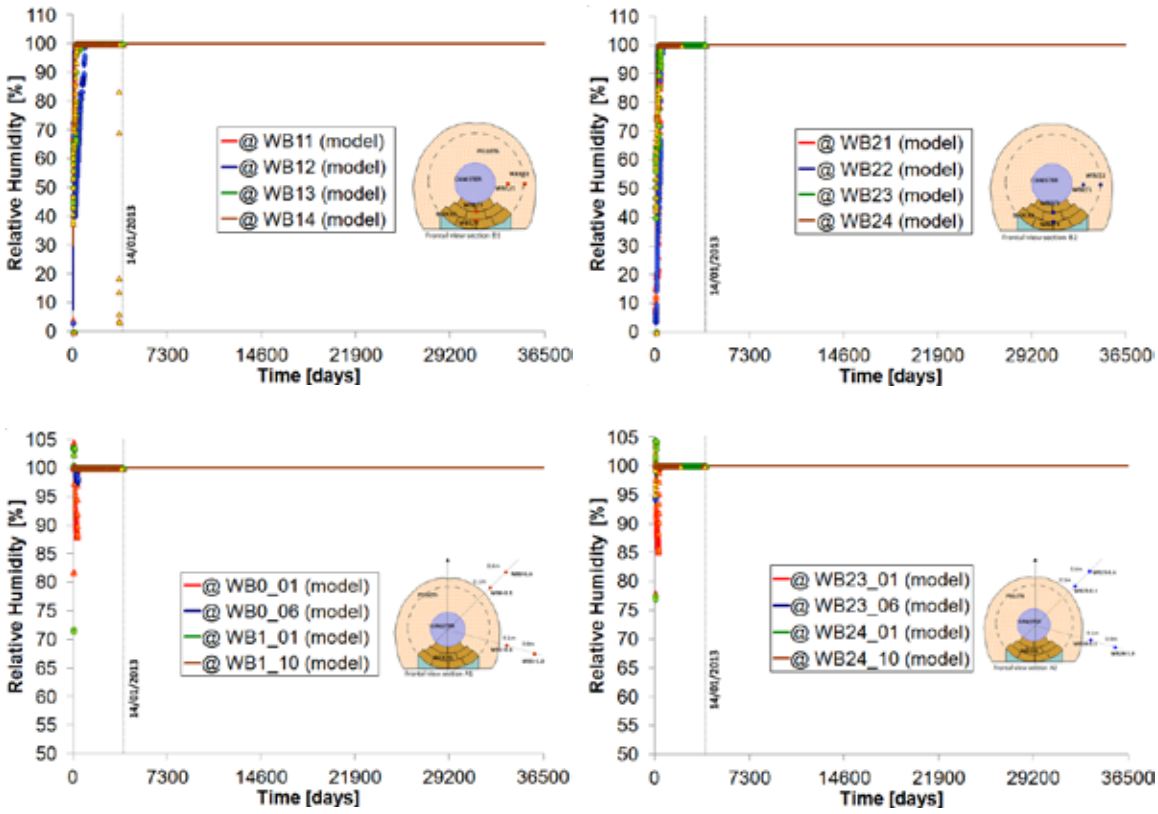

Fig. 3.3 Long-term computation for the evolution of relative humidity inside the buffer (up) and in the vicinity of the EB experiment site (down). Symbols represent the in situ observations.

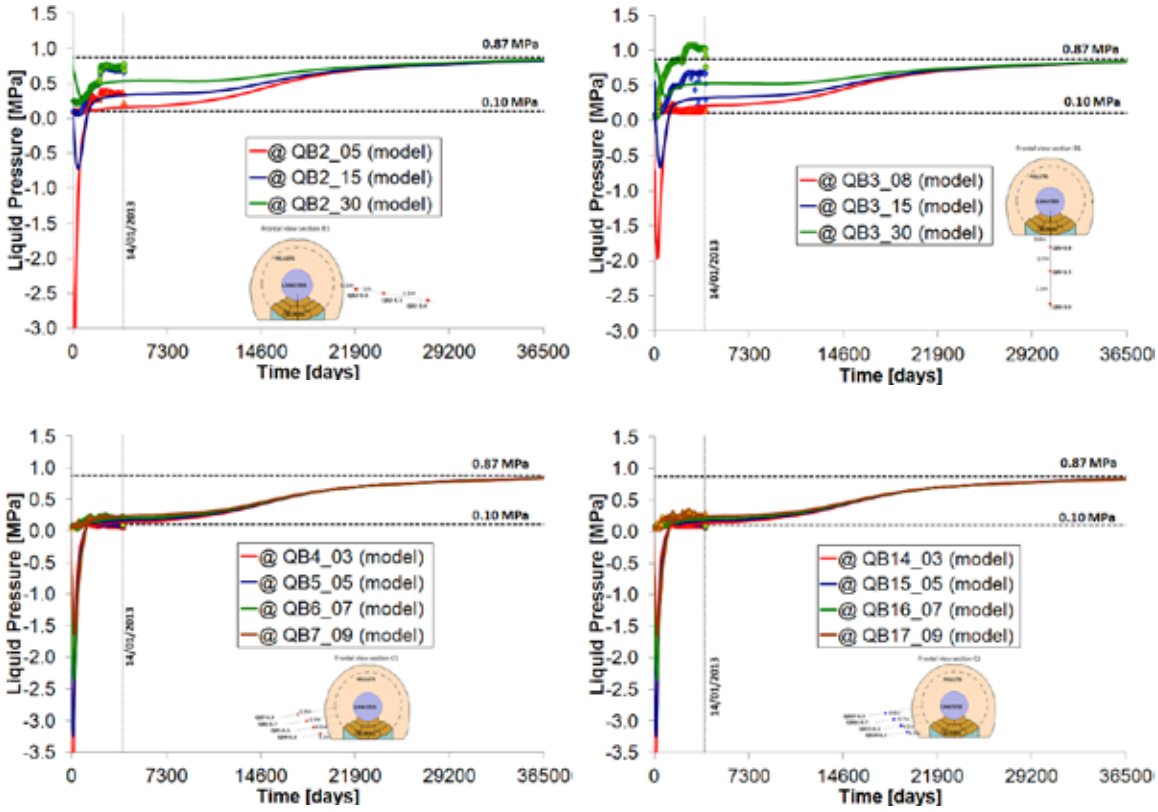

Fig. 3.4 Long-term computations for the evolution of pore water pressure in the near field of the experiment. Symbols represent measurements from the piezometers installed in section B1 (up) and sections C1 (down, at the left) and C2 (down, at the right).

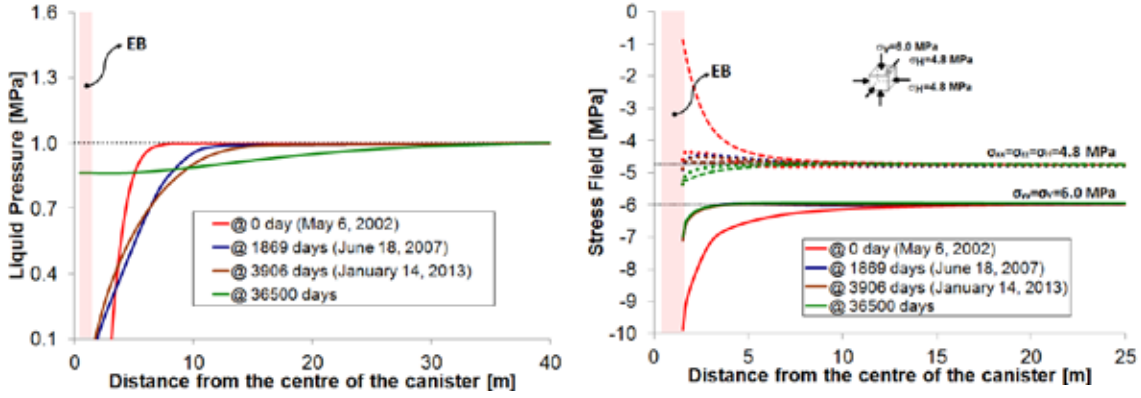

(a) (b)

Fig. 3.5 (a) Pore water pressure profiles at different times; (b) Stress field profiles in the rock at different times. Full lines represent the computed distribution of the vertical stress field (σ_{yy}) while dashed and pointed lines represent the distribution of the horizontal stresses (σ_{xx} and σ_{zz}, respectively).

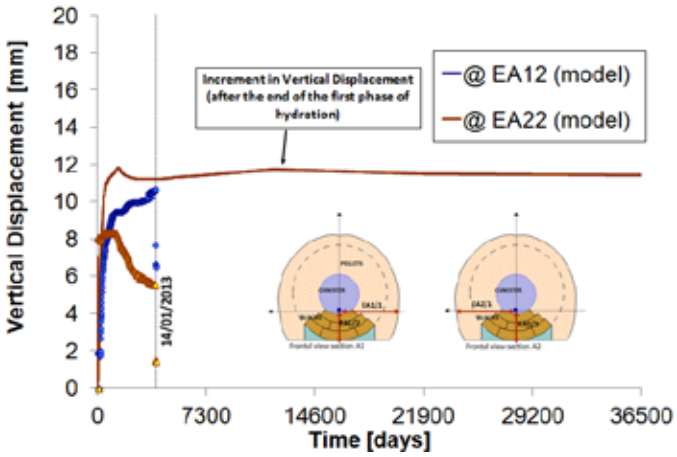

Fig. 3.6 Long-term evolution of the vertical movement of the canister after the first phase of hydration. Symbols represent the measurements recorded during the EB experiment.

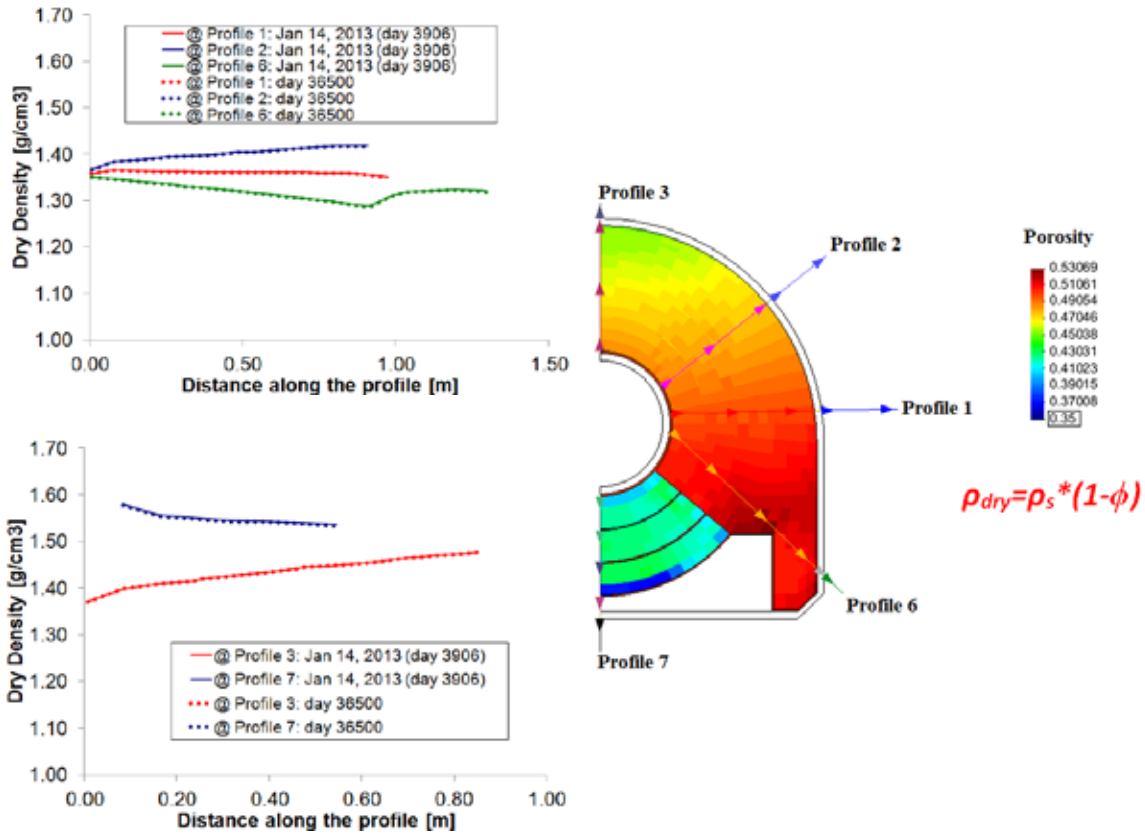

Fig. 3.7 Model computations of the distribution of dry density along radial profiles in the middle section of the EB experiment (section E) at dismantling time (full lines) and 100 years after the beginning of hydration test (dotted lines). Spatial distribution of porosity at the end of the long-term analysis is shown on the right.

3.3 Concluding remarks

The analysis of the EB experiment has been continued until reaching a time of 100 years to examine the long-term behaviour of an engineered barrier under isothermal conditions. Since the barrier is in a state of saturation or near saturation at the end of the EB field test, few changes are computed in the extended analysis. Basically, the rock mass returns to the initial state before excavation and buffer emplacement, and the barrier naturally stays saturated.

The most relevant observation is the fact that the degree of heterogeneity remains unchanged so the distribution of porosity (or dry density) observed at dismantling remains frozen in time. It is likely that this conclusion is quite dependent on the degree of irreversibility implicit in the constitutive model of the barrier material. Although the constitutive model and parameters used have proved very adequate when modelling the observed behaviour of the test, it is conceivable that different constitutive models could lead to potentially different results. This is an issue that probably deserves more attention in the future. It should also be noted that no creep phenomena (i.e. deformation under constant effective stress) have been considered either in the buffer or in the rock. If creep is relevant over the long period considered, it would probably lead to a higher degree of homogenization. Creep is potentially an important phenomenon in long-term predictions and should be the subject of focused research.

4 Modelling Case 2: Thermo-Hydro-Mechanical Evolution of the Buffer (T <= 100 °C)

This case is based on the Spanish disposal system in granitic rock and its expected early time evolution as described by the Enresa Performance Assessment exercise, named Enresa 2000 (Enresa, 2001) and the R&D programme on bentonite material, particularly the FEBEX project (Enresa, 2006). Two case variants are considered, one is a long-term simulation with constant thermal output after reaching a maximum temperature of 100 °C, which is not realistic but included for reference, the other incorporates a realistic thermal output of the emplaced canisters.

The repository concept in granite considers the disposal of spent fuel in carbon steel canisters in long horizontal disposal drifts. Canisters are surrounded by high-density bentonite. A canister measures 4.54 m in length and 0.90 m in diameter, and contains 4 PWR or 12 BWR fuel elements in a subcritical configuration. The thickness of the wall of the canister is 0.10 m at the cylindrical wall and 0.12 m at the ends, and is capable of withstanding the pressures to which it is subjected under disposal conditions and of providing a minimum period of containment of one thousand years. After being unloaded from the reactor, the fuel elements are temporarily stored for their thermal power to decay to a level at which they may be disposed of with a total thermal power of 1220 W per canister.

Canisters are disposed in cylindrical disposal cells, constructed with blocks of pre-compacted bentonite. Pre-compacted bentonite blocks, of 1700 kg/m^3 dry density (in order to achieve a final dry density of 1600 kg/m^3), are used. The blocks are initially non-saturated (degree of saturation of 66%). The disposal drifts of 500 m in length and 2.4 m in diameter (see Fig. 4.1) are located at a depth of 500 m in the host formation. The separation between canisters is determined mainly by thermal constraints. Separations of 2.0 m between canisters and 35 m between disposal drifts have been established, in order not to exceed a temperature of 100 ºC in the bentonite. Actual separation is a function of the properties of the host rock. The detailed dimensions of an individual “cell” are shown in Fig. 4.2. Once a disposal drift is completed, it is sealed with a 6 m long seal made of bentonite blocks and closed with a concrete plug at its entry.

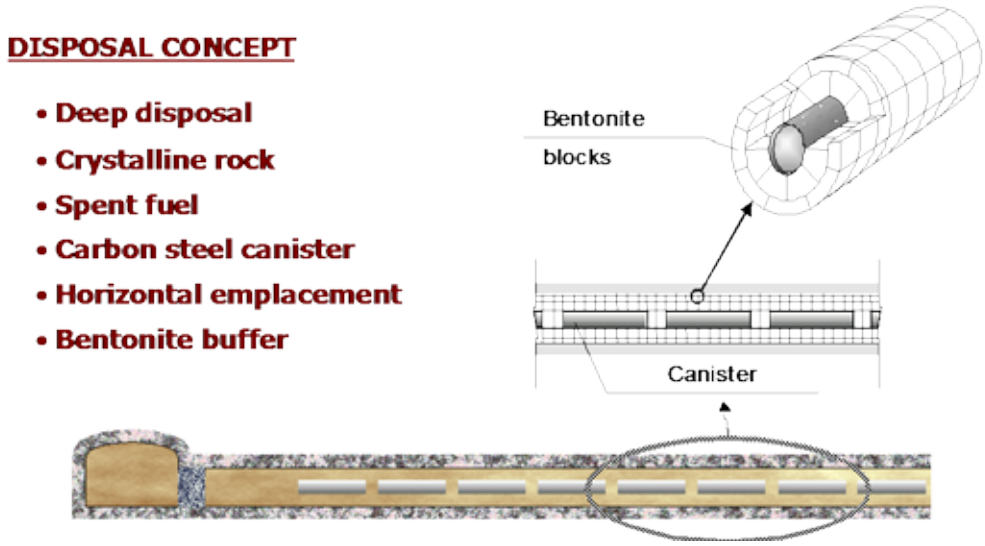

Fig. 4.1 Longitudinal section of a disposal drift

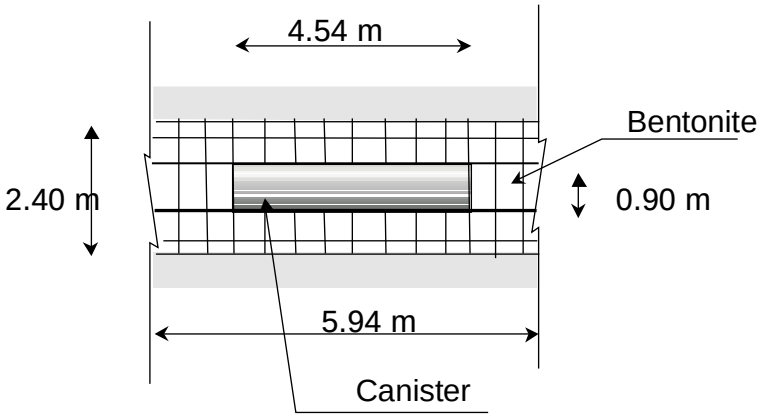

Fig. 4.2 Dimensions of an individual disposal cell

Figures 4.3 and 4.4 show a schematic top view of the disposal arrangement and details of an individual cell, respectively. Once a disposal drift is completed, it is sealed with a 6 m long seal made of bentonite blocks and closed with a concrete plug at its entry. After completion of all the disposal drifts, main drifts, ramp, shafts and other remaining rock cavities will be backfilled with a mixture of bentonite and natural sand or an appropriate crushed material.

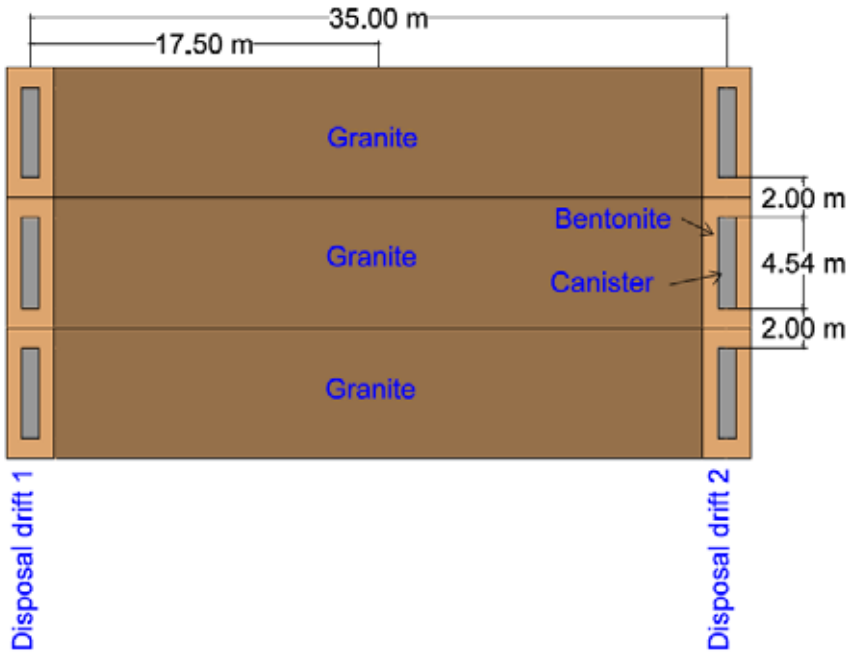

Fig. 4.3 Top view of disposal drifts in the repository system.

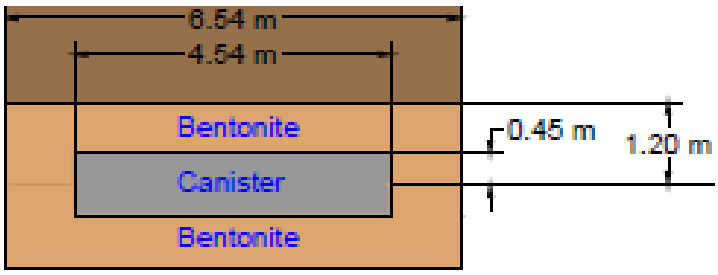

Fig. 4.4 Individual disposal cell.

The residual thermal power of a spent fuel element right after being unloaded from the nuclear reactor is 7114 W, and decreases rapidly (Fig. 4.5). After 5 years of cooling it is 1030 W, 305 W after 50 years, 29.5 W after 1000 years and 0.22 W after one million years. Enresa 2000 considered a cooling time of 50 years before disposing of the spent fuel in the geological repository. Enresa considers four elements per canister, leading to a thermal power of 1220W at the beginning of the geological storage.

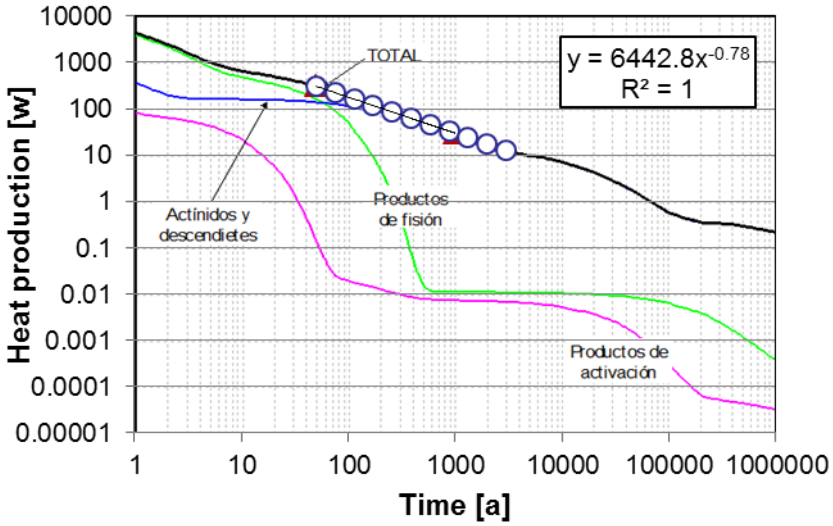

Fig. 4.5 Residual thermal power of a spent fuel element (Enresa, 2001)

4.1 Simulation by CIMNE

4.1.1 Description of the case

The proposed case attempts to replicate representative conditions in a repository envisaging a clay barrier surrounded by a hard rock. The simulations were carried out using:

- the conventional formulation (OBC model)
- a formulation incorporating thermo-osmosis (THO model)
- a formulation incorporating micro-fabric evolution using a double structure constitutive law (DS model)

The details of these formulations are presented in Deliverable 3.5-2 (Gens & Sanchez, 2014). This long term analyses were extended up to 1000 years and the evolutions of key main THM variables at different positions in the engineered and natural barrier were studied.

The main goal of the numerical analysis is to determine the evolution of the bentonite buffer in terms of its thermal, hydraulic and mechanical behaviour under natural repository conditions for a period of 1000 years. The problem was approached using a two-dimensonal axisymmetric section of an individual disposal cell that contains the host

rock (granite), the buffer (bentonite) and the canister (steel). Figure 4.6 presents a scheme showing the problem analysed. The 17.5 m length of the domain corresponds to the 35 m separation between disposal drifts.

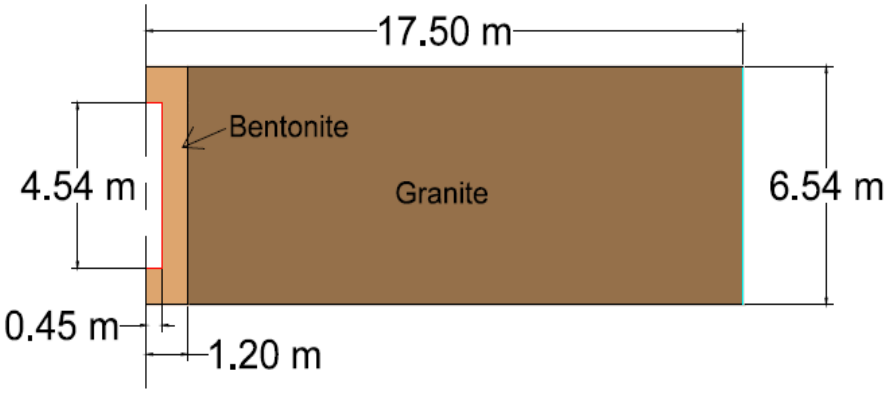

Fig. 4.6 Size of the individual disposal cell.

Figure 4.7 shows the 1565 quadrilateral-elements mesh adopted in the analyses. This mesh was adopted after a sensitivity analyses aimed at exploring the dependency of the model results on mesh size. Figure 4.8 illustrates the three materials considered in the analyses (i.e. steel canister, bentonite barrier and host rock) alongside the mechanical boundary conditions considered in the analyses.

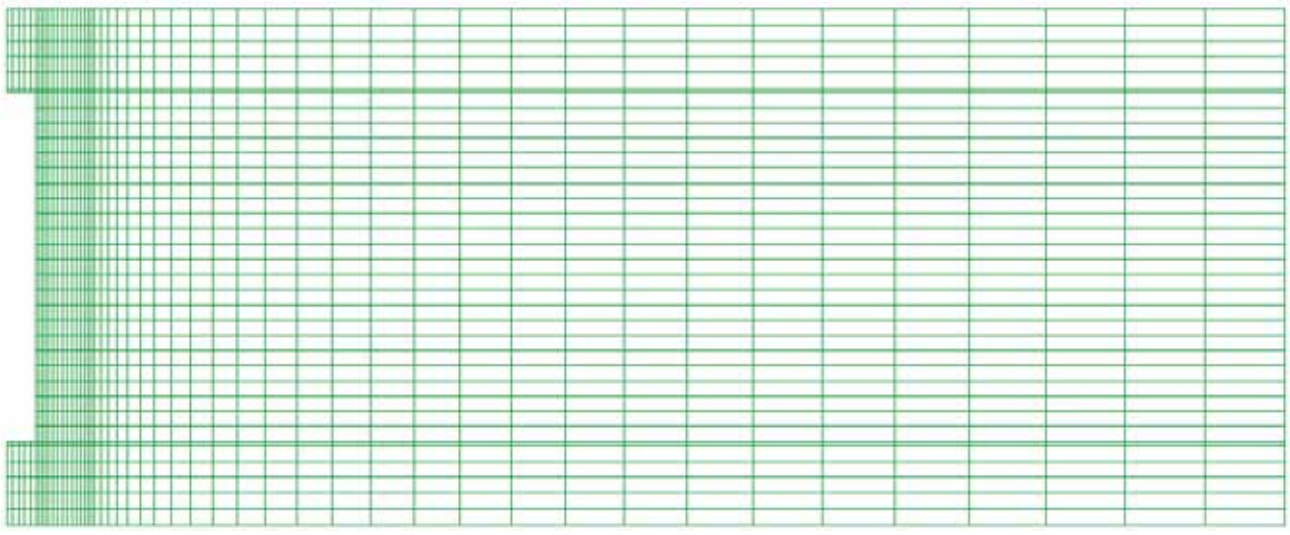

Fig. 4.7 Mesh adopted in the modelling.

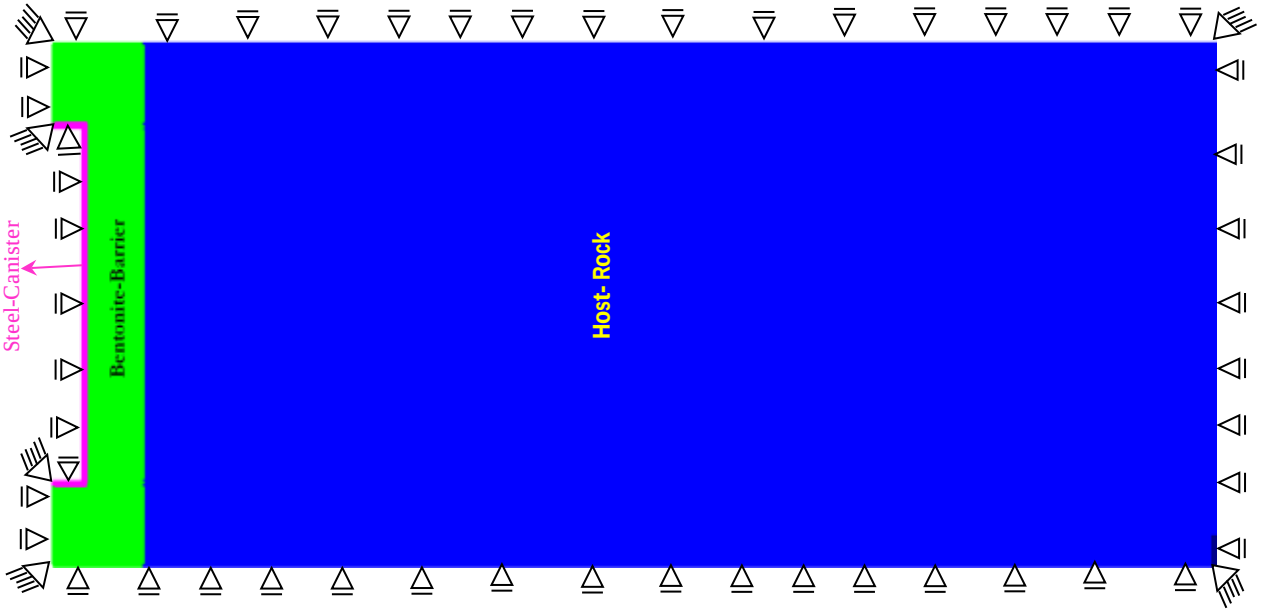

Fig. 4.8 Materials adopted in the analyses and mechanical boundary conditions considered (drawing not to scale).

The bentonite buffer was initially unsaturated with a degree of saturation of 66 %, which, according to the adopted retention curve correspond to a suction of around 44 MPa (liquid pressure of -43.9 MPa) and initial porosity of 41 %. On the other hand, the granite has an initial liquid pressure of 0.7 MPa and a porosity of 1 %. Initial isothermal conditions were assumed and a temperature of 30.5 °C was adopted for the entire domain. As for the mechanical conditions, initial stresses of 0.2 MPa and 28 MPa were considered for the bentonite and granitic rock, respectively.

Regarding the hydraulic boundary conditions, a liquid pressure of 0.7 MPa was applied at a distance of 17.50 m from the centre of the canister (green line in Fig. 4.6) at a mesh-wise temperature of 30.5 °C for a period of 30 days. This condition attempts to simulate the initial groundwater flow from the granitic rock during gallery closure. After 30 days, the hydration continues but now a thermal boundary condition is applied at the contact between the canister and the bentonite (i.e. red lines in Fig. 4.6). Two different scenarios have been considered in this study:

1. Constant Temperature of 100 °C at the contact between canister and bentonite (i.e. imposed constant thermal gradient).

2. Variable temperature accounting for the radioactive decay of the nuclear waste (i.e. variable thermal gradient)

The mechanical boundary conditions are indicated in Fig. 4.8.

The parameters used in the OBC, THO and DS models are the same as those adopted for the analyses of 1-D infiltration tests and the mock up tests reported in Deliverable D3.3-3 (Sanchez & Gens, 2014). For completeness, they are presented here as well. Specifically, parameters for the bentonite barrier for the mechanical, hydraulic and thermal problems for the OBC case are presented in Tables 4.1, 4.2 and 4.3.

Tab. 4.1 Mechanical parameters used for the bentonite in the OBC case to perform the numerical analysis in the buffer exercise.

Parameter	Value	Parameter	Value
k_{i0}	**0.05**	a_{ss}	**0**
k_{s0}	**0.25**	a_{is}	**-0.003**
m	**0.4**	a_{sp}	**-0.1609**
l_0	**1.5**	p_{ref} **[MPa]**	**0.01**
r	**0.75**	a_0	**1.50E-04**
b [MPa^{-1}]	**0.05**	T_{ref} [$^oC^{-1}$]	**20**
r_{oh} [$^oC^{-1}$]	**0.2**	a	**0.395**
k	**0.1**	p_c **[MPa]**	**0.1**
e_0	**0.5881**	**M**	**1.5**
p_0^* [MPa]	**50**		

Tab. 4.2 Hydraulic parameters used for the bentonite in the OBC case to perform the numerical analysis in the buffer exercise.

Parameter	Value	Parameter	Value
p_0 (MPa)	**30**	**Kxx.**	**6. 00x10^{-21}**
s_0	**0.072**	**Kyy.**	**6. 00x10^{-21}**
l	**0.39**	**Kzz.**	**6.00x10^{-21}**
s_{rl}	**0**	f_o	**0.399**
s_{ls}	**1**		
p_d (MPa)	**1000**		
l_d	**0**		

Tab. 4.3 Thermal parameters used for the bentonite in the OBC case to perform the numerical analysis in the buffer exercise.

Parameter	Value
λ_{dry} [W mK^{-1}]	**0.47**
λ_{wet} [W mK^{-1}]	**1.15**

For the thermo-osmosis case (THO) only one additional parameter is required, the thermo-osmotic coefficient, K_{HT}=2.73 10^{-13} m^2/K/s.

For the DS model, a new set of mechanical and hydraulic parameters are used. Thermal parameters are the same as in the OBC and THO models. The new parameters are listed in Tables 4.4 and 4.5.

The parameters for the rock are the same in all analyses. They are collected in Tables 4.6, 4.7 and 4.8.

Tab. 4.4 Mechanical parameters used in the DS model.

Parameter	Value	Parameter	Value
k_{i0}	0.005	λ_0	0.080
k_{s0}	0.001	r	0.900
n	0.400	b [MPa^{-1}]	0.200
a_{ss}	0	r_o	0.200
a_{is}	0	k	0.100
a_{sp}	0	p_c [MPa]	0.500
p_{ref} [MPa]	0.010	M	1.00
a_0	1.00x10^{-05}	a	0.530
T_{ref} [°C]	20	e_0	0.113
p_0^*[MPa]	6.00		

Tab. 4.5 Hydraulic parameters used in the DS model.

Parameter	Value	Parameter	Value
p_{0d} [MPa]	7	p_{sec} [MPa]	1100
s_0 [kN/m]	0.072	l_2	2.1
l	0.1	K_{xx} [m^2]	$5.00x10^{-20}$
s_{rl}	0	K_{yy} [m^2]	$5.00x10^{-20}$
s_{ls}	1	K_{zz} [m^2]	$5.00x10^{-20}$
p	0	f_0	0.14
d	0	**b**	50
s_d	0		

Tab. 4.6 Mechanical parameters used for the granitic rock in the OBC, THO and DS cases.

Parameter	Value
Kp [MPa]	**29166.70**
Ks [MPa]	**$1.0x10^{+09}$**
m	**0.3**
a_T	**$23.4x10^{-06}$**

Tab. 4.7 Hydraulic parameters used for the granitic rock in the OBC, THO and DS cases.

Parameter	Value	Parameter	Value
p_0 (MPa)	**2.1**	**K_{xx}**	**$8.00x10^{-18}$**
s_0	**0.072**	**K_{yy}**	**$8.00x10^{-18}$**
l	**0.70**	**K_{zz}**	**$8.00x10^{-18}$**
s_{rl}	**0**	**f_o**	
s_{ls}	**1**		
p_d (MPa)	**1000**		
l_d	**0**		

Tab. 4.8 Thermal parameters used for the granitic rock in the OBC, THO and DS cases.

Parameter	Value
λ_{dry} [W mK^{-1}]	**3.6**
λ_{wet} [W mK^{-1}]	**3.6**

In the following sections the cases considered in this project are presented organized according the thermal boundary conditions quoted above (i.e. constant canister temperature analysis, and ii) variable canister temperature considering thermal decay of the heat source).

4.1.2 Results of the analyses

4.1.2.1 Constant canister temperature analysis

The analyses presented in this section correspond to the hypothetical case in which the temperature in the canister is constant over the time. The main results related the operation base case (OBC), hydraulic threshold gradient (THO) and double structure models (DS)

The following figures show the evolution of temperature, degree of liquid saturation, liquid pressure and stresses at different locations along the system determined with the *OBC model*.

Figure 4.9 shows the evolution of temperature in the buffer for a period of 15 years at different positions from the canister. An increase in the temperature values in all the positions up to the first 30 days is observed. After this time, it can be noted that the values start to stabilize, reaching a steady state condition.

This can also be seen in the long-term predictions (Fig. 4.10) where the model predicts a constant temperature up to 1000 years. As expected, the value of temperature in the heat source reaches a maximum value of 100 °C. On the other hand, the location at 0.75 m from the canister shows the minimum temperature in the barrier after 1000 years, around 60 °C.

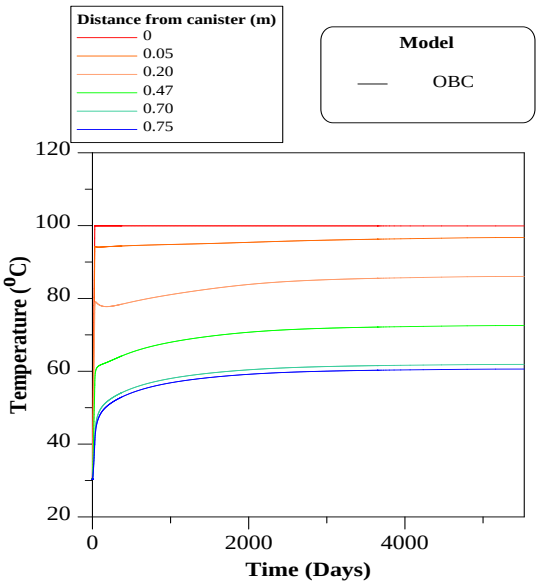

Fig. 4.9 Evolution of temperature inside the bentonite buffer up to 15 years at different positions from the canister.

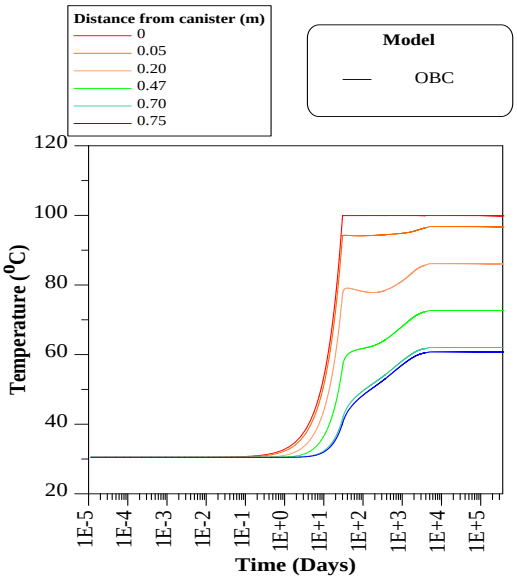

Fig. 4.10 Evolution of temperature inside the bentonite buffer up to 1000 years at different positions from the canister.

Figure 4.11 shows the evolution of temperature in the granitic rock for a period of one year at different positions from the canister. It is observed an increase in the temperature values in all the positions up to the first 30 days. After this time, it can be noted that the values start to stabilize, reaching a steady state condition. This can be seen in the long term predictions (Fig. 4.12) where the model predicts a constant temperature

up to 1000 years. According to the plot, the range of temperature expected in the granite is between 35 °C and 60 °C.

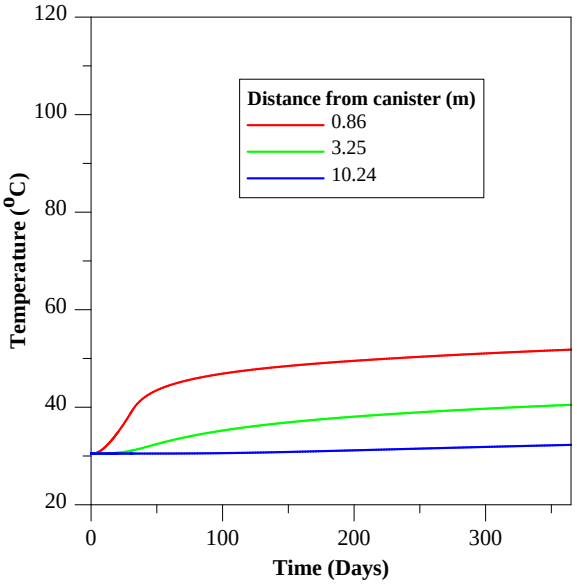

Fig. 4.11 Evolution of temperature inside the granitic rock up to 1 year at different positions from the canister.

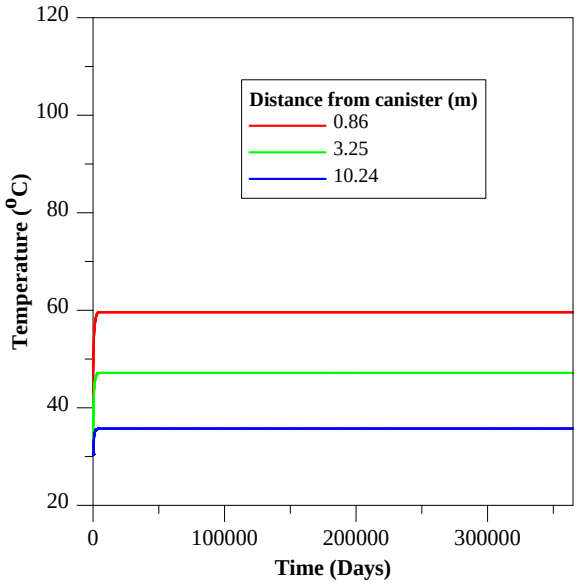

Fig. 4.12 Evolution of temperature inside the granitic rock up to 1000 years at different positions from the canister.

The results of liquid degree of saturation are shown in the following figures. Figure 4.13 shows the predicted values of the degree of saturation for different positions inside the buffer. In the positions close to the hydration front (i.e. away from the canister), an increase in the values can be observed as saturation continues. The saturation rate in

these positions is very high and as a result, they achieve a fully saturation condition in a short time (around 4 years). However, in positions closer to the canister, a longer period of time is necessary to reach fully saturation. Another important observation regarding the sections close to the heat source is the drying experienced in these locations at the early stages of the simulations. This episode starts with a reduction in the values of degree of saturation up to the first year. After that period of time, the values start to increase and saturation is achieved in the first 10 years.

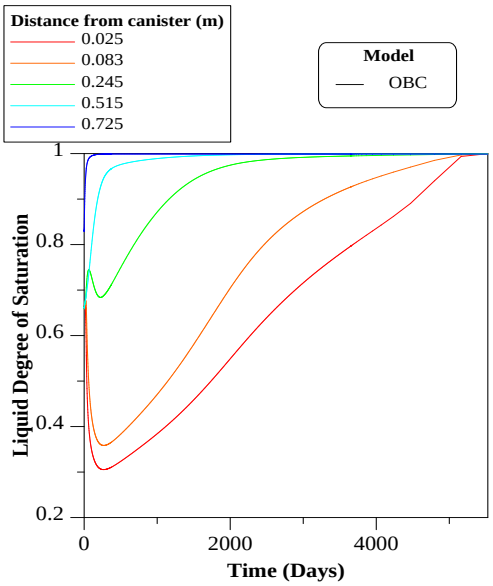

Fig. 4.13 Evolution of degree of liquid saturation inside the bentonite buffer up 15 years at different positions from the canister.

Therefore, the model is predicting that the buffer will be fully saturated after 10 years of hydration. Regarding the results obtained for the positions inside the host-rock, it can be noted from Fig. 4.14 that a fully saturation condition was achieved in a very short time. The host rock is initially saturated, it desaturates at the beginning of the analyses because of the very high hydraulic gradient that transfer water from the rock to the clays. However, in a relatively short time the position closer to the clay barrier, reached full saturation, in around 50 days. Figure 4.15 shows the long term evolution (i.e. 1000 years) of the degree of saturation in the clay barrier.

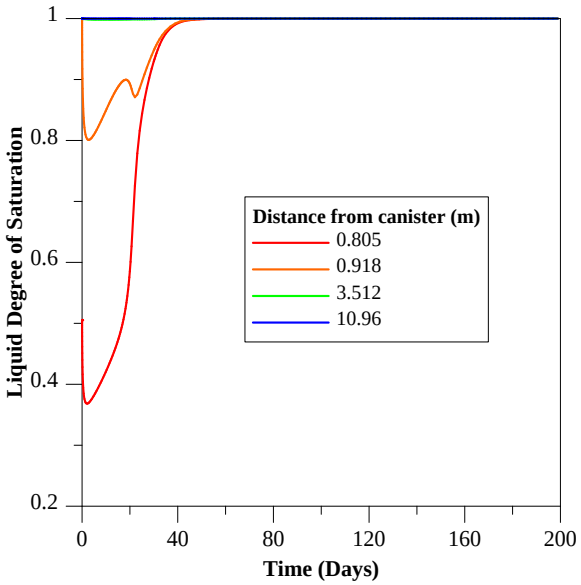

Fig. 4.14 Evolution of degree of liquid saturation inside the granitic rock up to 200 days at different positions from the canister.

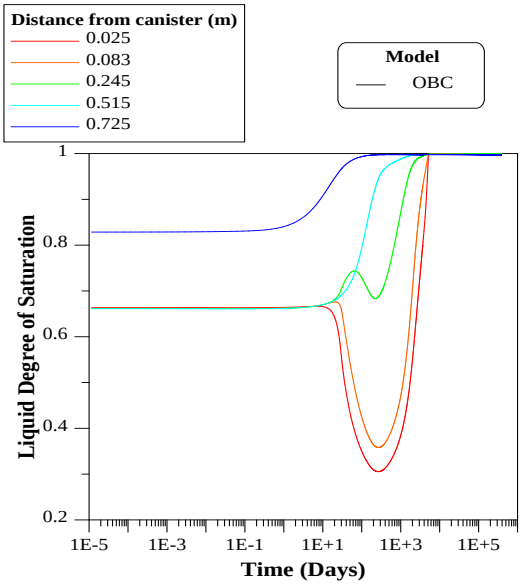

Fig. 4.15 Evolution of degree of liquid saturation inside the bentonite buffer up 1000 years at different positions from the canister.

Liquid pressure is another variable that can be examined to gain an insight the hydraulic behaviour in the barrier system. Figure 4.16 shows the numerical results of liquid pressure inside the bentonite buffer at different positions from the canister. The positions close to the hydration source, experience an increase in the liquid pressure because of the progressive saturation occurring in this boundary. A value of zero liquid pressure is achieved due to a fully saturation condition. On the other hand, the loca-

tions near to the canister experience a reduction in the values of liquid pressure because of the drying taking place in this area.

The drying process starts when there is a desaturation in the pore space. In this scenario, the liquid water inside the pores is transformed to vapour, resulting in an increase of gas pressure that leads to a decrease in the liquid pressure. After a period of time this process is reversed and the liquid pressure starts to increase until it reaches a fully saturation condition where it has a value equal to zero.

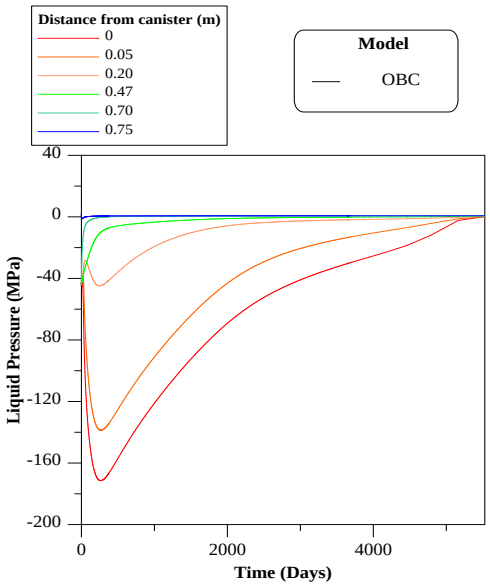

Fig. 4.16 Evolution of liquid pressure inside the bentonite buffer up to 15 years at different positions from the canister.

As determined previously, the time at which this condition occurs is around 10 years. The results from the points located inside the rock are shown in Figure 4.17. The long term predictions inside the clay-barrier in terms of liquid pressure are presented in Fig. 4.18.

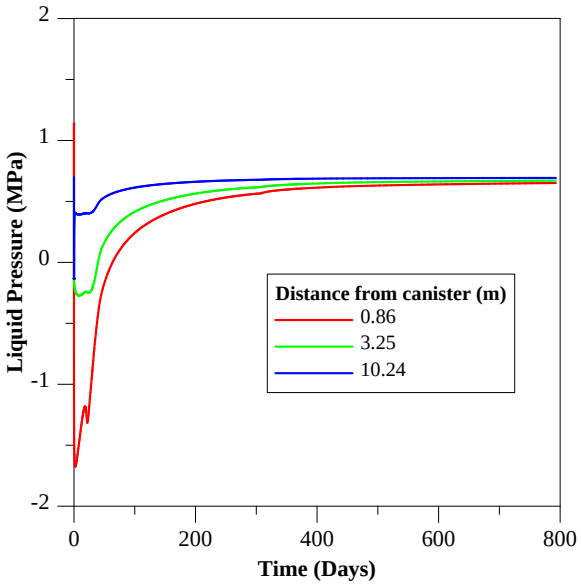

Fig. 4.17 Evolution of liquid pressure inside the host-rock up to 800 days at different positions from the canister.

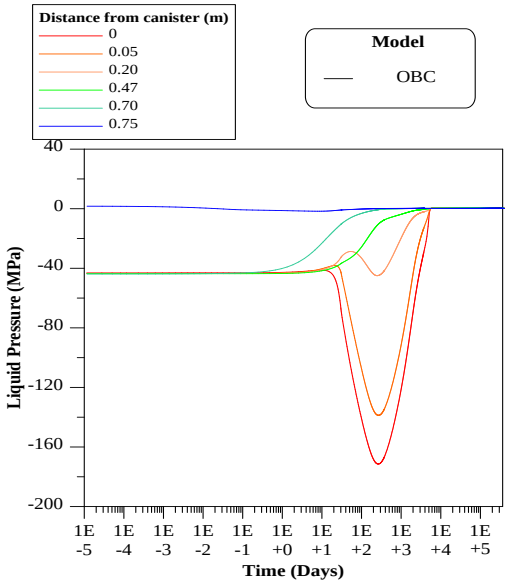

Fig. 4.18 Evolution of liquid pressure inside the bentonite buffer up to 1000 years at different positions from the canister.

The mechanical behaviour of the repository can be analysed by exploring the evolution of normal stresses on each component of the system. Figure 4.19 presents the numerical results of normal stress at different position in the clay-buffer. It can be observed that the stresses in all the positions increase as the buffer saturation progresses. Since this is a problem with displacement restrictions at the boundary (i.e. global constant

volume conditions), the stresses are induced by the swelling pressures of the bentonite under volume constraints conditions.

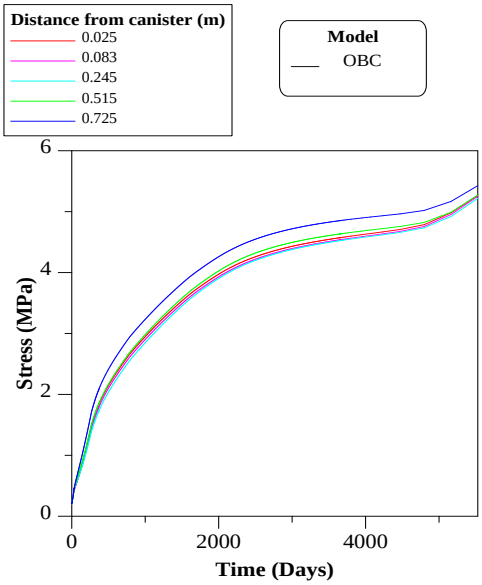

Fig. 4.19 Evolution of normal stress inside the bentonite buffer up to 15 years days at different positions from the canister.

As we can see from this Fig. 4.19, the point closest to the hydration front is the one with the maximum value of stress close to 5.60 MPa. Once saturation is achieved, the swelling pressure remains constant until the end of the simulation. Figure 4.20 presents the long term evolution of the stresses in the clay barrier and Figure 4.21 shows the stress evolution obtained at different positions along the host-rock.

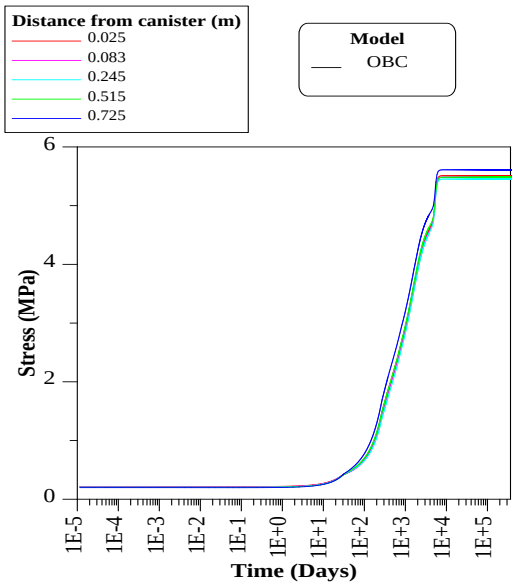

Fig. 4.20 Evolution of normal stress inside the bentonite buffer up to 10000 days at different positions from the canister.

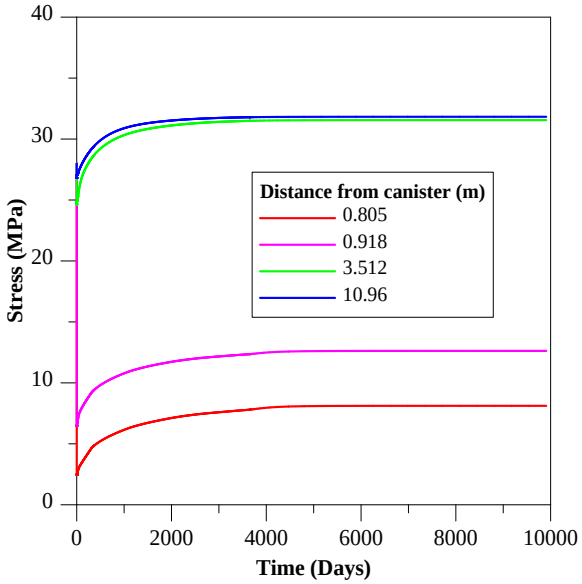

Fig. 4.21 Evolution of normal stress inside the granitic rock up to 10000 days at different positions from the canister.

The following figures show some selected results obtained using the *thermo-osmosis THO model* related to the evolution of temperature, liquid degree of saturation, liquid pressure and stresses at different locations along the system calculated with the thermo-osmosis model. In all the figures, the results related to the OBC model have included as a reference for the comparisons.

Figure 4.22 shows the evolution of temperature inside the buffer for a period of 15 years at different positions from the canister. It is observed an increase in the temperature values in all the positions up to the first 30 days. After this time, it can be noted that the values start to stabilize, reaching a steady state condition. This can be seen in the long term predictions Fig. 4.23 where the model predicts a constant temperature up to 1000 years. As expected, the value of temperature in the heat source reaches a maximum value of 100 °C. On the other hand, the location at 0.75 m from the canister shows the minimum temperature in the barrier after 1000 years with a value close to 57 °C.

For the plots commented above, it can be observed that the differences between the OBC and THO predictions are minimal.

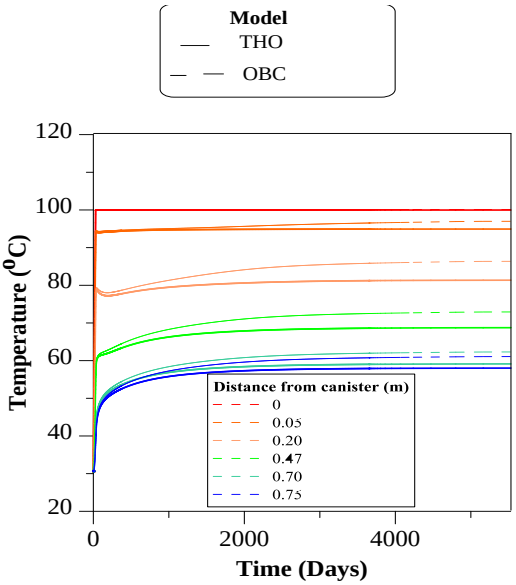

Fig. 4.22 Evolution of temperature inside the bentonite buffer up to 15 years at different positions from the canister.

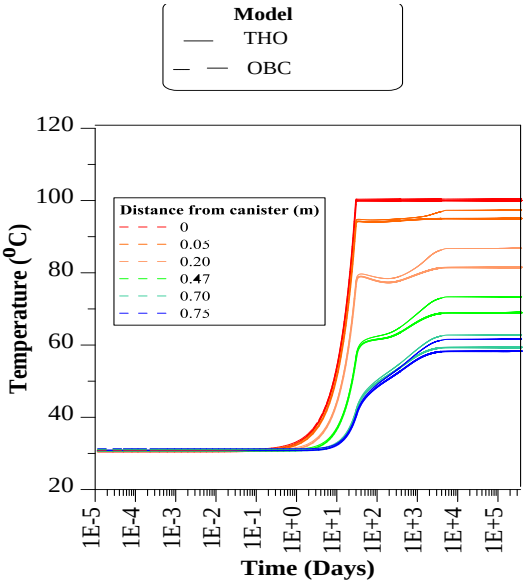

Fig. 4.23 Evolution of temperature inside the bentonite buffer up to 365000 days (1000 years) at different positions from the canister.

The results of degree of liquid saturation are shown in the following figures. Figure 4.24 shows the predicted values of degree of saturation with the thermo-osmosis and OBC models for different positions inside the buffer. It can be observed that the presence of the thermo-osmotic flow is able to slow down significantly the hydration rate inside the buffer, especially in the positions closer to the canister.

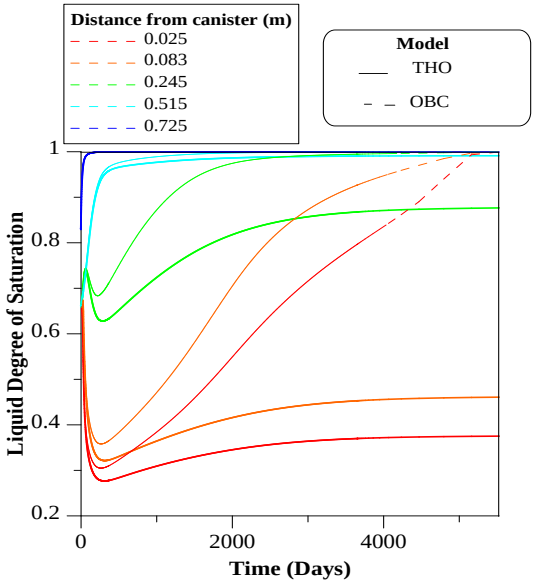

Fig. 4.24 Evolution of degree of liquid saturation inside the bentonite buffer up to 15 years at different positions from the canister.

As discussed before, this reduction in the hydration of the bentonite is mainly due to the thermo-osmotic flux that transfers water in the liquid phase from the zones close to the heater to those with lower temperature. Figure 4.25 presents the long term results in term of degree saturation inside the clay barrier. It can be noted that the incorporation of this model to the analysis prevented the full saturation of the clay barrier.

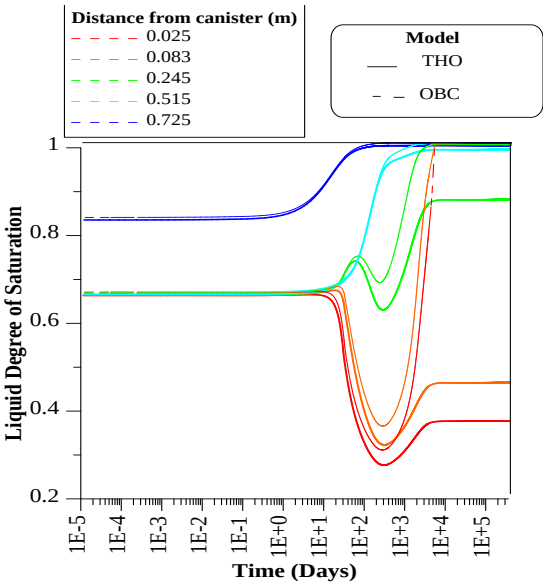

Fig. 4.25 Evolution of degree of liquid saturation inside the bentonite buffer up to 1000 years at different positions from the canister.

Figure 4.26 presents the evolution of the degree of degree saturation in the host rock. As explained for the OBC case. The host rock is initially saturated, but become unsaturated at the beginning of the analyses because of the water transfer driven by the very high hydraulic gradient that transfer water from the rock to the clays. However, in a relatively short time the position closer to the clay barrier, reached full saturation, in around 50 days. There are not significant differences between OBC and THO results.

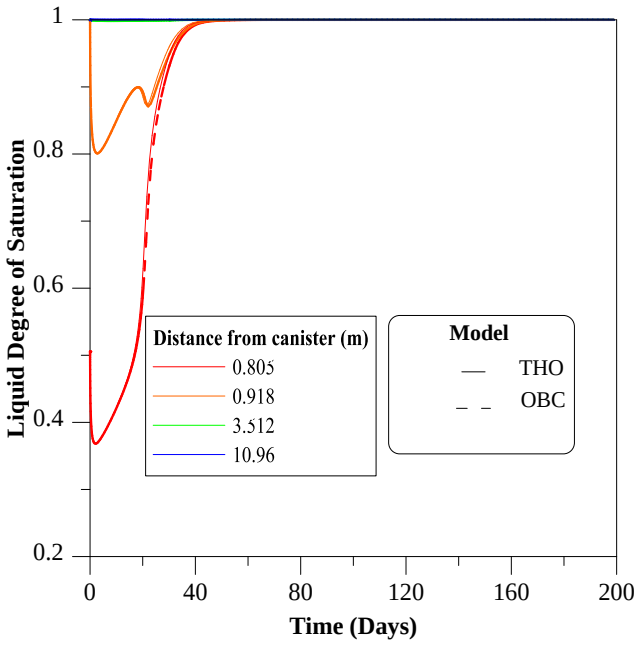

Fig. 4.26 Evolution of degree of liquid saturation inside the granitic rock up to 200 days at different positions from the canister.

Figure 4.27 shows the numerical results of liquid pressure in the bentonite buffer at different positions from the canister determined by the thermo-osmosis model. The positions close to the hydration source, experience an increase in the values of liquid pressure because of the progressive saturation occurring in this boundary.

These locations are barely affected by the thermo-osmotic flow and as a result, similar predictions are obtained from the two models. On the other hand, the locations near to the canister experienced an important reduction in the values of liquid pressure because of the drying taking place in this area.

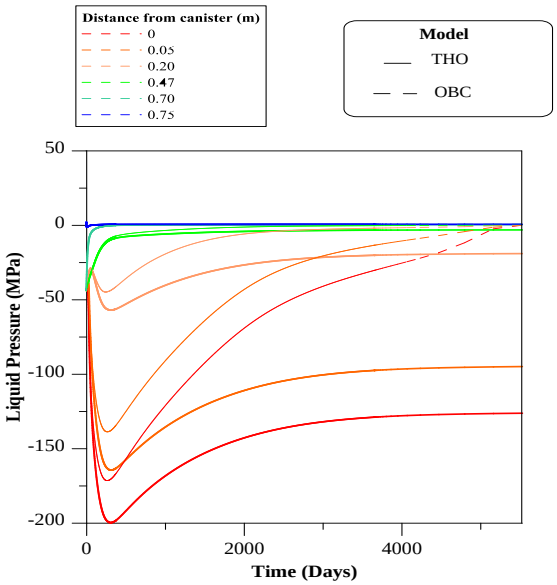

Fig. 4.27 Evolution of liquid pressure inside the bentonite buffer up to 3650 days (10 years) at different positions from the canister.

The results from the points located inside the host rock are shown in Fig. 4.28. Figure 4.29 shows the long term predictions related to the liquid pressure in the clay-barrier.

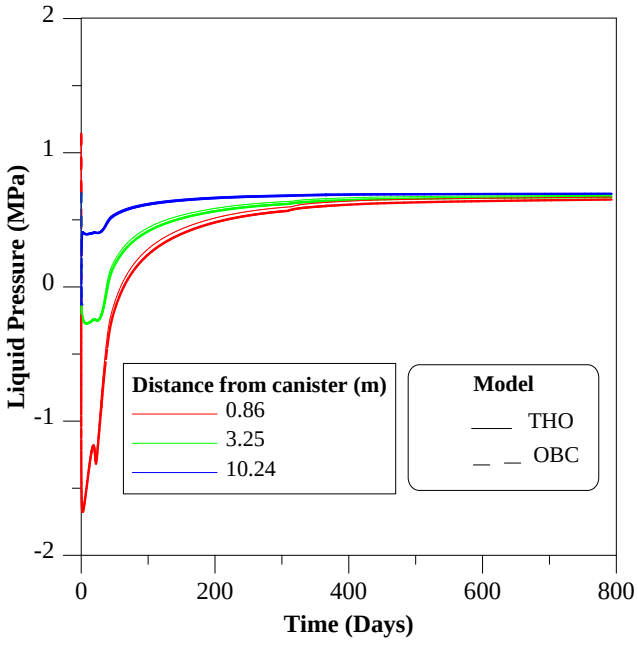

Fig. 4.28 Evolution of liquid pressure inside the granitic rock up to 800 days at different positions from the canister.

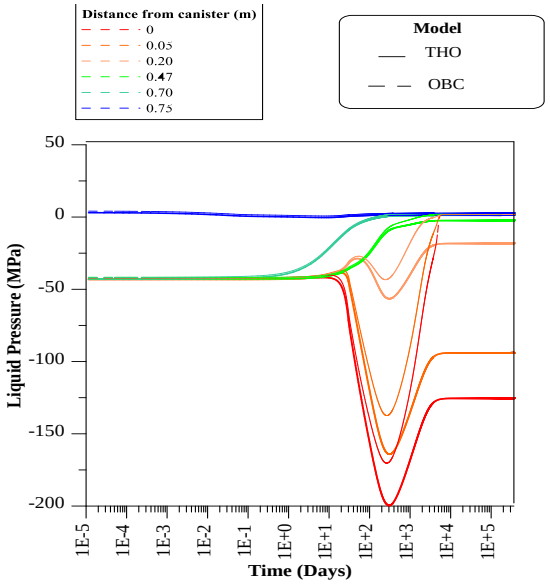

Fig. 4.29 Evolution of liquid pressure inside the bentonite buffer up to 1000 years at different positions from the canister.

The mechanical behaviour of the repository is analysed now by observing the evolution of normal stress on each component of the system. Figure 4.30 presents the numerical results of normal stress at different positions in the buffer determined with the thermo-osmosis and OBC models. It can be observed that the stresses in all the positions are increasing as the saturation in the buffer progresses.

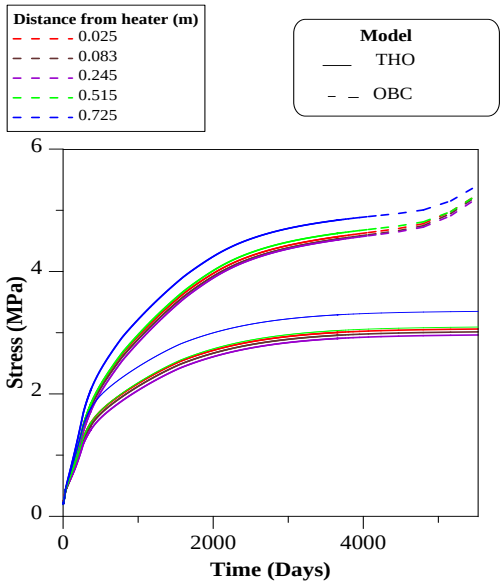

Fig. 4.30 Evolution of normal stress inside the bentonite buffer up to 15 years at different positions from the canister.

As we can see from the figure, the point closest to the hydration front is the one with the maximum value of stress close to 3.40 MPa. This value is significantly lower than the one obtained from the OBC model. This reduction in the swelling pressures is related to the reduction in the hydration rate inside the barrier. Figure 4.31 shows the results of the evolution of stress obtained from different positions in the host rock.

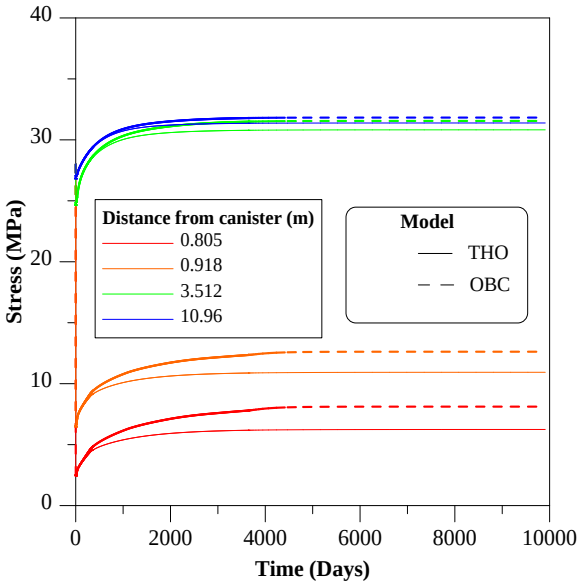

Fig. 4.31 Evolution of normal stress inside the granitic rock up to 10000 days at different positions from the canister.

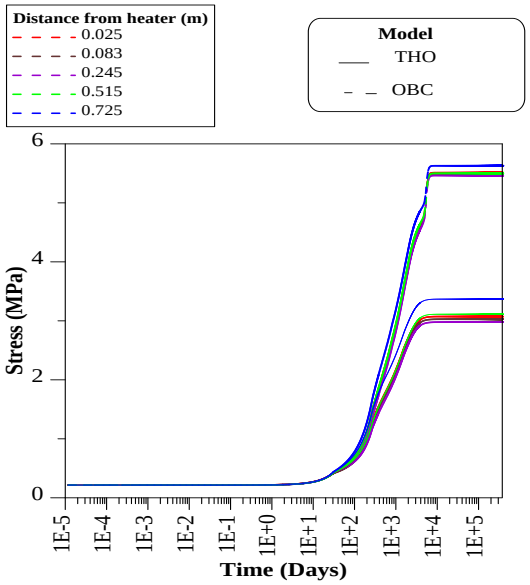

Fig. 4.32 Evolution of normal stress inside the bentonite buffer up to 10000 days at different positions from the canister.

Figure 4.32 presents the long term prediction of the stresses in the clay barrier. It can be seen that stresses predicted by the thermo-osmosis model are around 60% of the ones predicted by the OBC model.

The following figures show some selected results related to the evolution of temperature, degree of liquid saturation, liquid pressure and stresses at different locations along the system calculated with the *double structure DS model*. In all the figures, the results related to the OBC model have included as a reference for the comparisons.

Figure 4.33 shows the evolution of temperature inside the buffer for a period of 15 years at different positions from the canister. It is observed an increase in the temperature values in all the positions up to the first 30 days. After this time, it can be noted that the values start to stabilize, reaching a steady state condition. This can be seen in the long term predictions (Fig. 4.34) where the model predicts a constant temperature up to 1000 years. As expected, the value of temperature in the heat source reaches a maximum value of 100 °C.

For the plots commented above, it can be observed that the differences between the OBC and DS predictions are minimal at early stages. The differences are more noticeable in the central parts of the barrier (radii around 20 cm); they are quite small in any case (less than 1%).

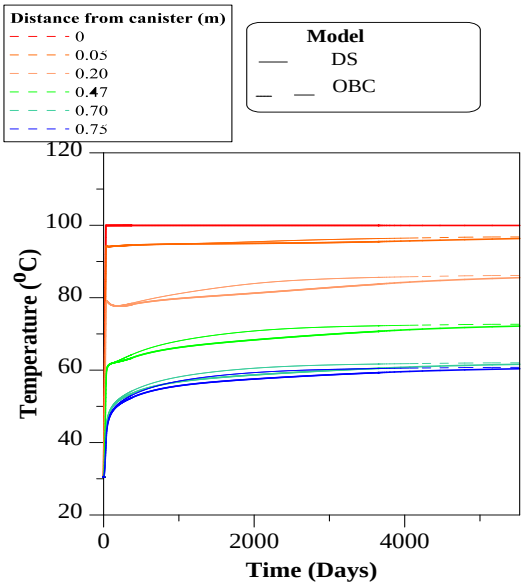

Fig. 4.33 Evolution of temperature inside the bentonite buffer up to 15 years at different positions from the canister.

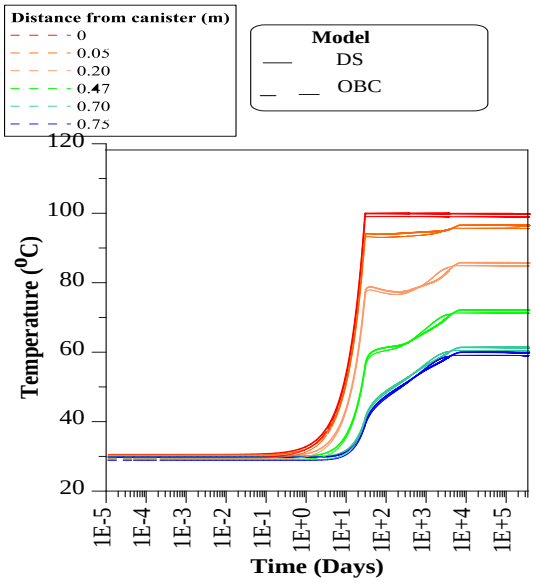

Fig. 4.34 Evolution of temperature inside the bentonite buffer up to 365000 days (1000 years) at different positions from the canister.

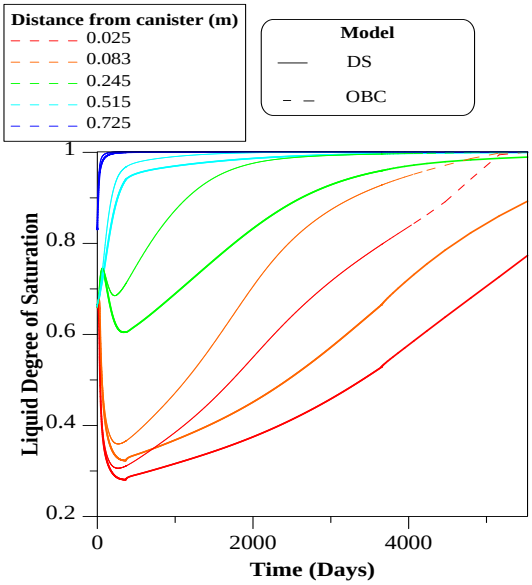

Fig. 4.35 Evolution of degree of liquid saturation inside the bentonite buffer up to 15 years at different positions from the canister.

The results of degree of liquid saturation are shown in the following figures. Figure 4.35 shows the predicted degree of saturation with the DS and OBC models for different positions inside the buffer. It can be observed that the model that considers the change in the clay fabric slows down the hydration rate inside the buffer, especially in the positions closer to the canister. Similar observations were made for the infiltration-cell and

mock-up tests. It is also clear that the impact of the changes in the clay fabric is less important than the ones observed for the thermo-osmosis effect (see Fig. 4.24).

Figure 4.36 presents the long term results in term of degree saturation inside the clay barrier. Figure 4.37 shows the numerical results of liquid pressure in the bentonite buffer at different positions from the canister determined by the thermo-osmosis model. The positions close to the hydration source, experience an increase in the values of liquid pressure because of the progressive saturation occurring in this boundary. These locations are barely affected by the change in the clay fabric and as a result, similar predictions are obtained from the two models. On the other hand, the locations near to the canister experienced an important reduction in the values of liquid pressure because of the drying taking place in this area.

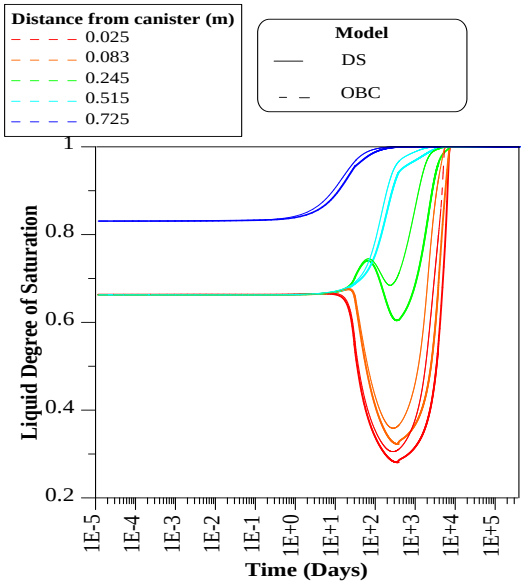

Fig. 4.36 Evolution of degree of liquid saturation inside the bentonite buffer up to 1000 years at different positions from the canister.

Figure 4.38 shows the long term predictions in term of liquid pressure. The mechanical behaviour of the repository is analysed now by looking at the evolution of normal stress on each component of the system. Figure 4.39 presents the numerical results of normal stress at different position in the buffer determined with the double structure and OBC models. It can be observed that the stresses in all the positions are increasing as the saturation in the buffer progresses.

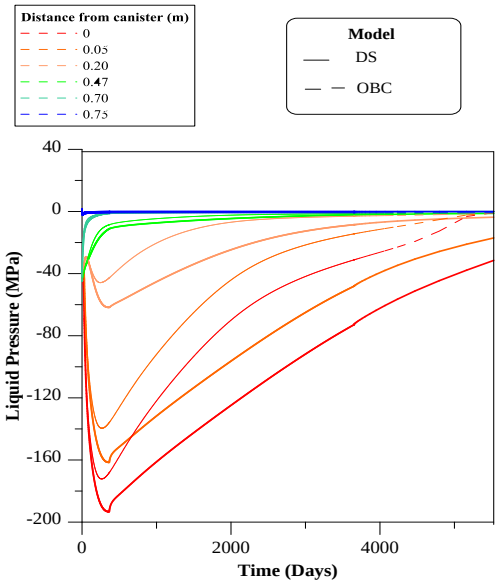

Fig. 4.37 Evolution of liquid pressure inside the bentonite buffer up to 3650 days (10 years) at different positions from the canister.

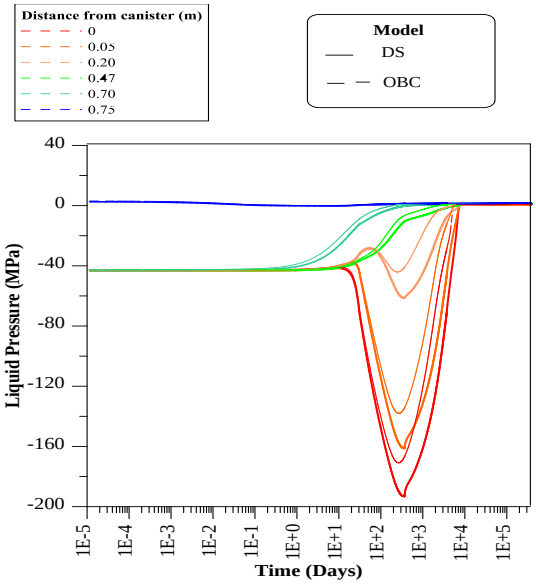

Fig. 4.38 Evolution of liquid pressure inside the bentonite buffer up to 1000 years at different positions from the canister.

It can also be seen in this figure that the point closest to the hydration front is the one with the maximum value of stress after 15 years near 4.0 MPa. This value is much lower than the one obtained from the OBC model. This reduction in the swelling pressures is related to the reduction in the hydration rate inside the barrier.

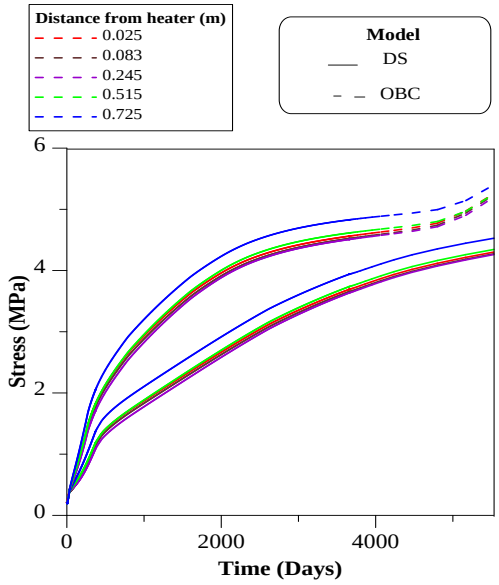

Fig. 4.39 Evolution of normal stress inside the bentonite buffer up to 15 years at different positions from the canister.

Figure 4.40 presents the long term prediction of the stresses in the clay barrier. It can be seen that stresses predicted by the double structure model are very similar to the ones predicted by the OBC model.

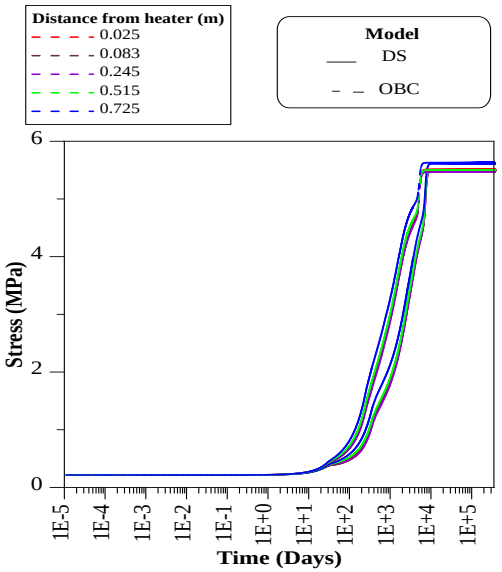

Fig. 4.40 Evolution of normal stress inside the bentonite buffer up to 10000 days at different positions from the canister.

4.1.2.2 Analysis considering thermal decay of the heat source

To maintain a constant temperature at the contact between the bentonite and the canister (as in the case variants presented in the previous Section 4.1.2.1) is not very realistic, because the power emitted by the nuclear waste will decrease in time due to the radioactive decay. Figure 4.5 presents the temporal evolution of the residual thermal power for one million years extracted from the Enresa 2000 exercise (Enresa, 2001).

Figure 4.41 presents the time evolution of the power considering the facts mentioned at the beginning of Chapter 4 (i.e. 1220 W at the start of the geological storage and a power decay following the heat evolution of Fig. 4.5). For comparison purposes the heat applied for the constant temperature case (used in the previous section) is also shown.

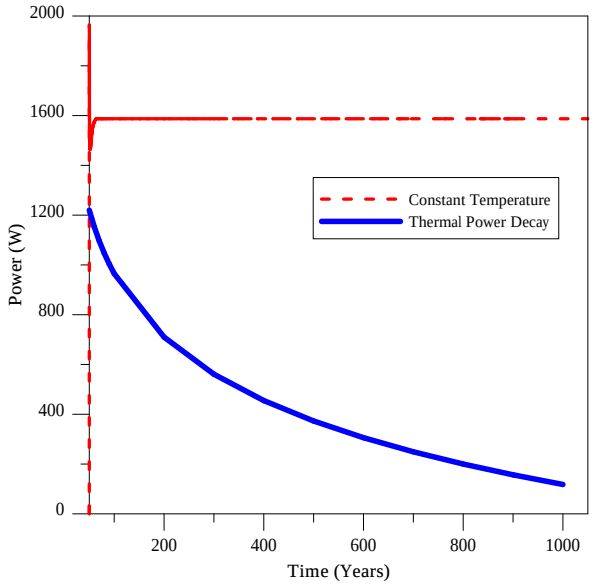

Fig. 4.41 Time evolution of the applied thermal power for the case with constant heating temperature and power decay, results up to 1000 years.

In the analyses presented in this section the heat power was reduced by steps, following the protocol indicated in Fig. 4.42. In the following sections the results corresponding to the OBC, THO and DS cases are presented.

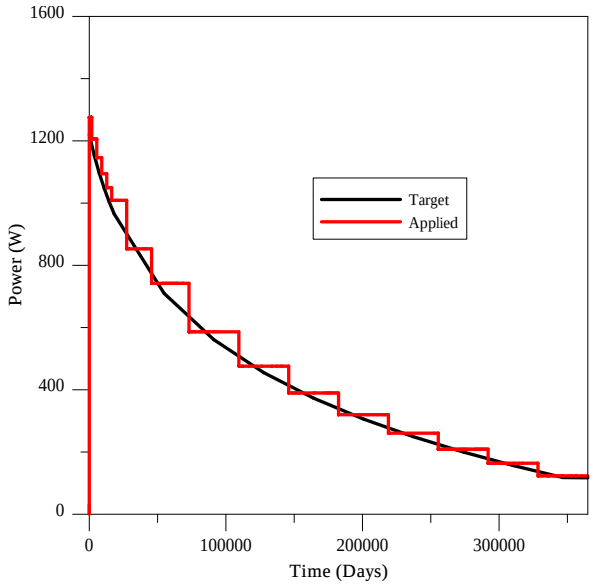

Fig. 4.42 Time evolution of the applied thermal power for the case with constant heating temperature and power decay, results up to 1000 years.

The model parameters adopted in Section 4.1.2.1 were also usedfor the *OBC analysis* presented here; with the exception that Fig. 4.42 was used for the thermal heat variation. The following figures show the evolution of temperature, degree of liquid saturation, liquid pressure and stresses at different locations along the system determined with the OBC model. Figure 4.43 shows the evolution of temperature in the buffer for a period of 15 years at different positions from the canister. An increase in the temperature values in all the positions during the first 30 days is observed. After around 500 days, it can be noted that the temperature starts to decrease at all the positions.

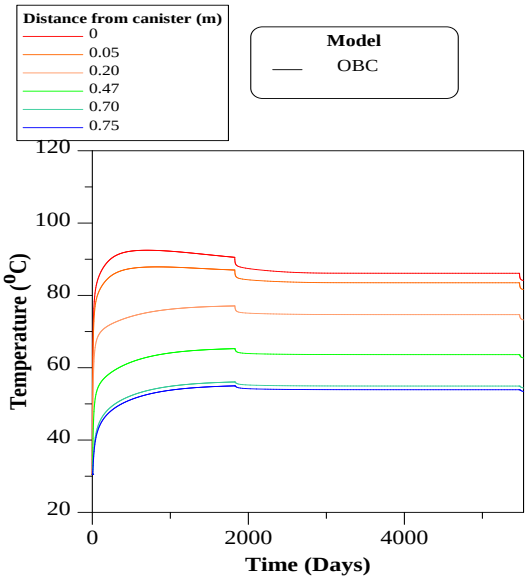

Fig. 4.43 Evolution of temperature inside the bentonite buffer up to 15 years at different positions from the canister.

This can also be observed in the long term predictions (Fig. 4.44), where the model predicts a noticeable decrease of temperature after 500 days, reaching very low values in practically all the positions of the barrier (i.e. below 40 °C) at the end of the analyses (i.e. 1000 years). As expected, the maximum temperature in the barrier is at the contact with the heater, reaching a maximum temperature just below the 100 °C (i.e. maximum around 97°C).

Figure 4.45 presents the comparisons between the case of constant temperature and thermal power decay for a period of 15 years. Figure 4.46 presents the same comparisons but for the long term (1000 years). The impact of the thermal power decay on the temperature field is evident in these two plots.

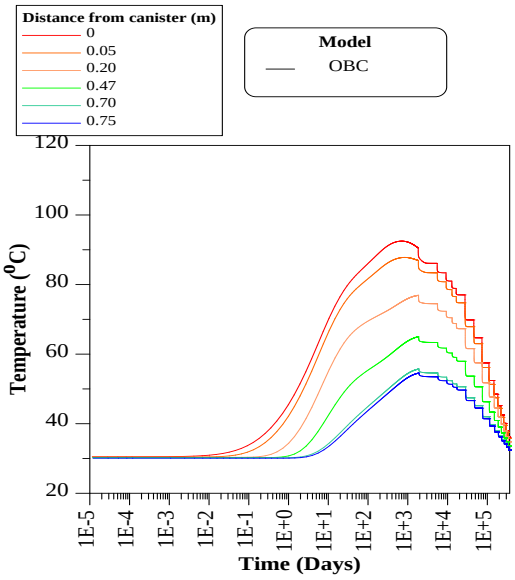

Fig. 4.44 Evolution of temperature inside the bentonite buffer up to 1000 years at different positions from the canister.

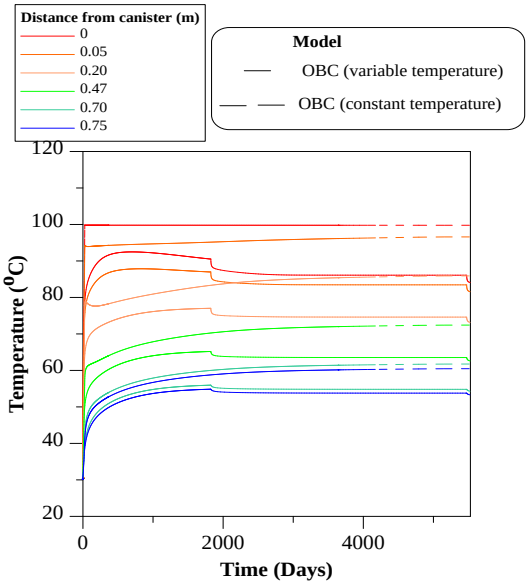

Fig. 4.45 Evolution of temperature inside the bentonite buffer up to 15 years at different positions from the canister, comparisons between variable and constant temperature analyses.

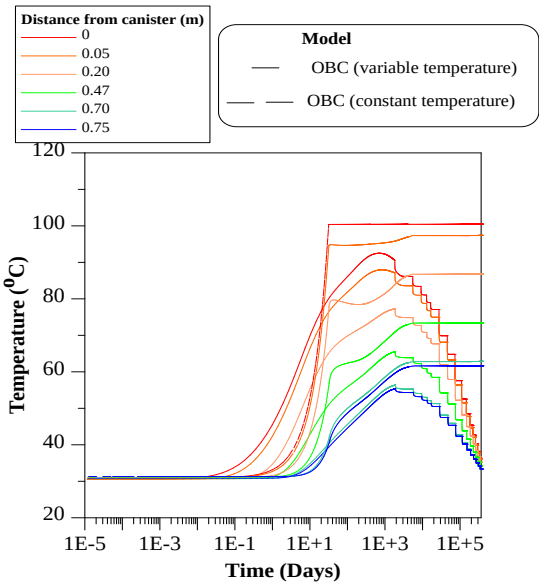

Fig. 4.46 Evolution of temperature inside the bentonite buffer up to 1000 years at different positions from the canister, comparisons between variable and constant temperature analyses.

The results of degree of liquid saturation are shown in the following figures. Figure 4.47 shows the predicted values of the degree of saturation for different positions inside the buffer.

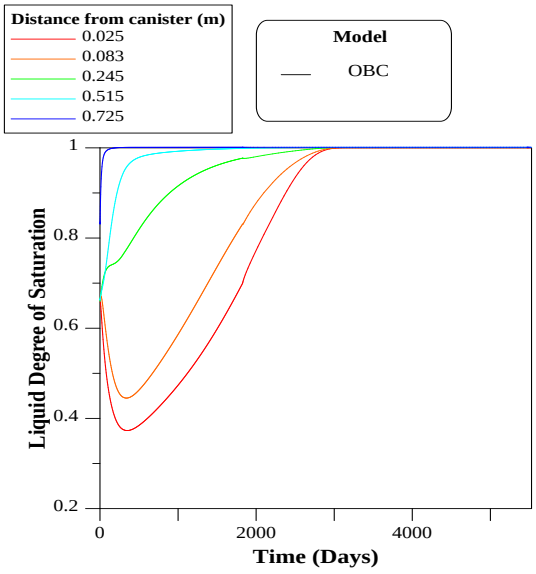

Fig. 4.47 Evolution of degree of liquid saturation inside the bentonite buffer up 15 years at different positions from the canister.

At the positions close to the hydration front (i.e. away from the canister), an increase in the values can be observed as saturation continues. The saturation rate at these posi-

tions is very high and as a result, they achieve a fully saturation condition in a considerable short time (around 3 years). However, at positions closer to the canister, a longer period of time is necessary to reach fully saturation. Another important observation regarding the sections close to the heat source is the drying experienced at these locations at early stages of the simulation.

The drying is associated with a reduction in the values of degree of saturation up to the first year. After that period of time, the values start to increase and saturation is achieved at around 8.5 years. This time is lower than the one predicted for the constant temperature case (i.e. around 10 years, Section 6.2.3.1). Figure 4.48 shows the long term evolution (i.e. 1000 years) of the degree of saturation in the clay barrier. Figure 4.49 presents the comparisons of liquid saturation between the case of constant temperature and thermal power decay for a period of 15 years. Figure 4.50 presents the same comparisons but for the long term (1000 years). It can be observed that the thermal decay contributes to a faster hydration of the barrier.

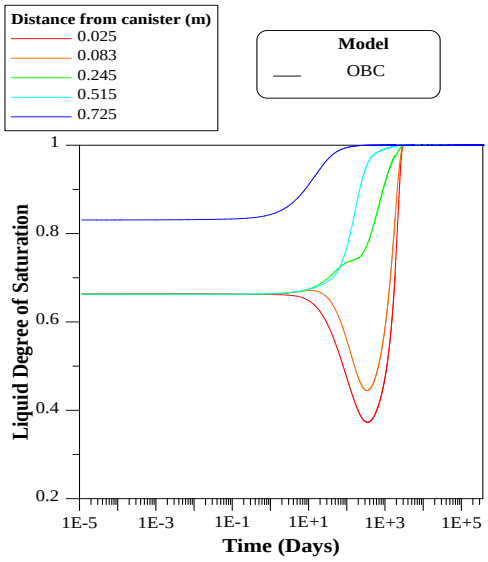

Fig. 4.48 Evolution of degree of liquid saturation inside the bentonite buffer up 1000 years at different positions from the canister.

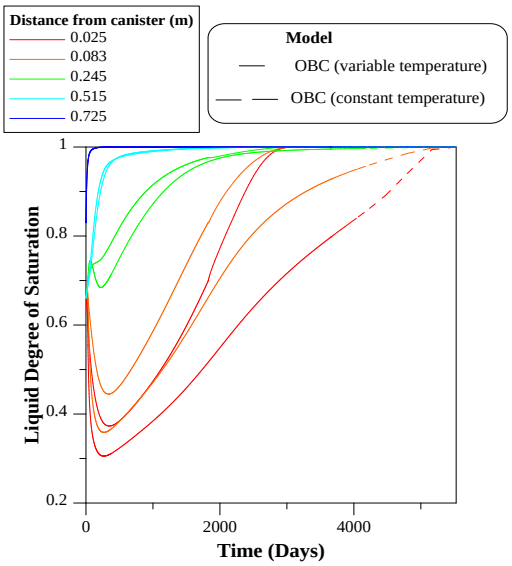

Fig. 4.49 Evolution of degree of liquid saturation inside the bentonite buffer up 15 years at different positions from the canister, comparisons between variable and constant temperature analyses.

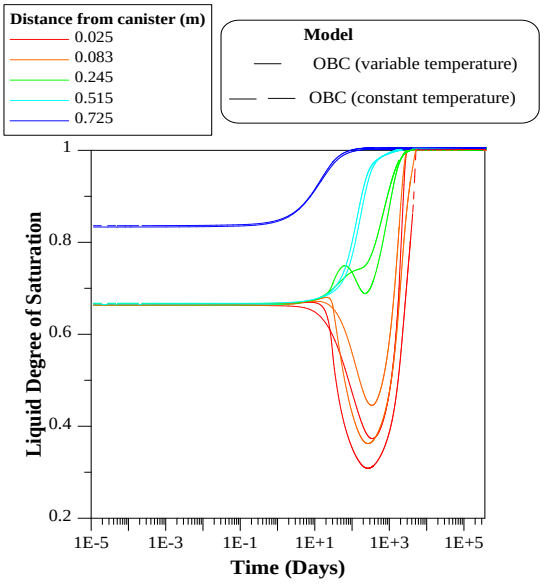

Fig. 4.50 Evolution of degree of liquid saturation inside the bentonite buffer up 1000 years at different positions from the canister, comparisons between variable and constant temperature analyses.

Liquid pressure is another variable that can be used to study the hydraulic behaviour in the barrier system. Figure 4.51 shows the numerical results related to the liquid pressure inside the bentonite buffer at different positions from the canister. The long-term predictions inside the clay-barrier in terms of liquid pressure are presented in Fig. 4.52.

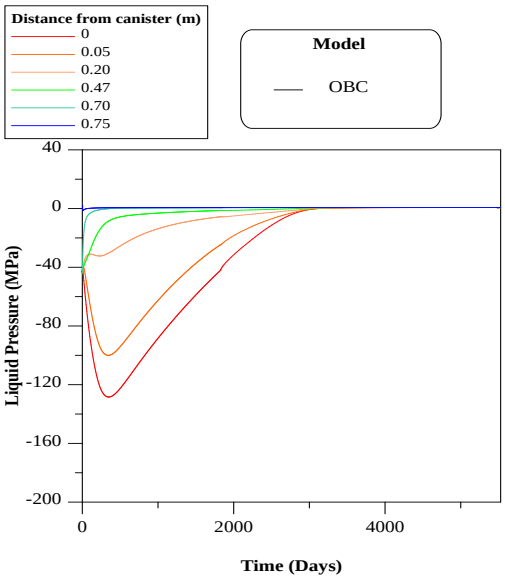

Fig. 4.51 Evolution of liquid pressure inside the bentonite buffer up to 15 years at different positions from the canister.

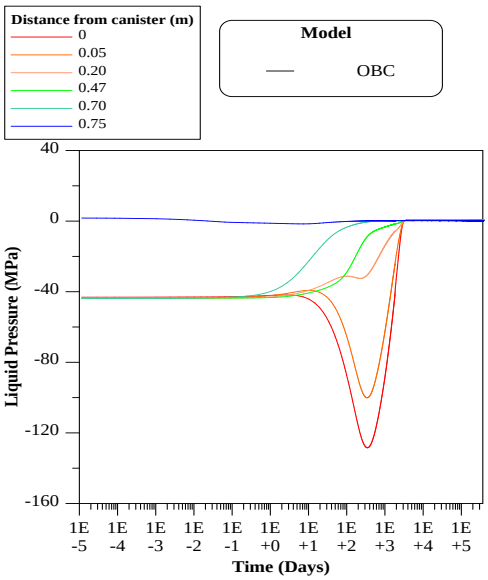

Fig. 4.52 Evolution of liquid pressure inside the bentonite buffer up to 1000 years at different positions from the canister.

Figure 4.53 presents the comparisons of liquid pressure between the case of constant temperature and thermal power decay for a period of 15 years. Figure 4.54 presents the same comparisons but for the long term (1000 years). It can be observed that the thermal decay contributes to a faster hydration of the barrier.

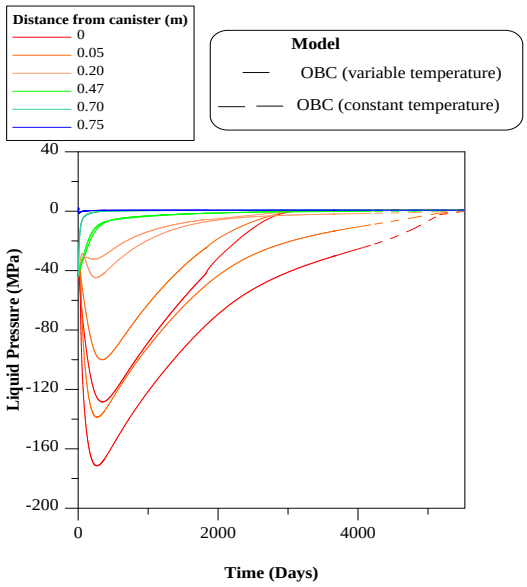

Fig. 4.53 Evolution of liquid pressure inside the bentonite buffer up to 15 years at different positions from the canister, comparisons between variable and constant temperature analyses.

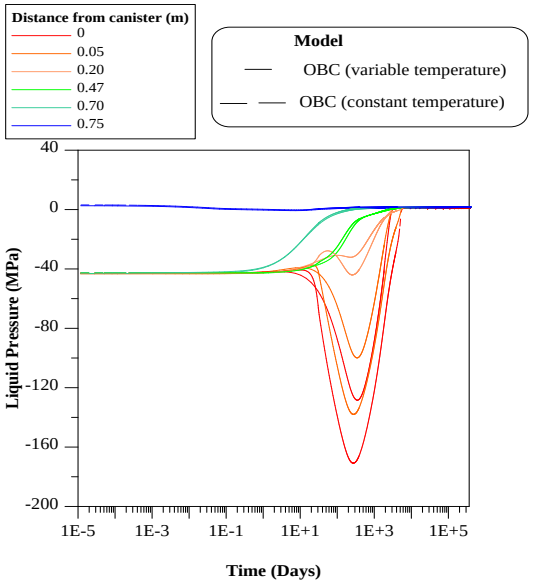

Fig. 4.54 Evolution of liquid pressure inside the bentonite buffer up to 1000 years at different positions from the canister, comparisons between variable and constant temperature analyses.

The mechanical behaviour of the repository can be analysed by exploring the evolution of normal stresses on each component of the system. Figure 4.55 presents the results of normal stress at different position in the clay-buffer. It can be observed that the stresses in all the positions increase as the buffer saturation progresses. Since this is a

problem with displacement restrictions at the boundary (i.e. global constant volume conditions), the stresses are induced by the swelling pressures of the bentonite under volume constraints conditions.

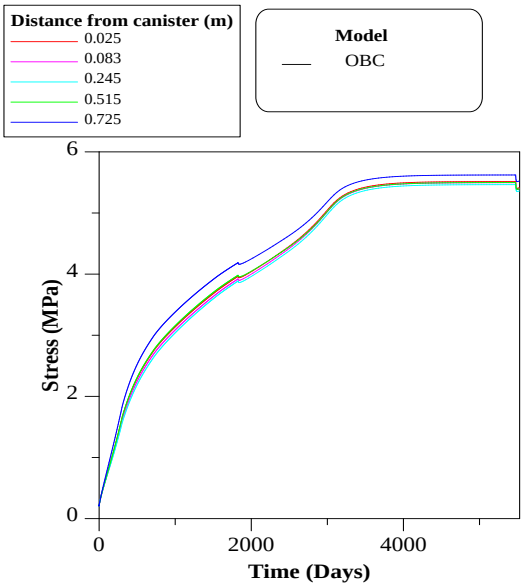

Fig. 4.55 Evolution of normal stress inside the bentonite buffer up to 15 years days at different positions from the canister.

As can be seen in Fig. 4.55, the point closest to the hydration front is the one with the maximum value of stress close to 5.60 MPa, achieved once the barrier is fully saturated.

Figure 4.56 presents the long-term evolution of the stresses in the clay barrier. It can be observed that after achieving the maximum values, the stresses reduce somewhat, because of the contraction associated with temperature reduction. The minimum stress value is around 5.3 MPa. Figure 4.57 presents the comparisons of normal stress between the case of constant temperature and thermal power decay for a period of 15 years.

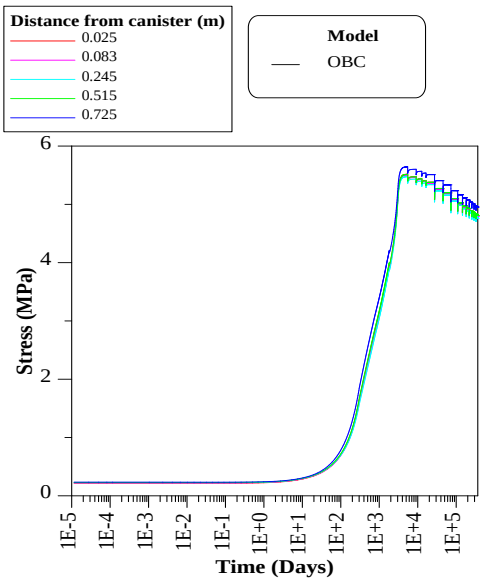

Fig. 4.56 Evolution of normal stress inside the bentonite buffer up to 10000 days at different positions from the canister.

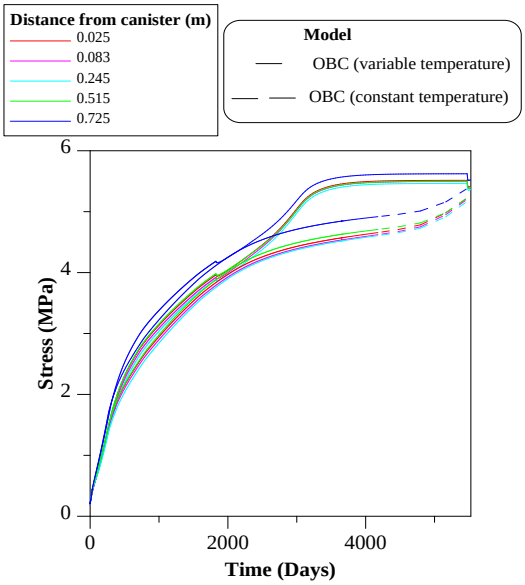

Fig. 4.57 Evolution of normal stress inside the bentonite buffer up to 15 years days at different positions from the canister, comparisons between variable and constant temperature analyses.

The following figures show some selected results related to the evolution of temperature, degree of liquid saturation, liquid pressure and stresses at different locations along the system calculated with the model considering *thermo-osmosis (THO)*. The results related to the OBC model have been included as a reference for the comparisons in the long term analyses.

Figure 4.58 shows the evolution of temperature inside the buffer for a period of 15 years at different positions from the canister. It is observed an increase in the temperature values in all the positions up to the first 30 days. After this time, it can be noted that the values start to stabilize, and then the decay of the heat power start to be more noticeable and after around 1000 days the temperature decrease. This can be seen in the long term predictions (Fig. 4.59), where the model predicts a continuous decrease of temperature after 1000 days. At the end of the analysis (i.e. 1000 years) the thermal field is rather constant across the barrier with an average temperature around 33 °C. For the plot commented above, it can be observed that the differences between the OBC and THO predictions are minimal at early stages (when the dominant effect on water transfer is the high hydraulic gradient prevailing at the beginning of the test) and also at later stages (where the thermal effects are practically irrelevant). The thermo-osmotic effects are somewhat more noticeable at intermediate stages of the analyses, where the hydraulic gradient has decreased and thermal gradient is still important.

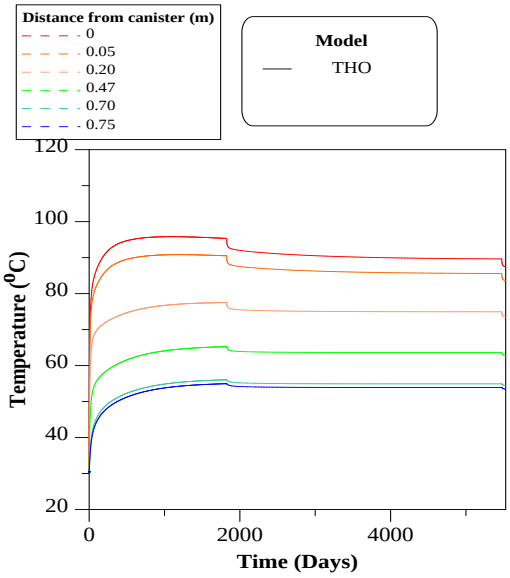

Fig. 4.58 Evolution of temperature inside the bentonite buffer up to 15 years at different positions from the canister.

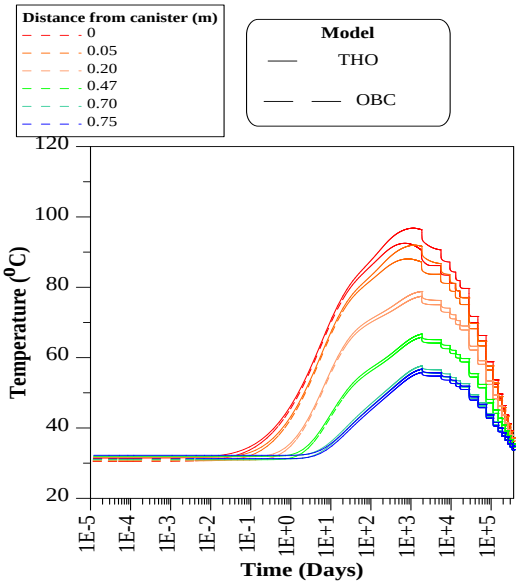

Fig. 4.59 Evolution of temperature inside the bentonite buffer up to 365000 days (1000 years) at different positions from the canister.

Figure 4.60 presents the comparisons of temperature between the case of constant temperature and thermal power decay for a period of 15 years. Figure 4.61 presents the same comparisons but for the long term (1000 years).

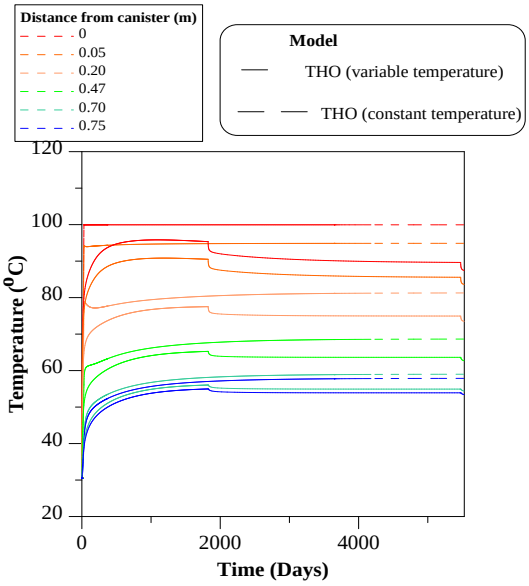

Fig. 4.60 Evolution of temperature inside the bentonite buffer up to 15 years at different positions from the canister, comparisons between variable and constant temperature analyses.

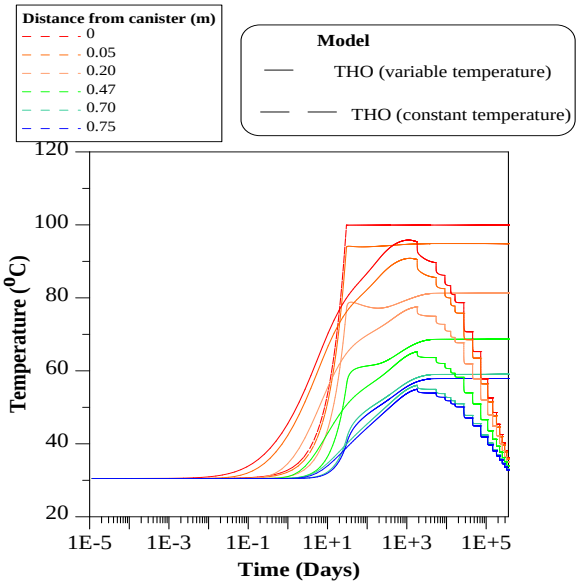

Fig. 4.61 Evolution of temperature inside the bentonite buffer up to 365000 days (1000 years) at different positions from the canister, comparisons between variable and constant temperature analyses.

The results of degree of liquid saturation are shown in the following figures. Figure 4.62 shows the predicted values of degree of saturation with the thermo-osmosis model for different positions inside the buffer. It can be observed that the presence of the thermo-osmotic flow is able to slow down significantly the hydration rate inside the buffer, especially at the positions closer to the canister.

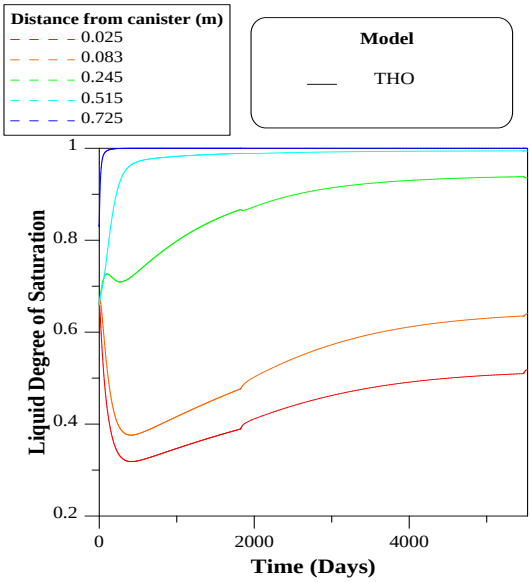

Fig. 4.62 Evolution of degree liquid of saturation inside the bentonite buffer up to 15 years at different positions from the canister.

As discussed before, this reduction in the hydration of the bentonite is mainly due to the thermo-osmotic flux that transfers water in the liquid phase from the zones close to the heater to those with lower temperature. As was explained in Section 4.1.2.1, the incorporation of this effect to the analysis delayed the time required to reach the full saturation of the clay barrier when a constant heater temperature was assumed. Figure 4.63 shows the long term results in term of degree saturation inside the clay barrier for the case of thermal decay. It can be observed that in this case the differences between THO and OBC models are minimal.

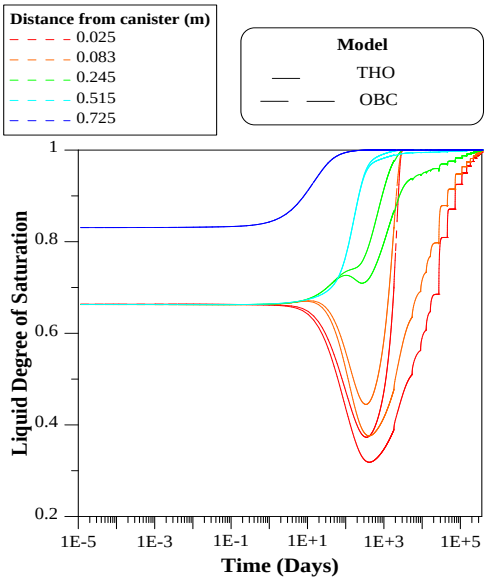

Fig. 4.63 Evolution of degree of liquid saturation inside the bentonite buffer up to 1000 years at different positions from the canister.

Figure 4.64 presents the comparisons of liquid saturation between the case of constant temperature and thermal power decay for a period of 15 years. Figure 4.65 presents the same comparisons but for the long term (1000 years). It can be observed that the thermal decay contributes to a faster hydration of the barrier.

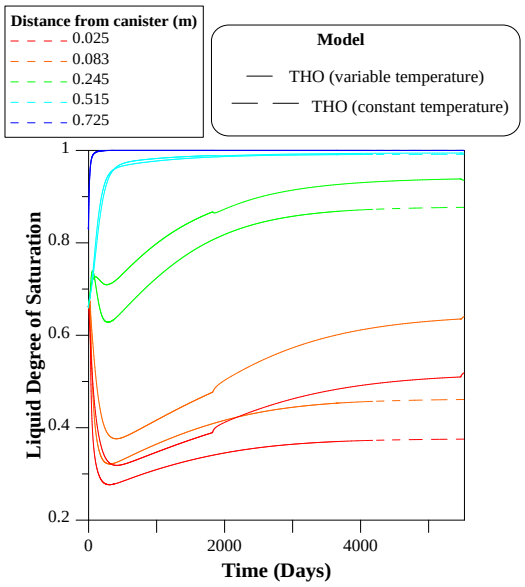

Fig. 4.64 Evolution of degree of liquid saturation inside the bentonite buffer up to 15 years at different positions from the canister. Comparisons between variable and constant temperature analyses.

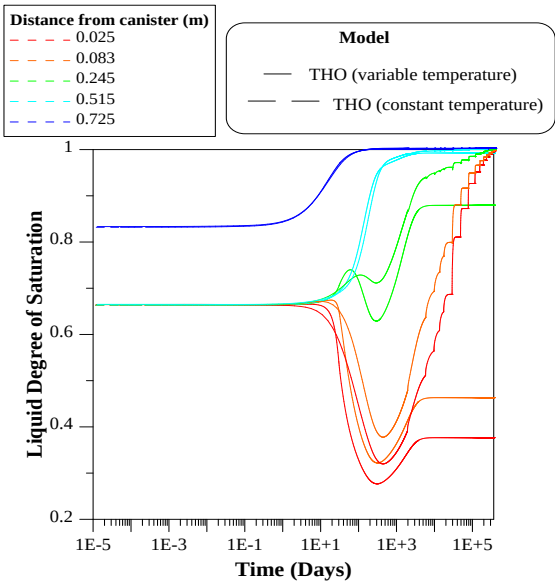

Fig. 4.65 Evolution of degree of liquid saturation inside the bentonite buffer up to 1000 years at different positions from the canister, comparisons between variable and constant temperature analyses.

Figure 4.66 shows the numerical results of liquid pressure in the bentonite buffer at different positions from the canister determined by the thermo-osmosis model. Figure 4.67 shows the long term predictions related to the liquid pressure in the clay-

barrier. As for the degree of saturation, the difference between THO and OBC are minor.

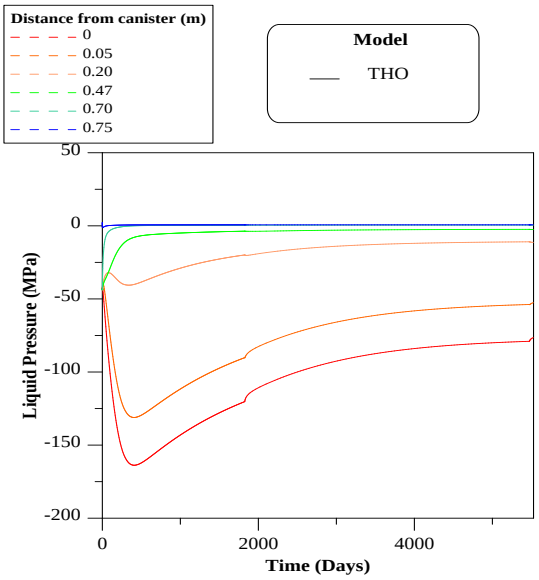

Fig. 4.66 Evolution of liquid pressure inside the bentonite buffer up to 3650 days (10 years) at different positions from the canister.

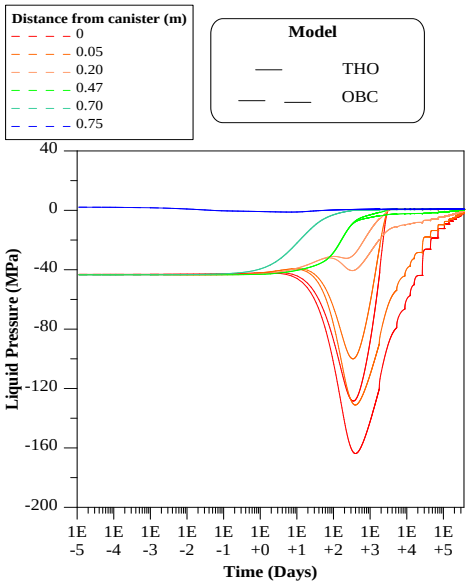

Fig. 4.67 Evolution of liquid pressure inside the bentonite buffer up to 1000 years at different positions from the canister

Figure 4.68 presents the comparisons of liquid pressure between the case of constant temperature and thermal power decay for a period of 15 years. Figure 4.69 presents the same comparisons but for the long term (1000 years). It can be observed that the thermal decay assist to a faster hydration of the barrier.

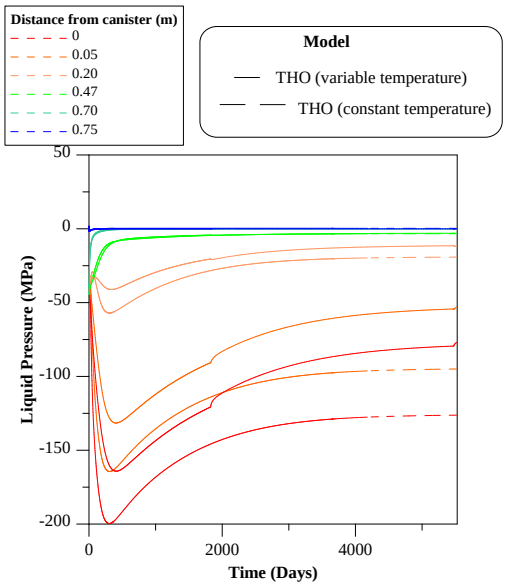

Fig. 4.68 Evolution of liquid pressure inside the bentonite buffer up to 3650 days (10 years) at different positions from the canister, comparisons between variable and constant temperature analyses.

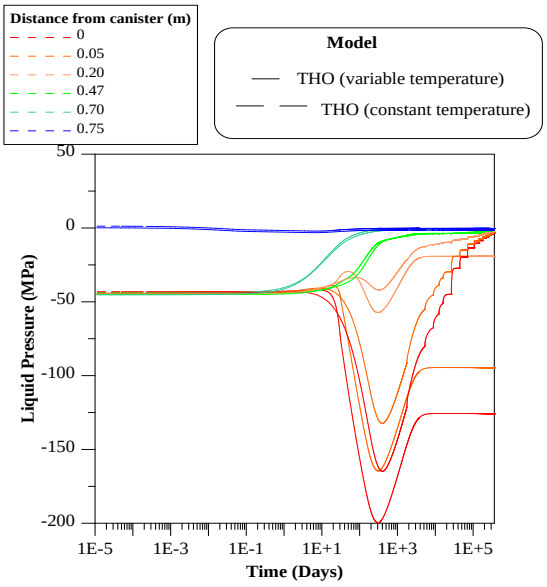

Fig. 4.69 Evolution of liquid pressure inside the bentonite buffer up to 1000 years at different positions from the canister, comparisons between variable and constant temperature analyses.

The mechanical behaviour of the repository is analysed now by looking at the evolution of normal stress on each component of the system. Figure 4.70 presents the numerical results of normal stress at different position in the buffer determined with the thermo-osmosis model.

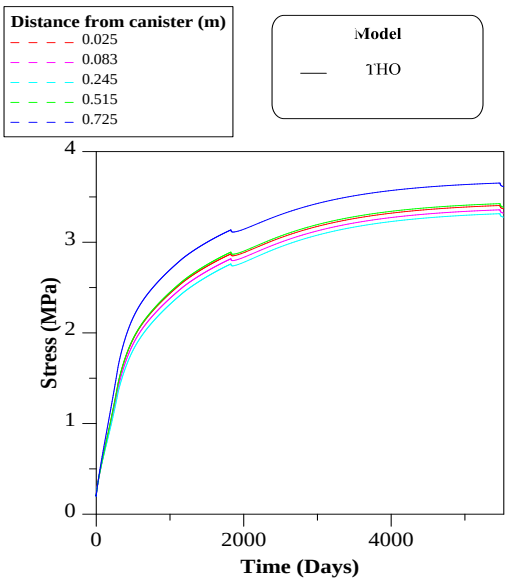

Fig. 4.70 Evolution of normal stress inside the bentonite buffer up to 15 years at different positions from the canister.

It can be observed that the stresses in all the positions are increasing as the saturation in the buffer progresses. As we can see from the figure, the point closest to the hydration front is the one with the maximum value of stress close to 3.50 MPa. This value is much lower to the one obtained from the OBC model. This reduction in the swelling pressures is related to the reduction in the hydration rate inside the barrier.

Figure 4.71 presents the long-term prediction of the stresses in the clay barrier for the OBC and THO cases. It can be seen that stresses predicted by the thermo-osmosis and OBC models are the same at the end of the analyses, because both cases used the BBM and in both analyses a full saturation is achieved at 1000 years. However, the transients for both cases are very different. As explained in the previous section, on one hand the OBC case reaches a maximum stress value (in coincidence with the full saturation of the barrier, i.e. around 8.5 years) and then the stresses decrease with the decay in the thermal field. On the other hand, the stresses calculated with the THO analysis after 8.5 years of hydration are around 60% of those predicted for the OBC (i.e. the maximum ones). The difference is that the THO delays the barrier hydration, and because of the strong HM coupling the stresses are smaller. However, after that time (i.e. 8.5 years), the stresses continue increasing, because of the progressive hydration of the barrier, which is enhanced by the heat decay (and the corresponding hampering of the thermo-osmosis effects).

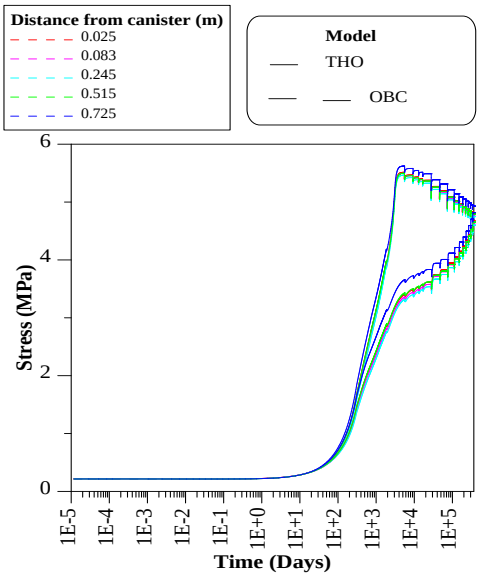

Fig. 4.71 Evolution of normal stress inside the bentonite buffer up to 10000 days at different positions from the canister.

Figure 4.72 presents the comparison of stresses between the case of constant temperature and thermal power decay for a period of 15 years. Figure 4.73 presents the same comparison but for the long term (1000 years). It can be observed that the thermal decay assists a faster hydration of the barrier. It can also be observed that the models predict higher stresses for the power decay case, a fact that is associated with the higher saturation (i.e. full saturation) of the barrier for this case.

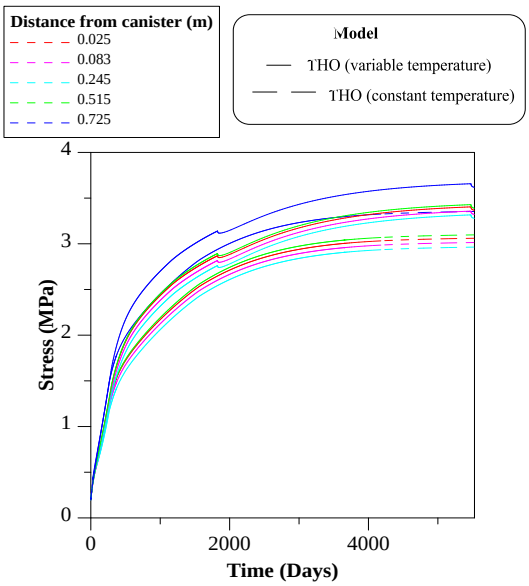

Fig. 4.72 Evolution of normal stress inside the bentonite buffer up to 15 years at different positions from the canister.

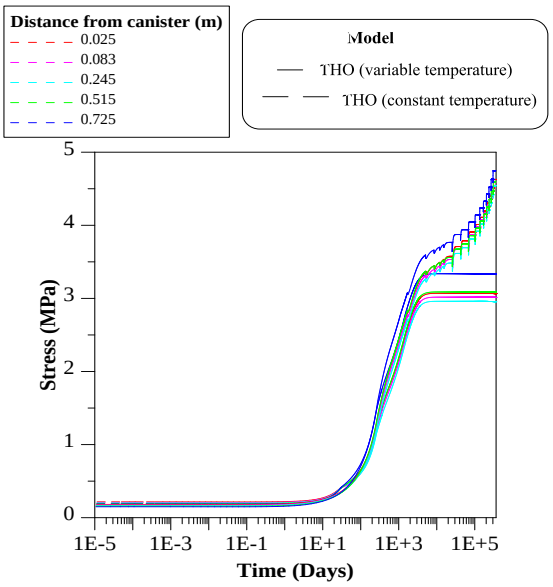

Fig. 4.73 Evolution of normal stress inside the bentonite buffer up to 10000 days at different positions from the canister, comparisons between variable and constant temperature analyses.

The following figures show some selected results related to the evolution of temperature, degree of liquid saturation, liquid pressure and stresses at different locations along the system calculated with the *double structure model (DS)* considering the effect of micro-structure changes. The results related to the OBC model have been included as a reference for the comparisons in the long term analyses.

Figure 4.74 shows the evolution of temperature inside the buffer for a period of 15 years at different positions from the canister. An increase in the temperature values at all the positions up to the first 30 days is observed. After this time, it can be noted that the values start to stabilize, and then decrease due to the decay of the thermal field. This can be seen more clearly in the long term predictions (Fig. 4.75) where the model predicts a continuous decay of temperature after around 10 years. A quite uniform temperature field is predicted by the models after 1000 years, with an average temperature around 34 °C. For the plot commented above, it can be observed that the differences between the OBC and DS predictions are minimal at early stages and also at later stages. The DS effects are somewhat more noticeable at intermediate stages of the analyses.

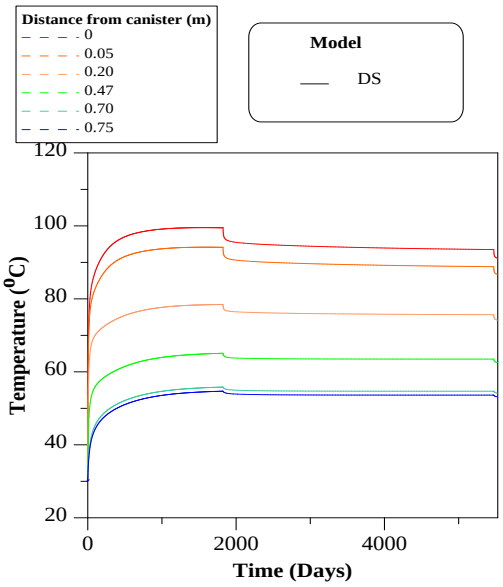

Fig. 4.74 Evolution of temperature inside the bentonite buffer up to 15 years at different positions from the canister.

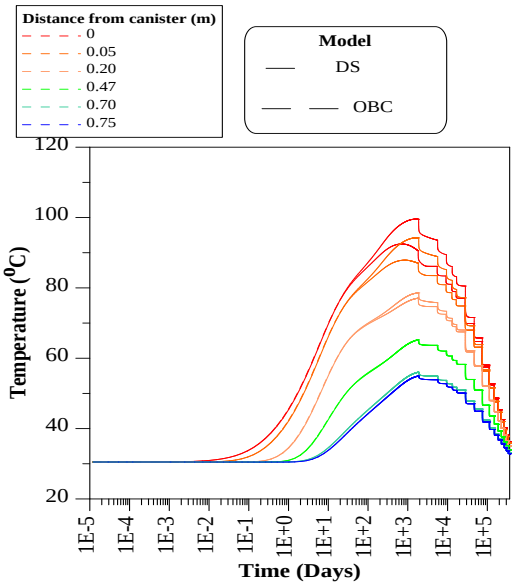

Fig. 4.75 Evolution of temperature inside the bentonite buffer up to 365000 days (1000 years) at different positions from the canister.

Figure 4.76 presents the comparisons of temperature between the case of constant temperature and thermal power decay for a period of 15 years. Figure 4.77 presents the same comparisons but for the long term (1000 years). It can be observed that the thermal decay contributes to a faster hydration of the barrier.

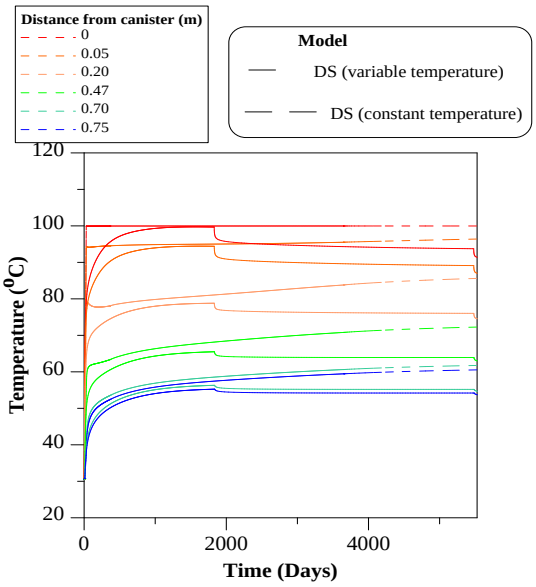

Fig. 4.76 Evolution of temperature inside the bentonite buffer up to 15 years at different positions from the canister, comparisons between variable and constant temperature analyses.

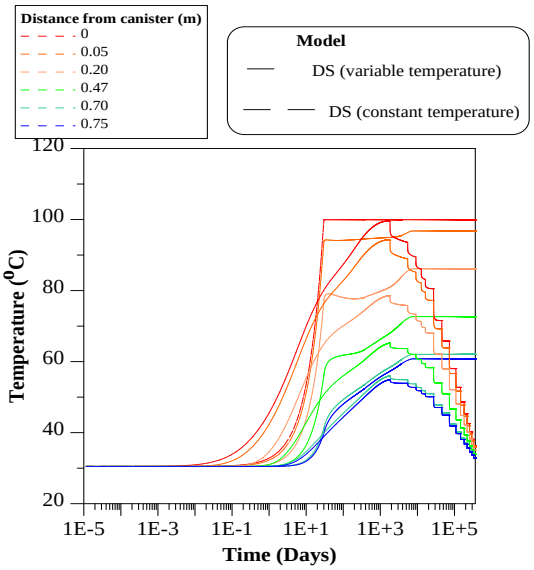

Fig. 4.77 Evolution of temperature inside the bentonite buffer up to 365000 days (1000 years) at different positions from the canister, comparisons between variable and constant temperature analyses.

The results of degree of liquid saturation are shown in the following figures. Figure 4.78 shows the predicted values of degree of saturation with the DS model for different positions inside the buffer. It can be observed that the model that considers the change in the clay fabric slows down the hydration rate inside the buffer, especially in the posi-

tions closer to the canister. Similar observations were made for the infiltration cell and mock-up tests. It is also clear that the impact of the changes in the clay fabric is less important than the one observed for the thermo-osmosis effect (see Fig. 4.62).

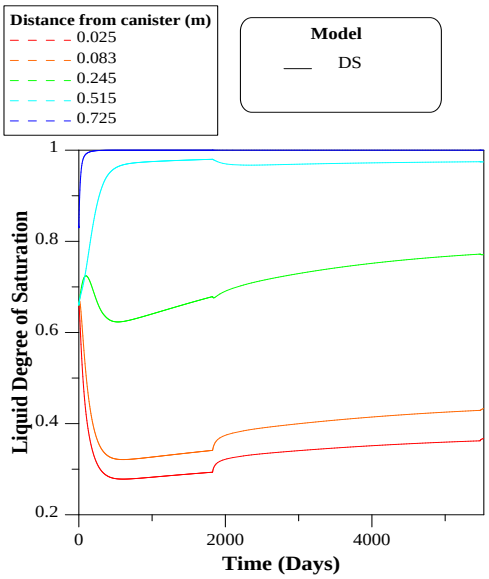

Fig. 4.78 Evolution of degree of liquid saturation inside the bentonite buffer up to 15 years at different positions from the canister.

Figure 4.79 presents the long term results in term of degree saturation inside the clay barrier for both DS and OBC models. It can be observed that DS delays the hydration time of the barrier considerably, but the model predicts full saturation after 1000 years.

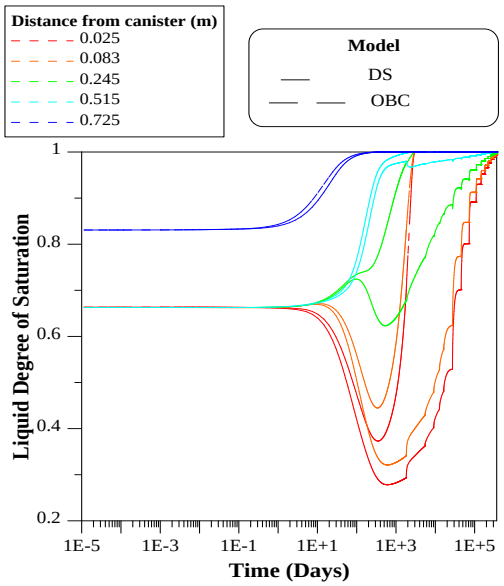

Fig. 4.79 Evolution of degree of liquid saturation inside the bentonite buffer up to 1000 years at different positions from the canister.

Figure 4.80 presents the comparisons of liquid saturation between the case of constant temperature and thermal power decay for a period of 15 years. Figure 4.81 presents the same comparisons but for the long term (1000 years). It can be observed that the thermal decay assist to a faster hydration of the barrier.

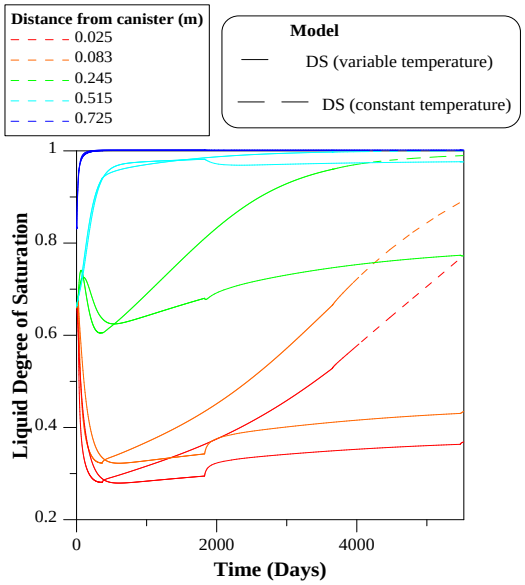

Fig. 4.80 Evolution of degree of liquid saturation inside the bentonite buffer up to 15 years at different positions from the canister, comparisons between variable and constant temperature analyses.

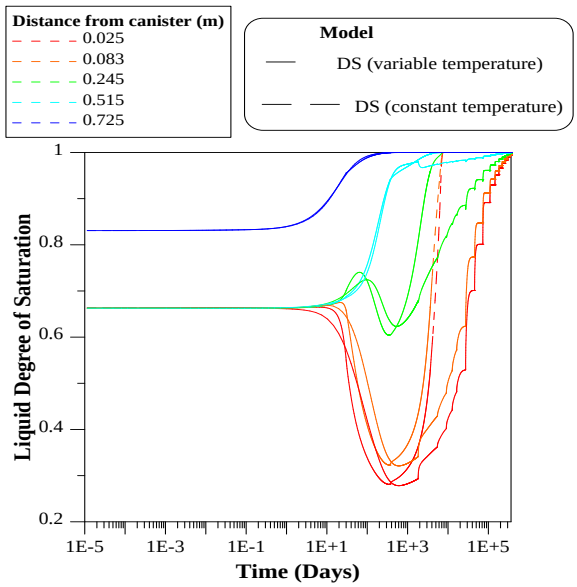

Fig. 4.81 Evolution of degree of liquid saturation inside the bentonite buffer up to 1000 years at different positions from the canister.

Figure 4.82 shows the numerical results of liquid pressure in the bentonite buffer at different positions from the canister determined by the DS model. The positions close to the hydration source experience an increase in the values of liquid pressure because of the progressive saturation occurring at this boundary.

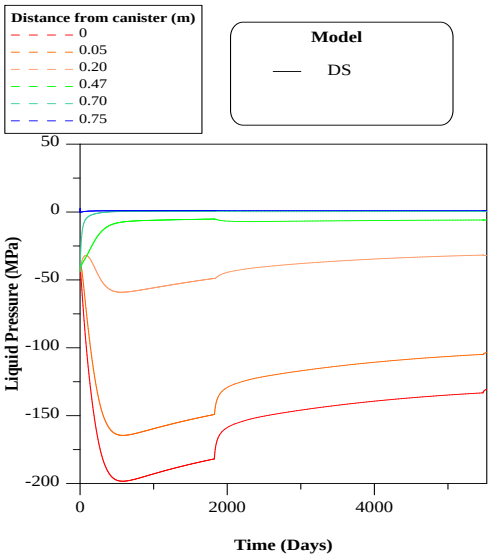

Fig. 4.82 Evolution of liquid pressure inside the bentonite buffer up to 3650 days (10 years) at different positions from the canister.

These locations are barely affected by the change in the clay fabric and as a result, similar predictions are obtained from the two models. On the other hand, at locations near to the canister the change in the micro-fabric has a more noticeable relevance. Figure 4.83 shows the long-term predictions in terms of liquid pressure.

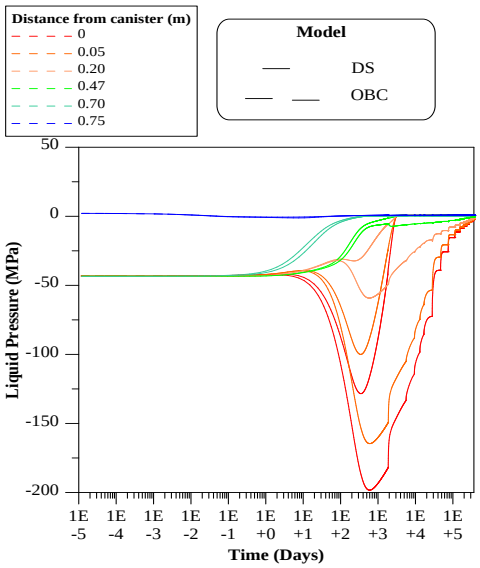

Fig. 4.83 Evolution of liquid pressure inside the bentonite buffer up to 1000 years at different positions from the canister.

Figure 4.84 presents the comparisons of liquid pressure between the case of constant temperature and thermal power decay for a period of 15 years. Figure 4.85 presents the same comparisons but for the long term (1000 years). It can be observed that the thermal decay assists a faster hydration of the barrier.

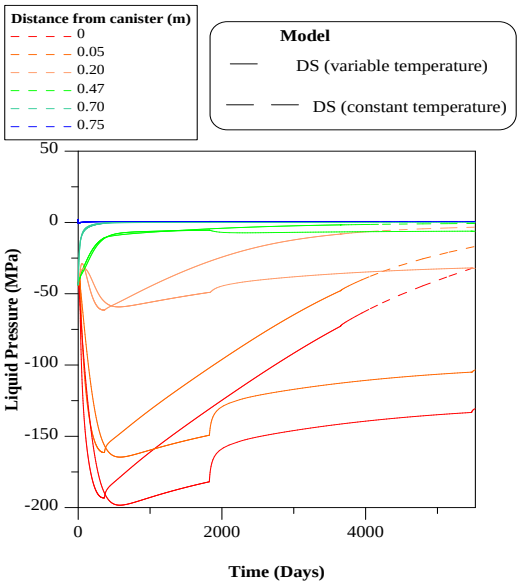

Fig. 4.84 Evolution of liquid pressure inside the bentonite buffer up to 3650 days (10 years) at different positions from the canister, comparisons between variable and constant temperature analyses.

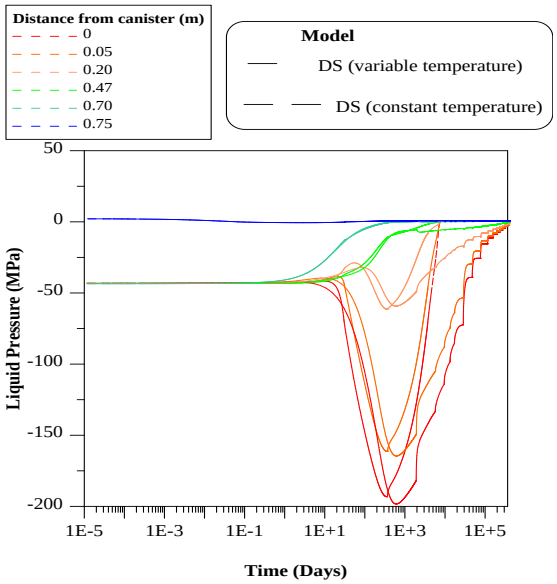

Fig. 4.85 Evolution of liquid pressure inside the bentonite buffer up to 1000 years at different positions from the canister, comparisons between variable and constant temperature analyses.

The mechanical behaviour of the repository is analysed now by looking at the evolution of normal stress on each component of the system. Figure 4.86 presents the numerical results of normal stress at different position in the buffer determined with the double structure model. It can be observed that the stresses in all the positions are increasing as the saturation in the buffer progresses.

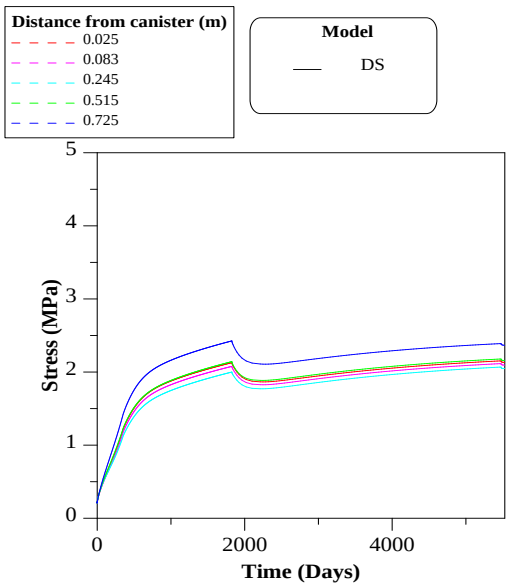

Fig. 4.86 Evolution of normal stress inside the bentonite buffer up to 15 years at different positions from the canister.

It can also be seen in this figure that the point closest to the hydration front is the one with the maximum value of stress after 15 years near 2.0 MPa. This value is much lower to the one obtained from the OBC model. This reduction in the swelling pressures is related to the reduction in the hydration rate inside the barrier. It is also smaller than the stress predicted for the constant temperature analysis.

Figure 4.87 presents the long-term prediction of the stresses in the clay barrier for both the DS and OBC models. Similar patterns to those indicated for the THO analyses can be observed in this figure, with a similar value of stresses at the end of the analyses (i.e. 1000 years), but different time evolution.

Figure 4.88 presents the comparisons of liquid pressure between the cases of constant temperature and thermal power decay for a period of 15 years. Figure 4.89 presents the same comparisons but for the long term (1000 years). It can be observed that the thermal decay contributes to a faster hydration of the barrier.

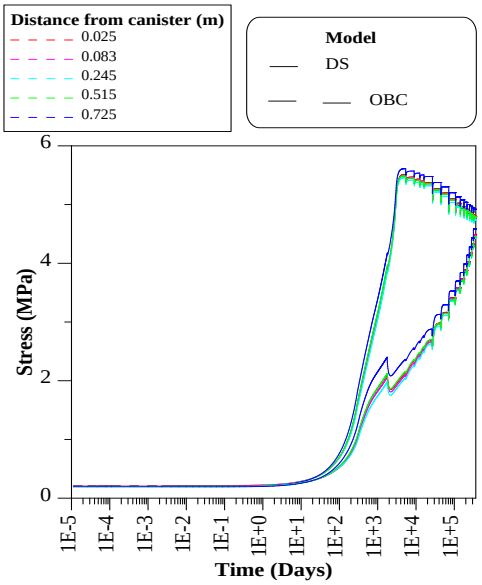

Fig. 4.87 Evolution of normal stress inside the bentonite buffer up to 10000 days at different positions from the canister.

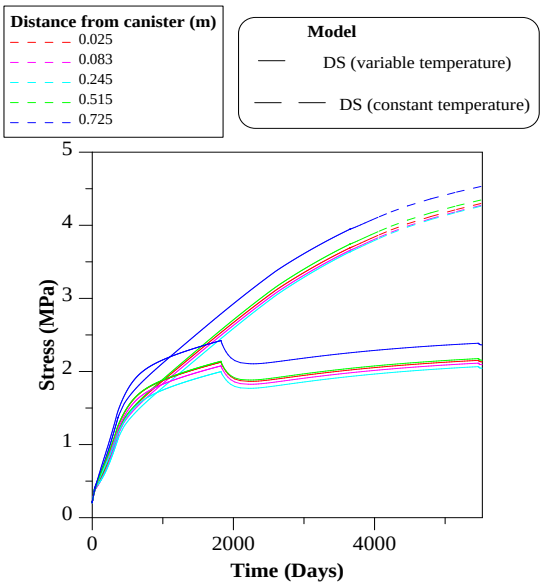

Fig. 4.88 Evolution of normal stress inside the bentonite buffer up to 15 years at different positions from the canister, comparisons between variable and constant temperature analyses.

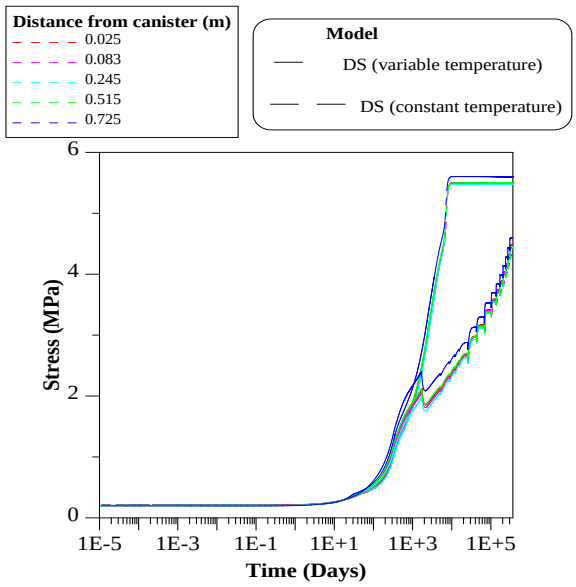

Fig. 4.89 Evolution of normal stress inside the bentonite buffer up to 10000 days at different positions from the canister, comparison between variable and constant temperature analyses.

4.1.3 Concluding remarks

Of the two long-term variant cases considered in this section only that incorporating heating power decay with time is realistic. The constant temperature variant has been

performed as a reference case that corresponds to the thermal boundary conditions of the laboratory and mock-up tests described in Deliverable 3.3-3 (Sanchez & Gens, 2014).

Naturally, the pattern of the early transient results in the variable temperature heat-decay case is very similar to that predicted by the constant temperature analysis. The long-term predictions are of course quite different. Thus, temperatures reach a peak and start to fall after a few centuries. Temperatures have practically recovered to the initial values at the end of the analysis (1000 years). It should be stated, however, that long-term temperature predictions are sensitive to the particular geometry adopted that, at those times, may not be quite representative of the actual repository.

In the heat decay case, full saturation of the barrier is achieved after approximately 8.5 years - a significantly shorter time than in the constant temperature analysis. Swelling pressure also fully develops over similar times. Observing the long-term results, it can be noted that, after achieving the maximum values, the stresses reduce somewhat, because of the contraction associated with temperature reduction.

The incorporation of thermo-osmosis changes significantly the hydration times of the barrier. In the constant temperature case it prevents full saturation indefinitely, but even in the heat decay analyses, full saturation is only achieved towards the end of the analysis (1000 years). Development of swelling pressure follows the progress of hydration, so the full final value is only achieved at the end of the analysis. Similarly, consideration of the micro-fabric evolution also delays full hydration (and full swelling pressure development) until the end of the analysis, i.e. 1000 years. As expected, temperature fields are affected very weakly by using the alternative hypotheses of the THO and DS models.

Naturally, the results presented correspond to a specific geometry and a single set of parameters. The parameters chosen have the only merit of providing a reasonable good representation of the observed short-term transient behaviour but here they are applied to long-term calculations, so a significant uncertainty inevitably remains. As shown in Gens et al. (2002), even modest variations of parameters can result in significant changes in predicted THM behaviour. A similar sensitivity study for the long-term situation would thus be quite valuable to assess the degree of uncertainty and the reliability of the reported results.

4.2 Simulation by Nagra/TK Consult

4.2.1 General description

4.2.1.1 Modelling Concept

The case variant “Long-term FEBEX in-situ extrapolation using real thermal source term” has been analyzed by application of the TH-code TOUGH2 (Pruess, et al., 2011). The repository as described above is simplified by an axisymmetric mesh of “finite volume” elements. Due to symmetry considerations only one cell from the array of disposal cells (see Fig. 4.2) is considered (i.e. quasi 2D slice model). In order to verify the latter assumption an additional sensitivity case will be investigated where the 3 ending disposal cells of the drift is followed by a bulk of granite host rock (quasi 3D model, see Section 4.2.6).

In order to ensure predictive reliability the involved hydraulic and thermal parameters have been derived (prior to extrapolation) from inverse modelling of a corresponding in-situ experiment (Kuhlmann and Gauss, 2014). The full-scale engineered barriers experiment (FEBEX) in crystalline host rock is an almost 1:1 physical model of the mentioned Spanish disposal concept and was carried out between 1995 and 2010 at the Grimsel Test Site located in the Swiss Alps. At the end, the heavily instrumented site provides pressure, temperature and saturation data in the buffer and the granite rock, from more than 600 installed sensors for a period of 15 years. The joint inversion of the whole set of measurement data results in parameter estimates of permeability, porosity, relative permeability and capillary pressure functions for both, granite host rock and bentonite buffer, so that model simulations largely agree with the observations. These parameter estimates will be applied in the present extension modelling to compute long term predictions of performance measures.

4.2.1.2 Error analysis

As by-products, the inverse modelling framework provides uncertainty estimates in form of the parameter covariance matrix or parameter standard deviations. Here, options of the code iTOUGH2 (Finsterle, 2007) are being applied in order to assess the quality of the predictions. The implemented linear or *First-Order-Second-Moment*

(FOSM) uncertainty propagation analysis quantifies the uncertainty in model predictions by linearization. FOSM is the analysis of the mean and covariance of a random function (the model prediction) based on its first-order Taylor series expansion. The covariance of the input parameters is translated into the covariance of the system response. This presumes that the mean and covariance are sufficient to characterize the distribution of the dependent variables, i.e., the model results are assumed to be normally or log-normally distributed.

4.2.2 Geometry

The TOUGH2-mesh used for the reference case is shown in Fig. 4.90. The dimensions of the disposal cell correspond to those indicated in Fig. 4.2. In addition, a zone of 0.1 m width was incorporated to represent the excavation damaged zone (EDZ) of the host rock. The extension of the modelled Granite in radial direction is 500 m in total.

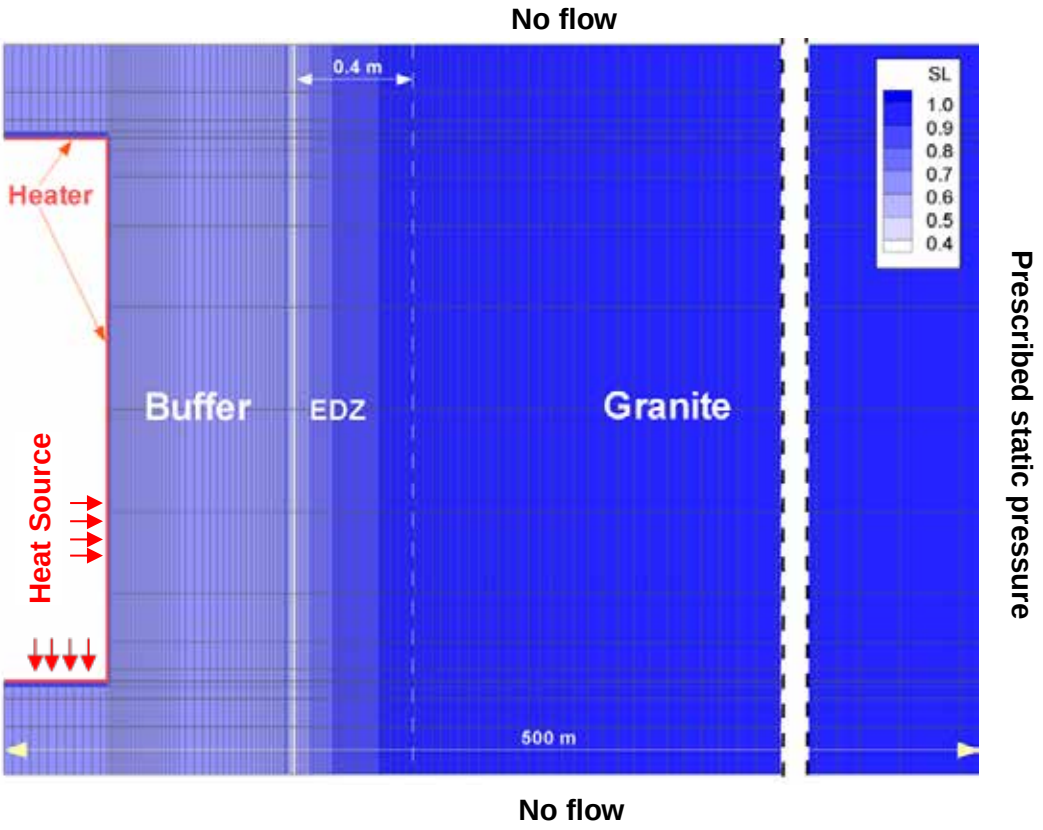

Fig. 4.90 TOUGH2-mesh of the "2D"-reference case (colored by degree of initial water saturation), boundary conditions

4.2.3 Considered processes

The analyses were performed applying TOUGH2 with equation of state module 4 (EOS4). TOUGH2 solves mass and energy balance equations that describe fluid and heat flow in general multiphase, multicomponent system, thus, considering process classes T and H. Fluid advection is described with a multiphase extension of Darcy's law; in addition there is diffusive mass transport in all phases. Heat flow occurs by conduction and convection, the latter including sensible as well as latent heat effects. Fluid and formation parameters can be (nonlinear) functions of the primary thermodynamic variables. The EOS4 module extends the standard description of water and air in its single- and two-phase states by the capability for vapour pressure lowering effects.

4.2.4 Input data and data sources

4.2.4.1 Initial and boundary conditions

Boundary and initial conditions of the reference case are illustrated in Fig. 4.90. The case is modelled by two stages in time. At first, a 10 years excavation/installation phase is simulated starting with uniform static pressure according the given depth below terrain of the repository (100 m, as in the FEBEX-experiment; 500 m, the value given by the repository concept will be considered in a sensitivity case described below in Section 4.2.6). Atmospheric boundary conditions are maintained in the drift, where elements representing buffer and heater are not yet present. Due to symmetry considerations lateral boundaries perpendicular to the axis of the drift get "no flow" conditions. Along the boundary at maximum radius of the model (500 m) the static pressure is maintained. The computed water saturation in the host rock after 10 years, then, serves as initial condition of the second (heating) phase.

During the second simulation phase, heat produced by canisters is imposed applying time dependent energy rates along the "heater" boundary (see Fig. 4.90) using real thermal source terms given by Enresa 2000 (Enresa, 2001). Here, a (slightly) simplified log-log-linear decrease is used starting with 1220 W (at 50 years) per disposal cell (see Fig. 4.5). Initial temperature is assumed to be 30.5 °C, initial saturation of the buffer is given by 66%. Distribution of the initial water saturation for this heating phase is illustrated in Fig. 4.90 by shades of blue.

4.2.4.2 Hydraulic and thermal parameters

As described in the modelling strategy above, resulting hydraulic and thermal properties were taken from the prior inverse modeling study of the FEBEX-in-situ experiment (Kuhlmann and Gaus, 2014) which represents an almost 1:1 physical model of the mentioned Spanish disposal concept. The parameter estimation procedure started from best guess parameters based on diverse measurement and modeling studies (Enresa, 2006, Gens et al, 2009). The resulting model parameters as used in the present extension modeling are listed in Tab. 4.9 below. The applied retention curves (Tab. 4.10) provided by a modified van Genuchten model (Finsterle, 2012) of both, the Grimsel granite and the FEBEX bentonite are illustrated in Fig. 4.91. Exponential law and parameters of the thermal conductivity model are shown in Fig. 4.92.

Tab. 4.9 Hydraulic, thermal and two-phase properties of the different materials resulting from parameter estimation of the FEBEX-in-situ experiment (in brackets the computed standard deviations)

	Unit	Granite	EDZ	FEBEX-Bentonite
Density	ρ [kg/m3]	2630	2630	1735
Specific Heat	C_r[$Jkg^{-1}K^{-1}$]	910	910	1170
Thermal Conductivity (Eq. 1) - Dry - Wet	T_k[$Wm^{-1}K^{-1}$)]	 3.63(0.16) 3.44(0.87)	 3.63(0.16) 3.44(0.87)	 1.22(0.06) 0.48(0.03)
Thermal Expansion	T_x[K^{-1}]	-	-	$1.5 \cdot 10^{-5}$
Initial Water Saturation	S_w[-]	1.0	1.0	0.66
Porosity	f [-]	0.012(0.0004)	0.033(0.004)	0.055(0.005)
Permeability	k [m^2]	$6.8 \cdot 10^{-19}$(0.02)*	$4.4 \cdot 10^{-19}$(0.03)*	$9.4 \cdot 10^{-22}$(0.03)*
Pore Compressibility	C_p[Pa^{-1}]	$2 \cdot 10^{-11}$	$2 \cdot 10^{-11}$	$2 \cdot 10^{-9}$
Van Genuchten parameters (s.) - n - 1/a - ɳ - ζ	 [-] [Pa] [-] [-]	 2.34(0.12) $0.6 \cdot 10^{-6}$(0.03)* 0.5(0.01) 0.02(0.003)	 2.34(0.12) $0.6 \cdot 10^{-6}$(0.03)* 0.5(0.01) 0.02(0.003)	 1.42(0.02) $2.96 \cdot 10^{-7}$(0.01)* 0.5(0.05) 0.4(0.05)
Residual Water Saturation	S_{lrk} [-] S_{lrc} [-]	0.01 0.01	0.01 0.01	0.01 0.01
Residual Gas Saturation	S_{gr}[-]	0	0	0
Vapor Diffusion Coefficient	[m^2/s]			

* Standard deviation refers to the log-value of the parameter

Tab. 4.10 Two-phase parameter models

Two-phase parameter model: modified van Genuchten (see Finsterle, 2012)	***capillary pressure***	***relative permeability***
	$P_c = P_o \left(S_{ec}^{n/(1-n)} - 1 \right)^{1/n}$ $S_{ec} = \frac{S_l - S_{lr}}{1 - S_{lr}}$ $m = 1 - 1/n$	$k_{r,l} = S_e^{h} \left[1 - \left(1 - S_e^{1/m} \right)^{m} \right]^2$ $k_{rg} = (1 - S_{ekg})^{z} \left[1 - S_{ekg}^{1/m} \right]^{2m}$ $S_e = \frac{S_l - S_{lr}}{1 - S_{gr} - S_{lr}}$ $S_{ekg} = \frac{S_l}{1 - S_{gr}}$

Following comments on the model parameters should be considered:

- Porosity of FEBEX bentonite.

  The porosity of about 6% resulting from inverse modeling of the FEBEX-in-situ experiment seems to be very low compared to about 40 % measured in laboratory tests. However, the estimated value is a best fit parameter which is able to reproduce the relative humidity measurements in the buffer reasonably well. It is understood, that this value represents a mean (TH-model) parameter reflecting the simplifications made by neglecting mechanical impacts such as bentonite swelling, etc.

- Two-phase parameters of granite.

  The estimated air entry pressure of ~0.6 MPa seems to be low compared to measurements and prior modeling studies (Finsterle & Pruess, 1995). Because in the inverse model (FEBEX-in-situ) both, intact host rock and EDZ have the same two-phase model parameters this value probably refers rather to the inner zone of the EDZ where micro-fractures may lead to reduced capillary pressure.

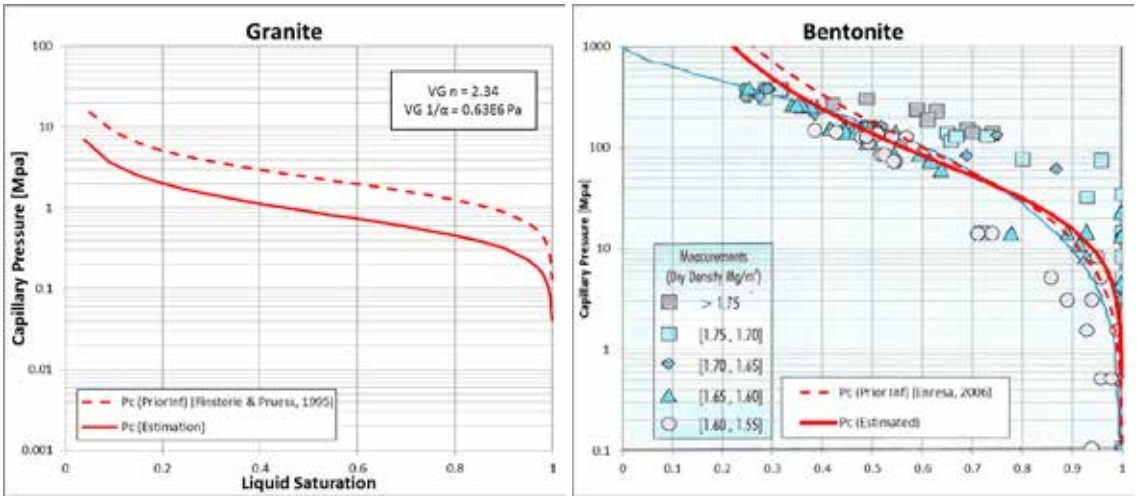

Fig. 4.91 Retention curves of Grimsel granite and FEBEX bentonite (adapted from Enresa, 2006)

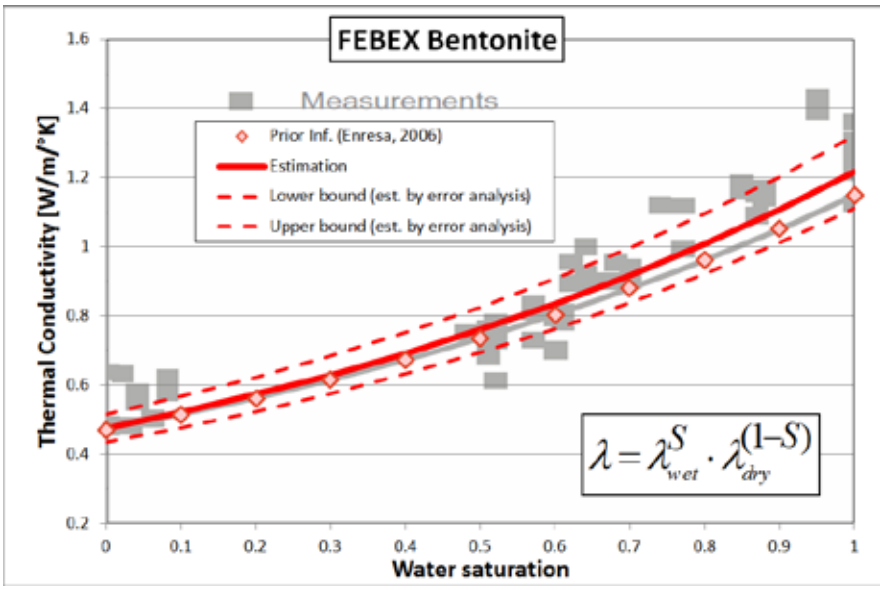

Fig. 4.92 Thermal conductivity and error range of FEBEX bentonite estimated by inverse modelling (adapted from Enresa, 2006)

4.2.5 Result description

The system described in Section 4.2.2 is simulated over a period of hundred years. The evolution of resulting temperatures is plotted at selected observation points in Fig. 4.93. The temperature in the buffer near the heater (location •) reaches a maximum after approximately 3 years at 90 - 95 °C, thereafter, slowly decreasing to 60 °C

after 100 years. The error range in form of 95% confidence bounds evaluates to approximately 10 °C at maximum. At a distance of about 3m from the disposal cells (location „) a maximum temperature of only 50 ± 2 °C is expected (after ~20 years).

Evolution of computed water saturations is shown Fig. 4.94. While the granite host rock at his boundary to the repository immediately starts to re-saturate (location *f*) response in the buffer material is much slower. At first, a slight desaturation is computed near the heater (location •) after that a relatively fast saturation process begins. The saturation front reaches the center of the buffer (location ,) after approximately 1 year. Full saturation of the buffer (location A) is predicted to happen after 15 - 20 years.

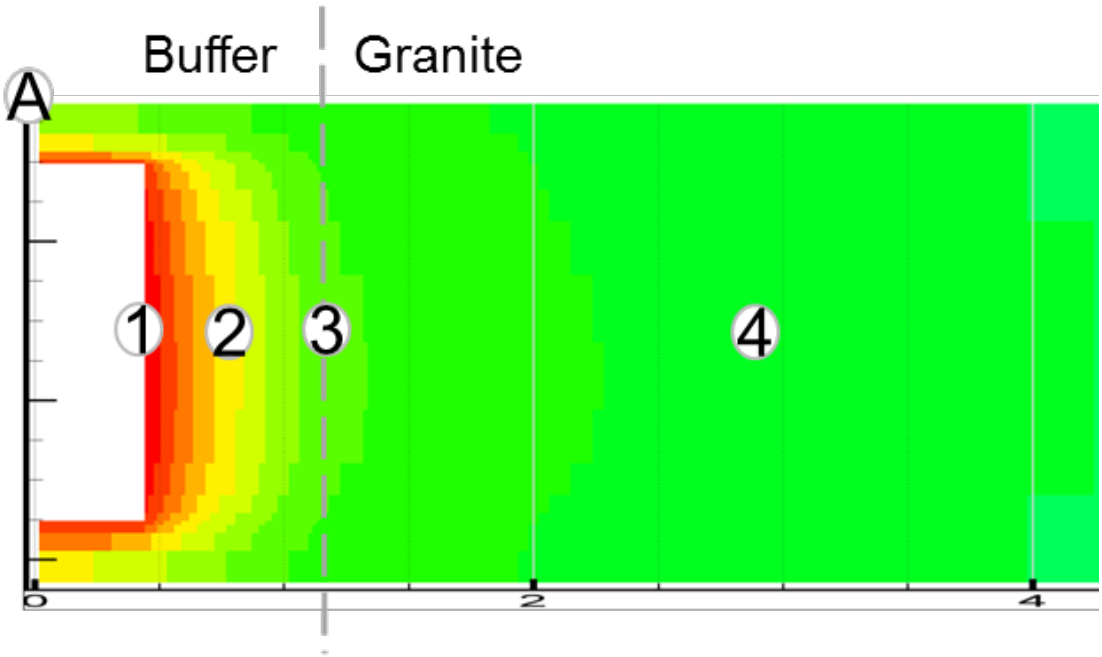

Fig. 4.93 Location of observation points

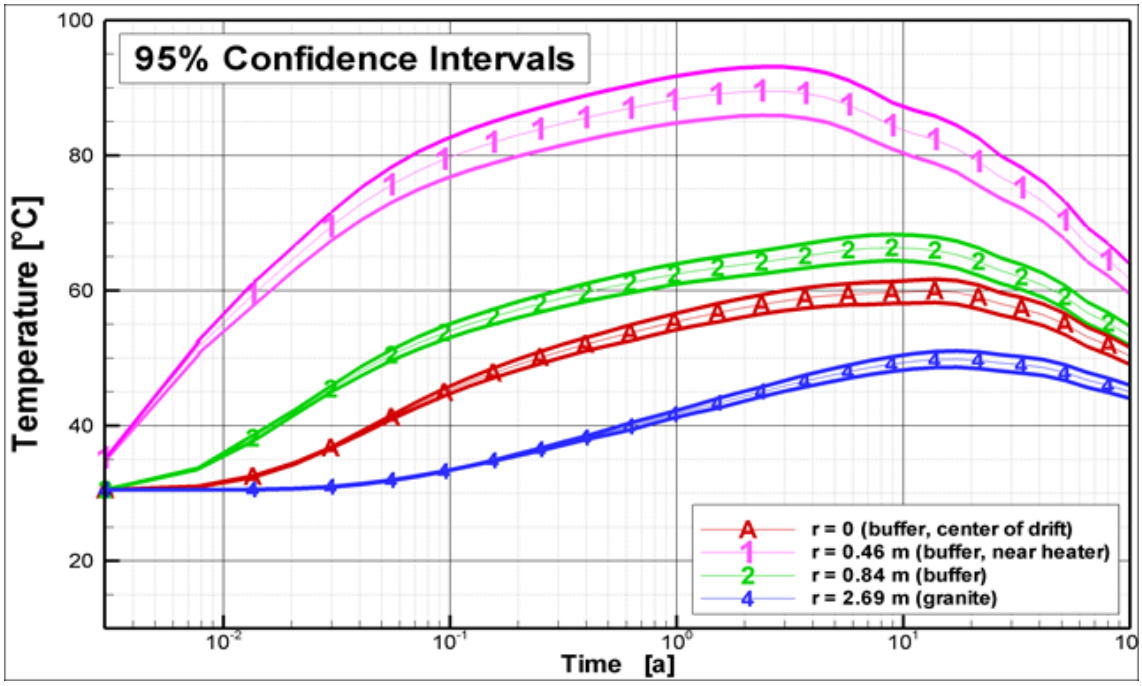

Fig. 4.94 Evolution of mean temperature with error range (95% confidence interval) at selected observation points (locations see Fig. 4.93)

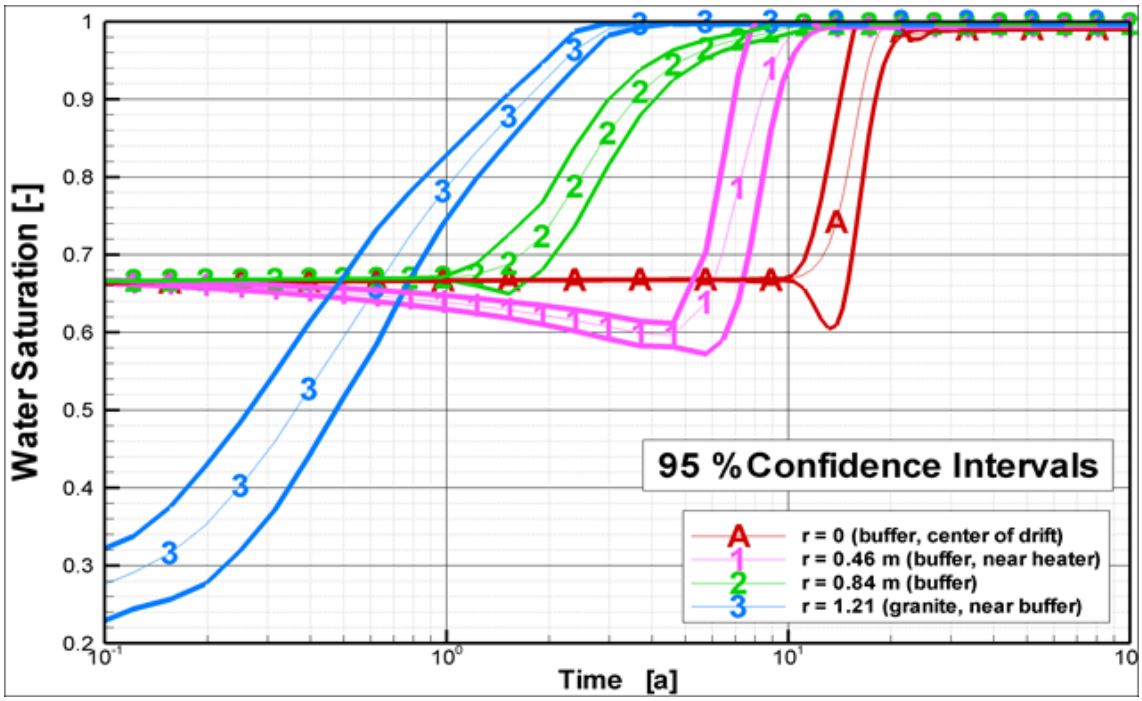

Fig. 4.95 Evolution of mean water saturation with error range (95% confidence interval) at selected observation points (locations see Fig. 4.93)

4.2.6 Impact of uncertainties and simplifications

4.2.6.1 Conceptual uncertainties, uncertainty due to geometric simplifications

To account for conceptual and parameter uncertainties not covered by the underlying inverse modelling study additional sensitivity cases have been analysed. These cases investigate the sensitivity of following impacts:

- Initial static pressure acc. 500 m depth of repository (sensitivity case *IP5*)
- Initial saturation of the buffer of 55% (case *S55*)
- Geometric simplifications (“3D” effect, case *3DE*)

Case *IP5*:
The evolution of temperature does not show essential differences compared to the reference case (Fig. 4.96) if the initial static pressure is increased. On the other sidethe saturation process is affected significantly (Fig. 4.97). The high initial pressure of about 5 MPa (compared to 1MPa in the reference case) reduces re-saturation by approximately 5 - 8 years (i.e. ~30%).

Case *S55*:
Lower initial water saturation of the buffer lead to higher near field temperatures (4 °C at maximum) because heat conduction is lower at dry conditions (Fig. 4.96). Re-saturation time is prolonged due to lower (relative) permeability and the increased pore volume to fill (Fig. 4.97).

Case *3DE:*
Figure 4.98 shows the computational mesh used to investigate the geometric simplification due to the “2D” model assumptions (see Fig. 4.90). Three disposal cells at the end of the drift are followed by a bulk of 500 m granite host rock. Compared to the reference case differences in late time temperatures only can be observed (Fig. 4.96, Fig. 4.97).

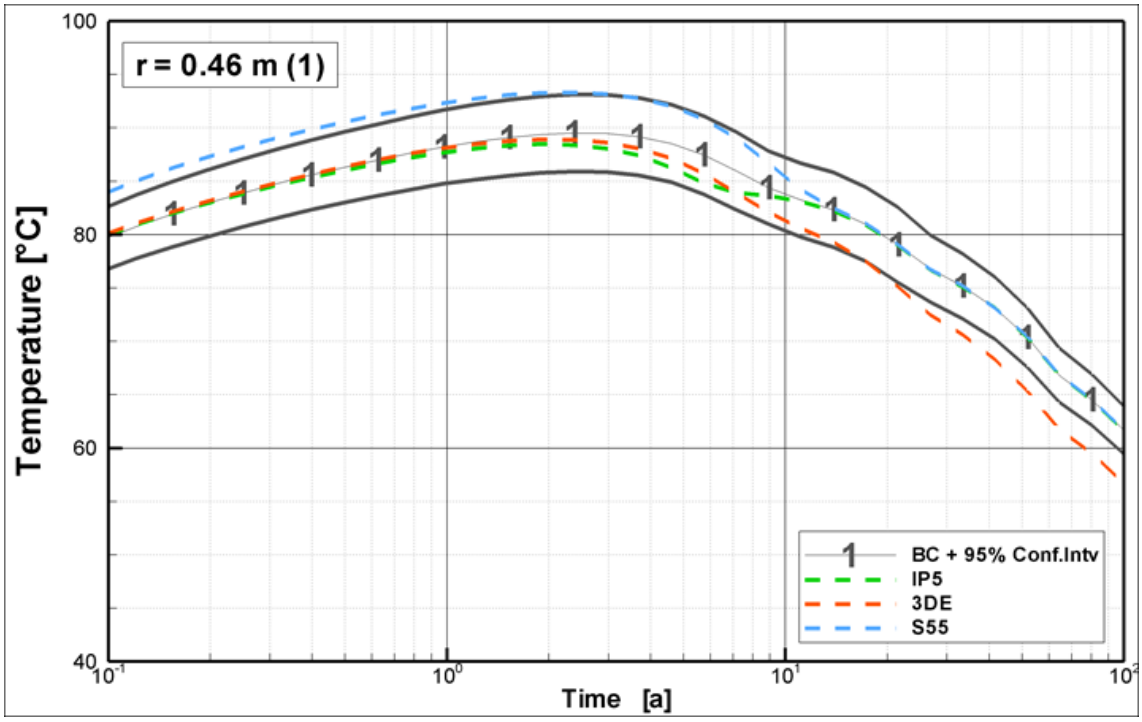

Fig. 4.96 Reference case (BC) and sensitivity cases - evolution of temperature at observation point • (location see Fig. 4.93)

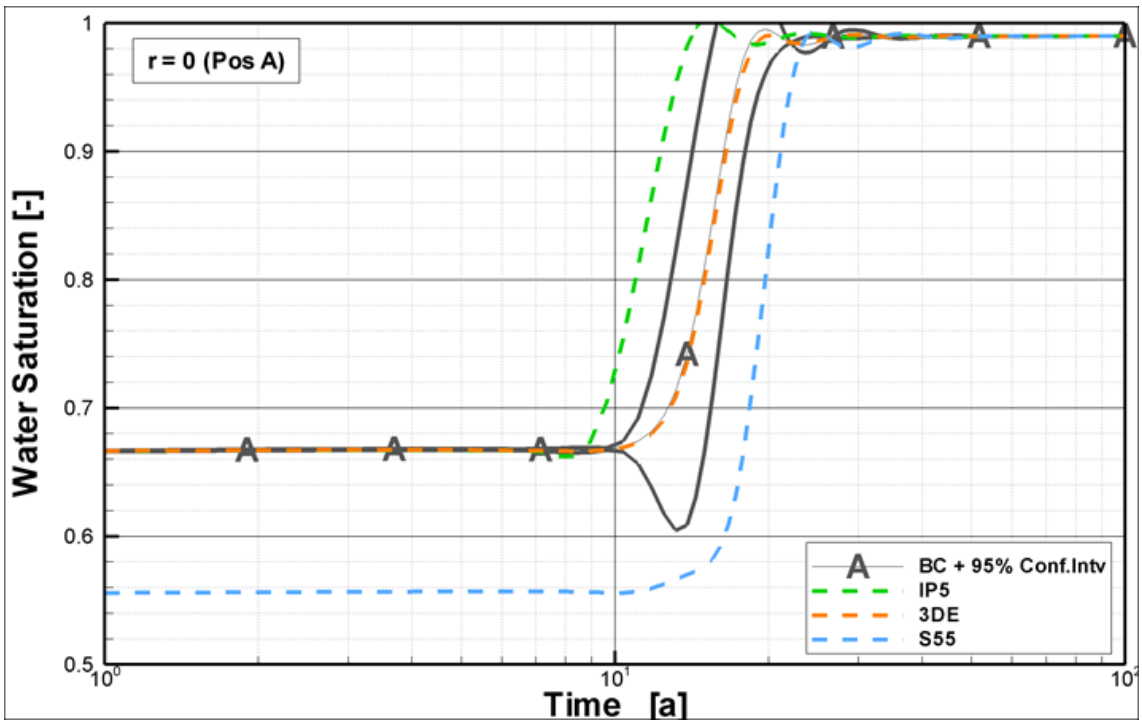

Fig. 4.97 Reference case (BC) and sensitivity cases - evolution of water saturation at observation point A (location see Fig. 4.93)

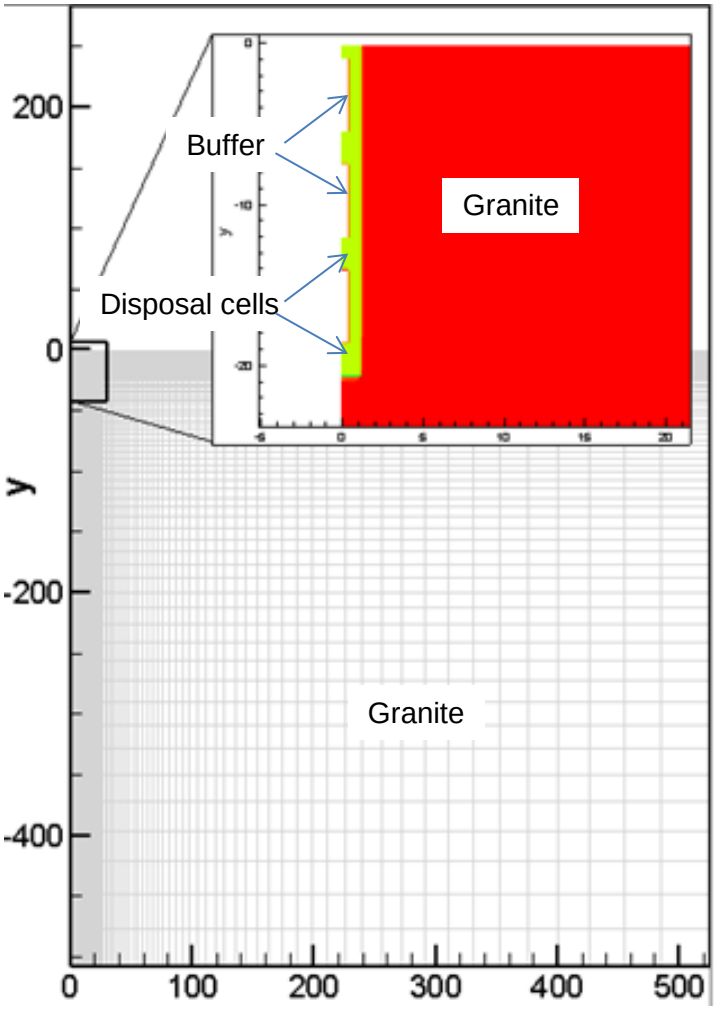

Fig. 4.98 Sensitivity case 3DE – quasi 3d simulation mesh

4.2.6.2 Uncertainty in material parameters

Uncertainty in material parameters has been accounted for by application of a linear error analysis as described in Section 4.2.5. The results quantify the uncertainty of predictions in form of 95% confidence intervals. Due to the small standard deviations of the input parameters predictive uncertainty becomes relatively small as well.

4.2.6.3 Influence of neglects and simplifications in processes

The TH-model at hand neglects mechanical processes such as e.g. bentonite swelling. However, the preceding inverse modelling study provides model parameters which are able to reproduce in reasonable agreement measured thermal and hydraulic conditions very similar to those proposed by the repository concept. Thus, one is drawn to the

conclusion that the estimated parameters may include the influence of neglected/simplified processes, so that some performance measures of interest (e.g. temperature, saturation) can be safely predicted.

The outcomes of the inverse modelling increases confidence in the description of the evolution of the EBS until full saturation as with significantly different approaches similar conclusions can be drawn. The systematic error analysis is novel for this type of simulations and aids constraining the uncertainties.

5 Modelling Case 3: Thermo-Hydro-Mechanical Evolution of the Buffer (T > 100 °C)

Modelling Case 3 is based on the Swiss reference concept of drift disposal, with waste canisters resting on compacted bentonite blocks and the remaining void backfilled by bentonite pellets. The heat power per canister is 1500 W at emplacement and decreases with time as shown in Fig. 5.1.

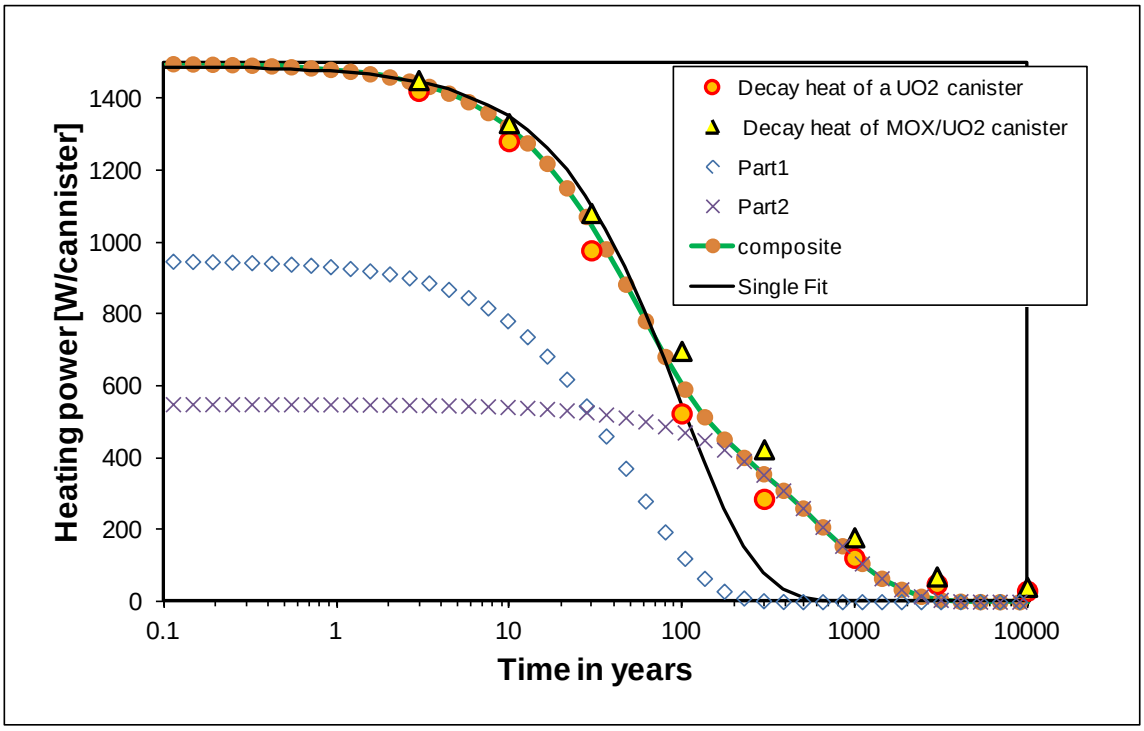

Fig. 5.1 Heat decay curve for UO2 and MOX/UO2 canisters and various curve fits ("composite" is the sum of "part 1" and "part 2")

Three teams (Nagra, GRS and CIMNE) were involved in the simulation of this case; all of them simulated a disposal cell including a single canister. Nagra and GRS both used a three-dimensional model, giving a realistic geometrical representation of the repository cell, but reduced the complexity of the problem by performing thermal-hydraulic simulations, neglecting mechanical effects. CIMNE used a full THM coupling with the simplification of a two-dimensional axisymmetric geometry which did not consider adjacent emplacement galleries.

5.1 Simulation by Nagra / TK Consult

5.1.1 Model dimensions and conditions

The used 3D model geometry (Fig. 5.2) represents a section of a full-scale emplacement tunnel, where the vertical boundaries represent symmetry planes between adjacent emplacement tunnels and between waste canisters. The top and bottom boundaries extend over the entire thickness of a host formation. This allows the simulation of the long-term temperature and pressure evolution without being noticeably affected by boundary conditions. The dimensions of the different components of the model are summarized in Tab. 5.1.

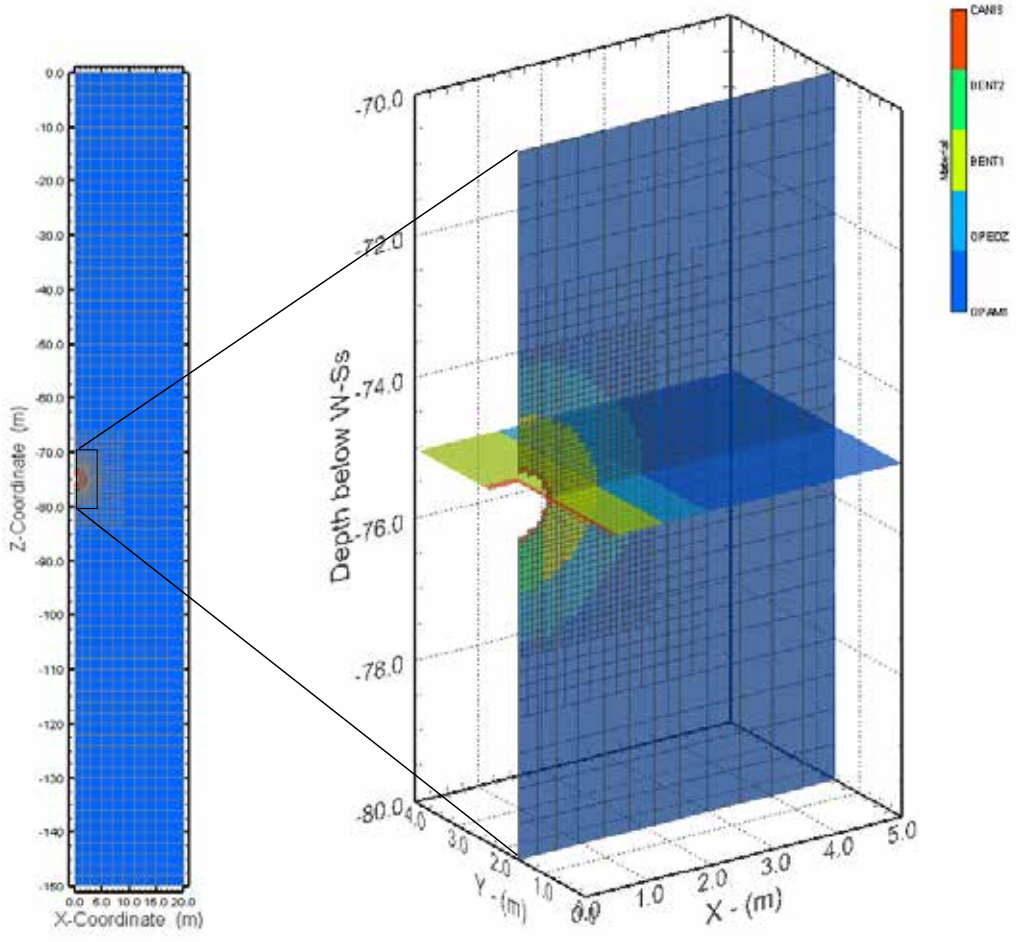

Fig. 5.2 Model geometry for the extension modelling

Tab. 5.1 Model dimension and initial conditions

	Values	**Comment**
Model Domain		
Height (m)	150	greater than typical OPA thickness of 100m
Lenght (m)	4	(half canister + bentonite)
Width (m)	20	(half distance between adjacent emplacement tunnels
Emplacement Tunnel:		
Tunnel Radius(m)	1.25	
Canister radius (m)	0.525	
Canister lenght (m)	2.5	(half length)
Initial Conditions:		
Pressure at z=75 m (MPa)	5.9	Hydrostatic at 600 m depth
Temperature at z=75 m (°C)	35.8	Temp. gradiet: 0.043 C/m, Surface Temperature: T_0=10°C
Capillary Suction (MPa)	2	Capillary suction for ventilated tunnel at atmospheric pressure (1.0135E+5 Pa)

The initial conditions represent hydrostatic pressure at a repository depth of 600 m. Initial temperatures correspond to a thermal gradient of 0.043 °C/m and a surface temperature of 10 °C resulting in a temperature of 35.8°C at the repository level. Boundary conditions are represented by prescribed pressure and temperatures at the top and bottom boundary. Vertical boundaries correspond to no-flow boundaries due to symmetry.

The original decay heat data for MOX or UO2 canisters are used, which are fitted by a composite exponential decay function as shown in Fig. 5.1, defined by:

$$N(t) = N_0 e^{-\lambda t} + N_1 e^{-\mu t}$$

with: N_0 = 950 W, l = 0.02 yr^{-1}, N_1 = 550 W, m= 0.0015 yr^{-1}.

5.1.2 Material parameters

Input parameters are based largely on the updated HE-E modellers data set, and summarized in Tab. 5.2. The focus is on thermal properties and two-phase parameter models of capillary pressure and relative permeability. Based on the HE-E modelling results, sensitivity analyses are performed on selected parameters to evaluate the impact of the parameter uncertainty on the temperature, saturation, and pressure evolution.

5.1.3 Modelling approach

The simulated phenomena involve the resaturation of the bentonite buffer (accounting for both bentonite blocks and pellets or sand/bentonite) and heat generation associated with radioactive decay of the waste material. That is, separate models can be used for either the sand/bentonite (GRS) configuration of the bentonite pellet (Nagra) section. Within the framework of the PEBS project extrapolation calculations were performed for the bentonite case only.

The modelling approach considered an initial phase, representing the excavation of the emplacement tunnel and operations period for one year, assuming a capillary suction of 2.0 MPa in the open tunnel. The corresponding ventilation period resulting in a depressurization and potential desaturation of the EDZ and near-field host rock was used as initial conditions for the heating/resaturation phase following the instantaneous emplacement of the waste canister and backfilling of the emplacement tunnels at the initial emplacement saturations of 63% and 20% for the bentonite blocks and pellets, respectively. A detail of the mesh is given in Fig. 5.3.

Tab. 5.2 Relevant input parameters in the model

	OPA	**EDZ**	**Bentonite blocks**	**Bentonite pellets**	**Heater**
Permeability: k(m^2)	1.0E-20	5.0E-20	2.5E-21	3.5E-20	1.0E-50
Porosity: f (-)	0.12	0.14	0.33	0.45	0.001
Pore compressibility: Cp [1/Pa]	1.7E-09	1.7E-09	3.0E-09	3.7E-09	0
Van Genuchten[1] P_0[Pa]	1.8E+07	9.0E+06	2.19E+07	1.0E+07	1.0E+06
Van Genuchten[1]; n (k_r)	1.67	1.67	1.42	*1.67*	2
Van Genuchten[1]; n (P_c)	1.67	1.67	1.42	1.67	2
Residual. Water Saturation: K_r-S_{wr} (Pc-S_{wr})	 0.1 (0.01)	 0.1 (0.01)	 0.1 (0.01)	 0.1 (0.01)	 0.01 (0.01)
Residual Gas Saturation: S_{gr}	0	0	0	0	0
Therm. Expansion T_x[1/K]	1.7E-05	1.7E-05	2.5E-05	2.5E-05	1.5E-05
Thermal conductivity (linear between T_{cs} and T_{cd})					
Wet: T_{cw}[W/m K]	1.9	1.9	1.3	1.3	52
Dry: T_{cd}[W/m K]	1.3	1.3	0.81	0.3	52
Specific Heat: S_h[J/kg C]	995	995	1058	893	440
Initial saturation (S_w)	1.0	1.0	0.63	0.2	0.01

Two-Phase Parameter Model	[1]van Genuchten		[1]van Genuchten/Mualem
	$P_c = P_o \left(S_{ec}^{\,n/(1-n)} - 1 \right)^{1/n}$	$S_{ec} = \frac{S_l - S_{lr}}{1 - S_{lr}}$ $m = 1 - 1/n$	$k_{r,l} = S_e^{\,g} \times \left[1 - \left(1 - S_e^{\frac{1}{1-n}} \right)^{\frac{n-1}{n}} \right]^2$ $k_{r,g} = (1 - S_e)^e \left(1 - S_e^{\frac{n}{1-n}} \right)^{2(1-1/n)}$ $S_e = \frac{S_l - S_{lr}}{1 - S_{lr}}$ g=0.33; e=0.5

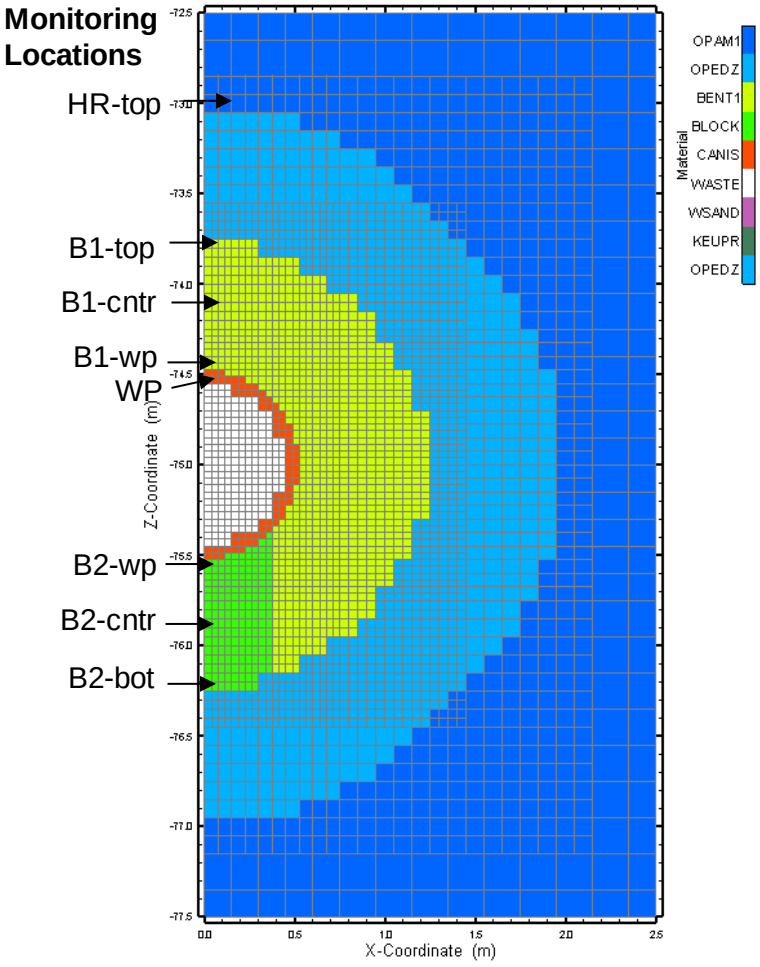

Fig. 5.3 2D refined mesh with monitoring locations

5.1.4 Modelling results

The reference case used the input parameters given in Tab. 5.2. The results are presented in terms of time histories of pressures, temperatures, gas saturations, and relative humidities at the specified locations in Fig. 5.3. The results show an early temperature increase peaking after about 5 years at 141°C followed by a gradual decline with maximum temperatures decreasing below 100°C after about 180 years. On the other hand, gas saturations in the buffer show a steep decline reaching full saturation after about 50 years. Gas saturation nearest to the canister show an increase due to heating and associated evaporation of pore water in the granular bentonite that corresponds to computed relative humidity to decrease to zero (i.e. pore water completely disappeared). The temperature plot in Fig. 5.4 shows vertical lines, indicating the time window (from 50 to 185 years) during which the bentonite buffer is at full saturation and

temperature exceeds 100°C. After full saturation, the pore pressure in the buffer and in the surrounding buffer increase due to the differential thermal expansion of the pore water relative to the rock framework (pores) that peak at about 10 MPa at a few meters distance from the tunnel (Fig. 5.6) which is greater than the peak shown in Fig. 5.4 corresponding to the Opalinus clay next to the EDZ (Fig. 5.3).

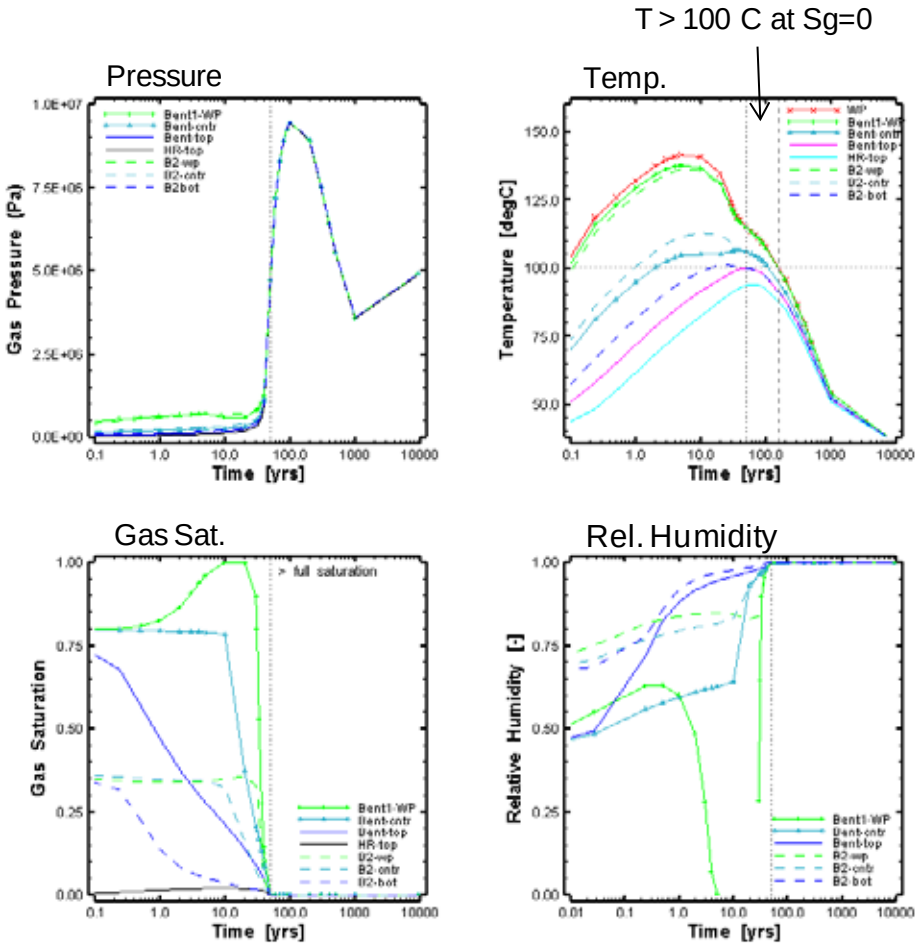

Fig. 5.4 Reference Case R0: Time histories of gas pressure (upper left), temperature (upper right), gas saturation (lower left), and computed relative humidity (lower right)

A detailed picture of the spatial distribution of temperatures and saturation is shown in Fig. 5.5, indicating the steep temperature gradient across the benonite buffer and the gas saturation that indicate the dry-out near the canister in the bentonite pellets, whereas the bentonite blocks remain partially water saturated. After 40 years, the 100°C contour extended to the outer bentonite/EDZ contact, whereby the peak tem-

peratures at the canister already declined. Gas saturation declined as the water from the surrounding host rock resaturates the buffer, preferentially the bentonite blocks.

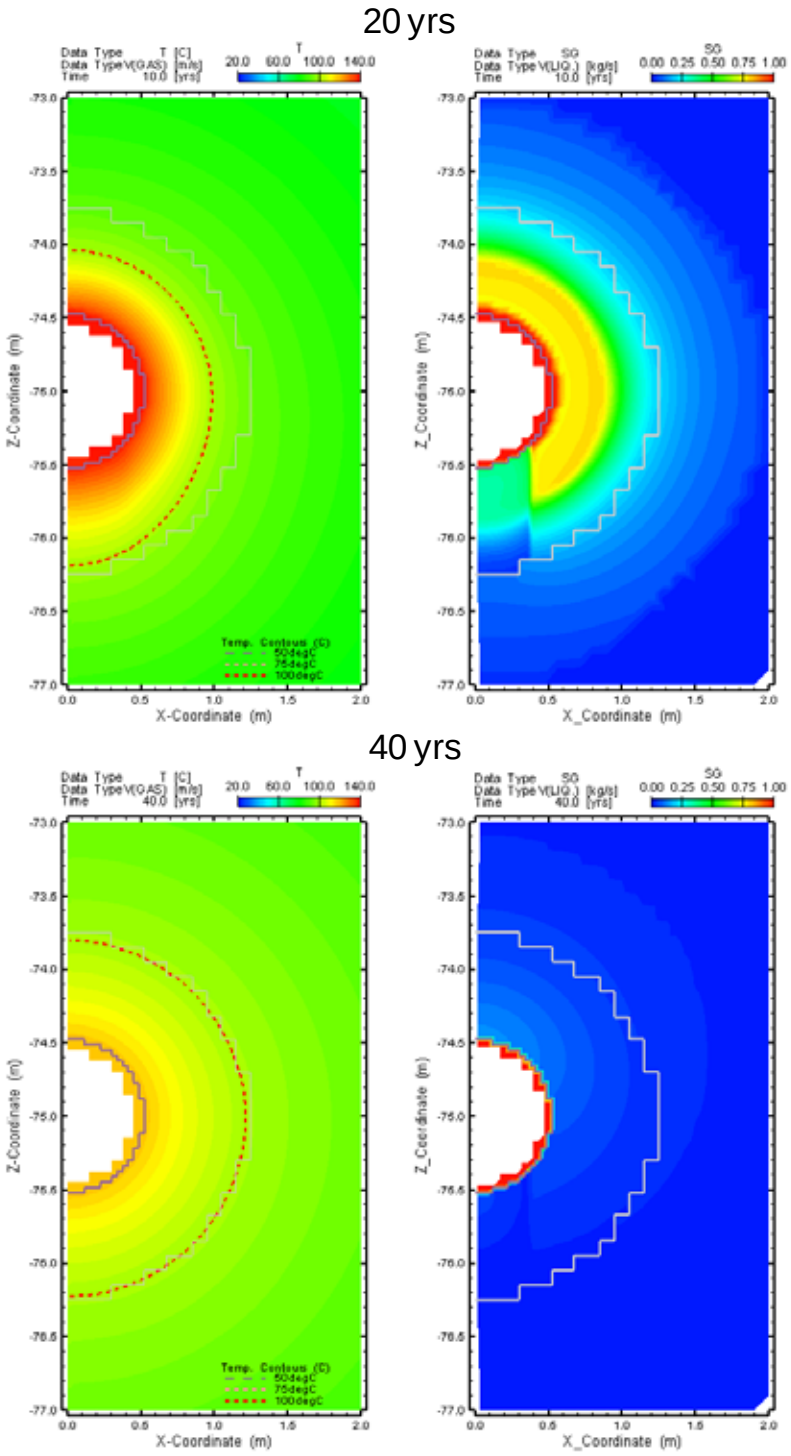

Fig. 5.5 Reference Case R0: Simulated distribution of temperatures (left) and gas saturations (right) after 20 years (top) and 40 years (bottom)

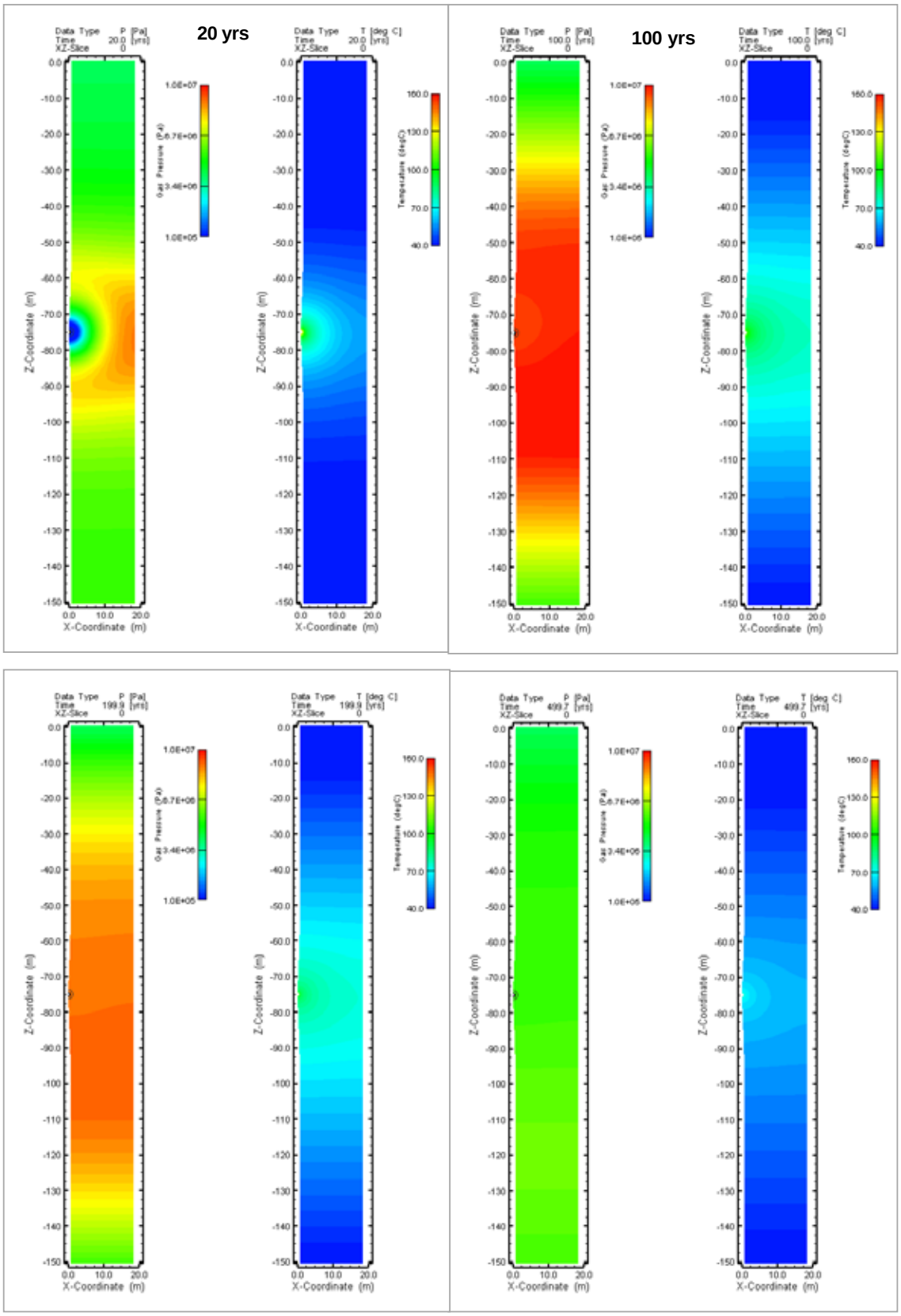

Fig. 5.6 Reference Case R0: Spatial distribution of pressures (left) and temperatures (right) after 20, 100, 200, and 500 years

The distribution of pore pressure and temperatures over the entire cross-sectional model (Fig. 5.6) showing the development of the pore pressures and temperatures through time. As indicated in Figure 5.4 the temperatures in near the canister peak after about 5 years, whereas peat temperatures farther away are delayed as the temperature front propagates into the surrounding host rock. Correspondingly, pore pressure increase reaching a peak of about 10 MPa and the greatest extent after 100 years. After 200 years, pore pressures and temperature declined, and after 500 years excess pore pressures have largely dissipated. For both the pressure and temperature front did not reach the upper and lower model boundaries, represented by prescribed hydrostatic pressures and temperatures in the surrounding formations.

In sensitivity case R1, the thermal conductivities for both bentonite pellets and blocks were set to 0.3 W/m K for dry bentonite and 1.0 W/m K for wet bentonite. These values better reproduced the measured temperatures in the buffer in the HE-E experiment. For case R1, a linear relationship between dry and wet thermal conductivity was used. The results in terms of pressure, temperatures, gas saturations, and relative humidities as a function of time are shown in Fig. 5.7. The simulated temperatures in the buffer indicate an increase in peak temperature from 141°C in Case R0 to 152°C. However, simulated temperatures in the surrounding Opalinus Clay did not indicate a noticeable increase. As a result, pore pressure in the buffer and surrounding Opalinus Clay, as well as resaturation timing did not change noticeably.

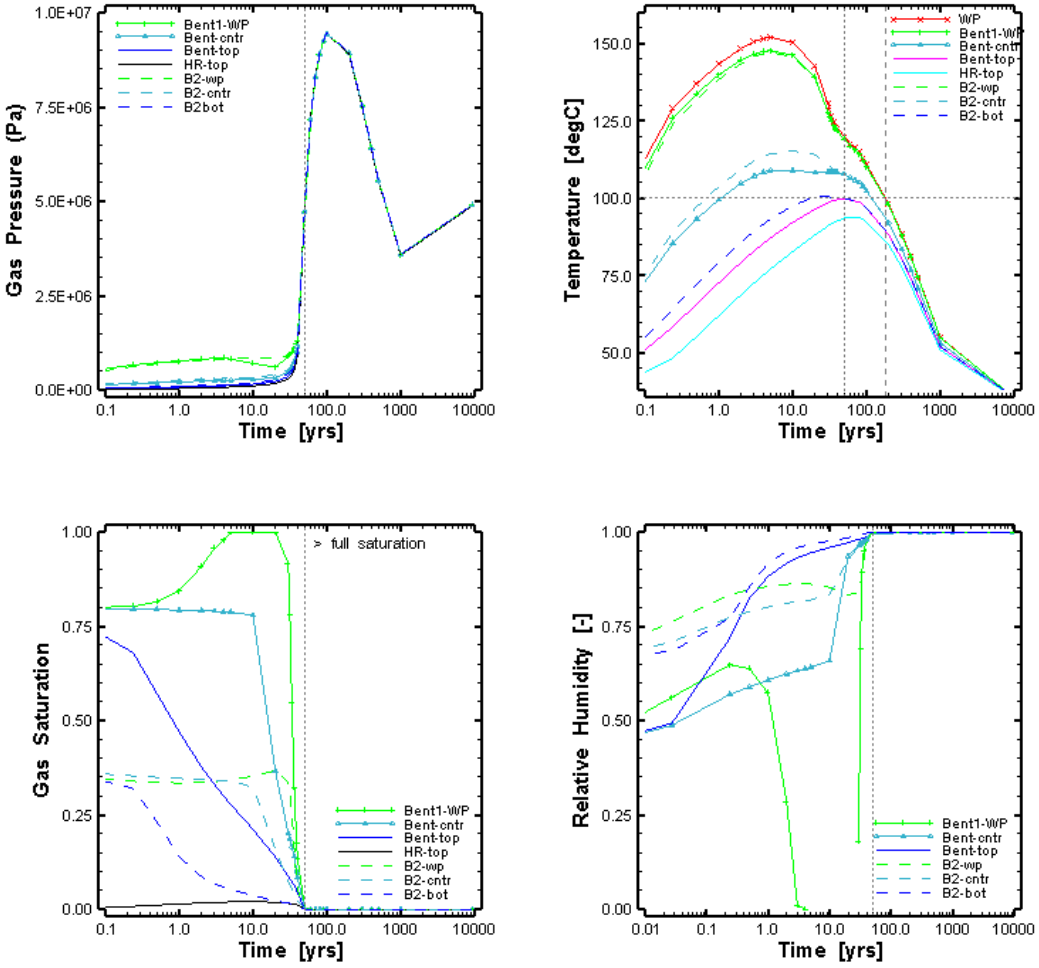

Fig. 5.7 Simulation Case R1: Time histories of gas pressure (upper left), temperature (upper right), gas saturation (lower left), and computed relative humidity (lower right)

In sensitivity case R2, the pore expansivity of the Opalinus Clay was reduced by one order of magnitude from 1.5E-5 $°C^{-1}$ to 1.5E-6 $°C^{-1}$. Lower values of pore expanisivity for the Opalinus Clay have been suggested based on the results from the HE-D experiment (Gens et al. 2007). In addition, case R2 used the same thermal conductivities as case R1. The results in terms of pressure, temperatures, gas saturations, and relative humidities as a function of time are shown in Fig. 5.8. The simulated pressures indicated only a minor increase of 0.2 MPa in peak pressures in the model. Temperatures and saturations in the buffer did not change.

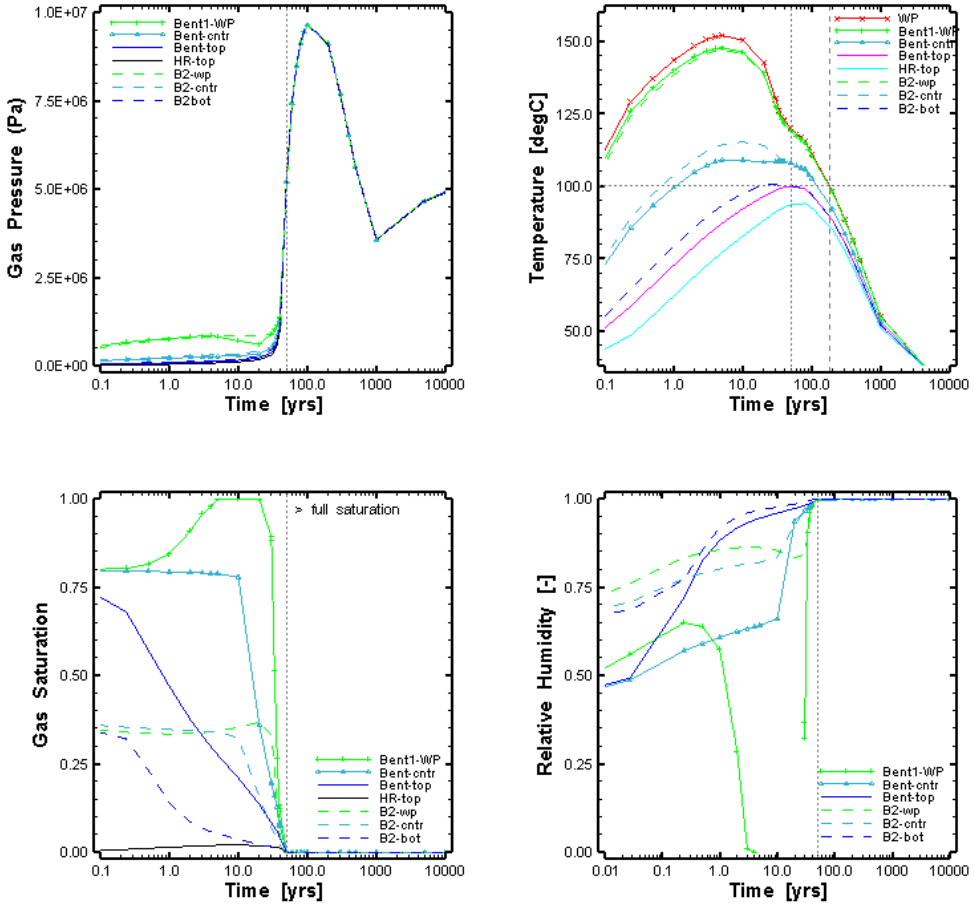

Fig. 5.8 Simulation Case R2: Time histories of gas pressure (upper left), temperature (upper right), gas saturation (lower left), and computed relative humidity (lower right)

Sensitivity case R3 is based on case R2 except that the permeability and the van Genuchten parameter P_0 for bentonite blocks is set to the same values as those for the pellets, whereas the initial saturation of the blocks were kept at 63%. The results are shown in Fig. 5.9 showing little difference. That is, the higher permeability for the blocks is counteracted by the lower capillary strength parameter and does not accelerate resaturation of the bentonite blocks.

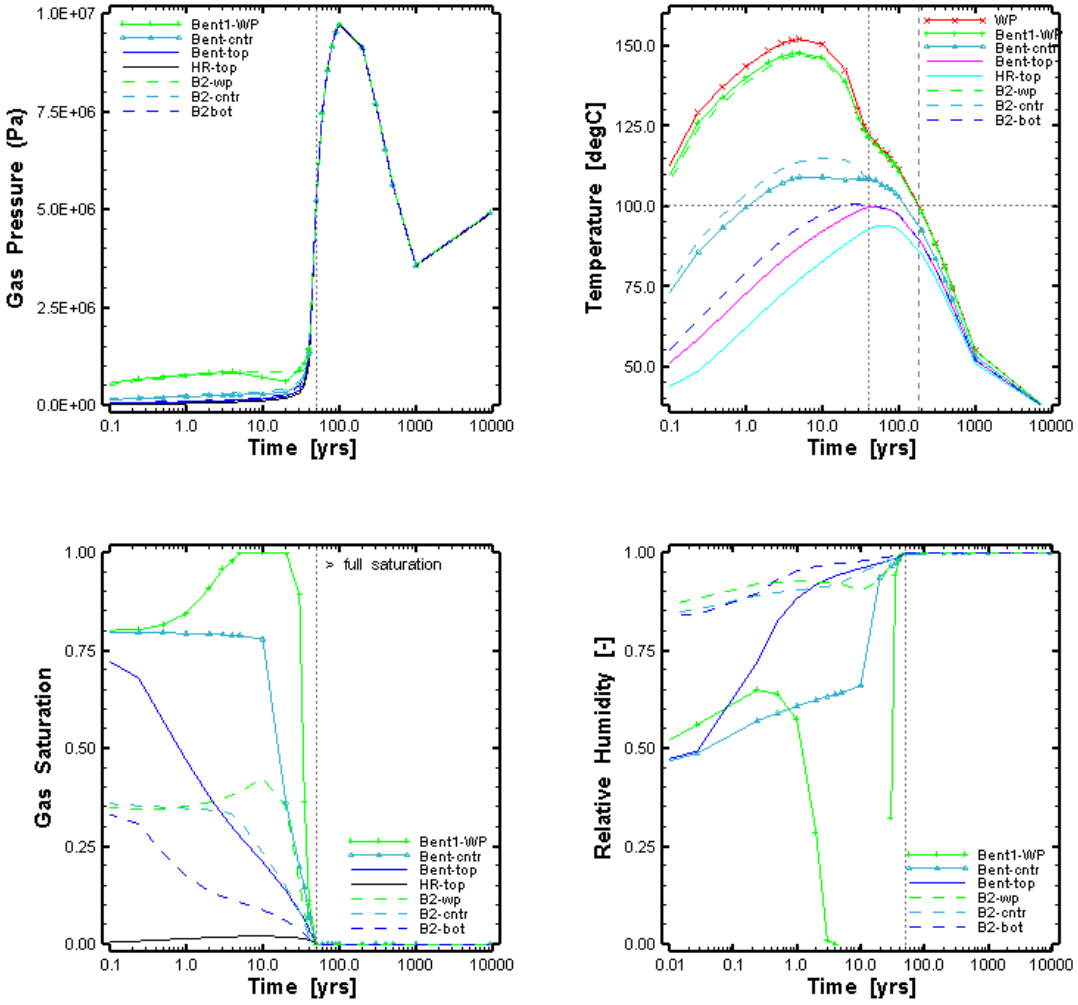

Fig. 5.9 Simulation Case R3: Time histories of gas pressure (upper left), temperature (upper right), gas saturation (lower left), and computed relative humidity (lower right)

In simulation case R4, the permeability of the bentonite pellets was reduced by one order of magnitude and the van Genuchten parameter P_0 for both pellets and blocks was set to 10 MPa. The results are shown in Fig. 5.10. With the overall reduced permeability of the pellets the resaturation of the buffer is delayed from 50 years to about 60 years. In addition, the desaturation of the pellets near the canister is also delayed, with complete dry-out after 75 years, followed by a rapid decrease in gas saturation as the resaturation front reached the canister. This delay is also indicated in the relative humidities. With the lower capillary pressures assumed for the bentonite block, the com-

puted relative humidities for the blocks start at higher values, and the saturation front is steeper compared to the previous cases (Fig. 5.10).

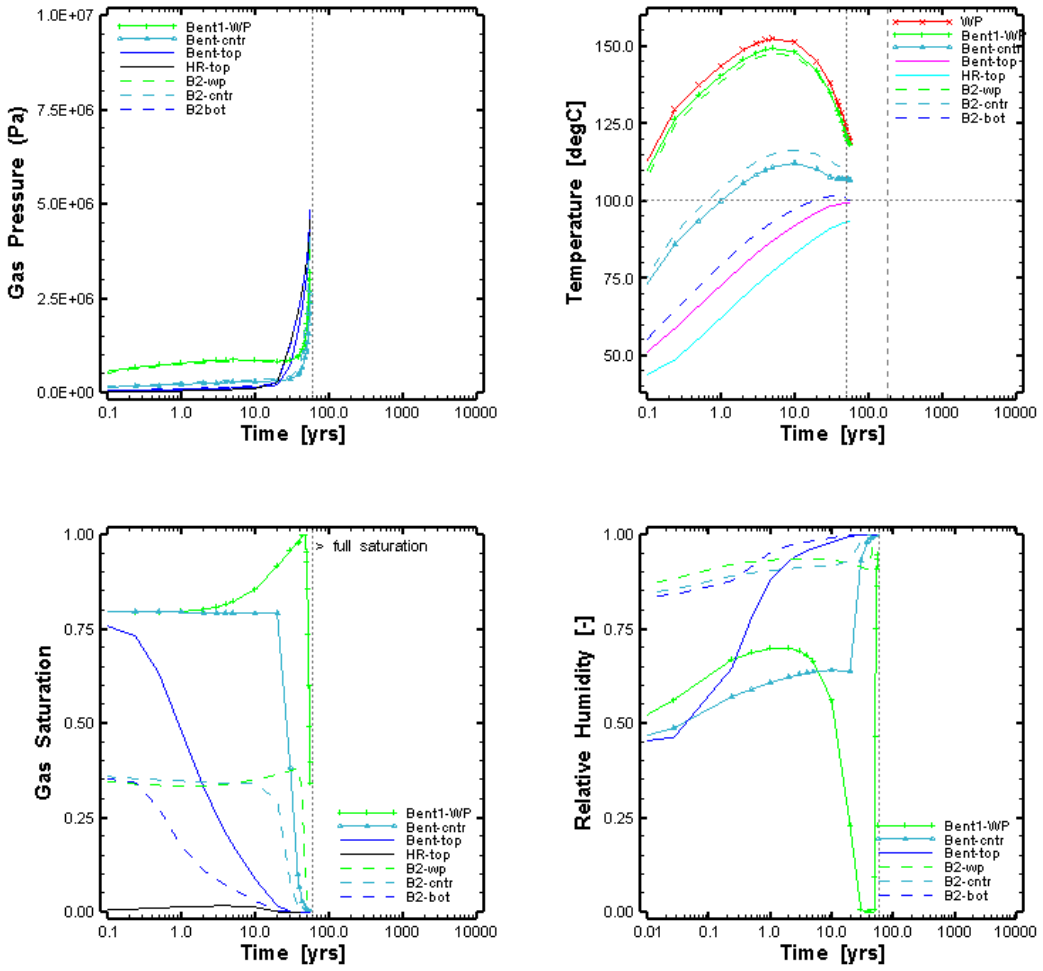

Fig. 5.10 Simulation Case R4: Time histories of gas pressure (upper left), temperature (upper right), gas saturation (lower left), and computed relative humidity (lower right)

Simulation case R5 is based on case R4 with the permeability of the Opalinus Clay reduced from 1.E-20 m^2 to 5.E-21 m^2, which is more representative for the deep Opalinus Clay (>500 m depth). The results in Fig. 5.11 indicate a further delay in resaturation of the buffer from 60 years in case R4 to about 100 years. With the delay in resaturation, the pressure peak is also delayed. Moreover, the time window for the temperature ex-

ceeding 100°C in the fully water-saturated bentonite buffer decreased to a range from 100 to 185 years.

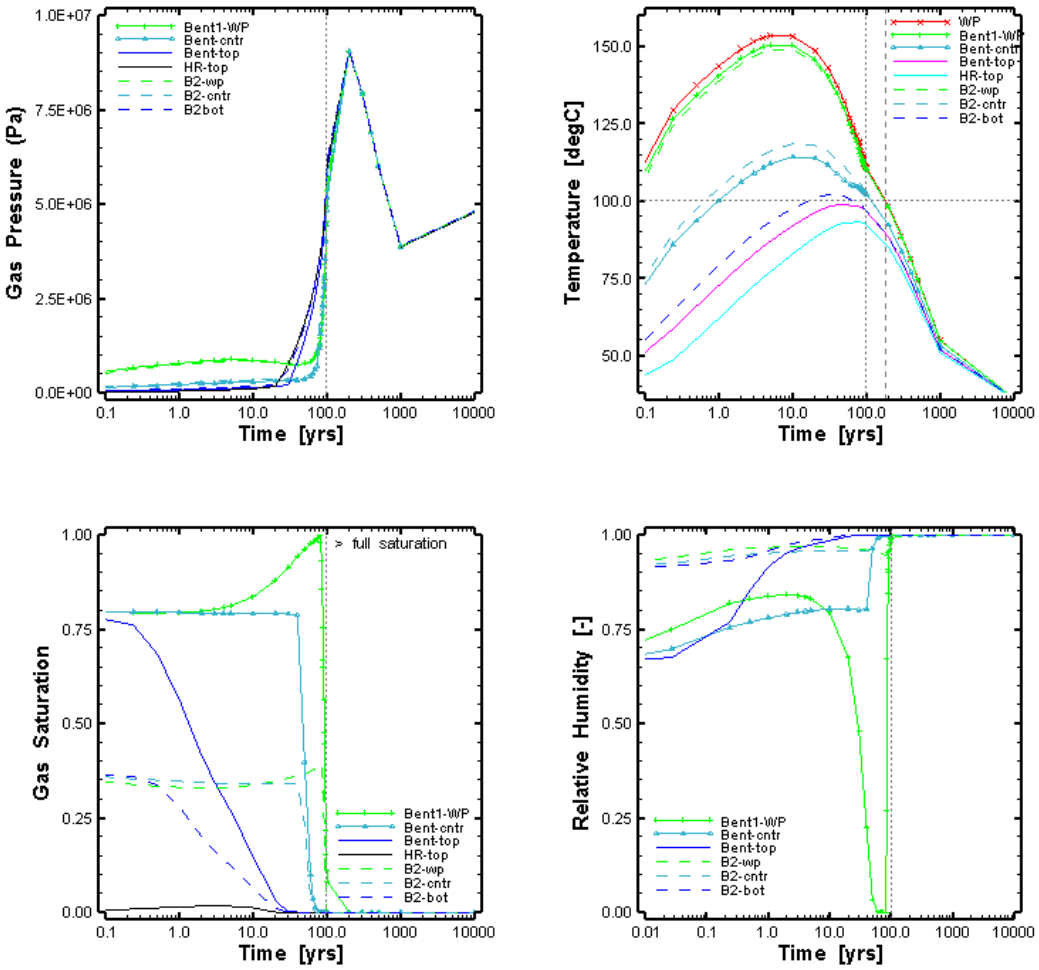

Fig. 5.11 Simulation Case R5: Time histories of gas pressure (upper left), temperature (upper right), gas saturation (lower left), and computed relative humidity (lower right)

5.1.5 Conclusions

The results of the TH modelling of Case 3 using the TOUGH2 code can be summarized as follows:

· Thermal Conductivity of bentonite has significant impact on peak temperatures in the buffer, particularly its dependence on saturation. On the other hand, the varia-

tion in thermal conductivities of the buffer has little impact on the temperatures in the surrounding Opalinus clay.

- The decrease in permeability of the bentonite pellets indicates only a small delay in reaching full saturation (from 50 to 60 years). A greater delay occurs in the case with reduced permeability of the Opalinus clay (case R5) where full saturation is achieved after about 100 years.
- The time window for the temperature in fully water-saturated bentonite buffer to exceed 100 °C ranges from 50 to 180 years.
- The effect of the pore expansivity (i.e., reduction by one order of magnitude) resulted only in a small increase (0.2 MPa) in peak pore pressure in the Opalinus clay.

5.2 Simulation by GRS

5.2.1 Modelling approach

GRS used CODE_BRIGHT for a coupled TH simulation with a 3D model, neglecting mechanical effects in the same way as Nagra with TOUGH2. Modelling starts with instantaneous construction of the emplacement gallery, which is then left open for one year. Afterwards, canister, bentonite blocks, and granular bentonite are emplaced also instantaneously. Initial saturation of the blocks is 63 %, while the granular bentonite starts at 20 % initial saturation.

The heat output of the canister could not be entered using a composite exponential function. Instead, the heat decay curve given in Fig. 5.1 was approximated by three individual exponential curves each active in a different time window, as shown in Fig. 5.12.

5.2.2 Geometry, conditions and material parameters

The dimensions of the model are identical to those of Nagra's simulation, as given in Tab. 5.1. The complete geometrical model and a detail near the emplacement gallery are shown in Fig. 5.13.

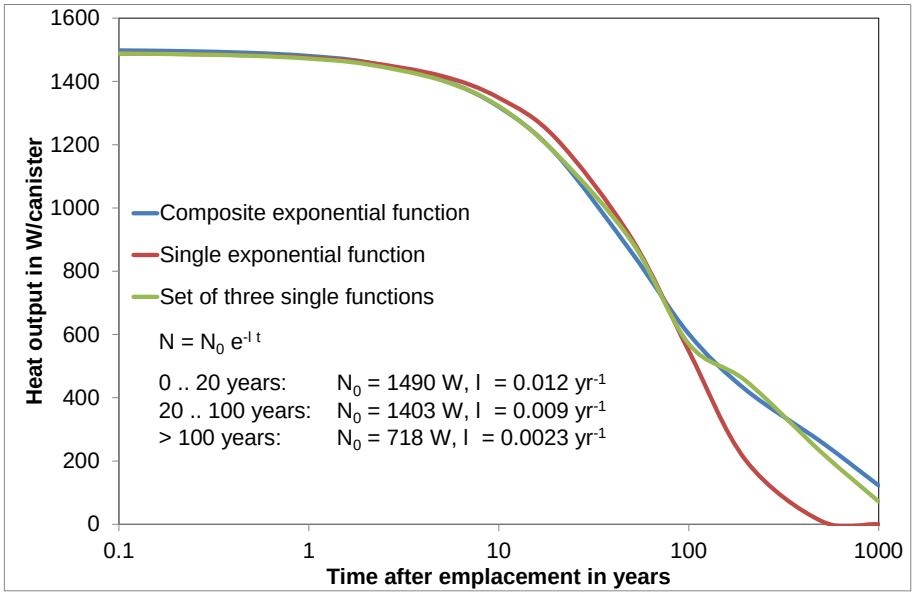

Fig. 5.12 Approximations of canister heat decay curve: The set of three single functions was used for the GRS simulation

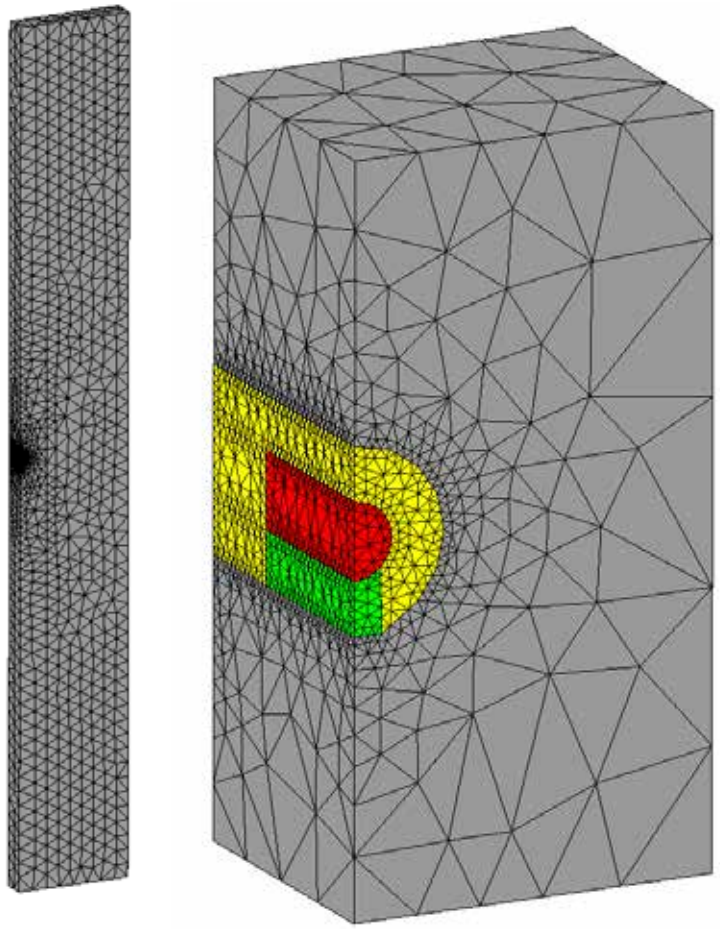

Fig. 5.13 Finite element model used for the simulation (left: detail near the gallery)

Boundary conditions at bottom and top of the model are given by prescribed temperatures and fluid pressures (32.575 °C and 5.15 MPa 75 m above the gallery axis and 39.025 °C and 6.65 MPa 75 m below the gallery axis). Initially, temperature and pressure increase linearly with depth, resulting in an initial temperature of 35.8 °C and a pressure of 5.9 MPa at gallery level. At the four model sides, no-flow boundary conditions are applied in consideration of the model symmetry. An excavation damaged zone with altered hydraulic properties was not considered.

During the gallery ventilation phase, a suction pressure of -29.5 MPa (corresponding to 94 % water saturation) is applied to the gallery wall.

The material parameters are those defined by the HE-E modellers data set, as given in Tab. 5.2 (see Section 5.1).

5.2.3 Modelling results

The actual simulation proved to be extremely time consuming. After a calculation time of several months only 220 years of repository evolution had been simulated. Therefore, an additional simplified model was used which is identical to the original model except for the fact that water evaporation is suppressed. This model worked much more efficient, so that a simulation time of 1000 years was reached. Of course, this simplification is not adequate for the early evolution when temperatures above 100 °C occur and when the buffer is only partially saturated. At later times sporting moderate temperatures and full buffer saturation, however, the full model and the simplified one yield identical results, as will be shown further down in this section.

The simulation results of the two models are shown for evaluation points on the canister surface, on the tunnel wall and the floor, and at various locations in the granular bentonite buffer and in the bentonite blocks, as shown in Fig. 5.14.

5.2.3.1 Temperature

The Figures 5.15, 5.16 and 5.17 show the temperature evolution on the canister and tunnel surface, in the granular buffer, and in the bentonite blocks, respectively. At simulation times up to 27 years there is a significant difference between the full (symbols) and the simplified (dashed lines) model, because suppressing of evaporation acceler-

ates saturation of the buffer, leading to higher thermal conductivity of the buffer. After 27 years simulation time, the curves are identical, so that the simplified model can be considered representative for the long term. The maximum temperature on the canister surface of 145 °C is reached at about five years after emplacement (Fig. 5.15). 1000 years after emplacement, the temperature has reduced to about 45 °C everywhere in the buffer.

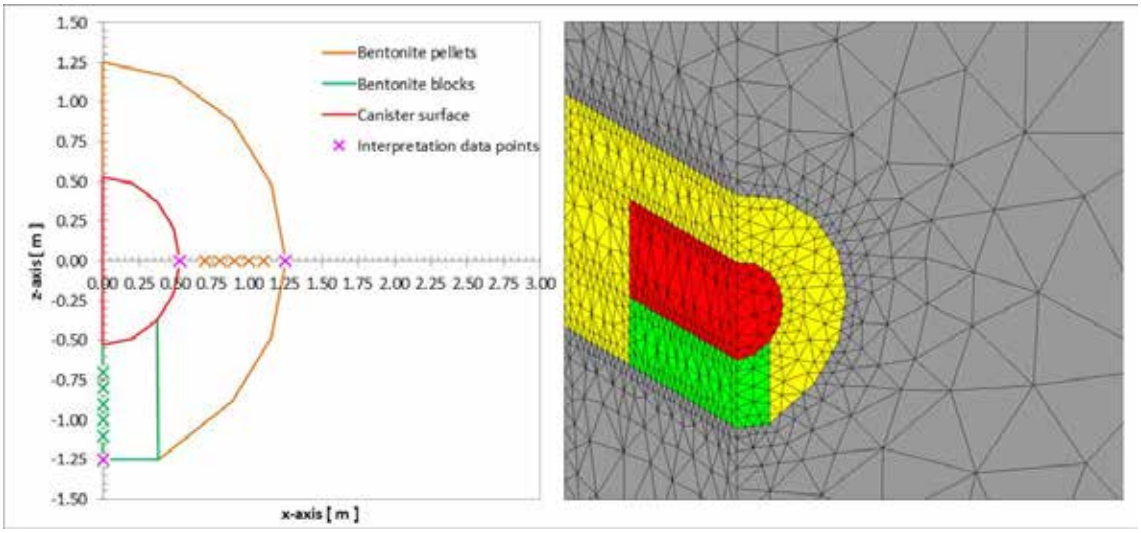

Fig. 5.14 Location of evaluation points on the canister, the tunnel surface, and in the buffer

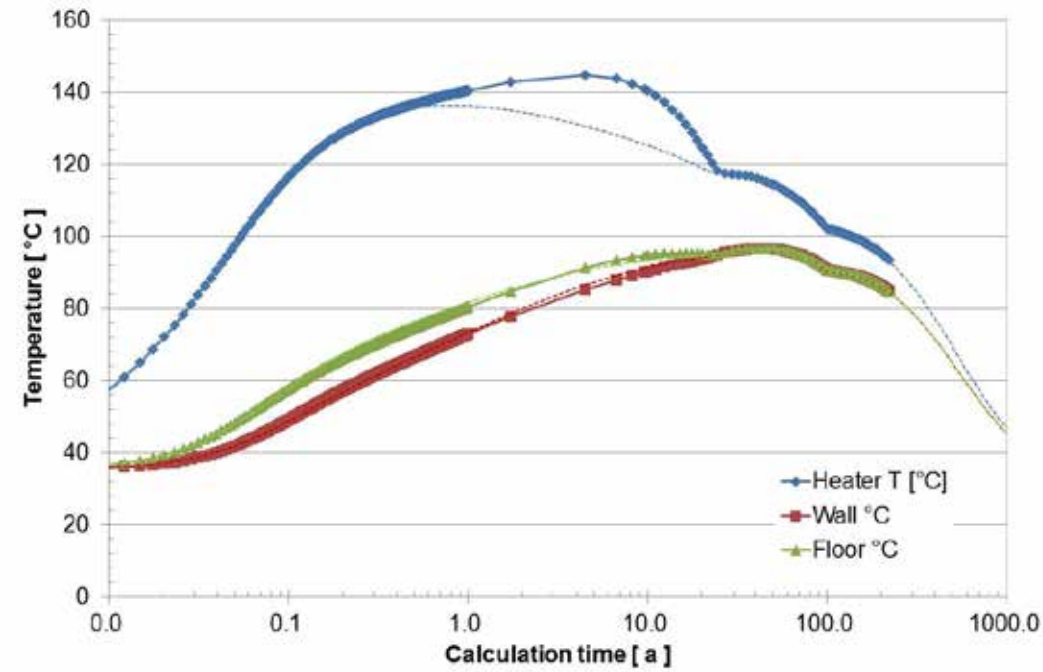

Fig. 5.15 Temperature evolution on the canister and on the tunnel surface

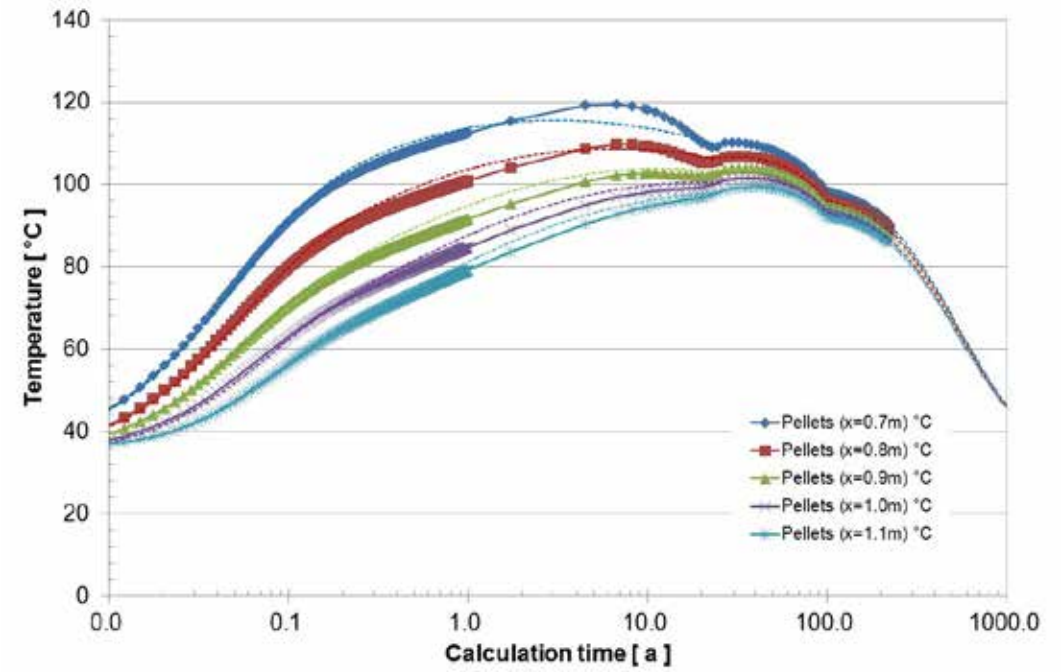

Fig. 5.16 Temperature evolution in the granular buffer

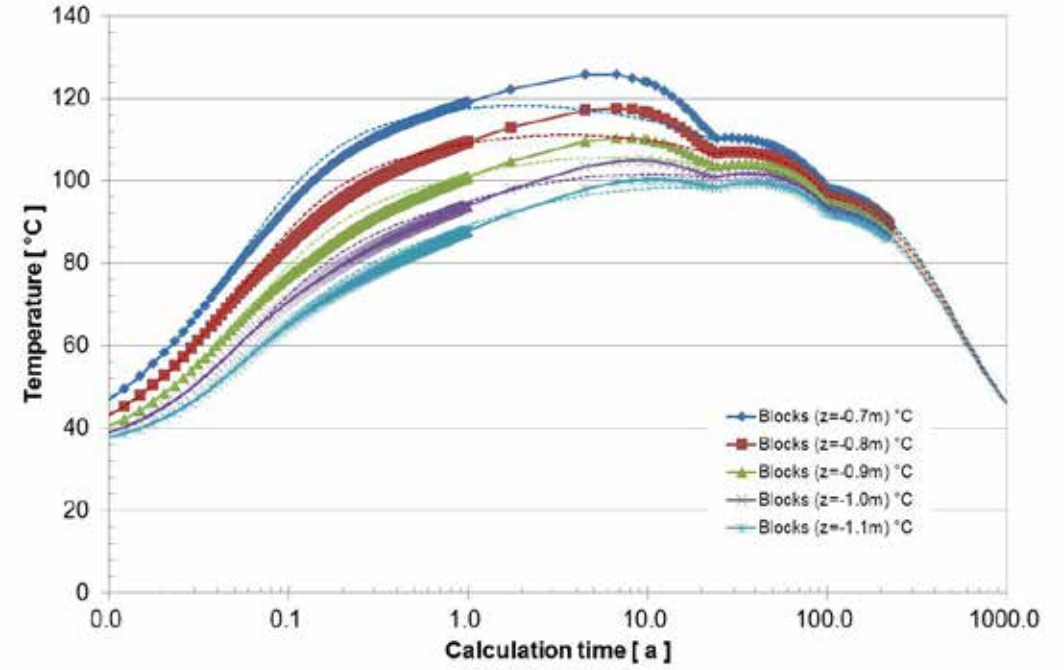

Fig. 5.17 Temperature evolution in the bentonite blocks

The temperature in the host rock is shown as profiles for different times in Fig. 5.18. The rock temperature remains below 100 °C all the time. The maximum temperature of 71 °C at the symmetry plane between two emplacement galleries is reached after 100 years; then, the temperature is decreasing everywhere in the model.

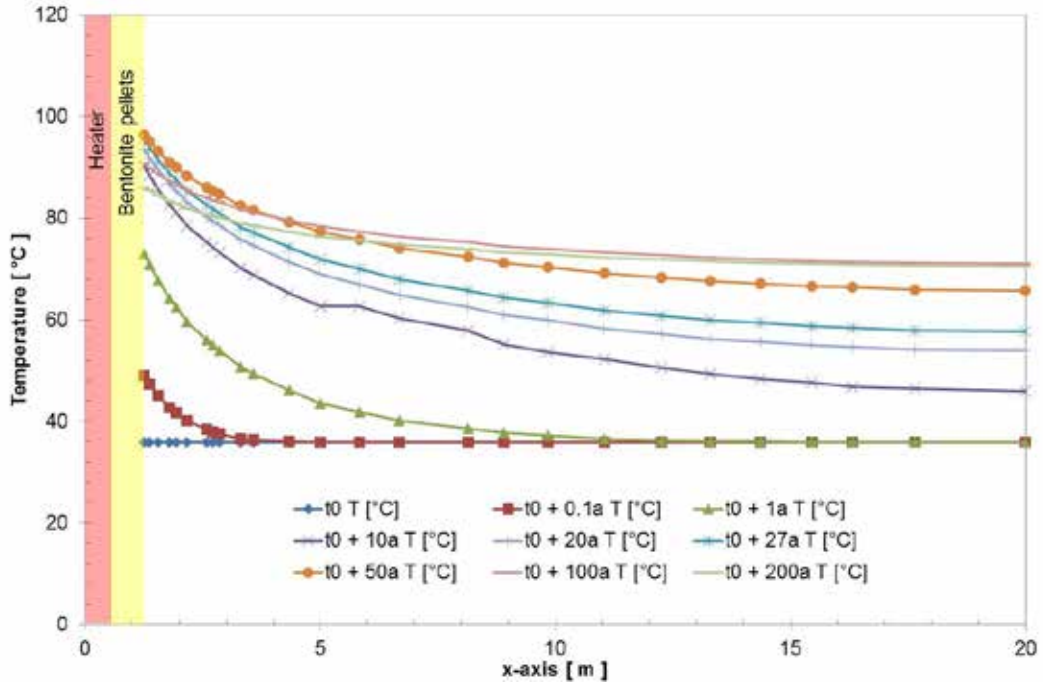

Fig. 5.18 Temperature profile in the rock for different simulation times

5.2.3.2 Saturation and relative humidity

The saturation evolution of the granular buffer and of the bentonite blocks is shown in Fig. 5.19 and Fig. 5.20, respectively. Naturally, the saturation curves of the simplified model (dashed lines) are not realistic, because evaporation is suppressed, which has a high effect on saturation rates. In particular, desaturation of the blocks at high temperature is nearly not observed in the simplified model. The time to full saturation is, however, not very different in the simplified and the full model.

In the full model (symbols in the figures), there is an early desaturation of the bentonite blocks close to the canister (Fig. 5.20) due to evaporation at high temperature. The pellets are at very low saturation from the beginning, therefore there is no further desaturation, but saturation rates are very low. Five years after emplacement, when the temperature starts to decrease, saturation rates are accelerated due to condensation of water vapour. 27 years after emplacement the buffer is fully saturated.

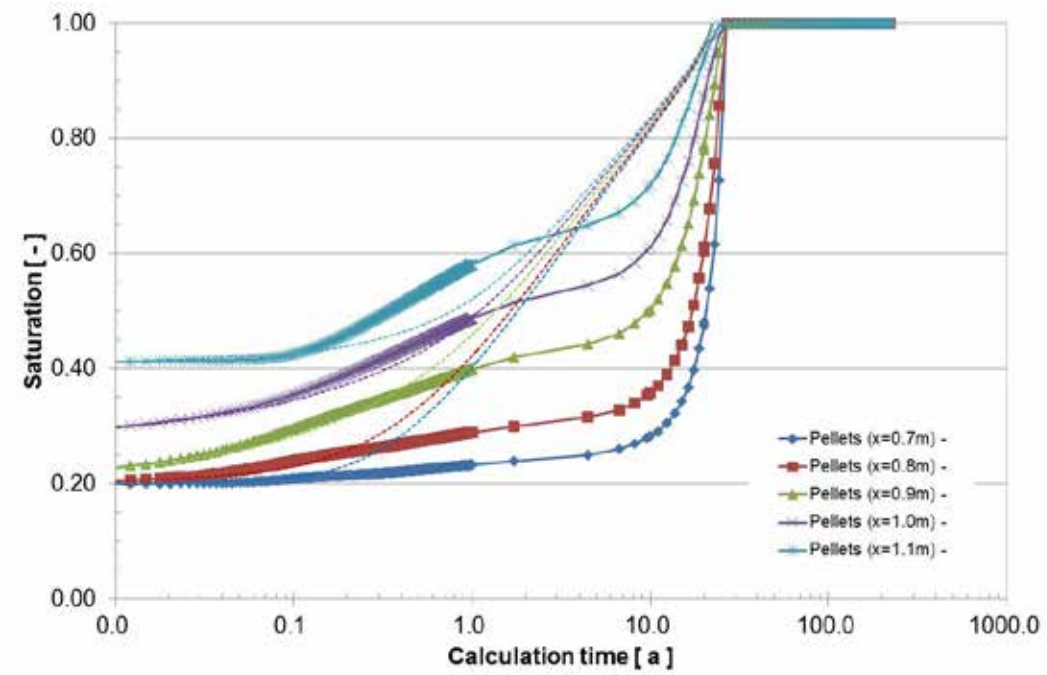

Fig. 5.19 Saturation evolution in the granular buffer

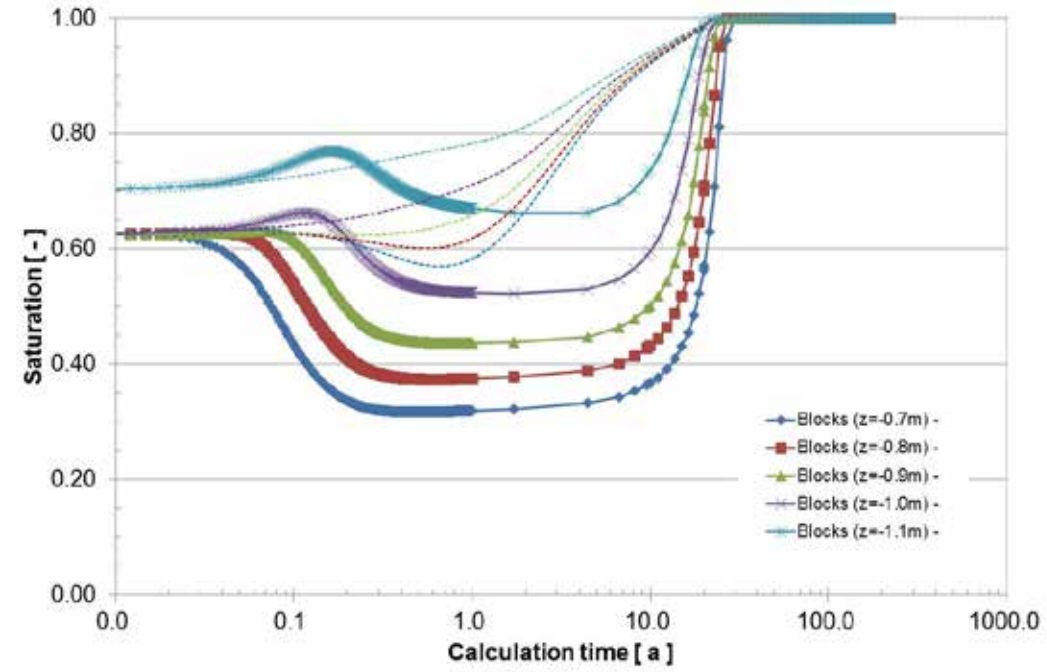

Fig. 5.20 Saturation evolution in the bentonite blocks

The Figures 5.21 and 5.22 show the evolution of relative humidity corresponding to the saturation for the granular pellet buffer and the bentonite blocks.

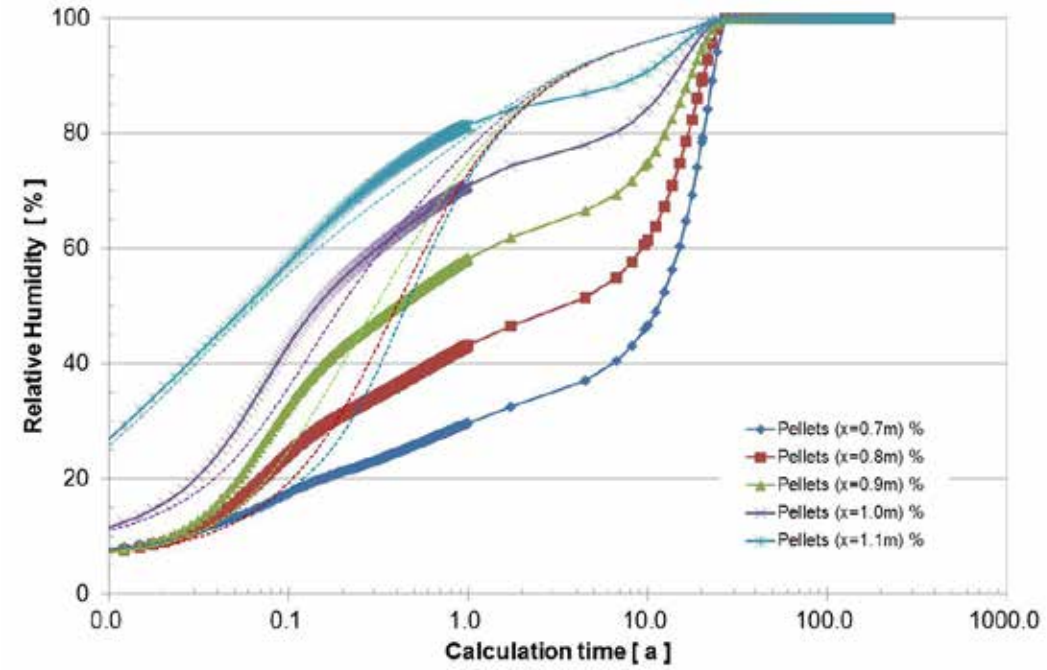

Fig. 5.21 Evolution of relative humidity in the granular buffer

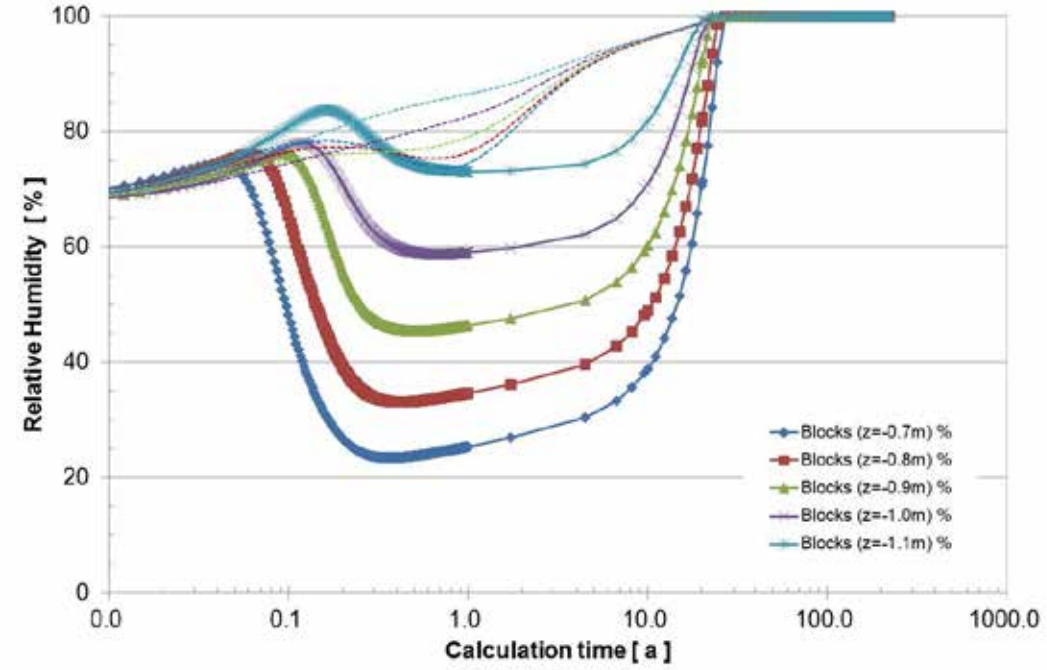

Fig. 5.22 Evolution of relative humidity in the bentonite blocks

5.2.3.3 Pore pressure in the rock

Pore pressure profiles in the rock for different simulation times are presented in Fig. 5.23. A pore pressure of 10 MPa is already reached after 10 years, later, the pore pressure increases even further. This is not realistic, but stems from the fact that in this calculation a distinction between thermal expansion coefficients for the solid grains, the pore liquid, and the grain skeleton was not possible. This improvement was introduced by CIMNE (see Section 5.3).

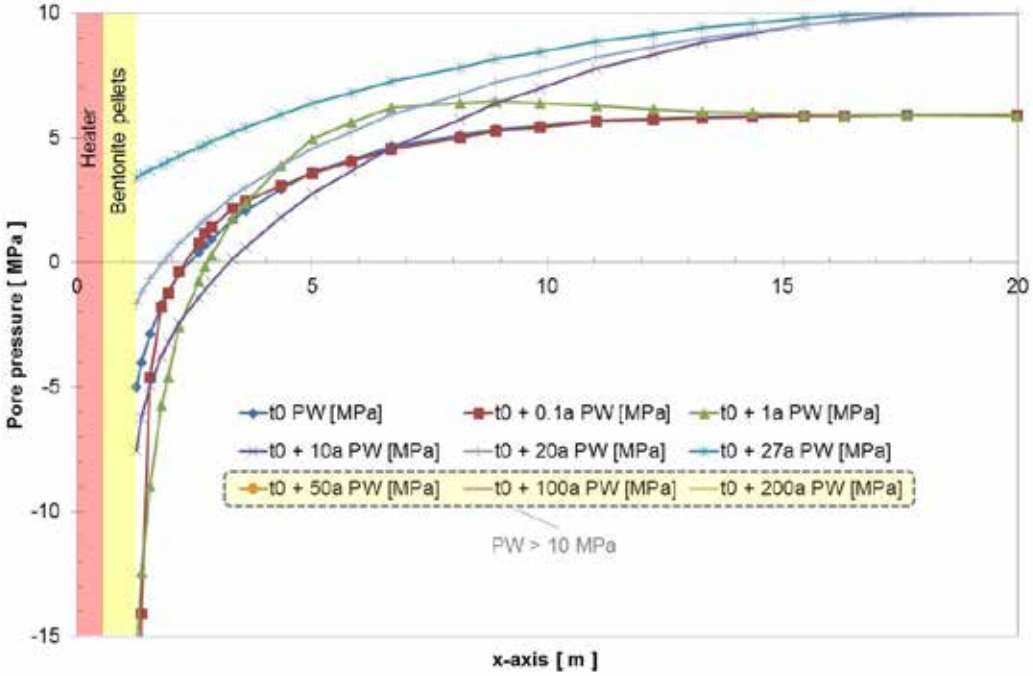

Fig. 5.23 Pore pressure profile in the rock for different simulation times

5.2.3.4 Alternative simulation case

Due to the very high simulation times with the full model, consideration of alternative cases was very limited. Only one alternative case with an altered saturation of the tunnel surface at emplacement time was considered, since this is a parameter which is not well defined. It was found, however, that the influence in terms of temperatures and buffer saturation time was negligible.

5.2.4 Conclusions

Simulation of a 3D TH model of an emplacement cell representing the Swiss repository concept proved possible with CODE_BRIGHT, although the calculation effort was very high. Compared to the results of Nagra using a similar model with TOUGH2, temperatures are similar, while saturation time is lower and pore pressures are higher. This is likely caused by two differences:

- In the GRS model, no EDZ with altered hydraulic properties was considered.
- Thermal expansion coefficients for the solid grains, the pore liquid, and the grain skeleton were possibly not in an adequate relation in the GRS model.

An improvement of the long-term simulations can be expected if the TH calculation is replaced by a full THM-coupled simulation, especially if a realistic representation of the rock behaviour including time-dependent deformation and damage can be used. With the calculation times of months for the TH simulation, this could not be performed with the 3D model. CIMNE, however, performed THM simulations using a 2D model. These are presented in Section 5.3.

5.3 Simulation by CIMNE

5.3.1 Description of the case

The proposed 3D geometry for the extrapolation to repository long-term modelling was simplified into an axisymmetric conceptual model covering the half length of a heater element (Fig. 5.24). Because the axisymmetric nature of the analysis prevents taking into account the actual heterogeneous section of the engineered barriers, two cases have been analysed: a homogenous one in which the space surrounding the canister is filled with just bentonite pellets and a heterogeneous one in which the space around the canister is filled with a combination of compacted blocks and pellets (see Fig. 5.25). The axisymmetric geometry is 100 m wide and 4.00 m long (corresponding to the length of half canister + bentonite barrier). The upper horizontal boundary represents the plane of symmetry between two adjacent canisters and the lower boundary is the middle section of a waste canister. The emplacement tunnel radius and the canister radius are 1.25 m and 0.525 m, respectively. The half length of a canister is assumed to be equal to 2.50 m. Adjacent emplacement tunnels are not taken into account in cal-

culations. The EDZ around the tunnel is assumed to be 0.60 m wide and is considered through a material with the same THM properties of the rock formation (Opalinus Clay) except for its initial porosity, water permeability and air entry suction.

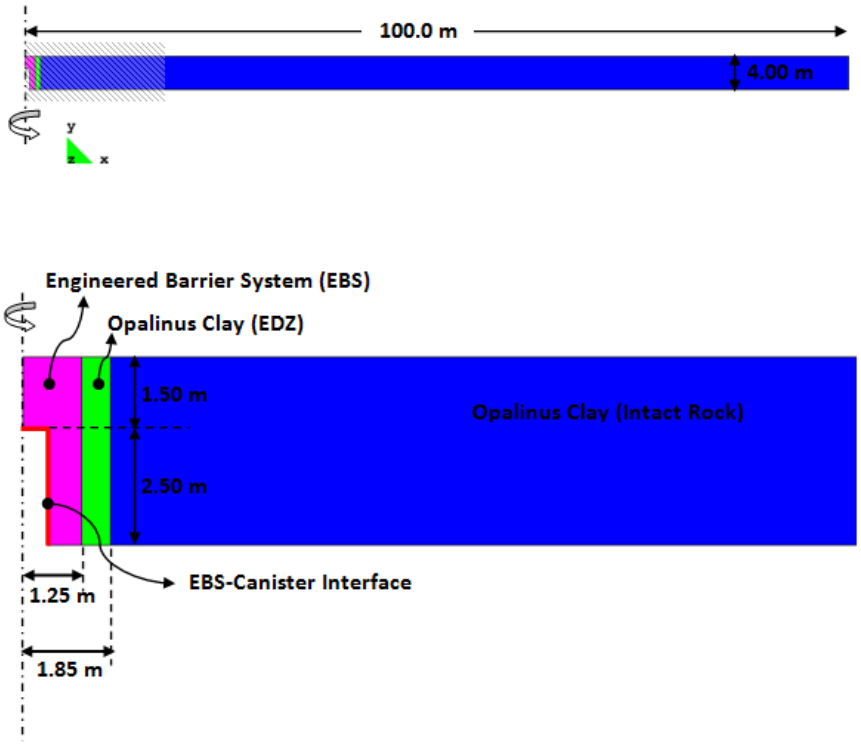

Fig. 5.24 Modelled domain (up) and detailed view of the EBS and the excavation damaged zone (down) for the axisymmetric model. The canister radius is 0.525 m

The following additional conditions are assumed in calculations:

- The upper and the lower horizontal boundaries are taken as symmetry borders. Therefore no fluxes across and no vertical displacements on those boundaries are allowed.
- A liquid pressure value of 5.90 MPa and a prescribed temperature of 35.8ºC are applied to the right hand side boundary of the model domain.
- No vertical displacements are allowed along horizontal symmetry boundaries. A compressive stress of 6.90 MPa is applied to the right hand side boundary of the model domain.
- A zero-stress condition is applied on the left hand side boundary before barrier emplacement in order to simulate the tunnel excavation.

- A suction of 2.0 MPa is imposed on the left boundary in order to represent the ventilation condition. This suction corresponds to a relative humidity around 98.5% and it is quite realistic for a tunnel closed condition.
- Prior to the excavation of the emplacement tunnel the rock mass is considered to be saturated.
- A pore water pressure of 5.90 MPa and a compressive stress of 6.90 MPa are taken to represent the initial liquid pressure and the initial isotropic stress state in the rock, respectively. The initial temperature was set to 35.8ºC.

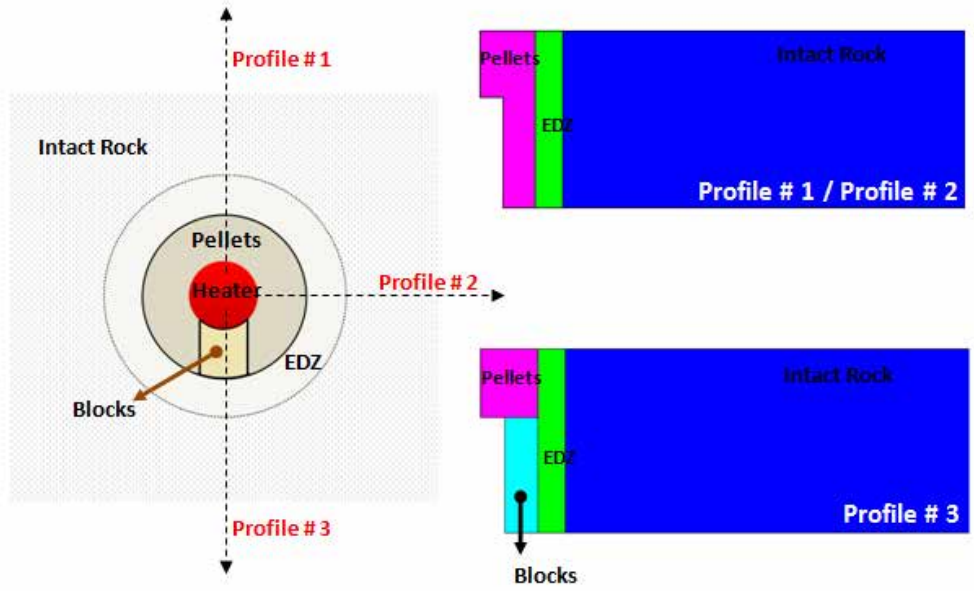

Fig. 5.25 Schematic layout of the engineered barrier system (left) and detailed view of the EBS of the two modelled cases (right) considered in calculations: the homogeneous buffer case (up) composed by bentonite pellets and the heterogeneous buffer case (down) with compacted bentonite blocks around the heater and pellets between two adjacent heaters

The modelling protocol is as follows:

- Construction of the tunnel about 10 years before the emplacement of the backfill. The excavation process is modelled by a relaxation of the total stresses on the tunnel wall and applying a low constant suction value. It is expected that the venti-

lation period results in a lowering of the pore pressure and possibly some desaturation in the area adjacent to the tunnel.

- Emplacement of the waste canister and bentonite barrier. A period of time of 75 days is left before the beginning of the heating phase. The initial emplacement saturation for the bentonite blocks and bentonite pellets are 63% and 18%, respectively, resulting in initial suctions of about 55 MPa for the compacted blocks and 123 MPa for the pellets.

- An initial prescribed heat flow of 1500 W is applied.

- Heat power decays according to the expected long-term evolution expected to take place during the lifetime of the radioactive waste repository. For that purpose, an exponential heat decay function has been proposed based on the decay heat data for MOX or UO2 canisters (Johnson et al., 2002) resulting in a composite function defined by:

$$N(t) = N_0 e^{-/t} + N_1 e^{-mt}$$

  where the fitting parameters are: $N_0 = 950$, $/ = 0.02$, $N_1 = 550$, $m = 0.0015$.

- The shape of the composite heat decay function is shown in Fig. 5.26.

- The analyses have been run up to a total duration of 10000 years. Special attention will be given to the results of the first 100 years where most of the variations of the hydraulic variables occur.

The evolutions of temperature, water saturation and pore water pressure in the clay barrier and in the host rock are computed using the formulation and computer code described in Deliverable 3.2-2. Thermal expansion for water, for solid particles and for porous skeleton is considered in the calculations due to the key role that differential thermal expansion of water and solid and thermal expansion of the pores (equivalent to thermal expansion of the skeleton) play in the generation of excess pore water pressure by thermal load. Due to the fact that high thermal gradients are expected during heat generation, water phase exchange (evaporation and condensation) is considered as well as the subsequent water vapour transport through the pores by diffusion. The dependence of water viscosity on temperature is also incorporated. Thermal conductivity and water permeability are taken as a function of water saturation. For simplicity, the mechanical behaviour of the host rock and of the bentonite filling materials is de-

scribed by means of elastic models. Material parameters used in the numerical calculations are based on the updated HE-E modellers' data set and are summarized in the Tables 5.3 - 5.7.

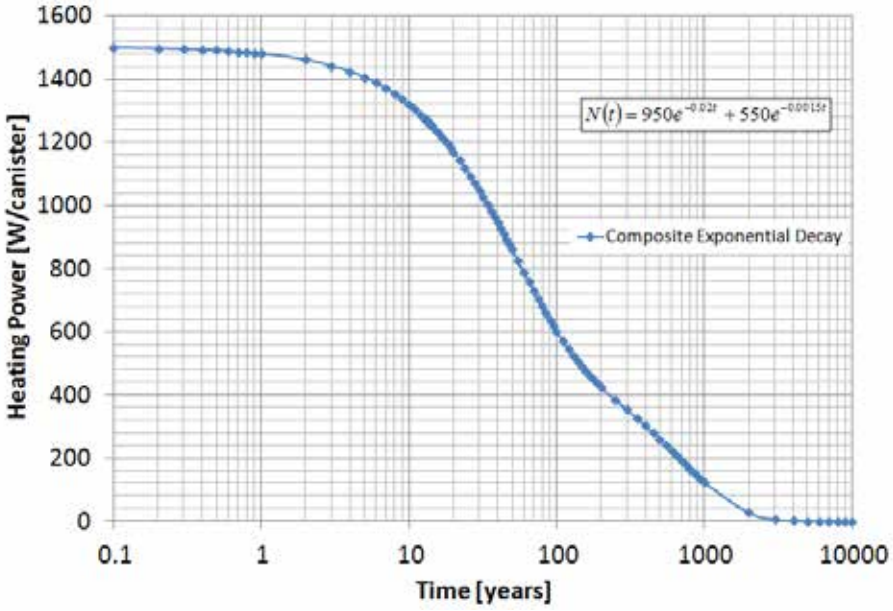

Fig. 5.26 Heat decay function used in the analyses. Time "zero" represents the beginning of heating at the canister

Tab. 5.3 Physical properties for water in pores

Water Density[a]	
Reference density, ρ_{l0} [kg.m^{-3}]	1002.6
Water compressibility, β [MPa^{-1}]	4.50e-04
Volumetric thermal expansion coefficient (at 40ºC), α [ºC^{-1}]	-3.40e-04
Water Viscosity[b]	
Pre-exponential parameter, A [MPa.s]	2.10e-12
Exponential parameter, B [K]	1808.5

[a] Input parameters for the dependence of water density on temperature:

$$\rho_l(T, p_l) = \rho_{l0} \exp[b(p_l - p_{l0}) + aT]$$

[b] Input parameters for the dependence of water viscosity on temperature: $\mu_l(T) = A \exp\left(\frac{B}{273.15 + T}\right)$

Tab. 5.4 Physical properties for the host rock and the buffer materials

Physical Properties	Opalinus Clay (Intact rock)	Opalinus Clay (EDZ)	Bentonite Pellets	Bentonite Blocks
Solid grain density [kg/m^3]	2700	2700	2700	2700
Solid phase specific heat [J/kg.K]	900	900	893	1058
Porosity	0.12	0.14	0.45	0.33
Linear thermal expansion for solid grain [K^{-1}]	1.70e-05	1.70e-05	2.50e-05	2.50e-05
Linear thermal expansion for the medium [K^{-1}]	1.70e-05	1.70e-05	2.50e-05	2.50e-05

Tab. 5.5 Thermal parameters for the host rock and the buffer materials

Thermal Properties	Opalinus Clay[a] (Intact rock)	Opalinus Clay[a] (EDZ)	Bentonite Pellets[b]	Bentonite Blocks[b]
Dry Thermal Conduct., λ_{dry} [W/m/K]	1.30	1.30	0.30	0.81
Saturated Thermal Conduct., λ_{sat}	1.90	1.90	1.30	1.30

[a] Dependence of thermal conductivity (λ) on degree of saturation (S_l) through: $\lambda = \lambda_{sat}\sqrt{S_l} + \lambda_{dry}\left(1 - \sqrt{S_l}\right)$

[b] Dependence of thermal conductivity (λ) on degree of saturation (S_l) through: $\lambda = \lambda_{sat}^{S_l} \times \lambda_{dry}^{(1-S_l)}$

Tab. 5.6 Hydraulic parameters for the host rock and the buffer materials

Hydraulic Parameters	Opalinus Clay (Intact rock)	Opalinus Clay (EDZ)	Bentonite Pellets	Bentonite Blocks
Retention Curve[a]				
P_0 [MPa]	18.0	9.00	10.0	21.9
σ_0 [N/m]	7.20e-02	7.20e-02	7.20e-02	7.20e-02
Shape Parameter, λ''	0.29	0.29	0.40	0.30
Pressure related to the suction at full dry state, P_d [MPa]	1.0e27	1.0e27	1.0e27	1.0e27
Shape Parameter, λ_d	0	0	0	0
Residual/maximum water saturation	0.01 – 1.00	0.01 – 1.00	0 – 1.00	0.01 – 1.00
Water Permeability				
Intrinsic Permeab. [m^2]	1.00e-20	5.00e-20	3.50e-20	2.50e-21
Shape Parameter, *A*	-	-	1.00[b]	1.00[b]
Shape Parameter, *λ'*	0.52[c]	0.52[c]	6.50[b]	9.00[b]
Diffusion Flux of Vapour				
Material Parameter,	5.90e-06	5.90e-06	5.90e-06	5.90e-06
Material Parameter, *n*	2.30	2.30	2.30	2.30
Tortuosity, *τ*	1.00	1.00	0.80	0.80

[a] Parameter for the Modified Van Genuchten model : $S_e = \left[1+\left(\frac{P_a - P_w}{P}\right)^{\frac{1}{1-\lambda''}}\right]^{-\lambda''} \times \left[1-\frac{P_a - P_w}{P_d}\right]^{\lambda_d}$.

[b] Parameter for the Relative Permeability Law: $k_{rw} = A \times S_e^{\lambda'}$

[c] Parameter for the Relative Permeability Law: $k_{rw} = \sqrt{S_e}\left[1-\left(1-S_e^{1/\lambda'}\right)^{\lambda'}\right]^2$

Tab. 5.7 Mechanical parameters for the host rock and the buffer materials

Mechanical Parameters	Opalinus Clay (Intact rock)	Opalinus Clay (EDZ)	Bentonite Pellets	Bentonite Blocks
Young Modulus [MPa]	7000	7000	1000	1000
Poisson's Ratio	0.24	0.24	0.24	0.24

5.3.2 Results

In this section, the results for temperature, pore water pressure and degree of saturation inside the engineered barrier and in the rock mass around the waste repository are discussed and the main features of the long-term THM behaviour due to heating and hydration of the bentonite barrier are highlighted. In order to understand the way in which heat propagates through the porous media and the progress of the clay barrier saturation, the evolution of those variables as a function of the distance to the tunnel centre (radial profiles) and to the symmetry plane between adjacent canisters (longitudinal profiles) are plotted. Cross section through the upper horizontal symmetry boundary (y=0.0) will be denoted as the “cold” section while the section through the middle of the canister (the lower symmetry boundary, y=-4.0) will be called the “hot” section. Time is referenced to the start of heating throughout.

As indicated above, two numerical calculations have been performed. In the first case the backfilling material is composed exclusively by bentonite pellets (this case will be known as the “homogeneous” case). In the second case the buffer material around the canisters is made of compacted bentonite blocks while the space between two consecutive canisters is filled with pellets (this case will be referred to as the “heterogeneous” case).

5.3.2.1 Temperatures

Temperature evolutions inside the clay barrier and in the surrounding rock due to a heat-emitting waste up to 10,000 years are shown in Figures 5.27 to 5.32. In Figures 5.27 and 5.28 the temperature results at several points in the cold and hot sections are plotted, for the homogeneous buffer (Fig. 5,27) and for the heterogeneous one (Fig. 5.28). The evolutions of temperatures at points along longitudinal profiles inside the clay barrier (Fig. 5.29 for the homogeneous case and Fig. 5.30 for the heterogeneous case), inside the excavation damaged zone (Figures 5.31a and 5.32a for the homogeneous and heterogeneous buffers, respectively) and in the sound rock (Figure 5.31b for the homogeneous case and Figure 5.32b for the heterogeneous one) are also depicted. Line y=0 represents the upper symmetry boundary of the modelled geometry.

It is interesting to note the high thermal gradients inside the bentonite barrier with maximum values close to the canister surface. In fact, temperature values higher than

165ºC are obtained in the pellets close to the heater and values as high as 80ºC are computed near the buffer-rock interface. These values are obtained in the middle section of the canister (hot section).

Temperature distributions along longitudinal profiles inside the clay barrier (Figures 5.29 and 5.30) highlight the fact that high temperatures are predicted in the “hot” section and lower values are obtained in the region between adjacent canisters (close to the cold section).In the cold section, the maximum temperature is about 75ºC. As expected, longitudinal thermal gradients become lower as the distance to the heater surface increases (Figures 5.31 and 5.32). Difference in thermal conductivities of the buffers (thermal conductivity for the compacted blocks is higher than for the bentonite pellets) explains the lower value of the maximum temperature reached in the blocks (around 115ºC). These temperature peaks are not achieved immediately but they are only observed after several years. For instance, for a point at only 2.5 cm from the canister surface (55 cm from the tunnel centre) the peak in temperature is achieved around 7 years after the start of the heat generation by the canister. At that time, temperature on the heater surface is already decreasing according to the proposed heat decay curve (Fig. 5.26). This fact shows that temperature distribution is mainly controlled by thermal conduction of the very dry buffer materials in the early stages of heating.

In Fig. 5.33, the spatial temperature distributions in the buffer and in the first 10 metres into the host rock at several times are shown. The rock volume with a temperature increase higher than 20ºC (coloured zone) is largest about 35 years after the start of heating. This zone extends up to a distance of 7.50 m from the tunnel centre (corresponding to a length of 6.25 m into the host rock).

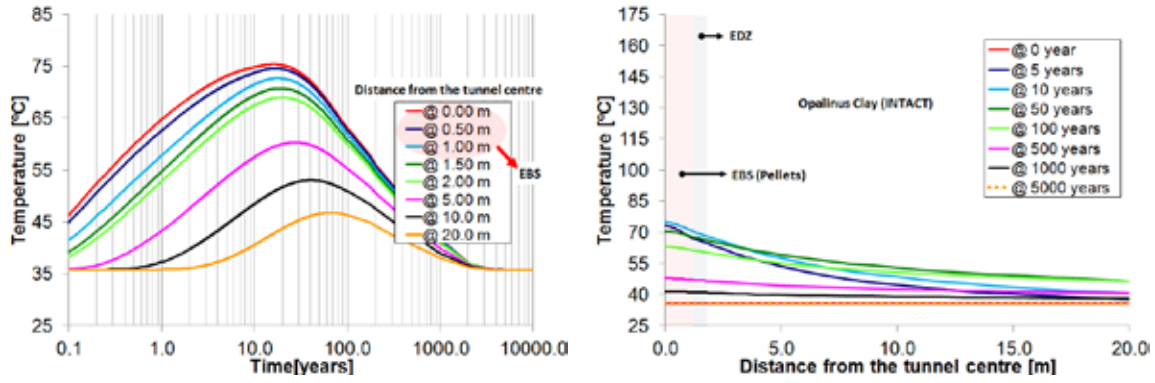

(a)

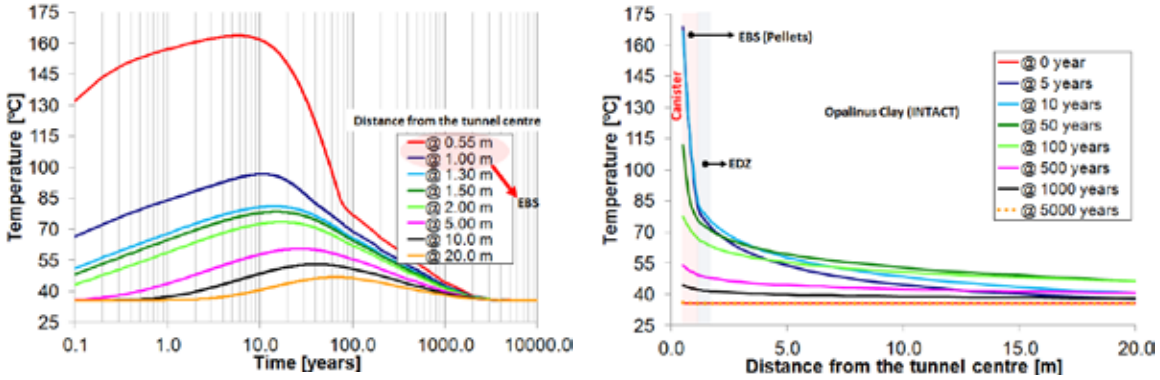

(b)

Fig. 5.27 Computed temperature evolution (left) and computed radial profiles of temperature (right) for the homogeneous case along (a) the cold cross section and (b) the hot cross section

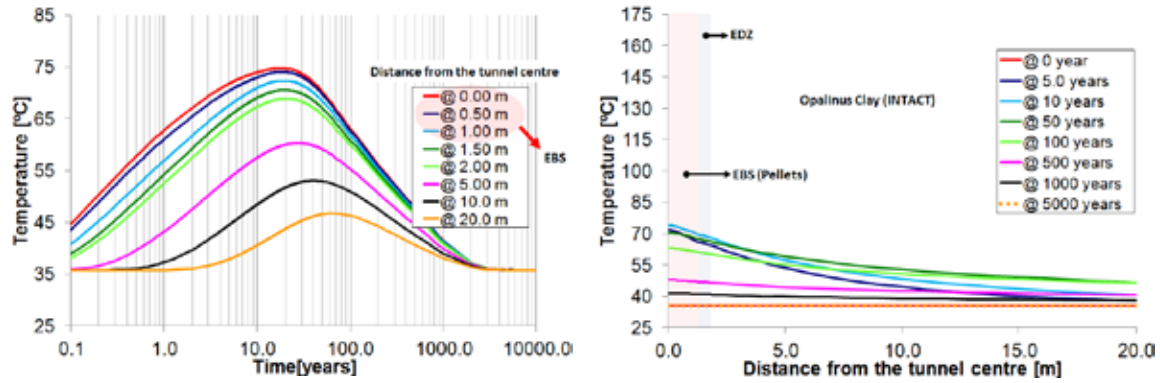

(a)

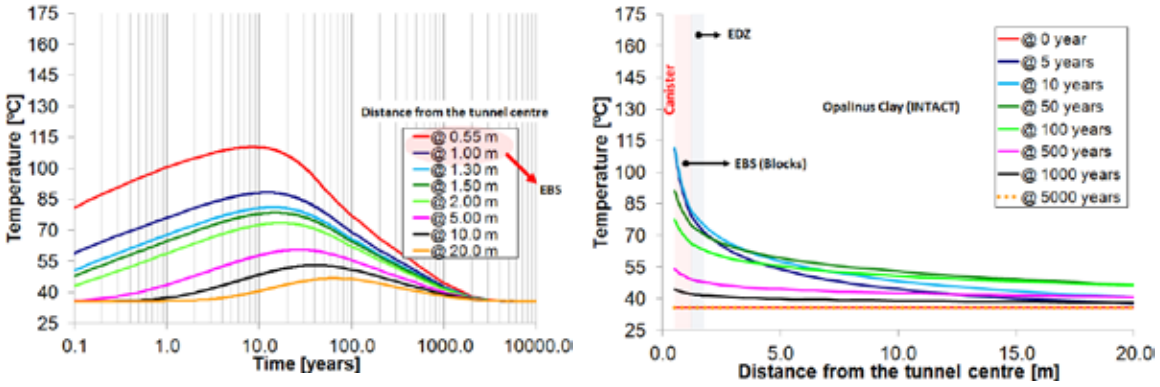

(b)

Fig. 5.28 Computed temperature evolution (left) and computed radial profiles of temperature (right) for the heterogeneous case along (a) the cold cross section and (b) the hot cross section. Results for points at distances up to 20 m from the tunnel axis

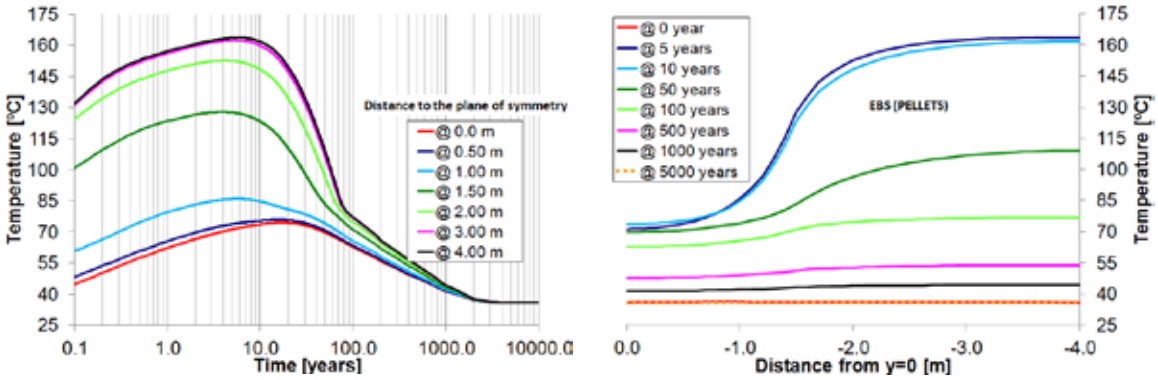

(a)

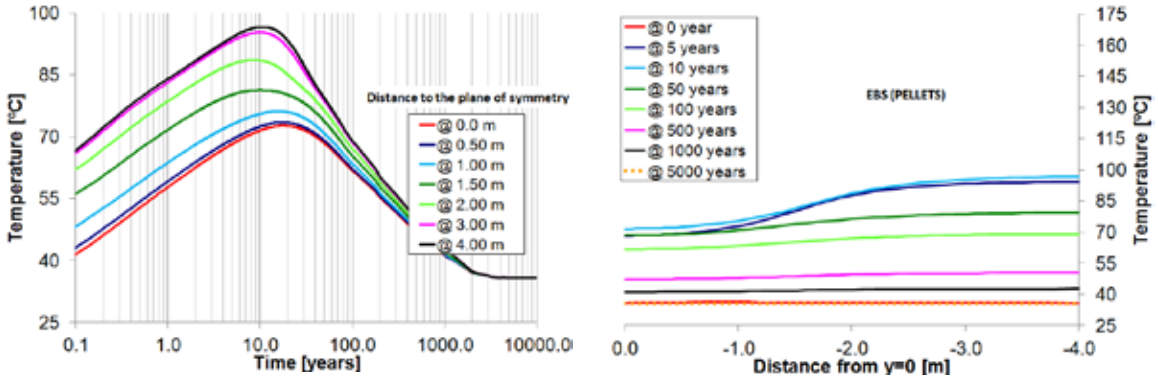

(b)

Fig. 5.29 Computed temperature evolutions (left) and computed distributions of temperature (right) inside the buffer for the homogeneous case. Longitudinal profiles at distances of (a) 55 ccm and (b) 100 cm from the tunnel axis

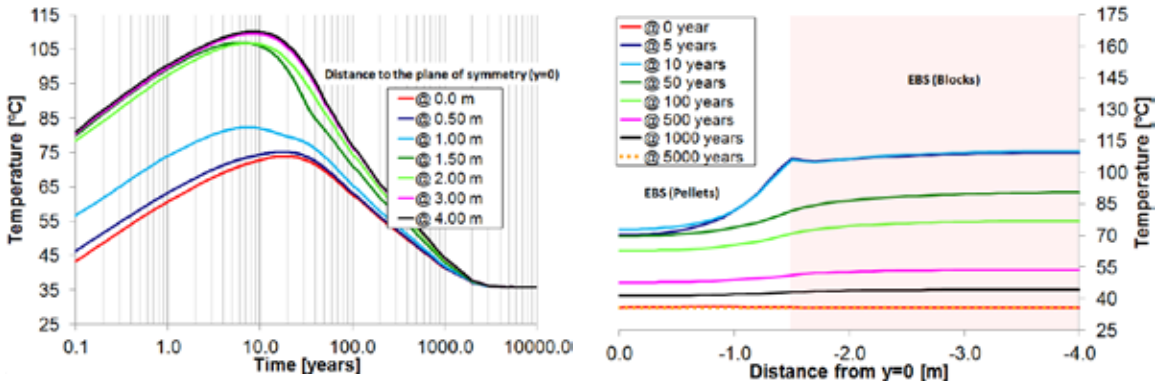

(a)

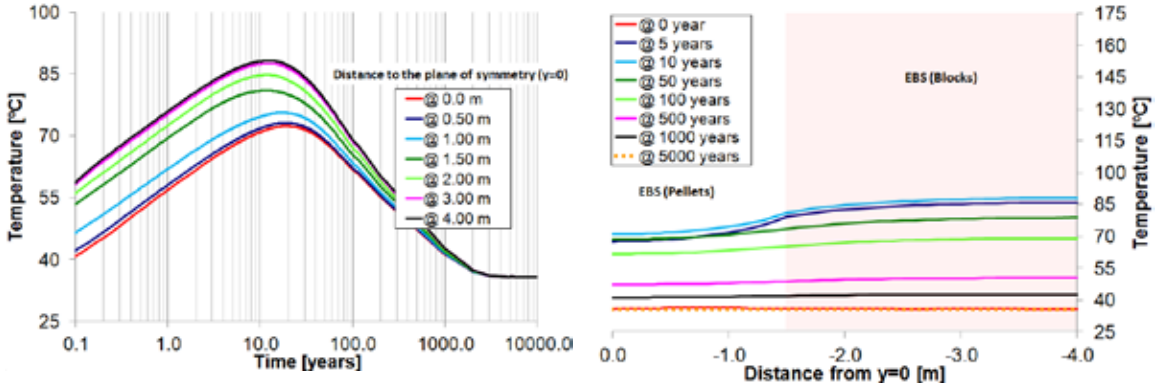

(b)

Fig. 5.30 Computed temperature evolutions (left) and computed distributions of temperature (right) inside the buffer for the heterogeneous case. Longitudinal profiles at distances of (a) 55 ccm and (b) 100 cm from the tunnel axis

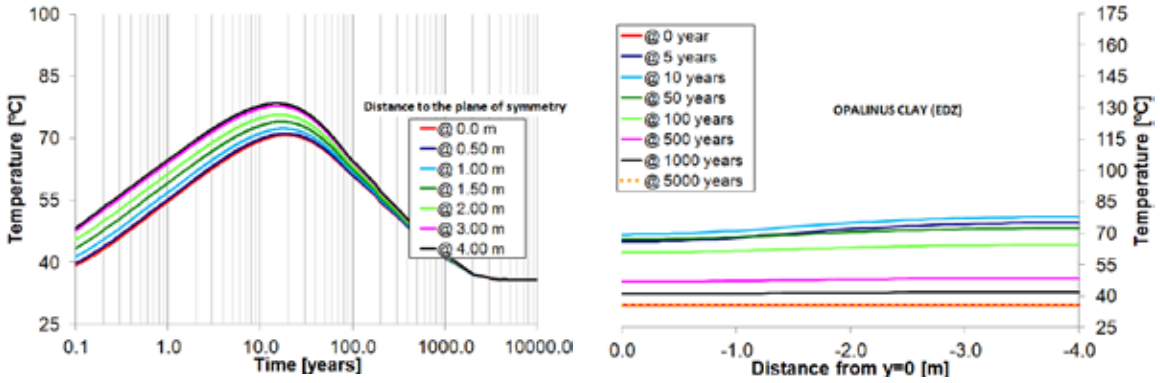

(a)

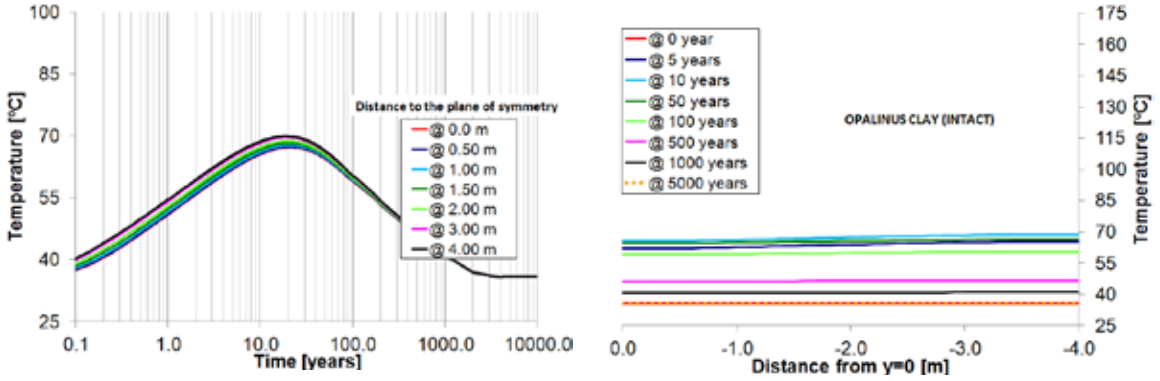

(b)

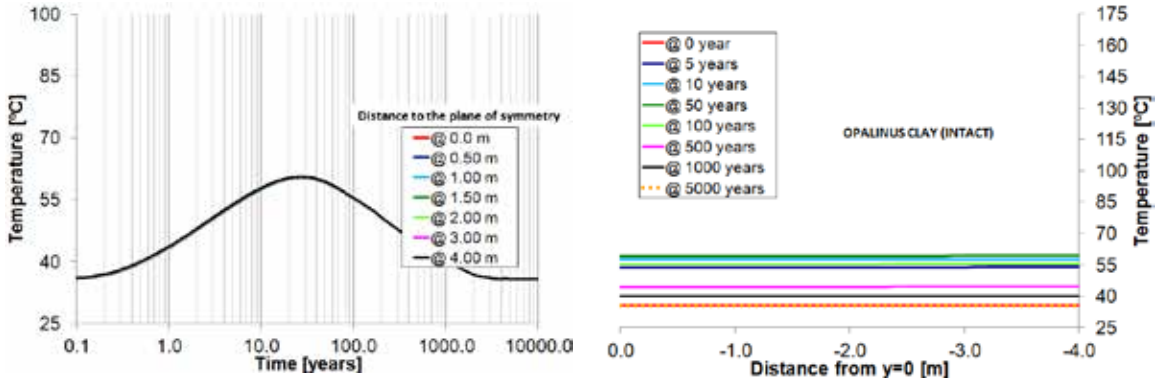

(c)

Fig. 5.31 Computed temperature evolutions (left) and computed profiles of temperature (right) in the Opalinus Clay for the homogeneous case. Longitudinal profiles at distances of (a) 25cm (inside the EDZ); (b) 125 cm and (c) 375cm from the tunnel axis

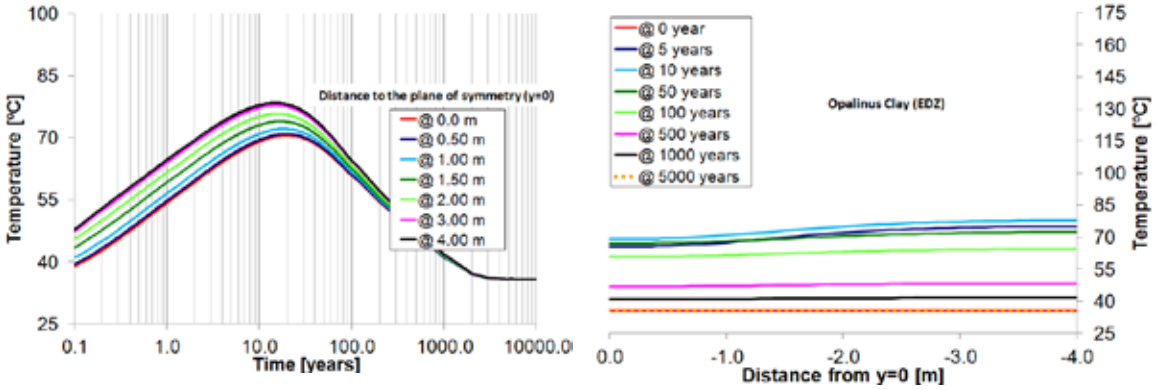

(a)

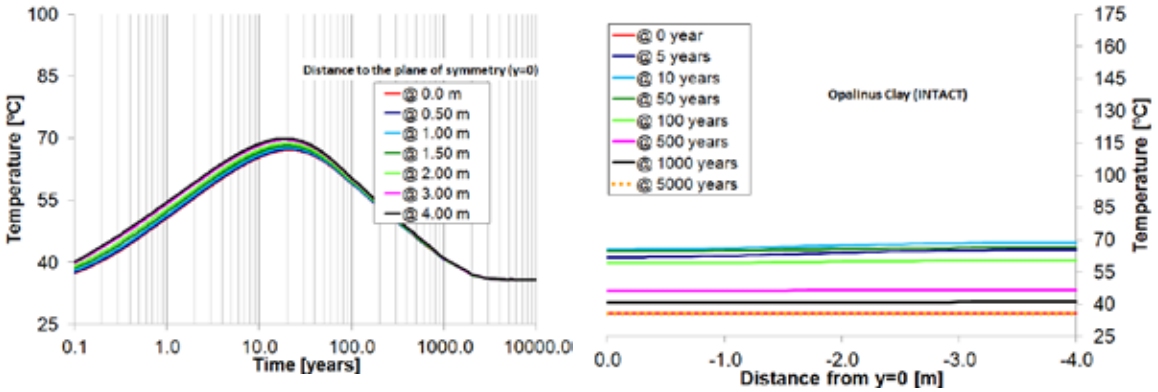

(b)

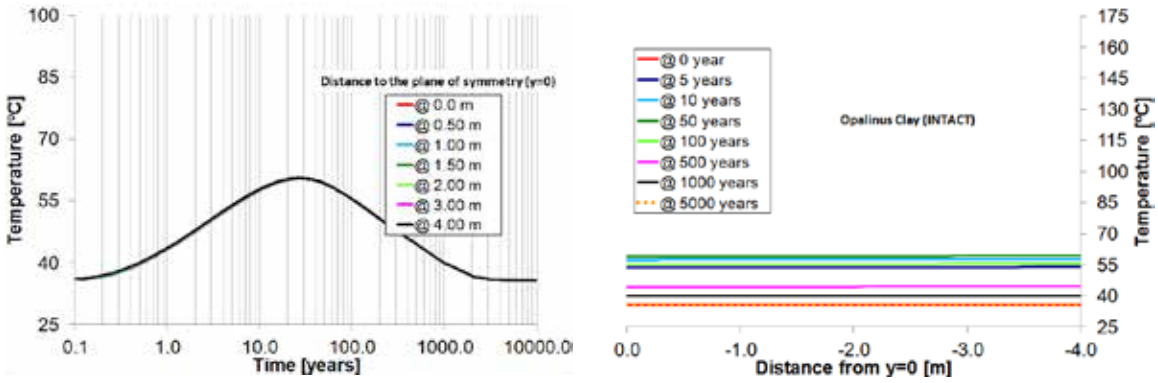

(c)

Fig. 5.32 Computed temperature evolutions (left) and computed profiles of temperature (right) in the Opalinus Clay for the heterogeneous case. Longitudinal profiles at distances of (a) 25cm (inside the EDZ); (b) 125 cm and (c) 375cm from the tunnel axis

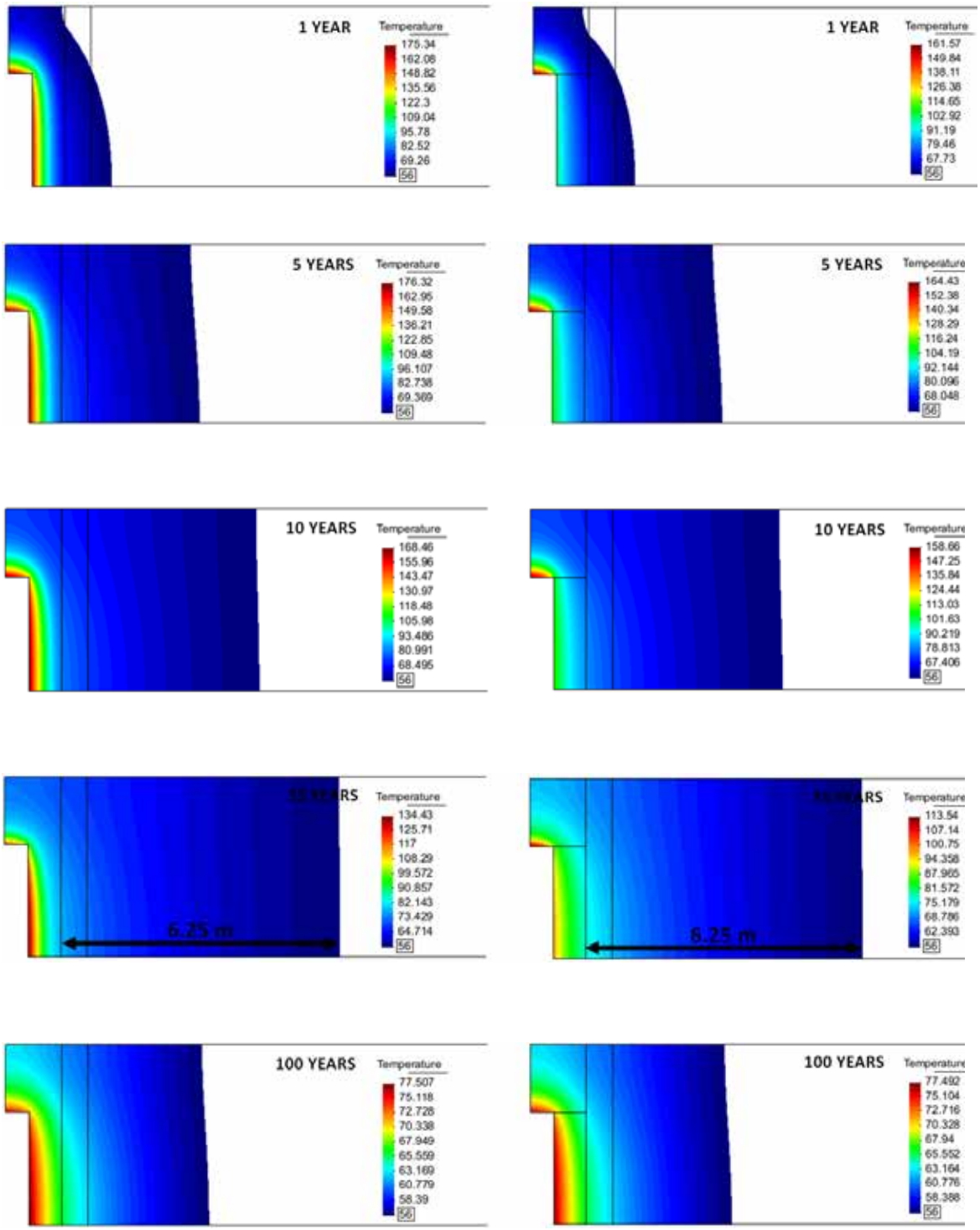

Fig. 5.33 Spatial distribution of temperature around the EBS for the homogeneous case (left) and the heterogoneous case (right) at several times after the onset of heating. Coloured zone represents the rock volume with a temperature increase larger than 20 ºC

5.3.2.2 Hydraulic variables

The excavation of the emplacement tunnel and the ventilation period of time that takes place before the construction of the clay barrier are considered during the numerical simulation as they induce a redistribution of the pore water pressure and a potential desaturation of the rock mass in the vicinity of the tunnel. The construction of the engineered barrier system enables a direct contact between an almost saturated material (the first few meters into the rock) and a very dry material (buffer) generating a water flow from the rock towards the buffer. As a consequence, the degree of saturation in the rock mass close to the clay barrier tends to decrease as the outermost portion of the buffer starts to hydrate. This is the main mechanism that governs the hydration process in the clay barrier under isothermal conditions.

When heat released by radioactive decay of nuclear waste starts, it introduces other mechanisms that influence the saturation of the buffer such as the thermal expansion of the liquid phase and the water phase changes (evaporation and condensation). Czaikowski et al. (2012) reported that evaporation close to the heater and the subsequent water vapour diffusion towards colder zones where it condensates may represent the major thermal-induced mechanism on the hydration of bentonite barriers. Therefore a significant reduction of the degree of saturation near the heater and a degree of saturation increase in the condensation zones are expected. As the radioactive decay progresses the amount of heating power released decreases (according to the proposed decay function of Fig. 5.26) implying a gradual cooling of the heater. Temperature tends to decrease around and inside the radioactive waste repository in the long-term (see Fig. 5.33). This overall temperature reduction contributes to the condensation of generated water vapour inside the buffer which, in combination with the water flow coming from the host rock lead to the full saturation of the clay barrier.

These main features of behaviour caused by the coupled processes that take place over the modelled lifetime of a waste repository can be observed in the numerical results presented from Fig. 5.34 to Fig. 5.37. In Fig. 5.34a, evolutions and distributions of degree of saturation along the cold section of the homogenous case are shown whereas Fig. 5.34b shows the same type of results for the hot section. Figure 5.35 presents the same results for the heterogeneous case. The results plotted along longitudinal profiles are depicted in Fig. 5.36 (homogeneous case) and Fig. 5.37 (heterogeneous case).

The time required for the saturation of the engineered barrier is about 85 years in the homogenous case whereas for the heterogeneous barrier this time is considerably shorter (about 56 years). This is due to the differences in thermo-hydraulic properties and initial conditions of pellets and compacted blocks (initial water content, thermal conductivity, retention curve properties). In fact, emplaced bentonite pellets are much drier than bentonite blocks and have a lower unsaturated thermal conductivity requiring a longer time to reduce the high temperatures generated by heating and, consequently, to stop water vapour generation by evaporation. In addition, it seems that the magnitude of the thermal gradient inside the buffers controls the hydration time of the clay barrier. In both simulated cases, the barrier saturation occurs earlier in the buffer volume between two adjacent heaters (points located between y=0 and y=-1.5 in Figures 5.36 and 5.37) although that zone is filled with pellets. It should be emphasized that the parameters governing the dependence of the hydraulic conductivity on the degree of saturation may strongly affect the saturation time of the clay barrier and they are subject to significant uncertainty. Another interesting finding regards the extension of the suction zone that reaches a distance of about 1.25 m into the Opalinus Clay (corresponding to a distance of 2.50 m to the tunnel centre) as shown in Figures 5.34 and 5.35.

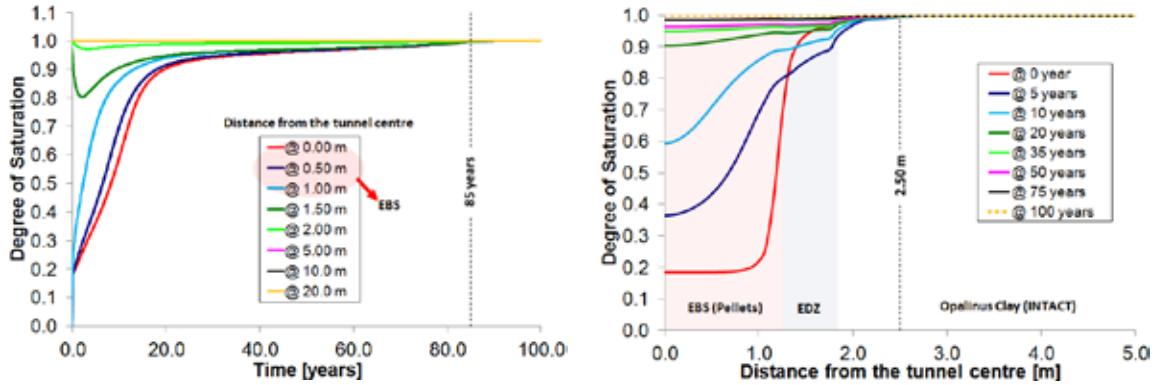

(a)

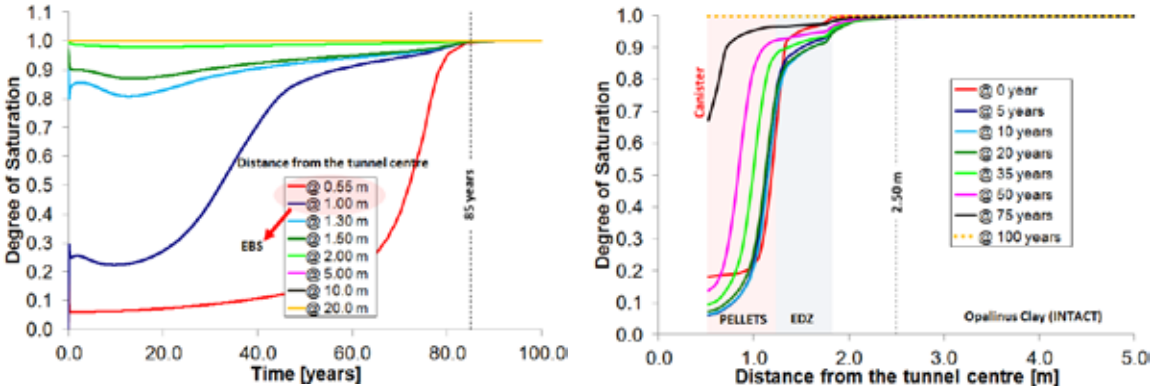

(b)

Fig. 5.34 Computed degree of saturation evolutions (left) and computed radial profiles of degree of saturation (right) for the homogeneous case along (a) the cold cross section and (b) the hot cross section. Numerical results are shown for points up to a distance of 20 m from the tunnel centre and for the first 100 years of heating

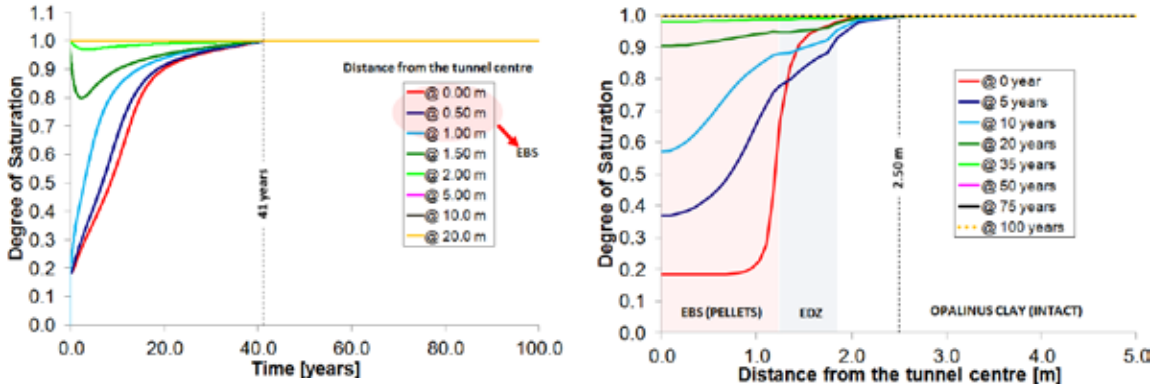

(a)

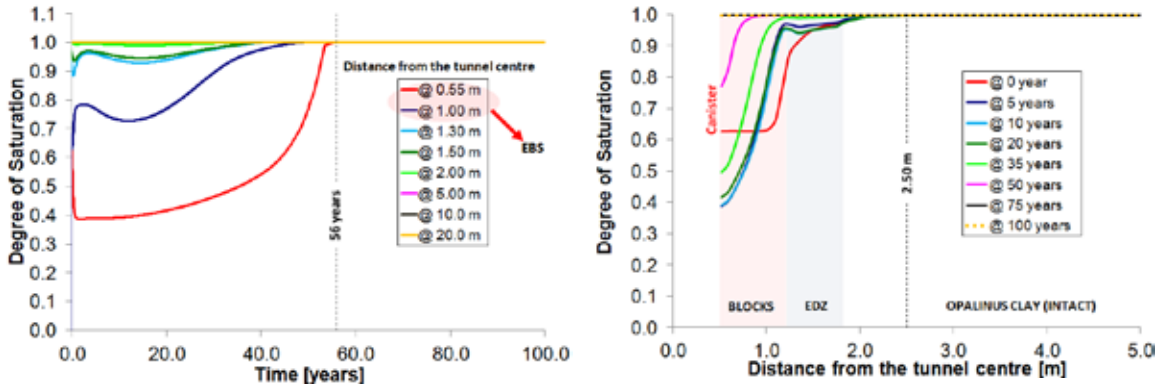

(b)

Fig. 5.35 Computed degree of saturation evolutions (left) and computed radial profiles of degree of saturation (right) for the heterogeneous case along (a) the cold cross section and (b) the hot cross section. Numerical results are shown for points up to a distance of 20 m from the tunnel centre and for the first 100 years of heating

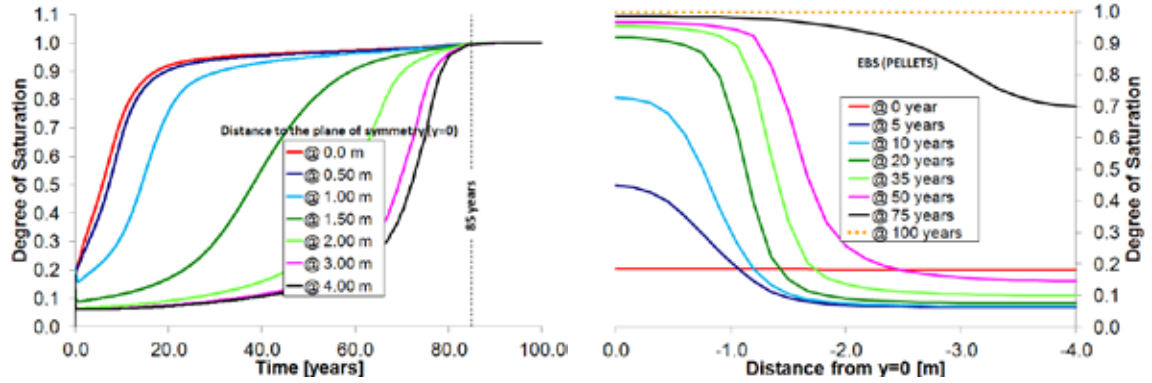

(a)

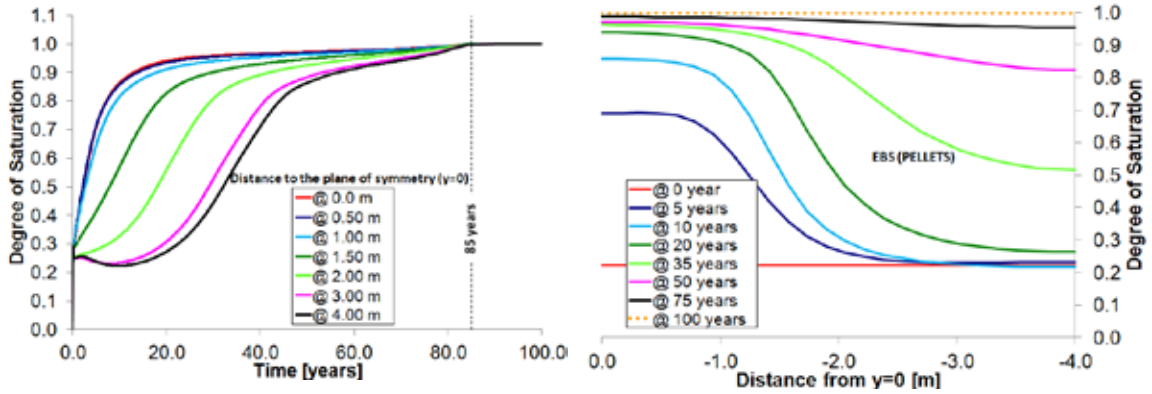

(b)

Fig. 5.36 Computed degree of saturation evolutions (left) and predicted longitudinal profiles of degree of saturation (right) inside the homogeneous buffer at a distance to the tunnel centre of (a) 55 cm and (b) 100 cm. Numerical results are shown for the first 100 years of heating

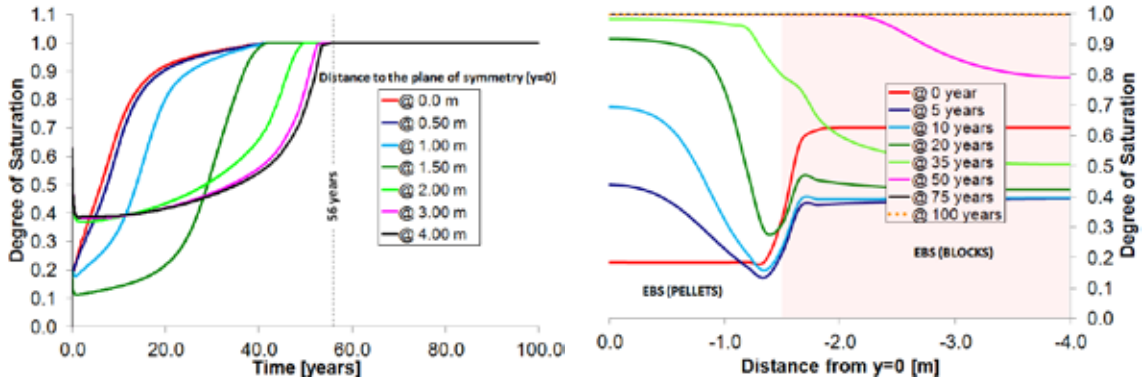

(a)

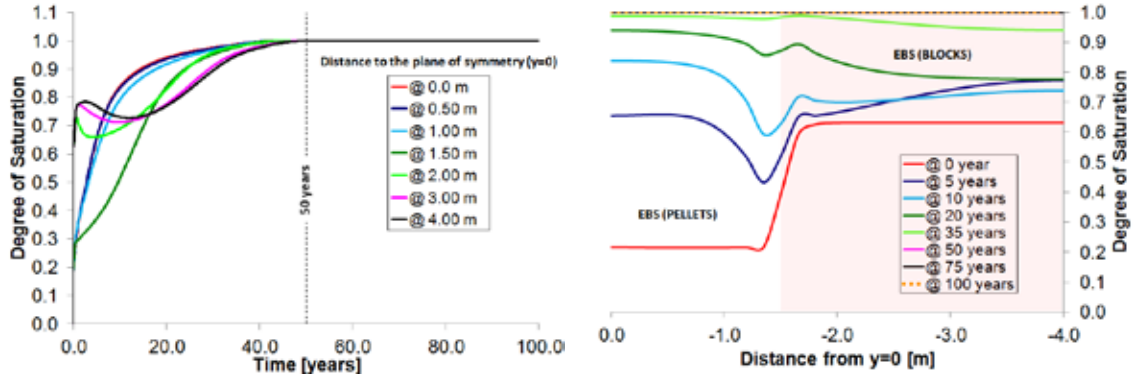

(b)

Fig. 5.37 Computed degree of saturation evolutions (left) and computed longitudinal profiles of degree of saturation (right) inside the heterogeneous buffer at a distance to the tunnel centre of (a) 55 cm and (b) 100 cm. Numerical results are shown for the first 100 years of heating

Pore water pressure changes due to thermal loads in saturated materials arise as a combined result of the differential thermal expansion of water and solid and the capacity of the porous medium to dissipate the excess liquid pressure (Gens et al., 2007). Furthermore, the water pressure generation is strongly dependent on the thermal expansion of the liquid and solid phases and the thermal expansion of porous skeleton. Thermal expansion coefficient of water has a positive effect on the magnitude of the pore pressure peak, i.e., the fact of considering that coefficient during the performance of a thermal problem leads to a positive increment of the excess water pressure due to heating. In contrast, the thermal expansion of the skeleton tends to reduce that pressure peak (Czaikowski et al., 2012). As mentioned previously, thermal expansion coef-

ficients for water, solid grain and porous skeleton are considered in the numerical simulations in order to obtain long-term predictions as realistic as possible.

The pore water pressure distribution in the near field of the tunnel prior to the start of heating is a consequence of the drainage effect of the tunnel. The influence of the tunnel construction and the ventilation period on the water pressure field extends to a distance close to 18 m into the rock (which corresponds to a distance of about 19 m from the tunnel centre). The extension of the suction zone due to the ventilation reaches a distance about 2.50-2.75 m from the tunnel axis. These modelling results can be seen from Fig. 5.38, 5.39 and 5.40. They show, for the two modelled cases, the liquid pressure evolution due to heating at several distances from the tunnel centre along the hot and the cold cross sections (Fig. 5.38) and some radial profiles of pore pressure at selected times in the centre of the canister (Fig. 5.39). Radial profiles of water pressure increment due to heating at different times along the hot cross section are given in Fig. 5.40.

During the heating phase, pore pressures reach maximum values in the range of 7.80-7.90 MPa at a distance between 16 m and 19 m from the tunnel centre, about 17 years after the onset of thermal load. At distances larger than 18 m into the rock, the increase in temperature leads to water pressure increments lower than 2.0 MPa (see Fig. 5.40). As time progresses and buffer hydration takes place, the excess water pressure inside the rock mass decreases as a consequence of the generated water flow towards the clay barrier and the decreasing temperature. In the long-term, the initial pore pressure state in the rock (before the tunnel excavation) is recovered so that the entire modelled domain (including the clay barrier) recovers a final liquid pressure state of 5.90 MPa.

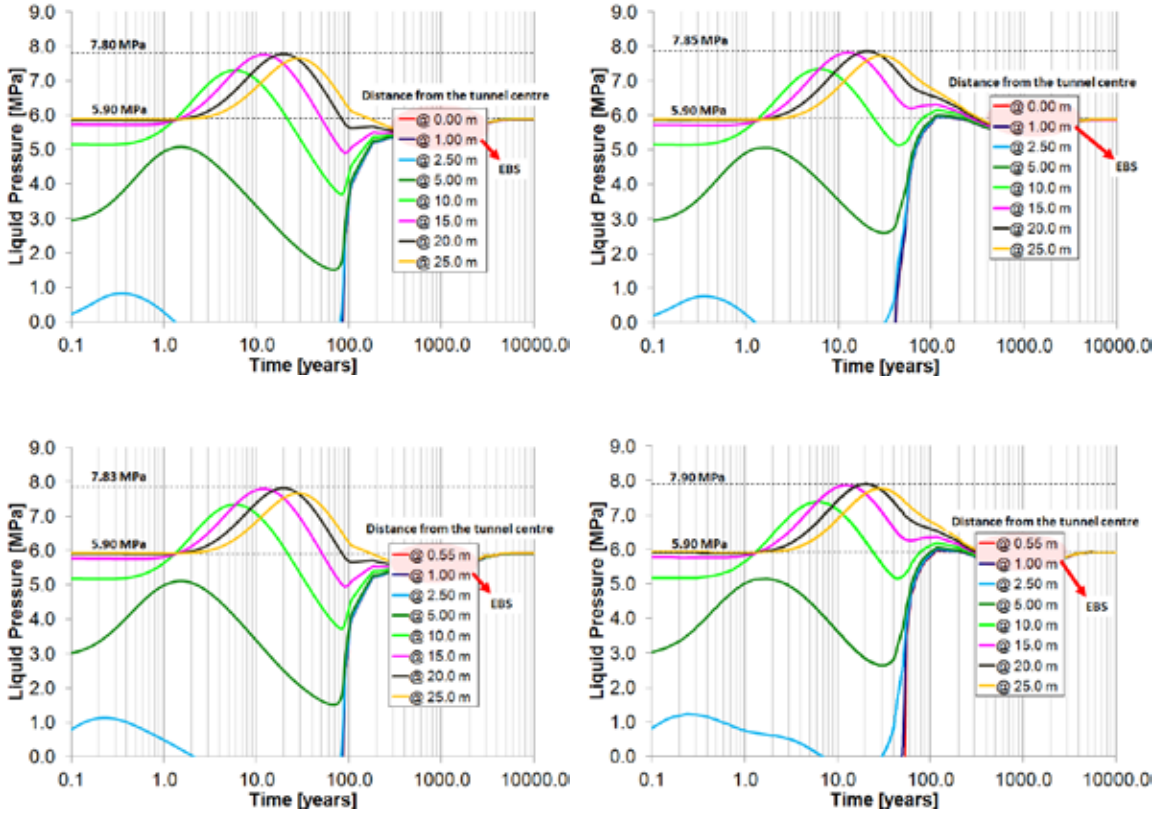

Fig. 5.38 Computed water pressure evolution for the homogeneous (left) and the heterogeneous cases (right) along the cold cross section (up) and the hot cross section (down). Numerical results are shown for points up to a distance of 25m from the tunnel centre. Pore water pressure peak is also indicated for each modelled case and cross section

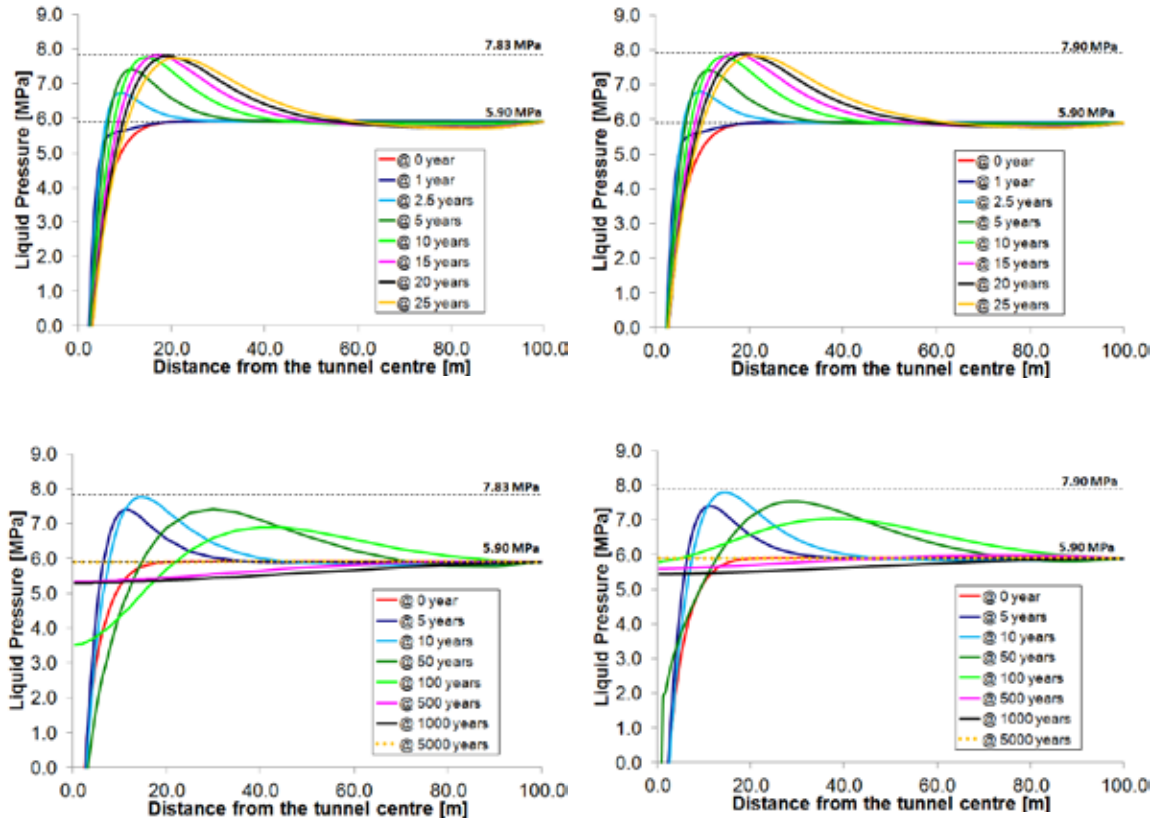

Fig. 5.39 Computed radial profiles of water pressure for the homogeneous (left) and the heterogeneous cases (right) along the hot cross section for the first 25 years (up) and 5000 years (down) of heating. The computed pore water pressure peak is also shown for each modelled case

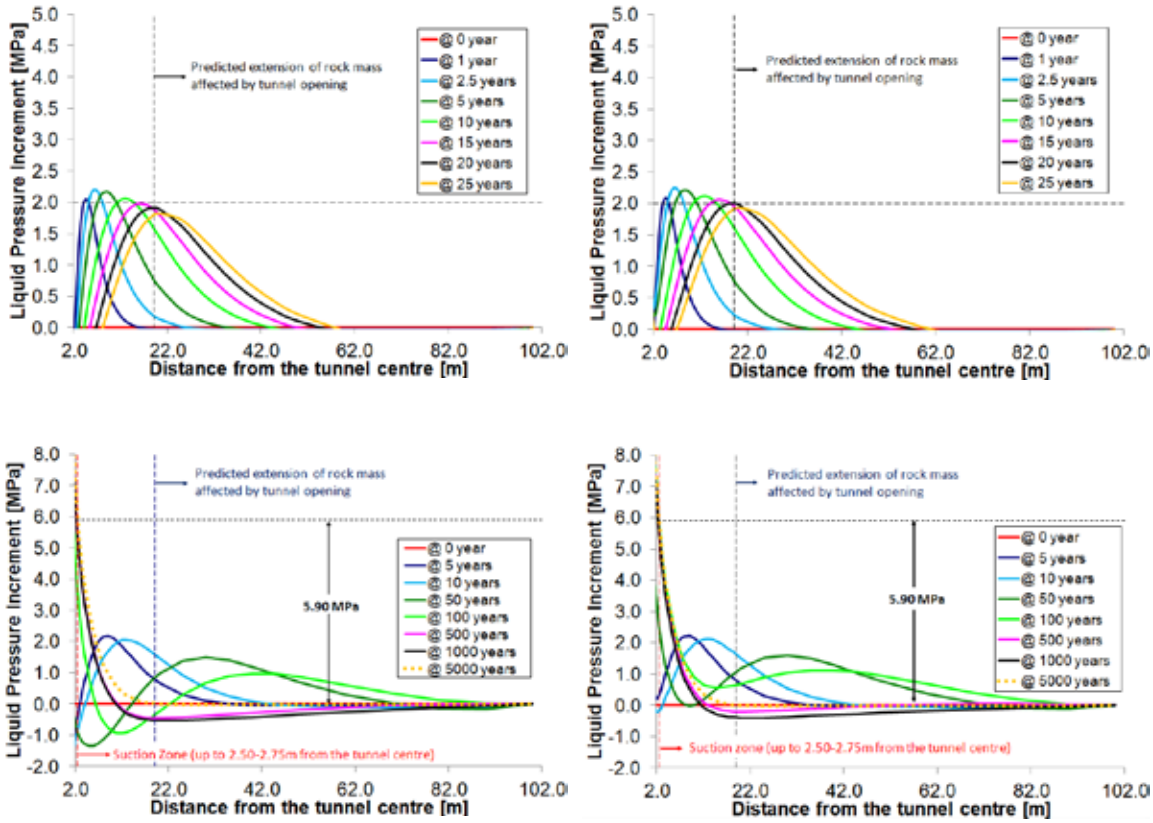

Fig. 5.40 Predicted radial profiles of liquid pressure increment for the homogeneous (left) and the heterogeneous cases (right) along the hot cross section for the first 25 years (up) and 5000 years (down) of heating

Mechanical results such as swelling stresses are not presented as the elastic constitutive law adopted for the barrier materials is not capable to capture the expansive nature of the bentonite.

5.3.3 Concluding remarks

This long-term analysis has required large computing resources leading to the adoption of a number of simplifications concerning geometry and constitutive laws for the materials. In spite of these simplifications, the analyses performed have supplied a very comprehensive picture of the long-term behaviour (up to 10,000 years) of a canister-barrier-rock system subjected to a representative variation of heating power. The patterns of heat dissipation, barrier saturation and the generation of pore pressures in the rock and subsequent variation appear very realistic both in the short term and in the very long term. Temperatures well above 100ºC have been reached that have been

easily accommodated by the numerical model without requiring any changes in the formulation used.

The main driving force for the phenomena simulated in the analyses is the heating power emitted by the canister containing the radioactive waste. It should be noted that the subsequent evolutions and distributions of temperatures are quite dependent on the overall geometry assumptions made that can be quite different from those of an actual repository. Other geometries could lead to different thermal results and therefore to potentially significant differences in the computed hydromechanical variables.

The material parameters used in the computations are the current best estimates based on a combination of laboratory and field experiments. However, there are uncertainties attached to quite a number of them. To clarify the potential effects of those uncertainties, a comprehensive sensitivity analysis would be required that has not been performed in the framework of this project.

6 Modelling Case 4: Geochemical evolution at interfaces

6.1 Study of the canister/bentonite interface

6.1.1 General description

Conceptual and numerical reactive transport models of the long-term geochemical evolution near the canister/bentonite interface of a spent-fuel carbon-steel canister repository in granite have been performed. The models account for canister corrosion, the interactions of corrosion products with bentonite and the pH buffering mechanisms. Simulations were performed for a time horizon of 1 Ma at a constant temperature of 25ºC, although some simulations were performed also with the thermal gradient to explore the temperature influence in the geochemical evolution.

6.1.2 Geometry

The geometry of the model corresponds to the Spanish reference concept of a spent-fuel carbon-steel canister repository in granite. An individual disposal cell is modelled by assuming axial symmetry of the system and by neglecting the canister border effects.

The Spanish reference concept for a repository in granite is based on the Enresa performance assessment project, named Enresa 2000 (Enresa, 2001), and the results of the FEBEX project (Enresa 2000, 2004, 2006). It consists on the disposal of spent fuel in carbon steel canisters in long horizontal disposal drifts. Canisters are surrounded by blocks of compacted bentonite. Figure 6.1 shows a view of the underground installations.

A canister contains 4 PWR or 12 BWR fuel elements in a subcritical configuration. After being unloaded from the reactor, the fuel elements are temporarily stored for their thermal power to decay to a level at which they may be disposed of with a total thermal power of 1,220 W per canister.

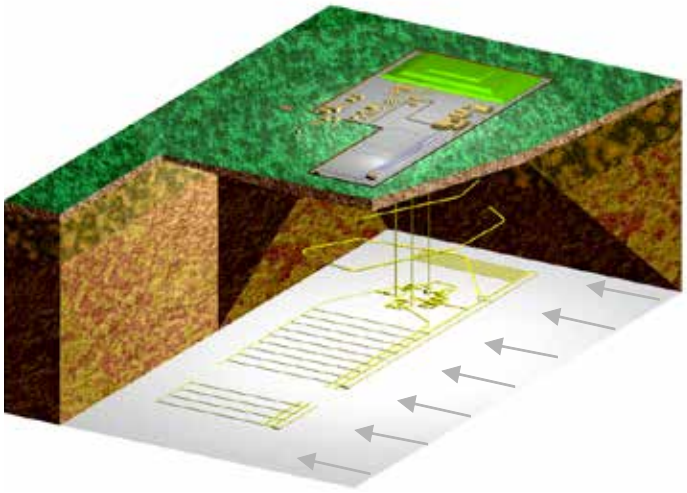

Fig. 6.1 Enresa repository concept: underground installations (Enresa, 2005)

Canisters are cylindrical and measure 4.54 m in length and 0.90 m in diameter (Fig. 6.3). Their thickness of 0.10 m at the cylindrical wall and 0.12 m at the ends is capable of withstanding the pressures to which it is subjected under disposal conditions and providing a minimum period of containment of 1000 years. Canisters are disposed in cylindrical disposal cells, constructed with blocks of pre-compacted bentonite (Fig. 6.2). Pre-compacted bentonite blocks, of 1,700 kg/m^3 dry density are used in order to achieve a final dry density of 1,600 kg/m^3. The blocks are initially unsaturated with a degree of saturation of 66%.

The disposal drifts, having 500 m in length and 2.4 m in diameter (see Fig. 6.3), are located at a depth of 500 m in the host rock formation. The separation between canisters along a drift and between drifts is determined mainly by thermal constraints. Separations of 2 m between canisters and 35 m between disposal drifts have been established in order not to exceed a temperature of 100 ºC in the bentonite.

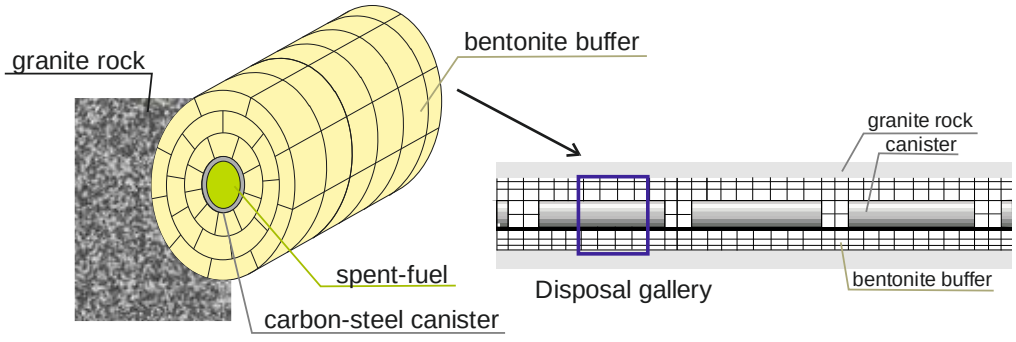

Fig. 6.2 Sections of a disposal drift

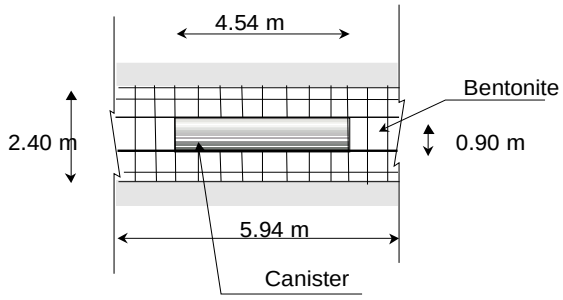

Fig. 6.3 Dimensions of the canister and the individual disposal cell (Enresa, 2001)

The disposal drift will be sealed with a 6 m long seal made of bentonite blocks and closed with a concrete plug at its entry. After completion of all the disposal drifts, main drifts, ramp, shafts and other remaining rock cavities will be backfilled with a mixture of bentonite and natural sand or an appropriate crushed material. The backfilling material will consist of 10 % bentonite (increasing up to 20 % at the top of the drifts) and suitably graded sand.

A 1D axisymmetric model of a disposal cell has been used to simulate canister corrosion and the long term evolution of the bentonite. It considers the canister and the bentonite (Fig. 6.4). Both of them are assumed to be homogeneous. The canister external radius is 0.45 m and its thickness is 0.10 m. The external radius of the bentonite barrier is 1.2 m. Water flow and solute transport through the granite has been simulated with a prescribed water flux of granite water parallel to the axis of the gallery.

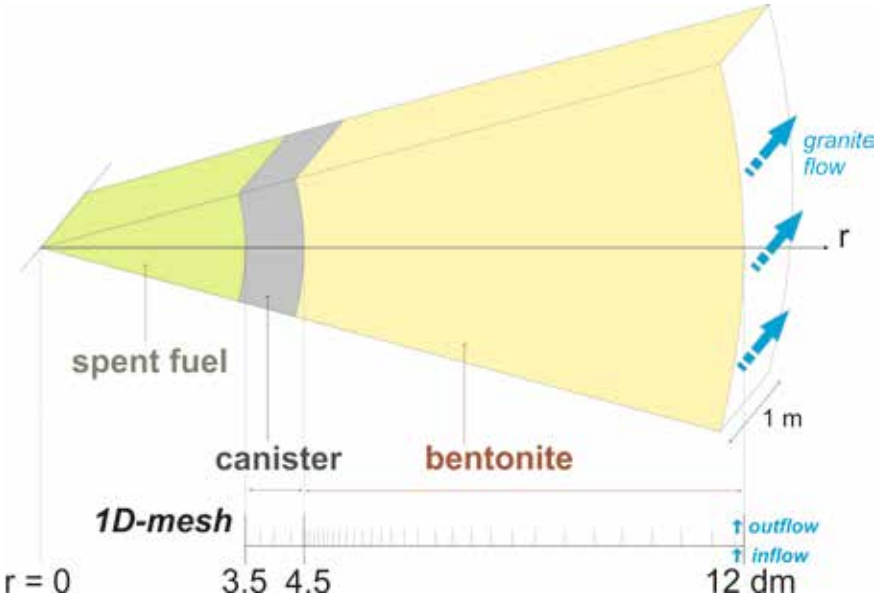

Fig. 6.4 Sketch and finite element grid of the 1D axi-symmetric model

A 1-D axi-symmetric finite element mesh has been used which has 93 nodes and 92 one-dimensional elements. The grid is shown in Fig. 6.4. The mesh is especially refined close to the canister/bentonite interface where the interaction between the corrosion products and the bentonite are strongest. The spatial discretization decreases with the distance to the canister.

6.1.3 Process classes (T, H, M, C) and coupling

The simulation and prediction of the long-term evolution of the engineered barrier in the repository is not a blind extension of the models developed for experiments to different space and time scales. It requires a careful assessment of the key long-term processes and their coupling as well as an evaluation of the resulting uncertainty and its consequences.

For most THM considerations, long-term extrapolation means to extrapolate from the time-scale that can be covered by experiments to the end of the resaturation phase of the buffer in a repository. The time span considered will possibly be several hundred to 1000 years. After this, THM processes will be of minor importance, although processes like thermo-osmosis may play a role.

Chemical processes, on the other hand, will take place at all temporal scales. Chemical reactions induced by canister corrosion take place during time scales much larger than that of buffer resaturation. The lifetime of the canister retaining the high-radioactive waste is related to the corrosion rate of the carbon steel. Once the canister fails and the water enters to it, radionuclides may migrate into the bentonite buffer. Canister corrosion may affect the chemistry of the bentonite porewater and thus result in changes in the migration behaviour of the radionuclides. Furthermore, the corrosion products may also induce buffer alterations which could result in changes in parameters such as porosity, permeability, sorption and swelling. It is understood that the gas production by corrosion could also have an effect on THM behaviour after resaturation phase, if production rates are so high that not all gas can be transported by dissolution and diffusion in the liquid phase.

As a consequence of these considerations, there are two levels of extrapolation in time:

1. Extrapolation to the end of the resaturation phase which defines the initial conditions of the buffer evolution after its resaturation and feeds the necessary input to

PA. It is the period which is especially interesting in terms of THM behaviour, because it involves temperature and saturation gradients as driving forces for physical and chemical processes.

2. Extrapolation to the end of PA-considered time (usually from 10^5 to 10^6 years). Some THM phenomena such as thermo-osmosis and the high density of adsorbed water may become patent at this time scale. On the other hand, chemical processes such as canister corrosion and chemical interactions of bentonite with canister corrosion products will occur also during this period of time.

A careful analysis should be made to review the validity of model assumptions at different time scales. This is the case for the local equilibrium assumption (LEA) versus a kinetically-controlled reaction. Some chemical reactions must be treated with kinetics at short time scales while they can be modelled with the LEA at large time scales.

6.1.4 Considered processes

According to Enresa (2005; 2006) the bentonite barrier will become fully saturated after 20 to 30 years for the Spanish reference concept. Therefore, the model assumes that the bentonite is initially water-saturated. In this stage (after resaturation), mechanical effects are not very relevant and, consequently, they are neglected.

Advection in the bentonite is negligible because its hydraulic conductivity is extremely low ($6 \cdot 10^{-14}$ m/s). Therefore, solute diffusion is the main solute transport mechanism in the engineered barrier. It is assumed that all the water is accessible to solutes.

The washing of the bentonite/granite interface by groundwater through the granite is simulated by imposing a granite porewater flow rate at the outer element of the model.

The geochemical model accounts for the following homogeneous (aqueous) reactions: 1) Aqueous complexation, 2) Acid/base reactions and 3) Redox reactions. The model accounts for the dissolution/precipitation of calcite, gypsum, quartz, magnetite, siderite and goethite. Magnetite, siderite and goethite are corrosion products which are not initially present in the system, but are allowed to precipitate. The model also accounts for the cation exchange of Na^+, Ca^{2+}, Mg^{2+}, K^+ and Fe^{2+} and surface complexation reactions, which are modelled with a triple sorption site model similar to that of Bradbury and Baeyens (1997; 2005), in the bentonite. All these reactions are assumed at equilib-

rium in the reference model. In the framework of the uncertainty analyses, some simulations are performed accounting for kinetically controlled precipitation of some minerals or including new mineral such as smectite.

It is assumed that the simulation starts after the thermal pulse has dissipated. Therefore the model is isothermal and all the chemical reactions are modelled at a constant temperature of 25ºC. The influence of the thermal transient on the geochemical evolution is analyzed in the Section of Uncertainty Analyses.

Samper *et al.* (2008a) showed that the changes in the bentonite porosity caused by mineral dissolution/precipitation are less than 0.1 for a corrosion rate of 0.2 μm/y after 0.3 Ma. Therefore, these changes were disregarded in all the simulations in order to reduce computation time.

Carbon-steel canister corrosion is simulated in a manner similar to mineral dissolution by using a constant kinetic rate. The available oxygen in the repository will be consumed after its closure and anaerobic conditions will prevail during the simulation. According to thermodynamic predictions, canister corrosion will occur under reducing conditions. Carbon-steel canister corrosion can be represented as:

$$Fe(s) + 2H_2O \rightarrow Fe(OH)_2(s) + H_2(g) \qquad (6.1)$$

where Fe(s) denotes an idealized mineral phase for carbon-steel and H_2O is assumed to be the oxidizing agent of the canister. The concentration of ferrous iron, Fe^{2+}, in the vicinity of carbon-steel canister is controlled by the solubility product of ferrous hydroxide, $Fe(OH)_2$(s). This metastable mineral can form magnetite, Fe_3O_4(s), according to:

$$3Fe(OH)_2(s) \rightarrow Fe_3O_4(s) + 2H_2O + H_2(g) \qquad (6.2)$$

Since magnetite is thermodynamically more stable than ferrous hydroxide, corrosion will lead to:

$$3Fe(s) + 4H_2O \rightarrow Fe_3O_4(s) + 4H_2(g) \qquad (6.3)$$

In addition to $Fe(OH)_2$(s) and Fe_3O_4(s), siderite and green rusts could form as corrosion products of carbon-steel canister under anaerobic conditions depending on the bentonite porewater composition. Siderite precipitation proceeds according to:

$$Fe^{2+} + CO_3^{2-} \rightleftharpoons FeCO_3(s) \quad (6.4)$$

However, the low concentration of carbonate in the bentonite porewater restricts siderite precipitation. As indicated by Enresa (2005), siderite is not the main corrosion product because bentonite limits the carbonate flux reaching the canister surface.

Green rusts are Fe(II)–Fe(III) hydroxyl compounds containing anions such as CO_3^{2-}, SO_4^{2-} and Cl^-. The redox potential of carbonate green rust, GR1, has been thermodynamically predicted by Drissi *et al.* (1995). Refait *et al.* (1997) reported that the formation of GR1 is unlikely if the initial concentration of CO_3^{2-} is lower than 0.005 mol/L. This is the case for bentonite porewater. The redox potential of sulphate green rust, GR2, is out of the expected range of redox potentials of bentonite porewater, and therefore its formation is also unlikely (Génin *et al.*, 1996). Furthermore, chloride green rust GR3 formation is even more unlikely than that of GR1 and GR2 because the typical sequence of affinity of green rust compounds is GR1 > GR2 > GR3 (Miyata, 1983).

Goethite precipitation is not expected to occur based on thermodynamic grounds. However, the model accounts for the precipitation of goethite according to:

$$Fe^{2+} + 1.5H_2O + 0.25O_2(aq) \rightleftharpoons FeOOH(s) + 2H^+ \quad (6.5)$$

The following kinetic rate expression has been used for mineral dissolution/precipitation:

$$r_m = k_m(\Omega_m - 1)^h \quad (6.6)$$

where r_m is the dissolution/precipitation rate (mol/m^2/s), k_m is the kinetic rate constant (mol/m^2/s), Ω_m is the ratio between the ion activity product and the equilibrium constant (dimensionless) and θ and η are parameters of the kinetic law.

Carbon-steel corrosion is modelled by using a kinetic formulation in a manner similar to mineral dissolution. The canister is treated as a porous material made of 100% metallic iron, Fe(s), which dissolves at a constant rate according to:

$$Fe(s) + 2H_2O \rightleftharpoons Fe^{2+} + 2OH^- + H_2(g) \quad (6.7)$$

which can be written in terms of primary species as:

$$Fe(s) + 2H^{+} + 0.5O_2(aq) \rightarrow Fe^{2+} + H_2O \qquad (6.8)$$

This is the chemical reaction used in the numerical model to simulate the canister corrosion. According to it, corrosion consumes protons and forces the reduction of water which in turn releases H_2(aq) according to:

$$H_{2(aq)} + 0.5O_{2(aq)} \rightarrow H_2O \qquad (6.9)$$

Hydrogen is simulated as a dissolved species, H_2(aq). The model does not account for H_2(g). Assuming that the H_2(g) is in equilibrium with the H_2(aq), one has:

$$H_2(g) \rightarrow H_2(aq) \qquad (6.10)$$

From the results of the simulation for H_2 (aq) it is possible to calculate the partial pressure of H_2(aq) according to:

$$P_P(H2(g)) = \frac{K_{H_2(g) \rightarrow H_2(aq)}}{[H_2(aq)]} \qquad (6.11)$$

where $K_{H2(g)\leftrightarrow H2(aq)}$ is the equilibrium constant at 25ºC of the Eq. (6.10) and [H_2(aq)] is the computed activity of H_2(aq).

The corrosion rate, r_c, in μm/year is calculated as:

$$r_c = \frac{r_m M_w}{r} \qquad (6.12)$$

where ρ is the density of the carbon steel (7.860 kg/m^3), M_w is its molecular weight (55.85 g/mol) and r_m is the corrosion rate per unit mineral surface (mol/m^2/year). A constant corrosion rate of 2 μm/year, which amounts to 0.281 mol/m^2/year, is assumed for the base run. It should be noticed that η = 0 for canister corrosion (Eq. 6.6).

The corrosion products formed at the canister–bentonite interface migrate into the bentonite where they undergo chemical interactions with the aqueous and the solid phases. The gas production by corrosion is assumed to be transported by dissolution and diffusion in the liquid phase.

6.1.5 Input data and data sources

6.1.5.1 Flow and transport

Flow and transport parameters are similar to those reported by Samper *et al.* (2008a; 2011). Hydraulic conductivity of the bentonite is extremely low ($6 \cdot 10^{-14}$ m/s). All dissolved chemical species are assumed to have the same effective diffusion of $4.07 \cdot 10^{-11}$ m^2/s. Bentonite porosity is 0.407. The canister is assumed to have the same transport properties of the bentonite.

No flow boundaries are considered in the model except for the bentonite/granite interface. A flow rate of 0.1 L/y is imposed at the outer element of the model to simulate the washing of that surface by groundwater water through the granite. The inflow water has the chemical composition of the granite porewater. This boundary condition has a significant effect on the geochemical evolution of the EBS.

6.1.5.2 Geochemical model

The chemical system is defined in terms of the follow primary species: H_2O, $O_2(aq)$, H^+, Na^+, K^+, Ca^{2+}, Mg^{2+}, Fe^{2+}, HCO_3^-, Cl^-, SO_4^{2-} and $SiO_2(aq)$. Relevant aqueous complexes were identified from speciation runs performed with EQ3/6 (Wolery, 1992). The homogeneous chemical reactions considered in the model and their equilibrium for aqueous complexes are listed in Tab. 6.1. All these reactions are assumed at local chemical equilibrium.

Table 6.2 lists the mineral dissolution/precipitation reactions and their equilibrium constants at 25 ºC. The initial volume fractions of calcite and quartz in the bentonite are similar to those reported by Samper *et al.* (2008a). Gypsum, magnetite, siderite and goethite are minerals which are not initially present in the system, but are allowed to precipitate.

Tab. 6.1 Homogeneous chemical reactions considered in the model and their equilibrium constants at 25ºC (Wolery, 1992)

Reaction	Log K (25°C)
$OH^- + H^+ \rightleftharpoons H_2O$	$1.3832 \cdot 10^1$
$CO_3^{2-} + H^+ \rightleftharpoons HCO_3^-$	$1.0284 \cdot 10^1$
$CaCO_3(aq) + H^+ \rightleftharpoons Ca^{2+} + HCO_3^-$	6.9197
$CaHCO_3^+ \rightleftharpoons Ca^{2+} + HCO_3^-$	-1.0493
$CaSO_4(aq) \rightleftharpoons Ca^{2+} + SO_4^{2-}$	-2.1186
$CaOH^+ + H^+ \rightleftharpoons Ca^{2+} + H_2O$	$1.2666 \cdot 10^1$
$MgCO_3(aq) + H^+ \rightleftharpoons Mg^{2+} + HCO_3^-$	7.2869
$MgHCO_3^+ \rightleftharpoons Mg^{2+} + HCO_3^-$	-1.0412
$MgSO_4(aq) \rightleftharpoons Mg^{2+} + SO_4^{2-}$	-2.4449
$MgOH^+ + H^+ \rightleftharpoons Mg^{2+} + H_2O$	$1.1607 \cdot 10^1$
$NaOH + H^+ \rightleftharpoons Na^+ + H_2O$	$1.3998 \cdot 10^1$
$NaCO_3^- + H^+ \rightleftharpoons Na^+ + HCO_3^-$	9.8367
$NaHCO_3(aq) \rightleftharpoons Na^+ + HCO_3^-$	$-1.2287 \cdot 10^{-1}$
$CO_2(aq) + H_2O \rightleftharpoons H^+ + HCO_3^-$	-6.3161
$HS^- + 2O_2(aq) \rightleftharpoons H^+ + SO_4^{2-}$	138.31
$Fe^{3+} + 0.5H_2O \rightleftharpoons H^+ + 0.25O_2 + Fe^{2+}$	-8.2077
$FeHCO_3^+ \rightleftharpoons Fe^{2+} + HCO_3^-$	-1.98
$FeCO_3(aq) + H^+ \rightleftharpoons Fe^{2+} + HCO_3^-$	5.67
$FeCl^+ \rightleftharpoons Fe^{2+} + Cl^-$	$1.54 \cdot 10^{-1}$
$FeCl^{2+} + 0.5H_2O \rightleftharpoons Fe^{2+} + H^+ + 0.25O_2(aq) + Cl^-$	-7.50
$FeOH^+ + H^+ \rightleftharpoons Fe^{2+} + H_2O$	$1.07 \cdot 10^1$
$FeOH^{2+} \rightleftharpoons Fe^{2+} + 0.5H_2O + 0.25O_2$	-3.95
$Fe(OH)_2(aq) + 2H^+ \rightleftharpoons Fe^{2+} + 2H_2O$	$2.02 \cdot 10^1$

Reaction	Log K (25°C)
$Fe(OH)_3(aq) + 2H^+ \rightleftharpoons Fe^{2+} + 0.25O_2 + 2.5H_2O$	3.96
$Fe(OH)_4^- + 3H^+ \rightleftharpoons Fe^{2+} + 0.25O_2 + 3.5H_2O$	$1.30 \cdot 10^1$
$Fe(OH)_2^+ + H^+ \rightleftharpoons Fe^{2+} + 0.25O_2 + 1.5H_2O$	-2.7424
$Fe(SO_4)_2^- + 0.5H_2O \rightleftharpoons Fe^{2+} + H^+ + 2SO_4^{2-} + 0.25O_2$	$-1.14 \cdot 10^1$
$FeSO_4(aq) \rightleftharpoons Fe^{2+} + SO_4^{2-}$	$-2.19 \cdot 10^1$
$FeHSO_4^{2+} + 0.5H_2O \rightleftharpoons Fe^{2+} + 2H^+ + SO_4^{2-} + 0.25O_2$	-9.7477
$Fe_2(OH)_2^{4+} \rightleftharpoons 2Fe^{2+} + H_2O + 0.5O_2$	-9.3067
$KOH(aq) + H^+ \rightleftharpoons K^+ + H_2O$	$1.44 \cdot 10^1$
$KSO_4^- \rightleftharpoons K^+ + SO_4^{2-}$	$-8.85 \cdot 10^{-1}$
$NaSO_4^- \rightleftharpoons Na^+ + SO_4^{2-}$	$-8.25 \cdot 10^{-1}$
$HSO_4^- \rightleftharpoons H^+ + SO_4^{2-}$	-2.0366
$H_{2(aq)} + 0.5O_{2(aq)} \rightleftharpoons H_2O$	$4.610 \cdot 10^1$

Tab. 6.2 Dissolution/precipitation reactions considered in the model and their equilibrium constants at 25ºC (Wolery, 1992)

	Reaction	Log K (25°C)
Calcite	$CaCO_3 + H^+ \rightleftharpoons Ca^{2+} + HCO_3^-$	1.8487
Gypsum	$CaSO_4 \cdot 2H_2O \rightleftharpoons Ca^{2+} + SO_4^{2-} + 2H_2O$	-4.4823
Quartz	$SiO_2(s) \rightleftharpoons SiO_2(aq)$	-3.9993
Magnetite	$Fe_3O_4(s) + 6H^+ \rightleftharpoons 3Fe^{2+} + 0.5O_2(aq) + 3H_2O$	-6.5076
Siderite	$FeCO_3^-(s) + H^+ \rightleftharpoons Fe^{2+} + HCO_3^-$	-0.1920
Goethite	$FeOOH + 2H^+ \rightleftharpoons Fe^{2+} + 1.5H_2O + 0.25O_2(aq)$	-7.9555

The cation exchange capacity (CEC) is 102 meq/100g (Fernández et al., 2004). Table 6.3 lists the cation exchange reactions and their selectivity coefficients at 25 ºC. The Gaines-Thomas convection is used in which Na is adopted as the reference cation (Gaines and Thomas, 1953). Exchange reactions are written so that exchanged Na+ is on the left side of the reaction with a unit stoichiometric coefficient. Cation selectivity coefficients for exchanged Ca2+, Mg2+ and K+ were calibrated so that the computed concentrations of exchanged cations of the FEBEX bentonite are within the range of those reported by Fernández et al. (2004) and Enresa (2004) (see Tab. 6.3). The selectivity coefficient for the exchange of iron was taken from Tournassat (2003). The base run was performed with the selectivities used by Samper et al. (2008a). The simulation results obtained with the calibrated selectivities are presented as part of the uncertainty analyses (Section 6.1.8).

Tab. 6.3 Cation exchange reactions and selectivity coefficients at 25ºC taken from Samper et al. (2008a) and calibrated for this study

Reaction	$K_{Na\text{-}cation}$ Used for base run (from Samper *et al.*, 2008a)	Calibrated $K_{Na\text{-}cation}$ Used for sensitivity analysis
$Na^+ + 0.5Ca\text{-}X_2 \rightleftharpoons 0.5Ca^{2+} + Na\text{-}X$	0.282	0.292
$Na^+ + 0.5Mg\text{-}X_2 \rightleftharpoons 0.5Mg^{2+} + Na\text{-}X$	0.344	0.280
$Na^+ + K\text{-}X \rightleftharpoons K^+ + Na\text{-}X$	0.091	0.138
$Na^+ + 0.5Fe\text{-}X_2 \rightleftharpoons 0.5Fe^{2+} + Na\text{-}X$	0.5	0.5

Surface complexation reactions in the bentonite are modelled with a triple sorption site model similar to that of Bradbury and Baeyens (1997; 2005). The total concentration of sorption sites is 0.322 mol/L. There are 3 types of sorption sites. The first type of sites corresponds to the strong sites which have a large binding affinity but a small concentration (0.0079 mol/L). The other two types are the weak sites (the so-called weak 1 and weak 2) have binding constants weaker than those of the strong sites although their concentrations (0.16 mol/L) are larger than those of the strong sites. Table 6.4 lists the protolysis constants at 25 ºC. According to Samper *et al.* (2008a; 2011), proton surface complexation plays a major role in controlling the pH of the bentonite porewater. Surface complexation and cation exchange reactions are not considered in the canister.

Tab. 6.4 Protolysis constants for surface complexation reactions for a triple-site model (Bradbury and Baeyens, 2005) at 25ºC

Reaction	Log K_{int}
$\equiv S^S OH_2^+ \rightleftharpoons \equiv S^S OH + H^+$	-4.5
$\equiv S^S O^- + H^+ \rightleftharpoons \equiv S^S OH$	7.9
$\equiv S^S OFe^+ + H^+ \rightleftharpoons \equiv S^S OH + Fe^{2+}$	0.6
$\equiv S^S OFeOH + 2H^+ \rightleftharpoons \equiv S^S OH + Fe^{2+} + H_2O$	10.0
$\equiv S^S OFe(OH)_2^- + 3H^+ \rightleftharpoons \equiv S^S OH + Fe^{2+} + 2H_2O$	20.0
$\equiv S^{W1} OH_2^+ \rightleftharpoons \equiv S^{W1} OH + H^+$	-4.5
$\equiv S^{W1} O^- + H^+ \rightleftharpoons \equiv S^{W1} OH$	7.9
$\equiv S^{W1} OFe^+ + H^+ \rightleftharpoons \equiv S^{W1} OH + Fe^{2+}$	3.3
$\equiv S^{W2} OH_2^+ \rightleftharpoons \equiv S^{W2} OH + H^+$	-6.0
$\equiv S^{W2} O^- + H^+ \rightleftharpoons \equiv S^{W2} OH$	10.5

Table 6.5 lists the chemical composition of the initial bentonite porewater and the boundary water at the bentonite/granite interface similar to granite porewater (Samper *et al.*, 2008a; 2011). The initial canister porewater is assumed to have the same chemical composition of the bentonite which is the chemical equilibrium with respect to calcite and quartz, proton surface complexation and cation exchange. This table includes the values reported by Samper *et al.* (2008a; 2011) as initial values and those computed with the code at the first time step which corresponds to $t = 5 \cdot 10^{-4}$ years. There are some differences in the concentrations of some chemical species which are especially relevant for dissolved iron, bicarbonate and silica. Such differences are caused by the lack of equilibrium with respect to calcite, quartz and goethite. In fact, the numerical model computes the following concentrations of mineral species after $t = 5 \cdot 10^{-4}$ years: 1) The dissolution of $5.92 \cdot 10^{-3}$ mol/L of calcite; 2) The precipitation of $7.45 \cdot 10^{-4}$ mol/L of quartz; and 3) The precipitation of $1.05 \cdot 10^{-9}$ mol/L of goethite.

Tab. 6.5 Chemical composition of the initial bentonite porewater and the boundary water at the bentonite/granite interface (Samper et al., 2008a)

Species	Initial bentonite porewater	Bentonite porewater computed at t = $5 \cdot 10^{-4}$ years	Boundary water (granite porewater)
pH	6.43	6.46	7.825
Eh (V)	-0.059	-0.078	-0.188
Ca^{2+} (mol/L)	$3.10 \cdot 10^{-2}$	$3.32 \cdot 10^{-2}$	$1.522 \cdot 10^{-4}$
Mg^{2+} (mol/L)	$3.47 \cdot 10^{-2}$	$3.67 \cdot 10^{-2}$	$1.604 \cdot 10^{-4}$
Na^{+} (mol/L)	$1.84 \cdot 10^{-1}$	$1.88 \cdot 10^{-1}$	$4.350 \cdot 10^{-3}$
K^{+} (mol/L)	$1.50 \cdot 10^{-3}$	$1.55 \cdot 10^{-3}$	$5.371 \cdot 10^{-5}$
Fe^{2+} (mol/L)	$6.58 \cdot 10^{-5}$	$1.43 \cdot 10^{-4}$	$1.791 \cdot 10^{-8}$
Cl^{-} (mol/L)	$2.75 \cdot 10^{-1}$	$2.75 \cdot 10^{-1}$	$3.949 \cdot 10^{-4}$
HCO_3^{-} (mol/L)	$1.69 \cdot 10^{-3}$	$7.59 \cdot 10^{-3}$	$5.049 \cdot 10^{-3}$
SO_4^{2-} (mol/L)	$2.05 \cdot 10^{-2}$	$2.05 \cdot 10^{-2}$	$1.561 \cdot 10^{-5}$
SiO_2 (aq) (mol/L)	$8.42 \cdot 10^{-4}$	$9.67 \cdot 10^{-5}$	$3.761 \cdot 10^{-4}$

6.1.5.3 Canister corrosion

Carbon-steel corrosion is modelled by using a kinetic formulation in a manner similar to mineral dissolution (Section 6.1.4). The canister is treated as a porous material made of 100% metallic iron, Fe(s), which dissolves at a constant rate of 2 μm/year.

A range of values of the corrosion rate between 0.1 and 5 μm/year has been explored in the sensitivity analyses. Simulations considering variable corrosion rate depending on temperature or saturation are also performed in the uncertainty analysis.

6.1.6 Computer code

Coupled hydrogeochemical calculations of the interactions of corrosion with bentonite have been performed with CORE^{2D}V4 (Samper *et al.*, 2003; 2011), a code for transient saturated and unsaturated water flow, heat transport and multicomponent reactive solute transport under both local chemical equilibrium and kinetic conditions in heterogeneous and anisotropic media. Flow and transport equations are solved with Galerkin triangular finite elements and an Euler scheme for time discretization. CORE^{2D}V4 solves problems with a wide range of geochemical reactions such as acid–base, aque-

ous complexation, redox, mineral dissolution/precipitation, gas dissolution/ex-solution, cation exchange and surface complexation. The chemical formulation is based on the ion association theory and uses an extended version of Debye–Hückel equation (B-dot) for the activity coefficients of aqueous species. CORE^{2D}V4 relies on thermodynamic data from EQ3/6 (Wolery, 1992). It uses the sequential iteration approach to solve for chemical reactive solute transport. The whole iterative cycle is repeated until prescribed convergence criteria are attained (Xu *et al.*, 1999; Samper *et al.*, 2009; 2011).

CORE^{2D} has been widely used to model laboratory and in situ experiments performed for HLW disposal (Molinero and Samper 2006; Samper *et al.*, 2008b; Zheng and Samper, 2008; Zheng *et al.*, 2008; 2010), evaluate the long-term geochemical evolution of radioactive waste repositories in clay (Yang *et al.*, 2008), model the transport of corrosion products and their geochemical interactions with bentonite (Samper *et al.*, 2008a; 2011) and evaluate the long-term transport and sorption of radionuclides through the bentonite barrier (Samper *et al.*, 2010).

6.1.7 Model results

Canister corrosion

Figure 6.5 shows the computed time evolution of canister Fe(s) corrosion. The canister is fully corroded after $5 \cdot 10^4$ years for a corrosion rate of 2 μm/y. After full canister corrosion, » 350 mol/L of Fe(s) are dissolved. It should be noticed that the cumulative amount of corroded Fe(s) remains constant once the canister has corroded entirely.

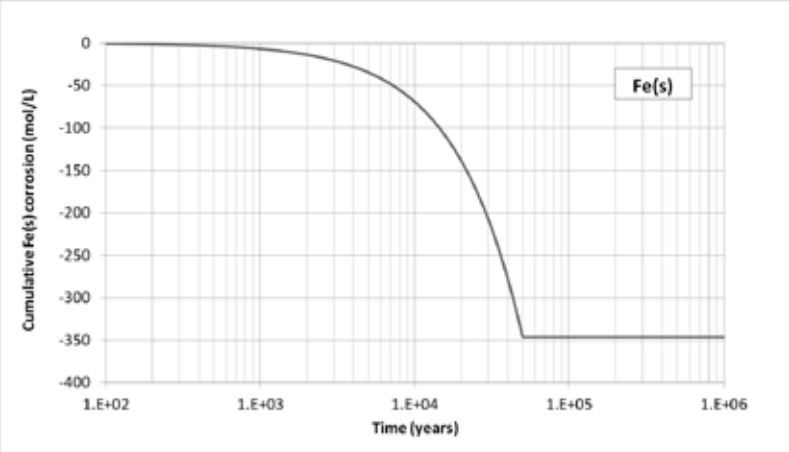

Fig. 6.5 Time evolution of the computed cumulative canister corrosion

Aqueous species

Canister corrosion causes an increase in Fe^{2+} concentration and pH, and a decrease in Eh. Most of the released Fe^{2+} diffuses from the canister into the bentonite where it precipitates or sorbs.

Figure 6.6 shows the time evolution of the computed concentration of dissolved Fe in the bentonite at radial distances, r = 4.6, 5.3 and 9.5 dm where r is measured from the axis of the disposal cell. Such radial distances correspond to the points located at 0.1, 0.8 and 5 dm from the canister/bentonite interface. Figure 6.7 shows the radial distribution of the computed concentration of dissolved Fe in the bentonite at several times. The time trends in the concentration of dissolved Fe are directly related to those of the sorbed species. For instance, the sudden decrease in dissolved Fe concentration after 80 years at r = 4.6 dm is associated with a sudden increase in Fe sorbed in weak 1 sites. The concentration of dissolved Fe after 100.000 years becomes lower than $5 \cdot 10^{-6}$ mol/L due to the aqueous diffusion of dissolved Fe from the bentonite to the granite.

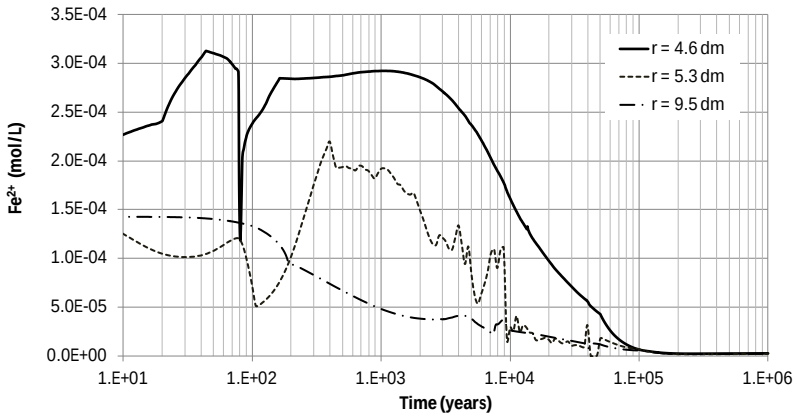

Fig. 6.6 Time evolution of the computed concentration of dissolved Fe in the bentonite at r = 4.6, 5.3 and 9.5 dm

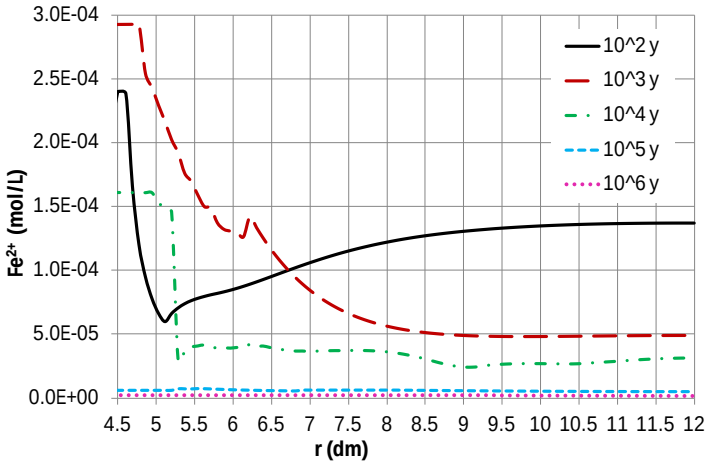

Fig. 6.7 Radial distribution of the computed concentration of dissolved iron in the bentonite at selected times (r is the radial distance from the axis of the disposal cell)

Figure 6.8 shows the time evolution of the computed pH in the bentonite at r = 4.6, 5.3 and 9.5 dm. At r = 4.6 dm the pH increases from its initial value of 6.4 to 7.1 at t = 80 years. Then, the pH increases sharply almost a unit. Such an increase in pH is caused by the sorption of Fe on weak 1 sites according to:

$$\equiv S^{W1}OH + Fe^{2+} \rightleftharpoons \equiv S^{W1}OFe^{+} + H^{+} \qquad (6.13)$$

Dissolved Fe^{2+} gets sorbed and releases protons. From 80 to $2 \cdot 10^5$ years the pH keeps increasing and reaches a peak value of 9.5 after $2 \cdot 10^5$ years. At the end of the simulation, t = 10^6 years, the computed pH gets below 9.

At r = 5.3 dm the sorption fronts induce a large decrease in pH at t = 10.000 years. Figure 6.9 shows the radial distribution of the computed pH in the bentonite at selected times. One can see clearly that pH reaches a minimum value of 4.5 at r = 5.3 dm from 10.000 to 20.000 years.

At points farther away from the canister such as r = 9.5 dm, the pH increases gradually reaching its maximum at t = $2 \cdot 10^5$ years the behavior of the pH is the same all along the bentonite (see Fig. 6.8).

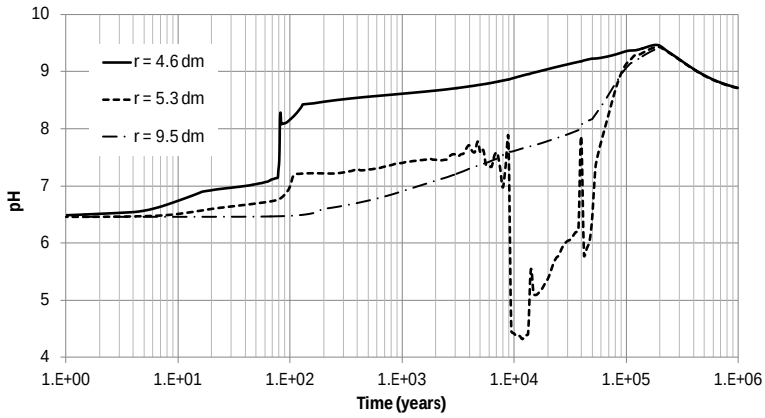

Fig. 6.8 Time evolution of the computed pH in the bentonite at r = 4.6, 5.3 and 9.5 dm

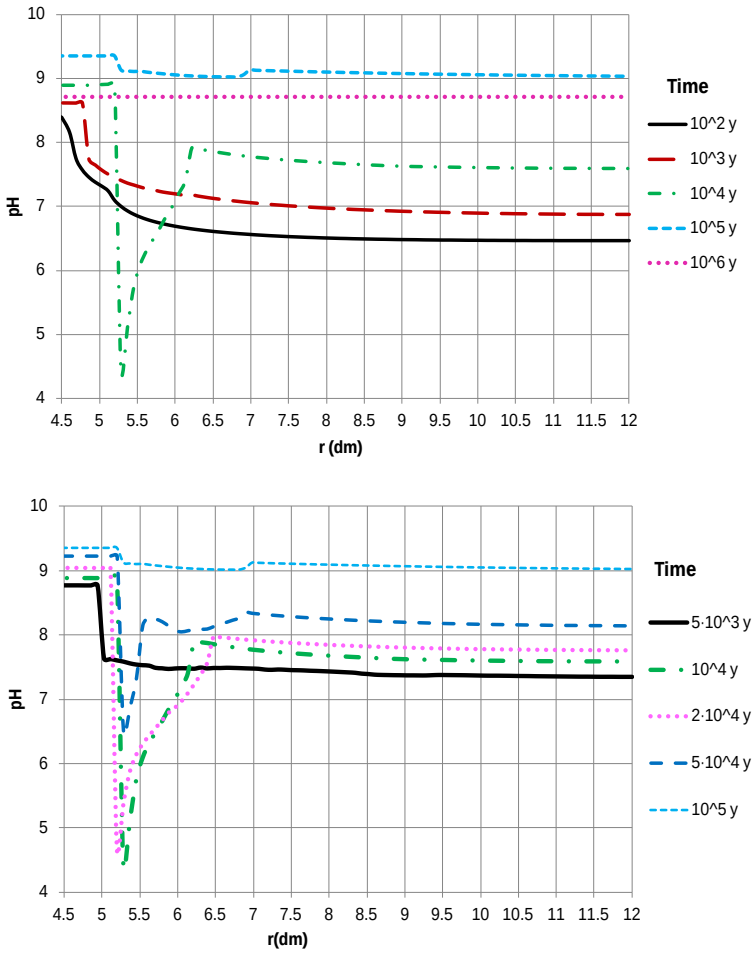

Fig. 6.9 Radial distribution of computed pH in the bentonite at selected times covering the ranges from 102 to 106 years (top) and from 5·103 to 105 years (bottom) (r is the radial distance to the axis of the disposal cell)

Figure 6.10 shows the time evolution of the computed Eh in the bentonite at r = 4.6, 5.3 and 9.5 dm. At r = 4.6 dm, the Eh decreases sharply from -0.2 V to -0.5 V at 80 years. Later, it decreases smoothly until 5·104 years, when the canister is full corroded. Finally, Eh increases to -0.4 V. At r = 5.3 dm the sorption fronts induce an increase in Eh at 10.000 years which is related to the front of pH (see Fig. 6.8).

The time evolution of the Eh after 2·105 years is the same at the three locations within the bentonite. Figure 6.11 shows the radial distribution of the computed Eh in the bentonite at several times. Eh shows a peak at r = 5.3 dm after 10.000 years. The time evolution of the Eh is directly related to that of pH and is affected by the sorption fronts.

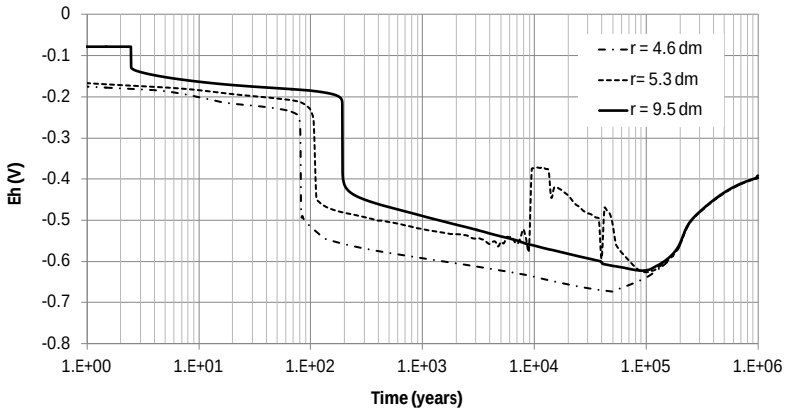

Fig. 6.10 Time evolution of the computed Eh in the bentonite at r = 4.6, 5.3 and 9.5 dm

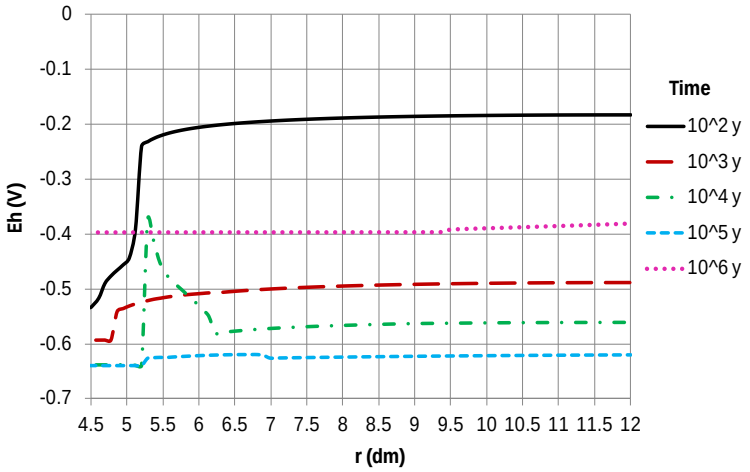

Fig. 6.11 Radial distribution of the computed Eh in the bentonite at selected times (r is the radial distance to the axis of the disposal cell)

Figure 6.12 shows the time evolution of the computed concentration of dissolved Cl^- in the bentonite. The concentration of a conservative species such as Cl^- is the same everywhere in the bentonite. The decrease of the concentration is due to the out diffusion of Cl^-. The diffusive solute flux is larger than the advective flux in the granite and therefore the gradient of the concentrations in the bentonite is very small. For these conditions, it can be shown that the plot of the log concentration of Cl^- versus time is a straight-line (Fig. 6.13) because the concentration, C, is given by

$$C\text{-}C_b = (C_0\text{-}C_b)\exp(-\alpha t) \qquad (6.14)$$

where C_0 is the initial concentration, C_b is the boundary concentration and α is a recession coefficient [T^{-1}] which for a water flow Q is equal to Q/V_w where V_w is the total volume of water in the bentonite and the canister (Samper *et al.*, 2010; Ma, 2010).

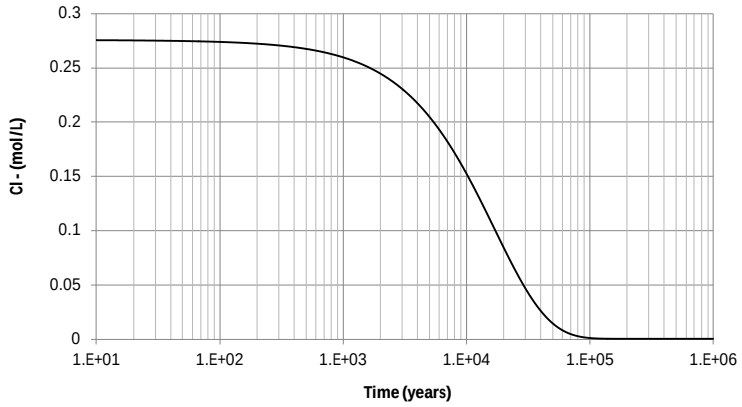

Fig. 6.12 Time evolution of the computed concentration of Cl- in the bentonite at r = 4.6, 5.3 and 9.5 dm

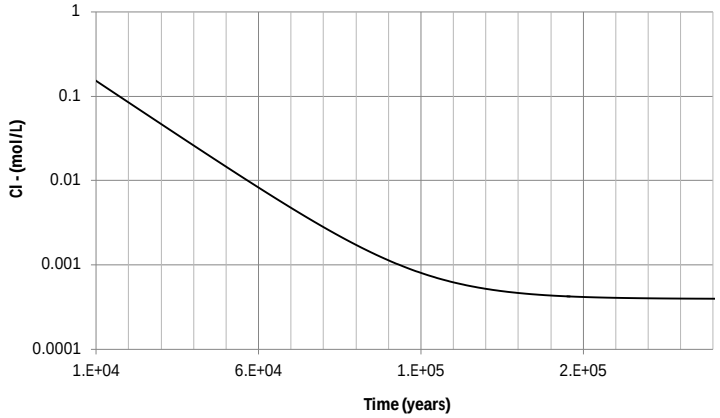

Fig. 6.13 Time evolution of the computed concentration of Cl- in the bentonite at r = 4.6, 5.3 and 9.5 dm. The log c-t plot at the bottom is a straight line for t < 110000 years, the time needed for Cl- to diffuse out of the EBS

The computed concentrations of the dissolved cations, Ca^{2+}, Mg^{2+}, Na^{+} and K^{+}, show trends similar to those of Cl^{-}. In addition to diffusion, these species are subjected to mineral dissolution/precipitation and cation exchange reactions. Figure 6.14 shows the time evolution of the computed concentration of dissolved Ca^{2+} in the bentonite at r = 4.6, 5.3 and 9.5 dm. There are small differences in the concentrations of Ca^{2+} in these points for t < 1000 years which are due to calcite precipitation near the canister/bentonite interface. This figure shows also the plot of the radial distribution of the concentration of dissolved Ca^{2+} at several selected times. One can see that the concentration of dissolved Ca^{2+} in the bentonite near the canister decreases due to calcite precipitation until t = 100 years. This creates a concentration gradient which induces the diffusion of dissolved Ca^{2+} towards this zone so that the concentration gradient dissipates after 3000 years. Later, the concentrations are the same everywhere throughout the bentonite.

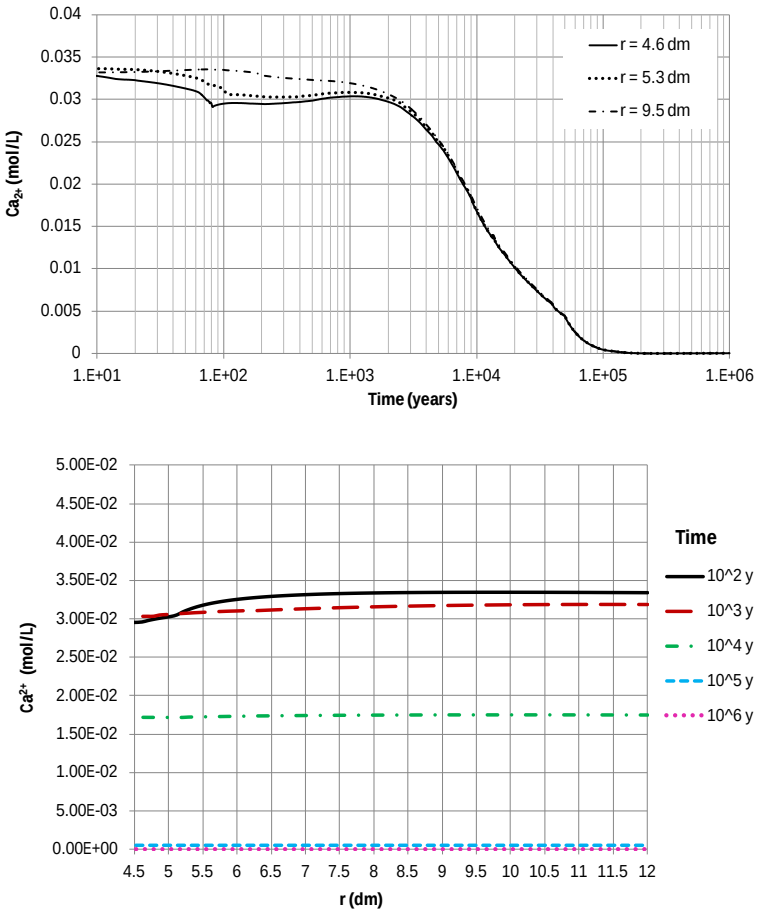

Fig. 6.14 Time evolution of the computed concentration of dissolved Ca2+ in the bentonite at r = 4.6, 5.3 and 9.5 dm (top) and radial distribution of the concentrations at several times (bottom). r is the radial distance to the axis of the disposal cell

Figure 6.15 shows the time evolution of the computed concentration of dissolved HCO_3^- in the bentonite at r = 4.6, 5.3 and 9.5 dm. This concentration decreases from its concentration of $7.6 \cdot 10^{-3}$ mol/L to the value at the granite boundary $5.05 \cdot 10^{-3}$ mol/L due to the solute diffusion. However, HCO_3^- is subjected to calcite and siderite dissolution/precipitation. The following stages can be established for the space-time patterns of the concentration of dissolved HCO_3^-:

1. For t < 80 years, the concentration of dissolved HCO_3^- near the canister decreases dramatically due to the rise in pH (Fig. 6.8) which induces the precipitation of calcite and siderite. In fact, there is a clear coincidence in the sharp fronts of increasing pH at t = 80 years and the fronts of decreasing HCO_3^-.

2. For $80 < t < 2 \cdot 10^5$ years, the concentration of dissolved HCO_3^- keep decreasing due to calcite and siderite precipitation near the canister/bentonite interface. Then, a spatial gradient in the concentration of dissolved HCO_3^- is created which induces the diffusion HCO_3^- towards the canister (Fig. 6.16).

3. For $t > 2 \cdot 10^5$ years, calcite and siderite dissolution has ceased (Fig. 6.19 and Fig. 6.21). The concentration of dissolved HCO_3^- is controlled by the in-diffusion of HCO_3^- from the granite porewater.

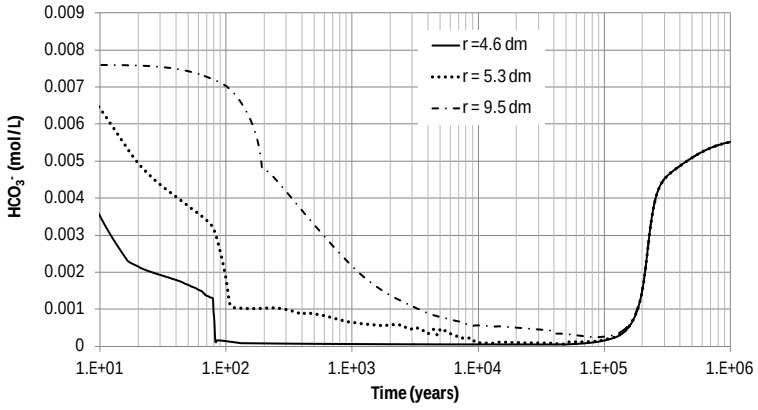

Fig. 6.15 Time evolution of the concentration of dissolved HCO3- in the bentonite at r = 4.6, 5.3 and 9.5 dm

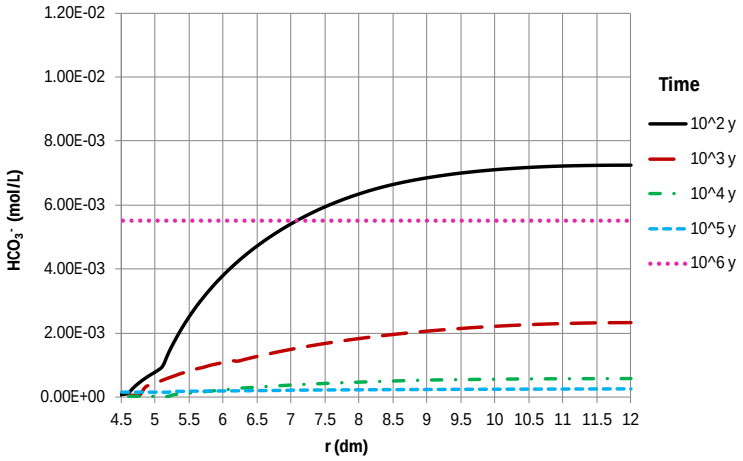

Fig. 6.16 Radial distribution of dissolved HCO3- concentration at selected times (r is the radial distance to the axis of the disposal cell)

Mineral phases

The products of the canister corrosion, hydrogen, iron and hydroxyl anions will diffuse from the canister into the bentonite. Hydrogen does not undergo chemical reactions and is transported only by aqueous diffusion of $H_{2(aq)}$. OH^- and iron, on the other hand, may diffuse and react. Dissolved iron may precipitate as mineral phases, sorb by surface complexation and exchange with the exchanged complex.

Model results show that magnetite is the main corrosion product in the bentonite. Siderite precipitation is much lower than magnetite precipitation due to the limited availability of dissolved carbonate. No goethite precipitation is simulated.

Figure 6.17 shows the time evolution of the concentration of cumulative precipitated magnetite in the bentonite at r = 4.6 dm. Magnetite starts to precipitate significantly after 1000 years close to the canister/bentonite interface (r = 4.5 dm). One can see that after $5 \cdot 10^4$ years, when the canister is fully corroded, magnetite precipitation stops. Figure 6.18 presents the radial distribution of the computed concentration of cumulative precipitated magnetite at several selected times. Magnetite precipitation increases with time and progresses as Fe^{+2} diffuses from the canister into the bentonite. The zone of bentonite affected by magnetite precipitation after 10^6 years has a thickness of approximately 6 cm.

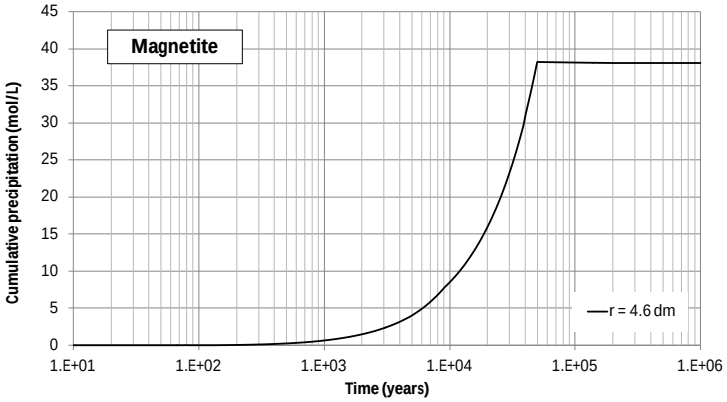

Fig. 6.17 Time evolution of the concentration of cumulative precipitated magnetite at r = 4.6 dm

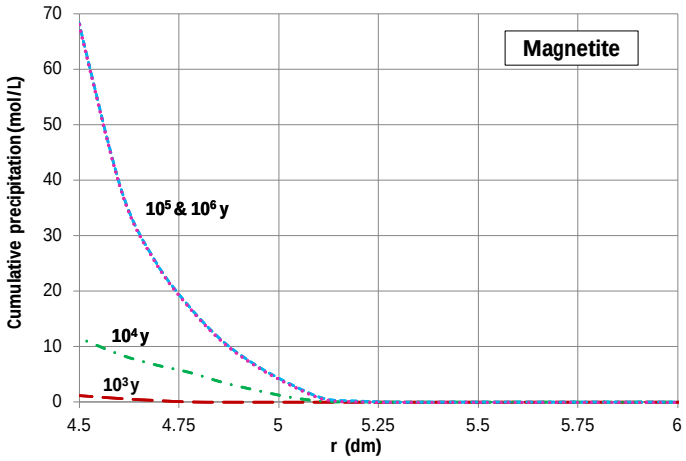

Fig. 6.18 Radial distribution of the concentration of cumulative precipitated magnetite at several selected times. r is the radial distance to the axis of the disposal cell

Figure 6.19 shows the time evolution of the computed concentration of cumulative precipitated siderite in the bentonite at several locations. Siderite starts precipitating near the canister/bentonite interface (r = 4.6 dm) after 100 years. Changes in the slope of the computed cumulative concentration are due to the competition of siderite and magnetite for the dissolved Fe^{2+} and siderite and calcite competition for dissolved bicarbonate. Siderite precipitation increases when magnetite stops precipitating after $t = 5 \cdot 10^4$ years. Siderite precipitation ceases after 200.000 years. At r = 9.5 dm siderite precipitation is negligible.

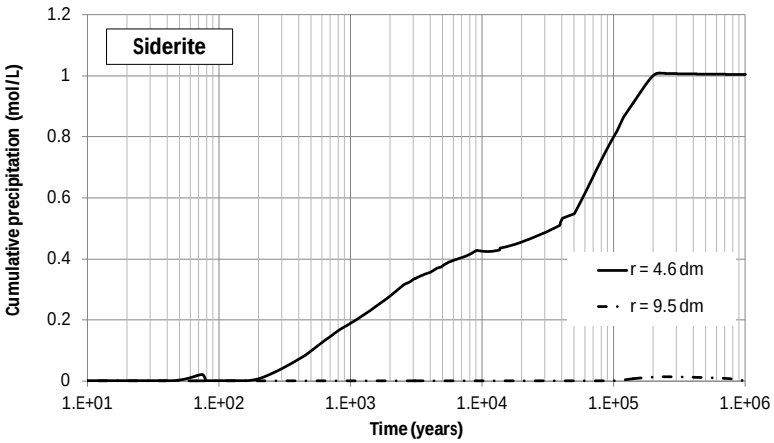

Fig. 6.19 Time evolution of the concentration of cumulative precipitated siderite at r = 4.6 and 9.5 dm. r is the radial distance to the axis of the disposal cell

Figure 6.20 shows the spatial distribution of the computed concentration of cumulative precipitated siderite in the bentonite at several selected times. The thickness of the siderite precipitation zone in the bentonite after 10^6 years is similar to that of magnetite precipitation (Fig. 6.18). The concentration of precipitated siderite is much lower than that of precipitated magnetite due to the limited availability of dissolved bicarbonate. While the concentration of siderite is about 1 mol/L after 10^5 years, the concentration of magnetite ranges from 5 to 70 mol/L (Fig. 6.18).

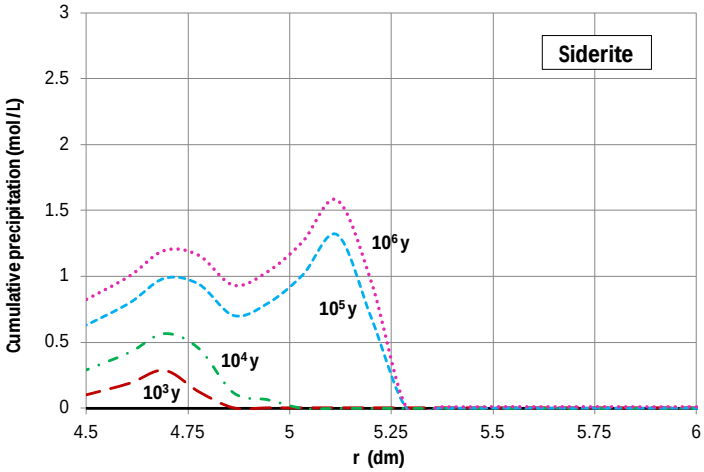

Fig. 6.20 Radial distribution of the concentration of cumulative precipitated siderite at several selected times. r is the radial distance to the axis of the disposal cell

The precipitation of the iron minerals contributes to a decrease in the concentration of dissolved Fe^{+2} and plays an important role on the pH evolution.

Figure 6.21 shows the time evolution of the computed concentration of precipitated calcite in the bentonite at r = 4.6, 5.3 and 9.5 dm. While calcite precipitates near the interface canister/bentonite (r = 4.6 dm), it dissolves at other locations (at r = 5.3 and 9.5 dm).

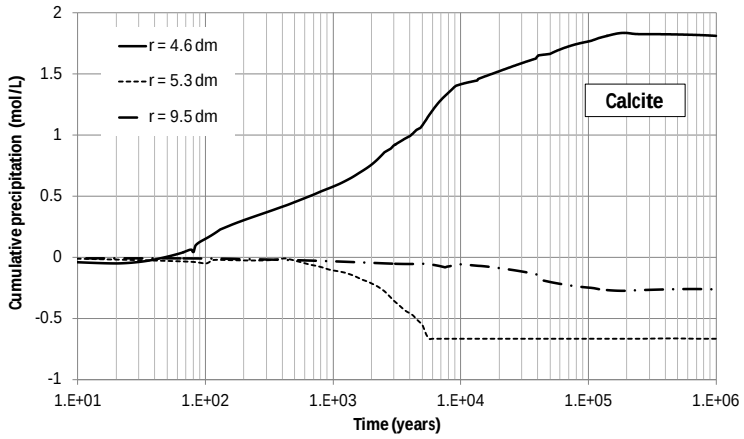

Fig. 6.21 Time evolution of the concentration of cumulative precipitated calcite at r = 4.6, 5.3 and 9.5 dm. r is the radial distance to the axis of the disposal cell

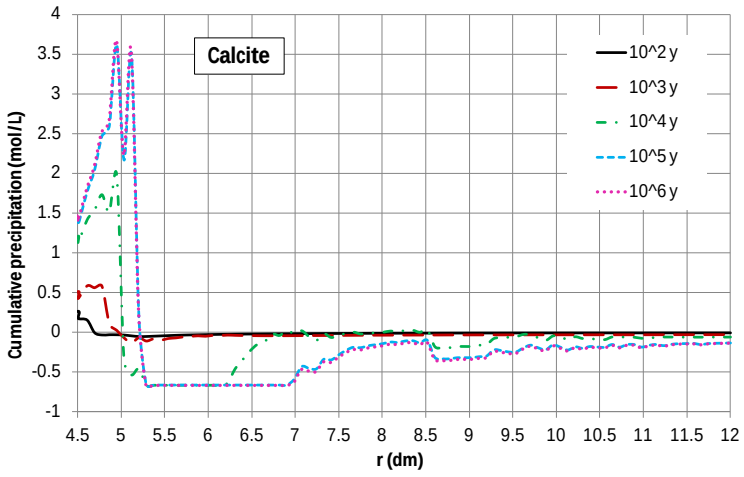

Fig. 6.22 Spatial distribution of the concentration of cumulative precipitated calcite at selected times. r is the radial distance to the axis of the disposal cell

Figure 6.22 shows the radial distribution of the concentration of precipitated calcite at several times. Calcite precipitates near the interface canister/bentonite due to the rise in pH. The zone where calcite precipitates has a thickness of about 7 cm. Far from the interface, the concentrations of dissolved Ca^{2+} and HCO_3^- decrease due to solute diffu-

sion from the bentonite into the granite. Such a decrease leads to the dissolution of calcite.

The dissolution/precipitation of quartz and gypsum are not significant.

Cation exchange

Figure 6.23 and Fig. 6.24 show the time evolution of the computed concentrations of the exchanged cations in the bentonite at r = 4.6 and 9.5 dm, respectively. At r = 4.6 dm the concentration of exchanged Ca^{2+} decreases slightly from 20 to 80 years in response to the decrease in the concentration of dissolved Ca^{2+} caused by calcite precipitation. The exchanged Ca^{2+} is replaced by the dissolved Mg^{2+}. From 80 to 10.000 years the cation exchange reverses and the exchanged Mg^{2+} is replaced by the dissolved Ca^{2+}. After 10.000 years, the ratio of the concentrations of Ca^{2+} and Na^{+} increases due to calcite dissolution and therefore, the dissolved Ca^{2+} replaces the exchanged Na^{+}.

Far from the canister interface (r = 9.5 dm) the computed concentrations of the exchanged cations remain constant until t = 3.000 years. Later, the trend is similar to that computed at r = 4.6 dm, that is, the dissolved Ca^{2+} replaces the exchanged Na^{+}.

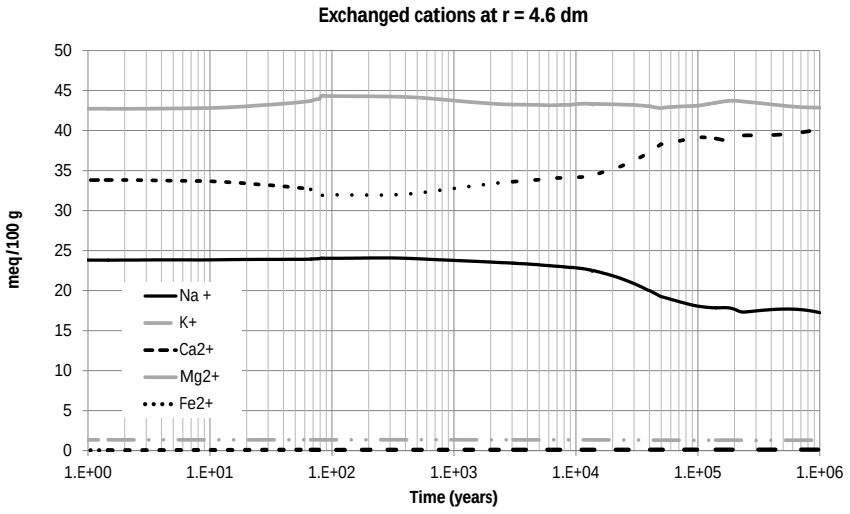

Fig. 6.23 Time evolution of the computed concentrations of the exchanged cations in the bentonite at r = 4.6 dm

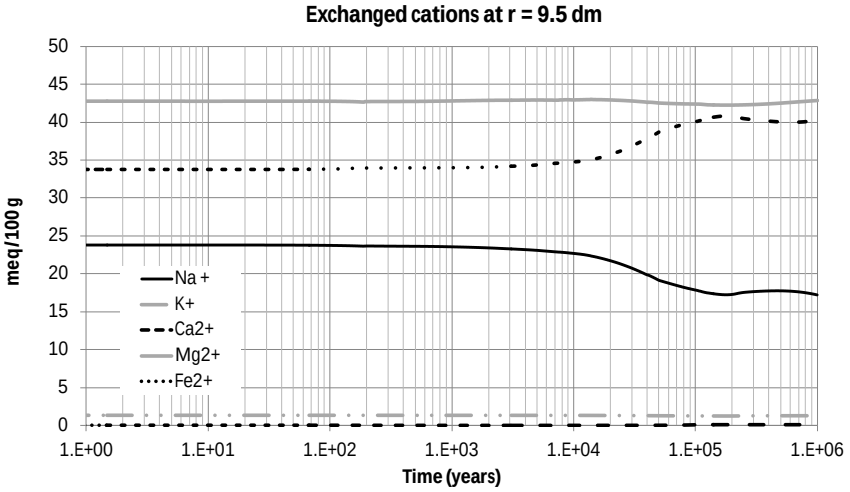

Fig. 6.24 Time evolution of the the computed concentrations of the exchanged cations in the bentonite at r = 9.5 dm

Figure 6.25 shows the time evolution of the computed concentration of exchanged Fe^{2+} in the bentonite near the interface (r = 4.6 dm) and near the centre of the bentonite buffer (r = 9.5 dm). The concentration of the exchanged Fe^{2+} follows a trend similar to that of the sorbed and dissolved Fe^{2+} (see Fig. 6.6 and Fig. 6.7). Figure 6.26 shows the spatial distribution of the computed concentration of exchanged Fe^{2+} at several selected times. The concentration of exchanged Fe^{2+} increases from its initial value of 0.04 meq/100 g to about 0.12 meq/100 g at the end of the simulation.

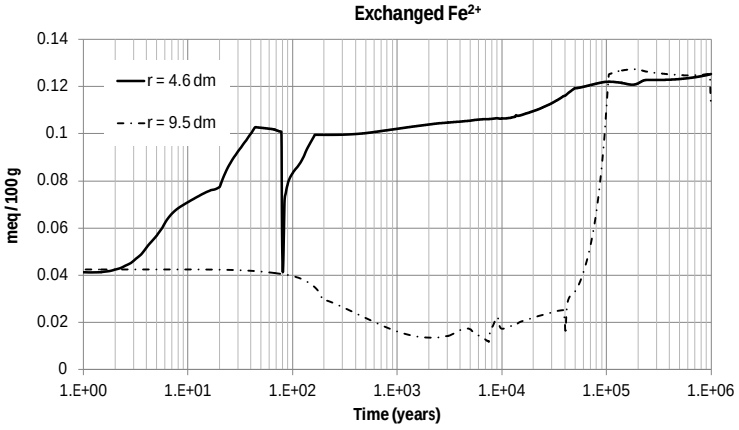

Fig. 6.25 Time evolution of the computed concentration of exchanged iron in the bentonite at r = 4.6 and 9.5 dm. r is the radial distance to the axis of the disposal cell

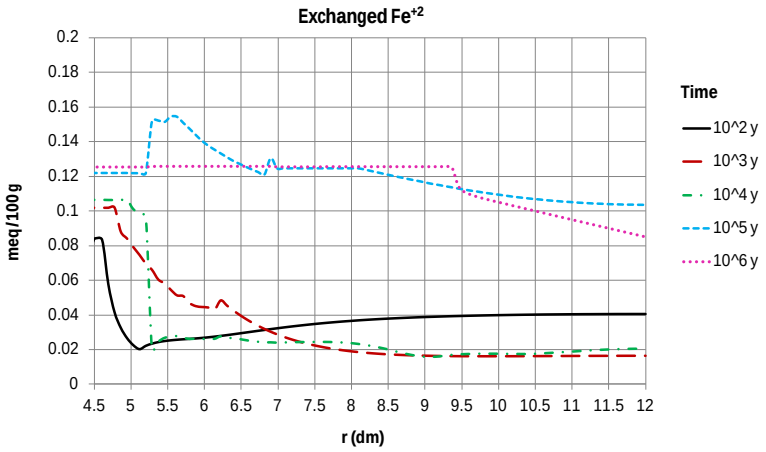

Fig. 6.26 Spatial distribution of the computed concentration of exchanged iron the bentonite at several times. r is the radial distance to the axis of the disposal cell

Sorbed species

Model results show that sorption play a very relevant role in the geochemical evolution of bentonite. Fe^{2+} and H^{+} compete for the weak 1 sorption sites near the canister. Such competition leads to the several sorption fronts and is relevant only at distances lower than 8 cm from the canister. There is no competition between Fe^{2} and H^{+} for weak 2 sorption sites because the model does not consider for sorption of Fe on weak 2 sites.

More details on the patterns of sorbed species can be found in the Deliverable 3.5.3 of the PEBS Project (Samper *et al.*, 2013).

Changes in porosity

Samper *et al.* (2008a) showed that changes in the bentonite porosity caused by mineral dissolution/precipitation are lower than 10% for a corrosion rate of 0.2 μm/y and after 0.3 Ma. Based on that, our model disregards porosity changes and its effects in the solute transport and geochemical processes. Our simulation accounts for a corrosion rate 10 times larger than that of Samper *et al.* (2008a; 2011) and therefore, porosity changes could be more significant.

The changes in bentonite porosity caused by chemical reactions have been calculated from the simulated results with a constant porosity (0.407) by adding and subtracting the volume of the amount of dissolved and precipitated minerals. Figure 6.27 and

Fig. 6.28 show the time evolution and the spatial distribution of the changes in bentonite porosities at several locations and times. For a corrosion rate of 2 μm/y, the porosity at the canister/bentonite interface is half its initial value after 10.000 years. The precipitation of the corrosion products close to the canister leads to a very relevant decrease of bentonite porosity. At the end of the simulation, the reduction of porosity can up to zero in a zone of 2.5 cm near the canister-bentonite interface and the changes in porosity are negligible for r > 5.25 dm.

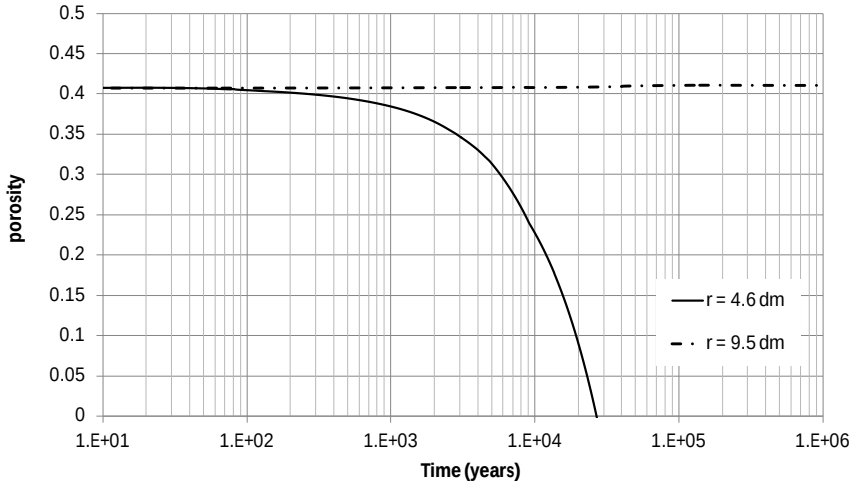

Fig. 6.27 Time evolution of the change in bentonite porosity due to mineral dissolution and precipitation at r = 4.6 and 9.5 dm

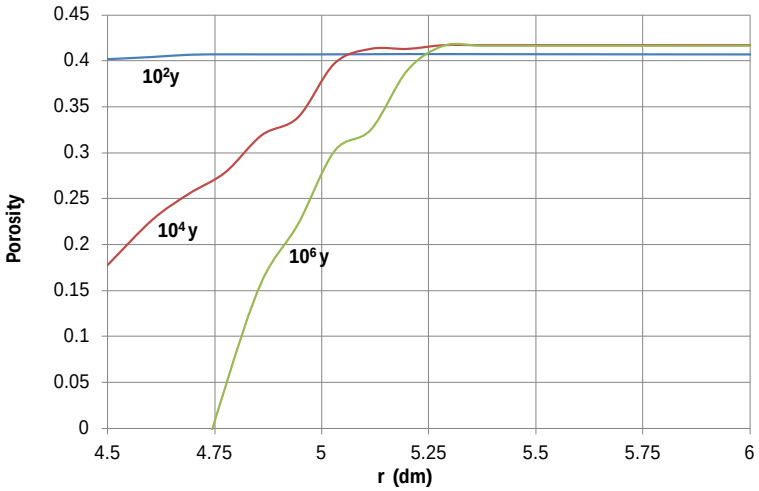

Fig. 6.28 Spatial distribution of the change in bentonite porosity due to mineral dissolution and precipitation at selected times. r is the radial distance to the axis of the disposal cell

Figure 6.29 presents the time evolution of the thickness of the bentonite affected by a porosity reduction larger than 10%. The bentonite thickness significantly affected by porosity reduction increases with time and it is ~7 cm after 1 Ma.

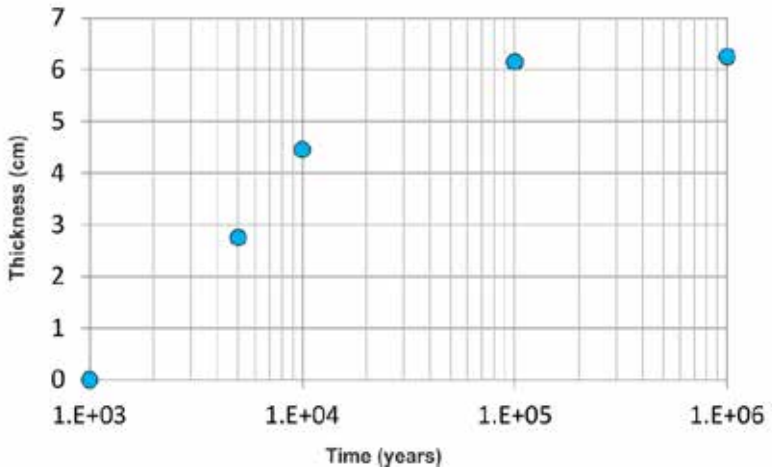

Fig. 6.29 Time evolution of the thickness of the bentonite affected by a porosity reduction larger than 10%

A variable porosity would provide more accurate simulations of the long term evolution of the repository.

Conclusions

The canister corrosion, the interactions of corrosion products with bentonite and the pH buffering mechanisms have been simulated during 1 Ma and at a constant temperature of 25ºC for a spent-fuel carbon-steel canister repository in granite.

The canister is fully corroded after $5 \cdot 10^4$ years for a constant corrosion rate of 2 μm/y. Canister corrosion causes an increase in the concentration of dissolved Fe^2 and pH, and a decrease in Eh. Most of the released Fe^{2+} diffuses from the canister into the bentonite where it precipitates or sorbs. The largest pH in the bentonite is almost 9.5 at $2 \cdot 10^5$ years. The evolution of the concentration of dissolved Fe^{2+}, pH and Eh are determined by the generation of corrosion products, the precipitation of magnetite and Fe sorption on weak sites. Several fronts are observed in dissolved Fe^{2+}, pH and Eh related to sorption fronts at the same times and locations.

Magnetite is the main corrosion product in the bentonite. Approximately 70 mol/L of magnetite precipitate in the canister/bentonite interface before the canister is full cor-

roded and the precipitation stops. Its precipitation progresses as Fe^{2+} diffuses into the bentonite. The thickness of the bentonite zone where magnetite precipitates is of ~7 cm. Siderite precipitation is much lower than magnetite precipitation due to the limited availability of dissolved bicarbonate (lower than 2 mol/L). The thickness of the bentonite zone where siderite precipitates (~8 cm) is similar to that of the magnetite. The precipitation of the corrosion products contributes to the decrease in the concentration of dissolved Fe^{2+} and influences the pH evolution. Calcite dissolves in most of the bentonite except near the canister where it precipitates due to the increase in pH induced by canister corrosion. Dissolution/precipitation of quartz and gypsum are not significant.

Conservative species such as Cl^- present a pattern of decreasing concentration with time in the bentonite because their diffusion to granite. Dissolved cations, Ca^{2+}, Mg^{2+}, Na^+ and K^+ and show trends similar to those of conservative species but they are also subjected to mineral dissolution/precipitation and cation exchange processes.

The computed concentrations of exchanged cations in the bentonite vary with time due to changes in cation porewater concentration. The concentration of exchanged Ca^{2+} increases after 1 Ma while those of Na^+ and Mg^+ decrease. Only a small part of the Fe released by canister corrosion is sobbed at exchanged sites. The evolution of the concentration of exchanged Fe^{2+} is related to that of sorbed and dissolved Fe^{2+}.

Model results show that sorption play a very relevant role in the geochemical evolution of bentonite. Fe^{2+} and H^+ compete for the weak 1 sorption sites near the canister. Such competition leads to the several sorption fronts and is relevant only at distances lower than 8 cm from the canister. There is no competition between Fe^2 and H^+ for weak 2 sorption sites because the model does not consider for sorption of Fe on weak 2 sites.

It is assumed that generated $H_2(g)$ is dissolved in porewater and diffuses through bentonite, disregarding gas migration and possible mechanic effects. The time evolution of the $H_2(g)$ pressures generated has been calculated from the computed activities of $H_2(aq)$. The partial pressure of $H_2(g)$ increases while the canister is being corroded until 16200 atm and decreases once the canister has been fully corroded.

Finally, the effects of mineral dissolution and precipitation in porosity have been evaluated. The precipitation of the corrosion products close to the canister leads to a very relevant decrease of bentonite porosity near the canister-bentonite interface. The bentonite thickness significantly affected by porosity reduction increases with time and it is

~7 cm after 1 Ma. A negligible increase of the porosity is observed in the rest of the buffer. A variable porosity would provide more accurate simulations of the long term evolution of the repository.

6.1.8 Impact of uncertainties and simplifications

The numerical predictions of the long term geochemical conditions of the EBS presented in the previous section have uncertainties due to uncertainties in the geometric model and the model structure (dimensionality), the conceptual model (processes) and the model parameters.

Samper *et al.* (2013) in the Deliverable 3.5.3 of the PEBS Project presented the sensitivity of the long-term geochemical predictions of the EBS to changes in the following model parameters: 1) The canister corrosion rate; 2) The effective diffusion coefficient of the chemical species in the bentonite; 3) The flow rate of granite porewater at the bentonite/granite interface; 4) The selectivity coefficients of the cation exchange reactions; and 5) The chemical composition of the initial bentonite porewater and granitic boundary porewater.

Such sensitivity analysis has been updated with the evaluation of:

- The thermal field across the EBS which may last for thousand years,
- The dependence of the corrosion rate on temperature,
- The dependence of the corrosion rate on the chemical conditions,
- The kinetic control of the magnetite precipitation,
- The dissolution of smectite and the neoformation of Fe-clay minerals and zeolites.

The influence of some geometric simplifications has been also analyzed.

6.1.8.1 Uncertainty in material parameters

A set of sensitivity runs have been performed to evaluate the uncertainty in the canister corrosion rate assuming the following values: 0.1, 0.5, 1, 3 and 5 μm/y. The main conclusions of this sensitivity analysis include:

1. The increase in pH takes place sooner the larger the corrosion rate.

2. Magnetite is the main corrosion product regardless the corrosion rate. The larger the corrosion rate, the larger the magnetite concentration close to the canister/bentonite interface but the lower its penetration in the bentonite. Magnetite penetration ranges from 4 to 10 cm for corrosion rates from 5 to 0.5 μm/y.

3. Similar to magnetite, the larger the corrosion rate the lower the penetration of the siderite front into the bentonite. Siderite penetration ranges from 4 to 12 cm for corrosion rates from 5 to 0.5 μm/y.

4. The thickness of the zone where calcite precipitates in the bentonite increases with the decrease of corrosion rate and ranges from 4 to 12 cm for corrosion rates from 5 to 0.5 μm/y.

5. The computed concentrations of exchanged cations in the bentonite are not sensitive to changes in the corrosion rate.

6. The larger the corrosion rate, the faster the porosity reduction near the canister interface. The larger the corrosion rate, the lower the thickness of bentonite affected by pore clogging (Fig. 6.30).

7. Computed results for a corrosion rate of 0.1 μm/y shows a different behaviour of computed pH related to the sorption on weak 2 sorption sites, a much larger penetration and smaller concentrations of the corrosion products and a significantly larger thickness of bentonite affected by pore clogging than those for the other corrosion rates.

More details can be found in the Deliverable 3.5.3 of the PEBS Project (Samper et al. 2013).

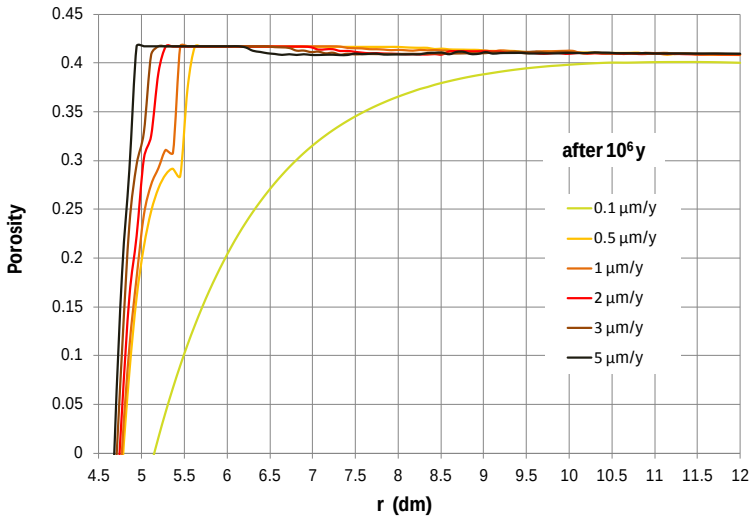

Fig. 6.30 Sensitivity of the spatial distribution of the changes in bentonite porosity due to mineral dissolution and precipitation for several corrosion rates at t = 106 years. r is the radial distance to the axis of the disposal cell

All dissolved chemical species are assumed to have the same effective diffusion, D_e, which is equal to $4.07 \cdot 10^{-11}$ m^2/s for the base run. Cationic species may have an effective diffusion larger than $4.07 \cdot 10^{-11}$ m^2/s while anionic species may diffuse slower. A set of sensitivity runs have been performed to evaluate the uncertainty in the value of the effective diffusion of the dissolved species. The effective diffusion for the sensitivity runs was taken equal to half and double the reference value, D_e, of $4.07 \cdot 10^{-11}$ m^2/s. The sensitivity runs will be denoted as $0.5D_e$ and $2D_e$, respectively.

The main conclusions of the sensitivity analysis to the D_e of the bentonite include:

1. The computed concentrations of most dissolved species, except for the dissolved Fe^{2+} are not sensitive to the changes in D_e. The larger the D_e, the smoother is the increase of the curve if the concentration of dissolved Fe^{2+}.

2. The computed pH is not very sensitive to the change in the De of the bentonite.

3. The larger the De, the larger the thickness of the zone where magnetite, siderite and calcite precipitate (Fig. 6.31). The thickness of bentonite where magnetite precipitates increases from 4 to 9 cm when the De increases from 0.5De to 2De.

4. The computed concentrations of exchanged cations in the bentonite are not sensitive to changes in the De of the bentonite.

5. The larger the De of the bentonite, the larger the thickness of bentonite affected by pore clogging (Fig. 6.32).

More details can be found in the Deliverable 3.5.3 of the PEBS Project (Samper *et al.* 2013).

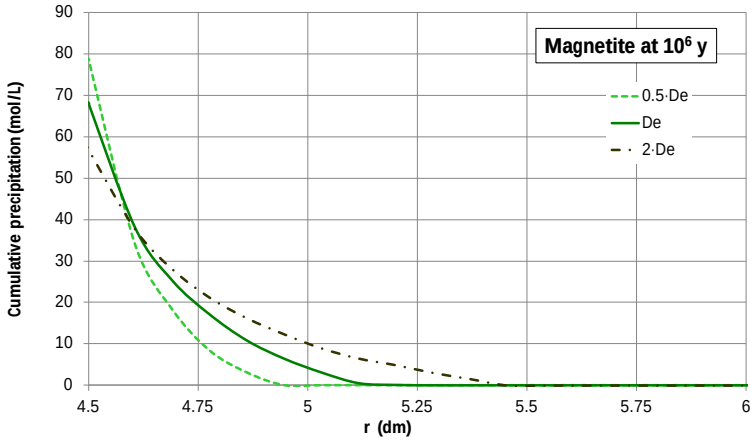

Fig. 6.31 Sensitivity of the spatial distribution of the concentration of cumulative precipitated magnetite in the bentonite at t = 106 years to changes in the De of the bentonite. r is the radial distance to the axis of the disposal cell

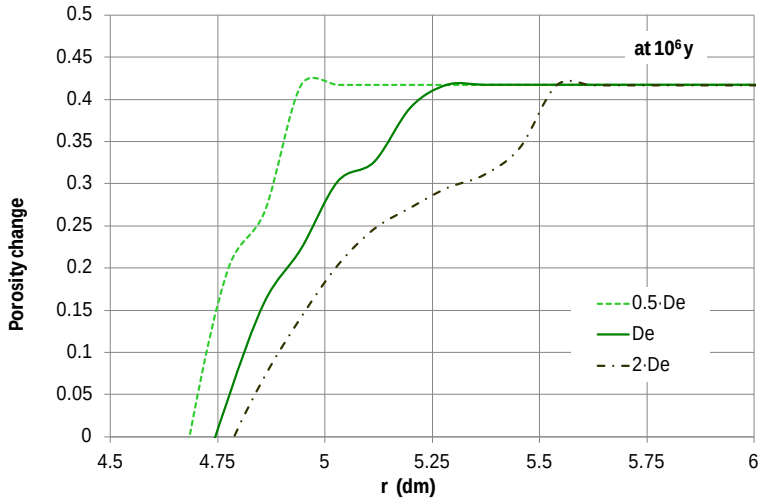

Fig. 6.32 Sensitivity of the spatial distribution of the changes in bentonite porosity at t = 106 years due to mineral dissolution and precipitation for several values of the De of the bentonite. r is the radial distance to the axis of the disposal cell

A flow rate of 0.01 L/y per canister is imposed at the outer element of the model to simulate the washing of the bentonite surface by groundwater water through the granite. This water flow could be larger than 0.01 L/year in areas where the rock is more

fractured. In fact, Samper *et al.* (2010) and Lu *et al.* (2012) used a value of 0.06 L/year. Several sensitivity runs were performed to evaluate the model uncertainties caused by uncertainties in the groundwater flow through the granite. The following groundwater flows (Q) were taken for the sensitivity runs: equal to 0.05 and 0.1 L/y.

The following are the main conclusions of the sensitivity analysis to the groundwater flow Q:

1. The computed concentrations of most dissolved species are very sensitive to the changes in the water flow Q because the solute flux from the bentonite into the granite is controlled mostly by the advective transport of the granite water flow. The larger the Q, the faster the decrease of the concentrations.

2. The computed pH is slightly sensitive to the change in Q after 400 years. The larger the Q the larger the pH from 400 to 6·104 years. After 6·104 years, the computed pH is largest for the smallest groundwater flow. The relevance of the observed pH front related to the competition of Fe2+ and H+ for sorption sites decreases when Q increases.

3. The computed Eh is not sensitive to changes in Q before 6·104 years. After, the larger Q the larger the Eh.

4. The concentration of precipitated magnetite in the bentonite is strongly sensitive to the increase in the groundwater flow, Q. The larger the Q, the lower the concentration of precipitated magnetite close to the canister and the lower the thickness of the zone where magnetite precipitates (Fig. 6.33).

5. The concentration of precipitated siderite is very sensitive to Q. The larger the Q, the larger the precipitation of siderite and the lower the thickness of the zone where siderite precipitates.

6. The concentration of precipitated calcite near the canister/bentonite interface is very sensitive to the changes in groundwater flow, Q. The larger the Q, the lower the zone where calcite precipitates.

7. The concentration of the exchanged Fe^{2+} is slightly sensitive to Q after $t = 4 \cdot 10^3$ years. Opposite, the rest of exchange cations are not sensitive to changes in Q.

8. Sorption fronts are less pronounced when the groundwater flow increases.

9. The larger the groundwater flow Q, the lower the zone affected by the pore clogging (Fig. 6.34).

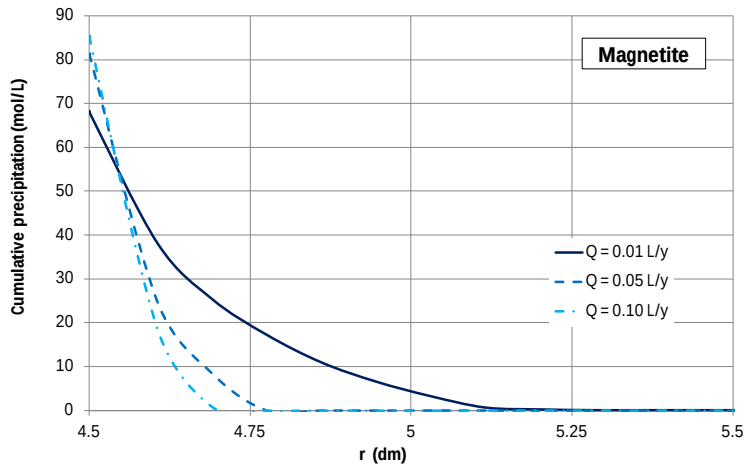

Fig. 6.33 Sensitivity of the spatial distribution of computed concentration of cumulative precipitated magnetite in the bentonite at t = 106 years to changes in the groundwater flow, Q(L/year)

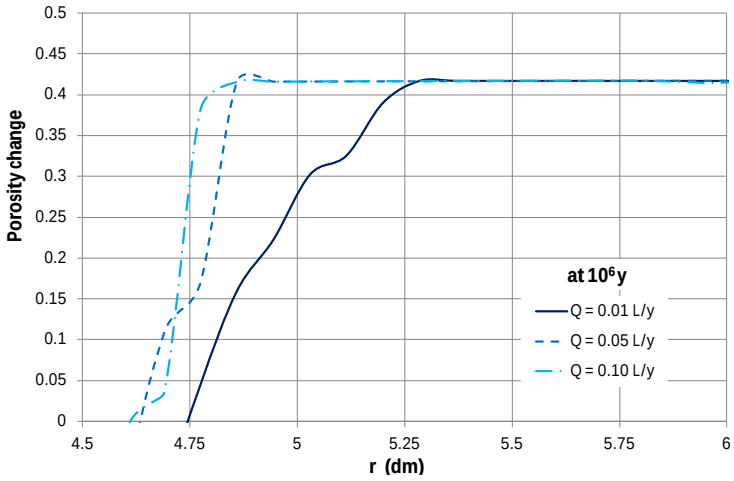

Fig. 6.34 Spatial distribution of the changes in bentonite porosity at t = 106 years due to mineral dissolution/precipitation for several values of the groundwater flow, Q (L/year). r is the radial distance to the axis of the disposal cell

The Deliverable 3.5.3 of the PEBS Project (Samper *et al.* 2013) presents more details of these sensitivities.

Cation selectivity coefficients for exchanged Ca^{2+}, Mg^{2+} and K^{+} in the model were derived from Samper *et al.* (2008a). The selectivity coefficient for exchanged iron was

taken from Tournassat (2003). Cation selectivities were calibrated in order to reproduce the reported concentrations of exchanged cations for the FEBEX bentonite by Fernández *et al.* (2004) and Enresa (2004). The changes in the selectivities affect strongly the concentrations of the exchanged Ca^{2+} and Mg^{2+}. Computed pH, Eh, concentration of dissolved species and mineral precipitation lack sensitivity to the selectivities.

The conceptual model assumes that the bentonite is initially water-saturated and granite porewater will transport away the solutes at the bentonite/granite interface. The initial chemical composition of the bentonite porewater and the composition of the boundary granite porewater were taken from Samper *et al.* (2008a; 2011) and Samper *et al.* (2007). Given the difficulties of deriving reliable data on saturated bentonite porewater chemistry, a sensitivity run was performed by changing the chemical compositions of the initial bentonite porewater and the granitic boundary. These compositions were derived by Samper *et al.* (2005) from a squeezing experiment and were previously used by Samper *et al.* (2008b). The main conclusions of the sensitivity analysis to the change in the chemical compositions of the bentonite porewater are:

1. The initial concentration of Cl^- in the sensitivity run is lower than that in the base run and therefore, the computed Cl^- concentration in the sensitivity run is lower and decreases slower than in the base run.

2. The initial concentration of dissolved Fe2+ is lower than that of the base run and the computed Fe2+ concentration for the sensitivity run remains significantly lower along all the simulation.

3. The initial pH in the sensitivity run is larger than that of the base run. The computed pH for the sensitivity run is generally larger than of the base run too.

4. Magnetite remains the main corrosion product in the bentonite for the sensitivity run. The computed concentration of magnetite in the sensitivity run near the canister/bentonite interface is much larger than that in the base run while the thickness of the zone where magnetite penetrates (≈ 2.5 cm) is half of that computed for the base run (Fig. 6.35).

5. Siderite precipitation in the sensitivity run starts much later than in the base run. The thickness of the zone of siderite precipitation in the sensitivity run is always lower than 4 cm, half of that of the base run. All the precipitated siderite is subsequently dissolved, no siderite remains in the bentonite at the end of the simulation.

6. The concentration of sorbed Fe^{2+} and the thickness of the zone of sorption fronts in the sensitivity run are much lower than those of the base run.

7. The thickness of the bentonite zone affected by pore clogging in the sensitivity run with the modified chemical composition is lower than that of the base run (Fig. 6.36).

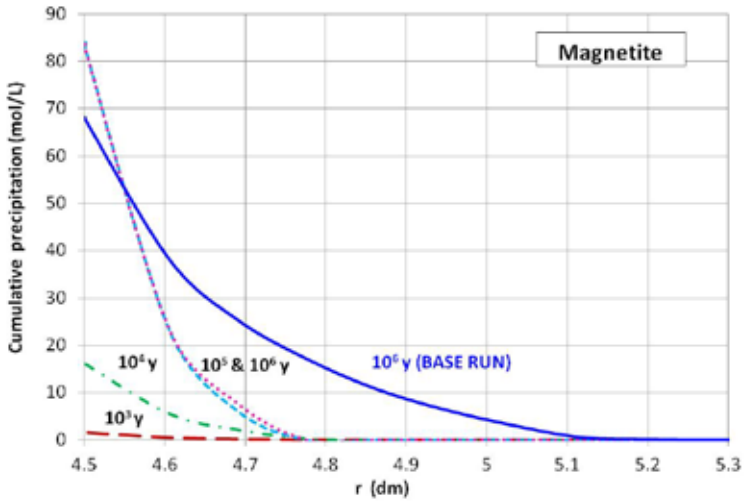

Fig. 6.35 Spatial distribution of the computed concentration of precipitated magnetite in the bentonite at t = 106 years for the base run and at selected times for the sensitivity run in which the chemical compositions of the bentonite and granite porewaters are changed

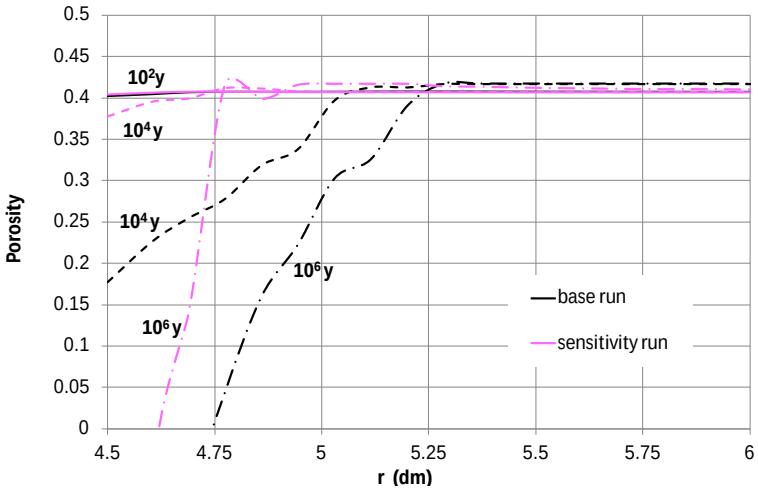

Fig. 6.36 Spatial distribution of the change in porosity caused by mineral dissolution/precipitation at selected times for the base run and the sensitivity run in which the chemical compositions of the bentonite and granite porewaters are changed

More details can be found in the Deliverable 3.5.3 of the PEBS Project (Samper *et al.* 2013).

6.1.8.2 Uncertainties in the conceptual model

Influence of the thermal transient

The reference scenario assumes that the thermal pulse has dissipated already at the beginning of the simulation. Therefore, all chemical reactions were modelled at a constant temperature of 25ºC. However, the thermal gradients across the EBS may last for thousands of years and therefore could influence the geochemical evolution of the bentonite.

Long-term simulations have been performed for a variant scenario similar to the reference scenario, but accounting for the thermal field across the bentonite barrier. The thermal transient stage is taken into account by solving for the heat transport through the bentonite buffer. The computed temperatures were used to update the temperature-dependent chemical parameters such as equilibrium constants and the activity coefficients. The impact on long-term predictions of accounting for/neglecting the thermal transient was evaluated by comparing the results of both scenarios.

The time evolution of temperature was prescribed at the canister/bentonite interface according to thermal simulations of Enresa (2001). The temperature at the canister surface increases up to 97 ºC after 24 years and then decreases smoothly. The temperature at the canister/bentonite interface gets to 30 ºC after 1 Ma. The granitic boundary porewater is considered at a constant temperature of 30 ºC.

The thermal aquifer parameters were taken from Enresa (2001). The specific heat capacity is of 846 J/kg ºC and 480 J/kg ºC for the bentonite and the canister, respectively. The saturated thermal conductivity is of 1.15 W/mol ºC in bentonite and 50 W/mol ºC in the steel canister.

Figure 6.37 presents the time evolution of prescribed temperature at the canister/bentonite interface and computed temperature at three different locations within the bentonite. The temperature gradients dissipate progressively and computed temperature becomes nearly uniform throughout the bentonite barrier after $5 \cdot 10^3$ years.

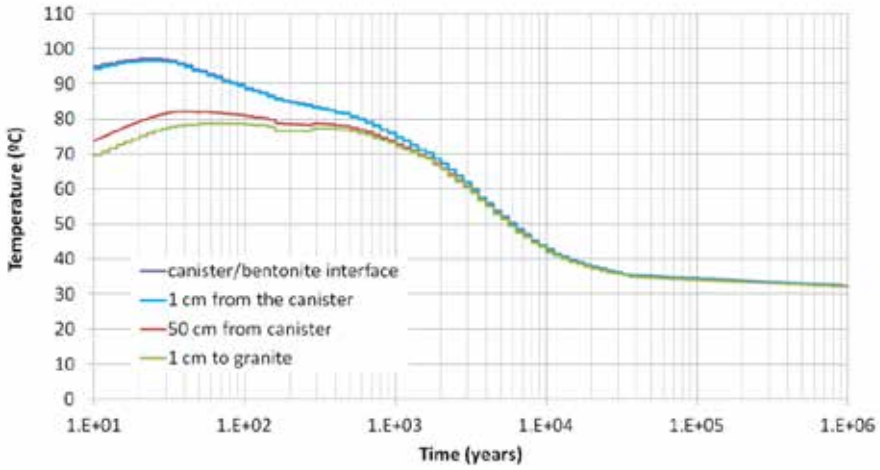

Fig. 6.37 Time evolution of the computed temperature at the canister/bentonite interface and in the bentonite at 1 cm from the canister, 50 cm from the canister and 1 cm to the granite for the sensitivity run which accounts for the thermal transient.

This sensitivity run does not account for changes in the corrosion rate related to temperature. Therefore, canister corrosion is the same as that of the reference model.

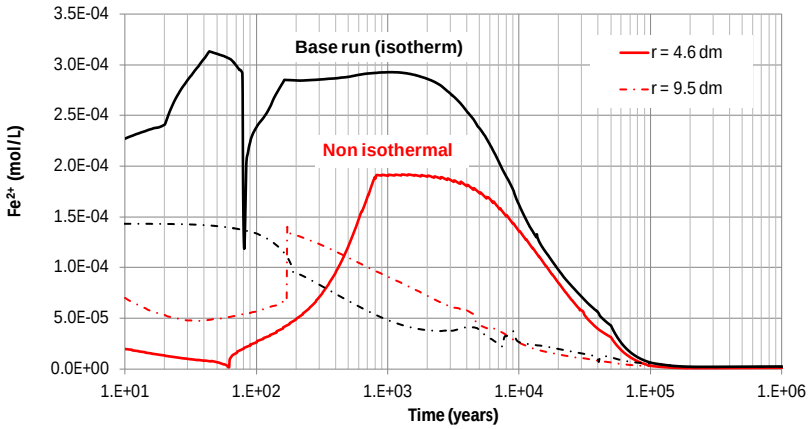

Fig. 6.38 Time evolution of the computed concentrations of dissolved Fe2+ in the bentonite at r = 4.6 and 9.5 dm for the base run (isothermal) and the sensitivity run which accounts for the thermal transient.

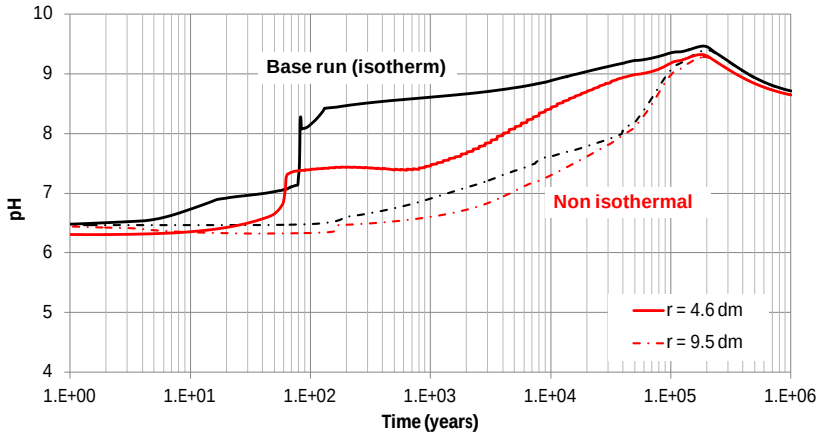

Fig. 6.39 Time evolution of the computed pH in the bentonite at r = 4.6 and 9.5 dm for the base run (isothermal) and the sensitivity run which accounts for the thermal transient.

The computed concentration of dissolved Fe^{2+} and the pH for the non-isothermal run are significantly lower than those of the isothermal simulation for t < 10^5 years (Fig. 6.38 and Fig. 6.39, respectively).

The fronts of dissolved Fe^{2+}, pH and Eh related to sorption fronts are similar to those of the isothermal simulation, although they take place before. The first sorption front takes place at r = 4.6 dm after 60 years with the deprotonation of the weak 1 and weak 2 sorption sites (Fig. 6.40). The sorption front migrates through the bentonite while it gets smother. It reaches r = 9.5 dm at ~ 150 years (Fig. 6.41). A front can be observed at the same times and locations for the dissolved Fe^{2+} concentration (Fig. 6.38), pH (Fig. 6.39) and Eh. The second sorption front takes place similar to that observed in the reference scenario simulation and at the same position between 10^3 and $5 \cdot 10^4$ years (Fig. 6.42). Again, simultaneous fronts are observed at the same location for dissolved Fe^{2+} concentration, pH (Fig. 6.43) and Eh.

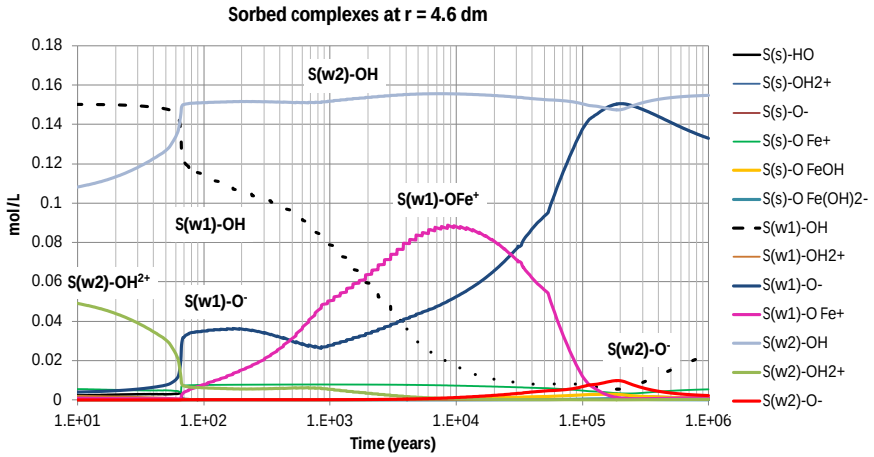

Fig. 6.40 Time evolution of the computed concentrations of the sorbed species in the bentonite at r = 4.6 dm for the sensitivity run which accounts for the thermal transient. The first sorption front can be observed at t = 60 y

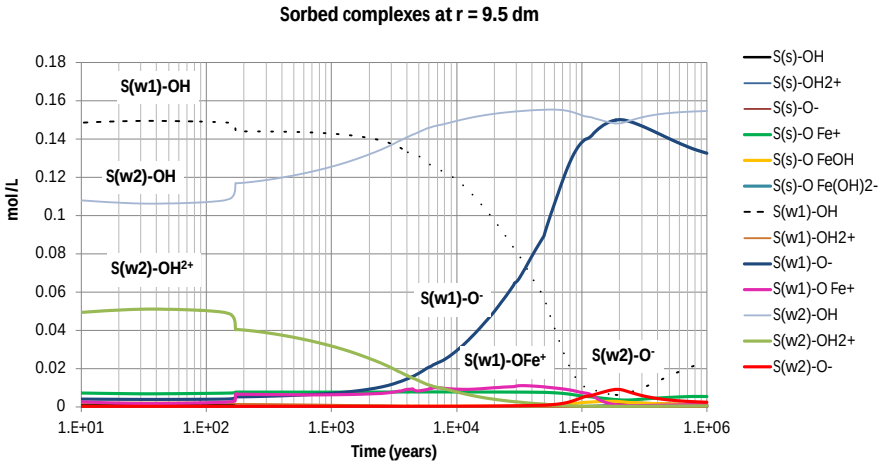

Fig. 6.41 Time evolution of the computed concentrations of the sorbed species in the bentonite at r = 9.5 dm for the sensitivity run which accounts for the thermal transient. The first sorption front reaches r = 9.5 dm at t = 150 y

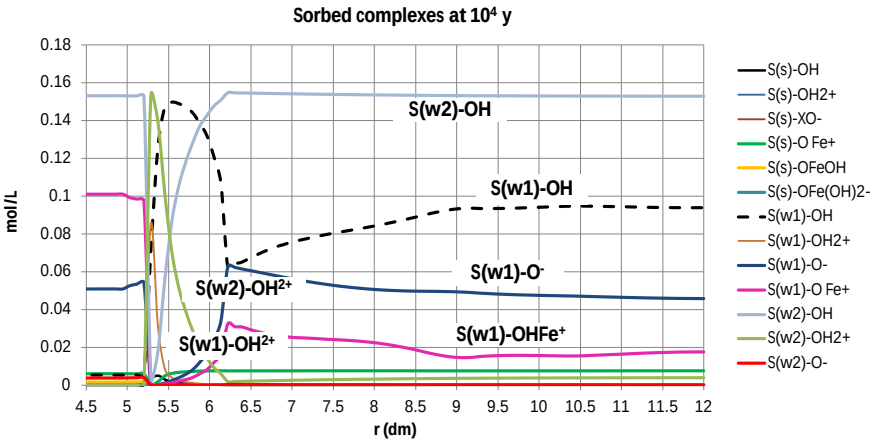

Fig. 6.42 Spatial distribution of the computed concentrations of the sorbed species in the bentonite at 104 years for the sensitivity run which accounts for the thermal transient. r is the radial distance to the axis of the disposal cell. The second sorption front can be clearly observed between r = 5 and r = 6 dm

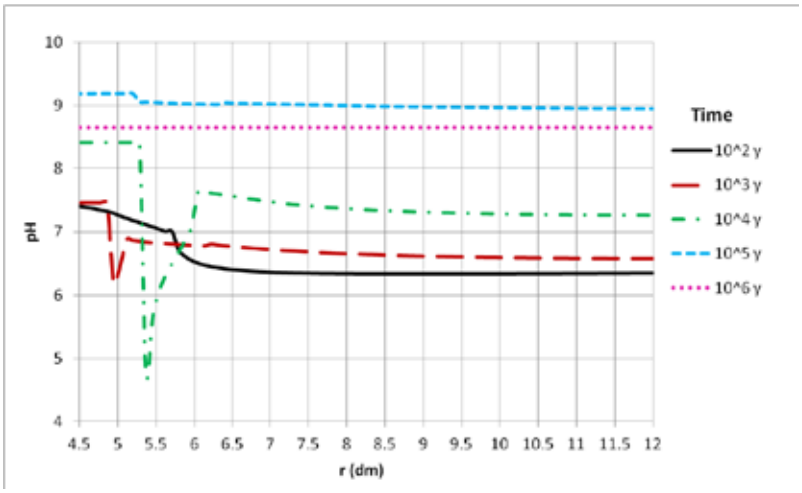

Fig. 6.43 Spatial distribution of the computed pH in the bentonite at selected times in which a pH front can be observed at t = 103 and t = 10 years for the sensitivity run which accounts for the thermal transient

The long-term geochemical evolution of conservative species is not very sensitive to the thermal transient stage. Only small changes are observed in other dissolved species related to changes in the precipitation of calcite, siderite and quartz.

Most of the released Fe^{2+} precipitates as magnetite after diffusing from the canister into the bentonite. Magnetite precipitation at t = 1 Ma is almost the same as that in the iso-

thermal reference model (Fig. 6.44). Cumulative precipitated siderite concentration in the non-isothermal run is slightly lower and its penetration is larger than those of the isothermal case at $t < 10^5$ years. At $t \geq 10^5$ years, the non-isothermal simulation predicts siderite precipitation slightly lower in the first 5 cm and slightly larger for $5 < r < 8$ cm than that of the isothermal case (Fig. 6.45). The thickness of the bentonite zone where corrosion products precipitate does not change when the thermal field is taken into account.

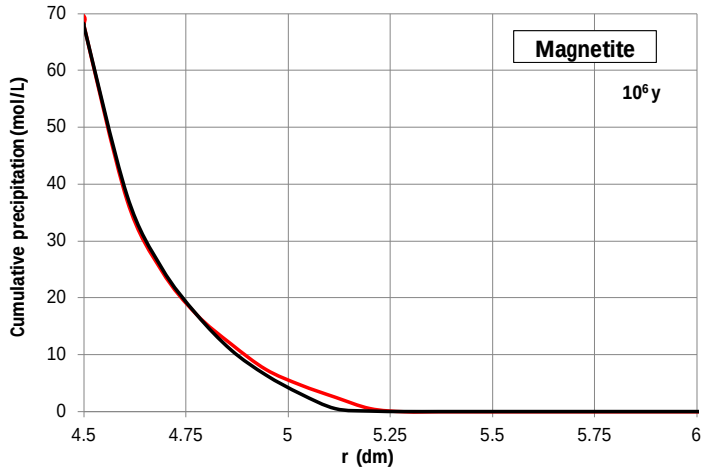

Fig. 6.44 Spatial distribution of the computed concentration of cumulative precipitated magnetite in the bentonite at t = 1 Ma for the base run (isothermal) and the sensitivity run which accounts for the thermal transient

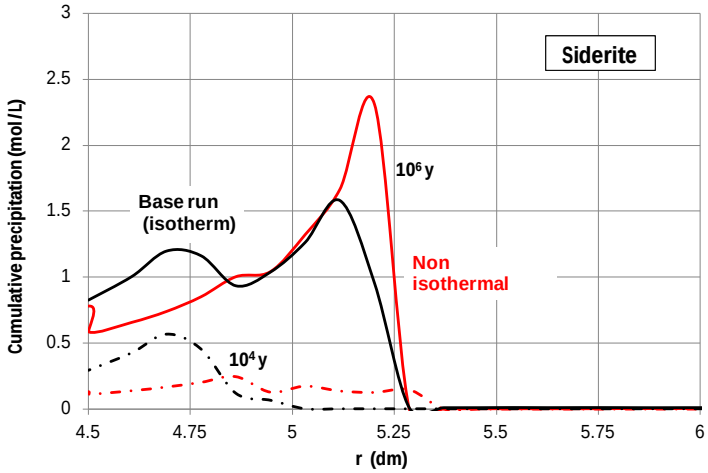

Fig. 6.45 Spatial distribution of the computed concentration of cumulative precipitated siderite in the bentonite at t = 1 Ma for the base run (isothermal) and the sensitivity run which accounts for the thermal transient

The changes in the dissolution/precipitation of calcite when the thermal gradient is considered are similar to those of siderite. On the other hand, silica dissolves near the canister/bentonite interface when the temperature increases (Fig. 6.46).

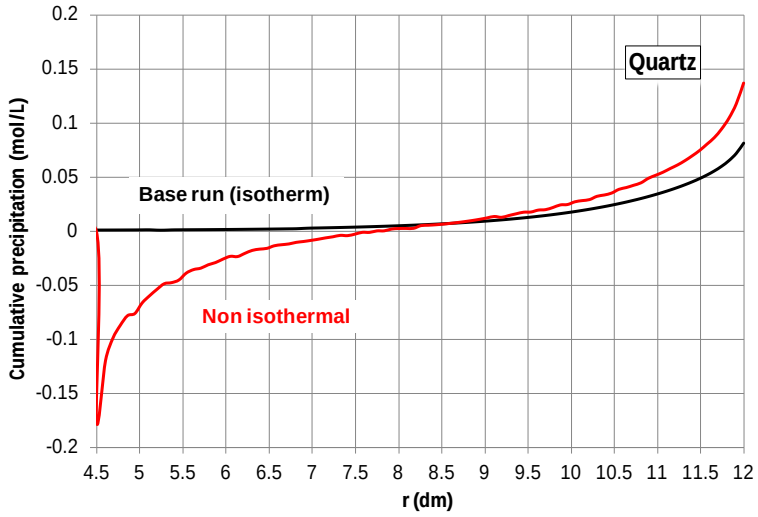

Fig. 6.46 Spatial distribution of the computed concentration of cumulative precipitated/dissolved silica in the bentonite at 1 Ma for the base run (isothermal) and the sensitivity run which accounts for the thermal transient

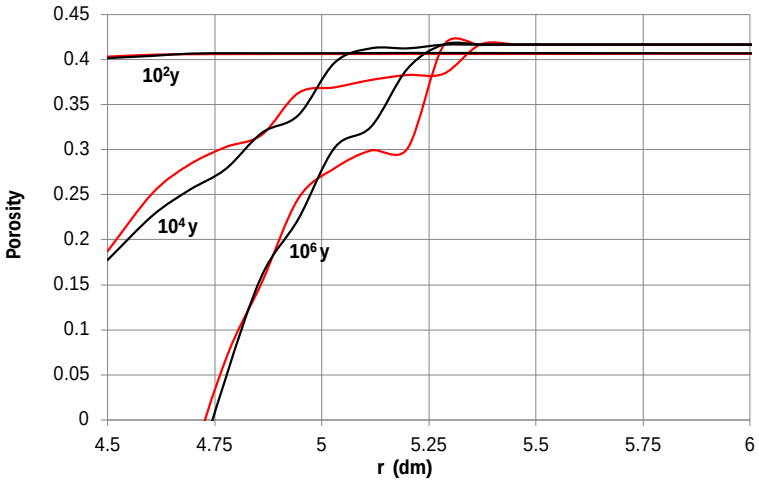

Fig. 6.47 Spatial distribution of the changes in bentonite porosity at selected times due to mineral dissolution/precipitation for the base run (isothermal) and the sensitivity run which accounts for the thermal transient

Finally, Fig. 6.47 presents the spatial distribution of the changes in bentonite porosity at selected times which changes due to mineral dissolution/precipitation for the reference isothermal scenario and for the sensitivity run which accounts for the thermal transient. The reduction of the porosity is slightly larger for r > 5 cm and the thickness of the ben-

tonite affected by a decrease of porosity increases 1 cm (up to 7-8 cm) when the thermal gradient is considered.

Dependence of the corrosion rate on temperature

The dependence of the corrosion rate on temperature has been analyzed by performing a sensitivity run which accounts for the thermal transient and also for the temperature dependence of the corrosion rate.

Carbon-steel corrosion is modelled by using a kinetic formulation in a manner similar to mineral dissolution. The canister is treated as a porous medium made of 100% metallic iron, Fe(s), which dissolves according the kinetic law of Eq. 6.6. The parameter η of the kinetic law is considered null and, therefore, the dissolution/precipitation rate, r_m (in mol/m^2/s), is equal to the kinetic rate constant, k_m (in mol/m^2/s). The corrosion rate, r_c (in μm/year) is directly related to r_m according to Eq. 6.12. The reference scenario considers a constant corrosion rate, r_c, equal to 2 μm/year.

Feron *et al.* (2008) reported the study of the kinetics of corrosion under oxic and anoxic conditions and considering the temperature dependence of corrosion according to an Arrenhius equation. They proposed the following expression:

$$r_m = k_{m(25ºC)} \cdot e^{-Ea/RT} \qquad (6.15)$$

where $k_{m\ 25ºC}$ is the kinetic rate constant at 25 ºC; *Ea* is the activation energy which is assumed equal to 11 KJ/mol (Feron *et al.,* 2008), *R* is the gas constant and *T* is the temperature measured in ºK.

The model results of the sensitivity run which accounts for the thermal field and the influence of temperature on corrosion show that the corrosion rate increases from 2 to 4.75 μm/y and then smoothly decreases (Fig. 6.48). After $1.3 \cdot 10^4$ years, the corrosion rate is lower than 2.5 μm/y. Therefore, canister corrosion in this run is faster than in the reference scenario. In this case, the canister is fully corroded after $4 \cdot 10^4$ years (instead of $5 \cdot 10^4$ years).

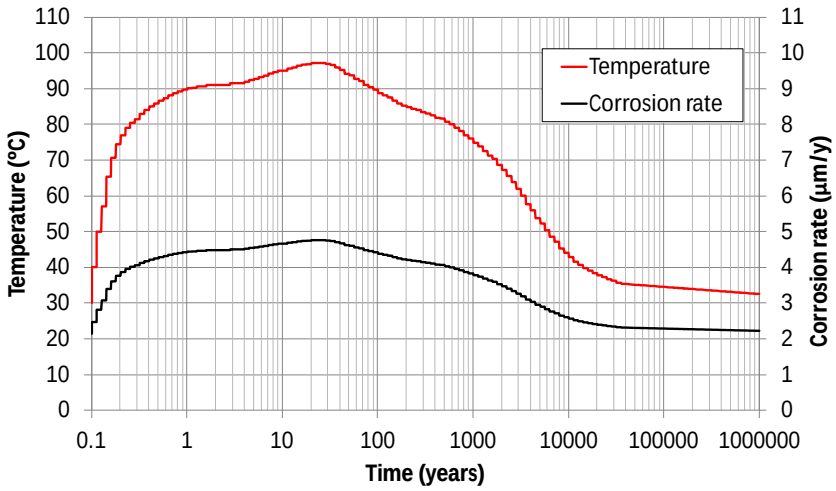

Fig. 6.48 Time evolution of the computed temperature at the canister/bentonite interface and the corrosion rate for the sensitivity run which accounts for the thermal transient and the dependence of the corrosion rate on temperature

The computed concentration of dissolved Fe^{2+} and the pH in this sensitivity run increase initially faster than those of the constant corrosion rate run (Fig. 6.49 and Fig. 6.50). They coincide after 10^3 years. The fronts of the dissolved Fe^{2+}, pH and Eh, related to sorption fronts, are observed similar to those of the reference scenario and the scenario accounting for the thermal transient and a constant kinetic rate. However, they take place sooner than those for a constant corrosion rate.

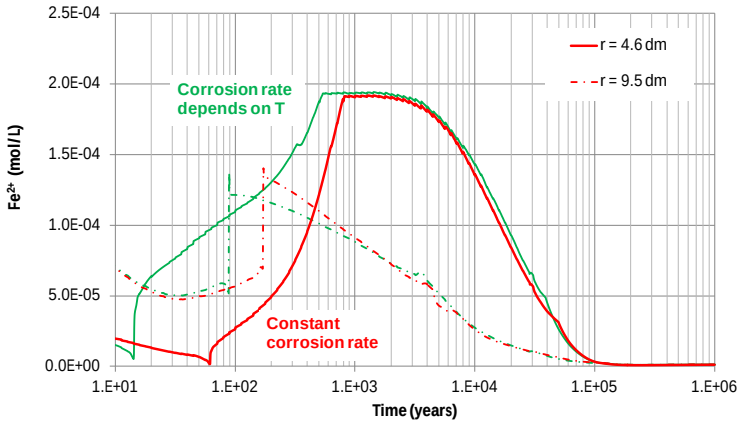

Fig. 6.49 Time evolution of the computed concentrations of dissolved Fe2+ in the bentonite at r = 4.6 and 9.5 dm for the sensitivity runs which account for the thermal transient and a corrosion rate constant or dependent on temperature

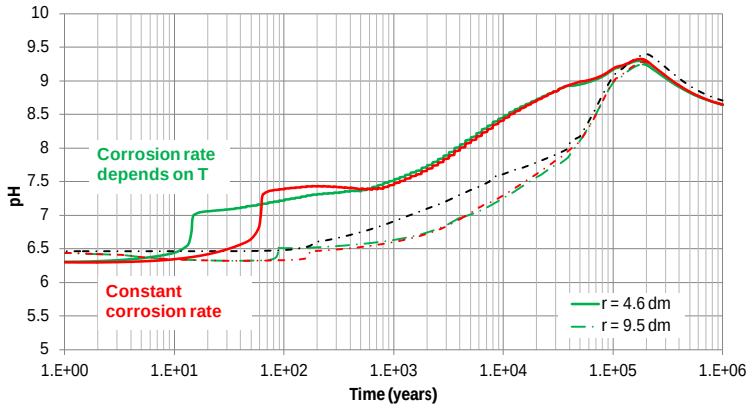

Fig. 6.50 Time evolution of the computed pH in the bentonite at r = 4.6 and 9.5 dm for the sensitivity runs which account for the thermal transient and a corrosion rate constant or dependent on temperature

The precipitation of corrosion products occurs before and their penetration is lower in this sensitivity run than in the reference scenario. Magnetite is the main corrosion product. Magnetite precipitation at 1 Ma is slightly lower than that of the isothermal reference scenario and the non-isothermal scenario which accounts for a constant corrosion rate (Fig. 6.51). The penetration of magnetite into bentonite is of 6 cm. Siderite precipitation is in the range of the other two scenarios. The penetration of siderite into bentonite reaches the 7 cm during the simulation but it is of 6 cm after 1 Ma (Fig. 6.52).

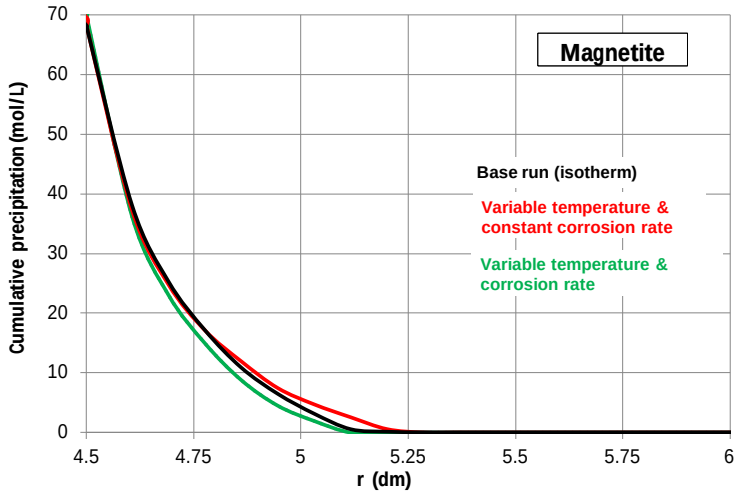

Fig. 6.51 Spatial distribution of the computed concentration of cumulative precipitated magnetite in the bentonite at 1 Ma for the isothermal reference scenario and for the sensitivity runs which account for the thermal transient and a corrosion rate constant or dependent on temperature

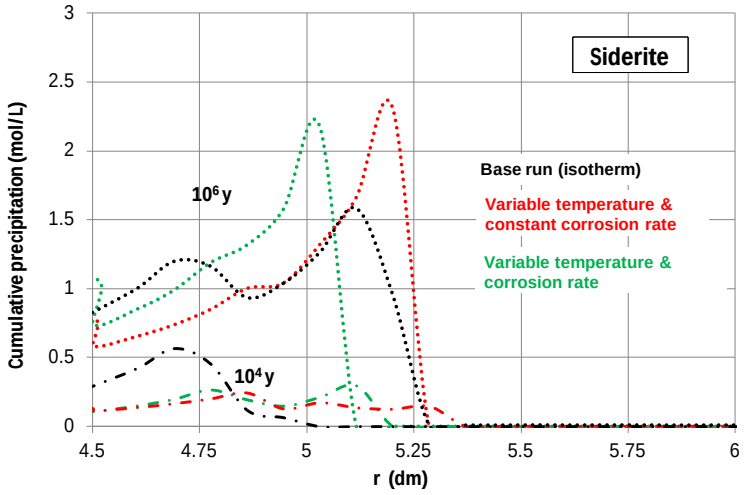

Fig. 6.52 Spatial distribution of the computed concentration of cumulative precipitated siderite in the bentonite at 1 Ma for the isothermal reference scenario and for the sensitivity runs which account for the thermal transient and a corrosion rate constant or dependent on temperature

The decrease of porosity is faster near the canister than those of the isothermal and non-isothermal sensitivity runs which account for a constant corrosion rate (Fig. 6.53). The thickness of the bentonite affected by a decrease of porosity reaches 7 cm after 10^4 years and is of 6 cm after 1 Ma.

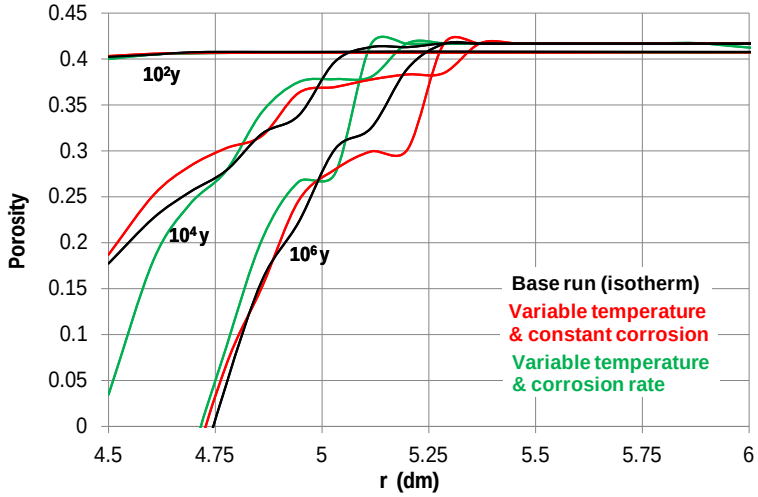

Fig. 6.53 Spatial distribution of the changes in bentonite porosity at selected times due to mineral dissolution/precipitation for the isothermal reference scenario and for the sensitivity runs which account for the thermal transient and a corrosion rate constant or dependent on temperature

Finally, the partial pressure of $H_2(g)$ increases faster and reaches larger values than those of the isothermal and non-isothermal sensitivity runs accounting for a constant corrosion rate due to the increase of the corrosion rate (Fig. 6.54).

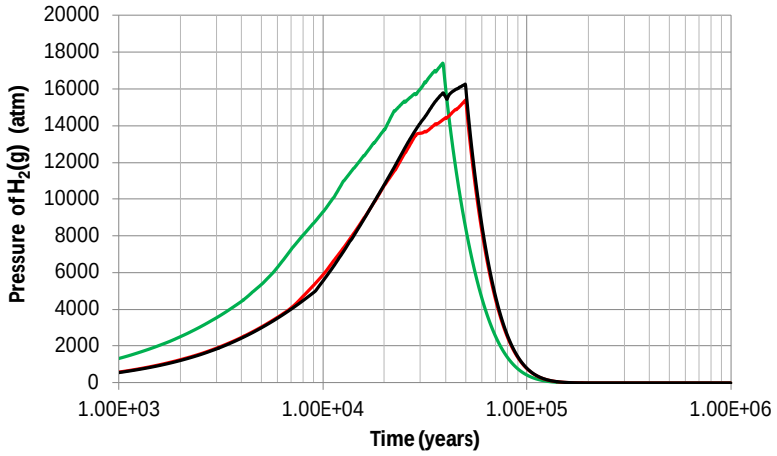

Fig. 6.54 Time evolution of the hydrogen partial pressure in the bentonite for the isothermal reference scenario and for the sensitivity runs which account for the thermal transient and a corrosion rate constant or dependent on temperature

In summary, accounting for the dependence of the corrosion rate on temperature does not lead to significant changes of the long term geochemical evolution of the bentonite.

Dependence of the corrosion rate on the chemical conditions

The dependence of the corrosion rate on the chemical conditions (pH, Eh, Fe concentration) has been analyzed by performing an isothermal sensitivity run similar to that of the reference scenario but accounting for a variable corrosion rate.

Similar to the reference scenario, carbon-steel corrosion is modelled by using a kinetic formulation. However, the parameters η and θ of the kinetic law are considered equal to 1 in this case. In this way, the corrosion rate is not constant. The dissolution/precipitation rate, r_m (in mol/m^2/s), depends on the Ω_m, which is the ratio between the ion activity product and the equilibrium constant for Fe(s) dissolution and, therefore, depends on the pH, the Eh and the dissolved Fe^{2+} concentration according to:

$$r_m = k_m(W_m - 1) \qquad (6.16)$$

Model results show that canister corrosion slows down after 10^3 years and the canister is fully corroded after nearly $8 \cdot 10^5$ years (Fig. 6.55). This change leads to important change in patterns of Fe^{2+} concentration, pH, Eh, sorption and mineral dissolution/precipitation after 10^3 years.

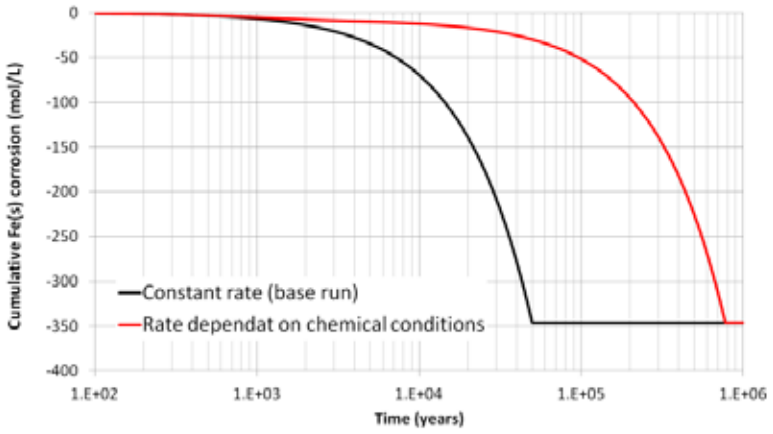

Fig. 6.55 Comparison of the time evolution of the Fe(s) corrosion computed with the reference scenario (constant corrosion rate) and the sensitivity run with a corrosion rate dependent on chemical conditions

The computed concentrations of dissolved Fe^{2+} after 10^3 years are slightly sensitive to the variation of the corrosion rate related to the chemical conditions (Fig. 6.56).

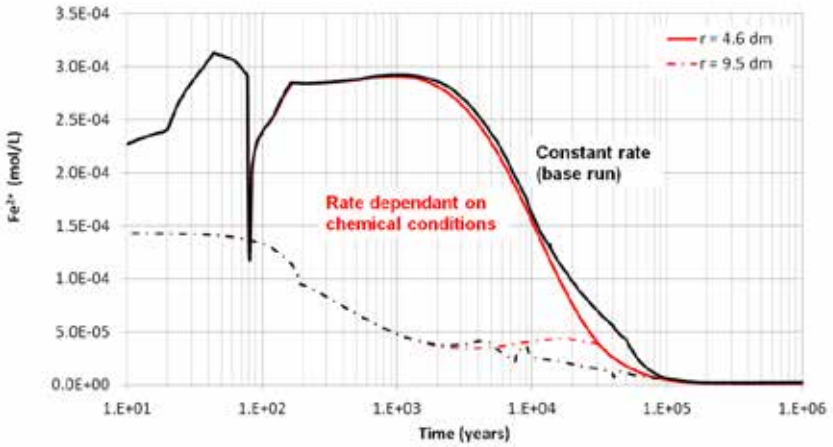

Fig. 6.56 Time evolution of dissolved Fe2+ in the bentonite at r = 4.6 and 9.5 cm computed with the reference scenario and the sensitivity run with a corrosion rate dependent on the chemical conditions

The pH computed with the reference scenario and the sensitivity run show differences after 10^3 years (Fig. 6.57). The pH computed for the sensitivity run keeps increasing after $2 \cdot 10^5$ years and reaches a maximum pH larger than 10 after $8 \cdot 10^5$.

The sorption fronts caused by the competition of Fe^{2+} and H^+ for sorption sites and the associated fronts of dissolved Fe^{2+}, pH and Eh in the sensitivity run take place at the same positions and times as the base model run. However, the second sorption front of the base run and the associated fronts of dissolved Fe^{2+}, pH and Eh do not take place in the sensitivity run because the canister corrosion slows down (Fig. 6.58).

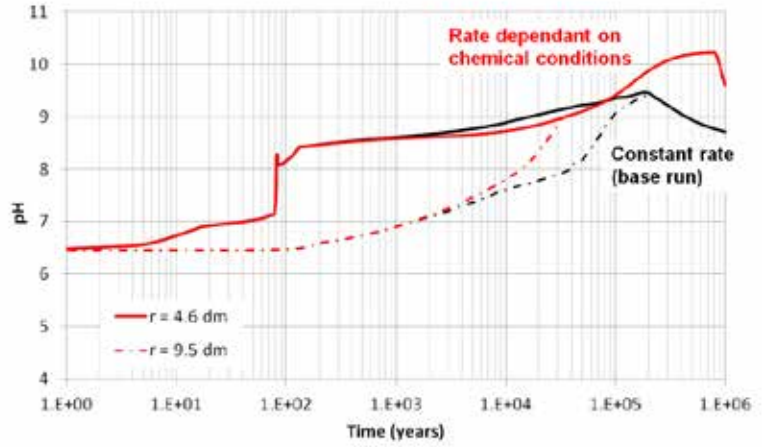

Fig. 6.57 Time evolution of the pH in the bentonite at r = 4.6 and 9.5 cm computed with the reference scenario and the sensitivity run with a corrosion rate dependent on the chemical conditions

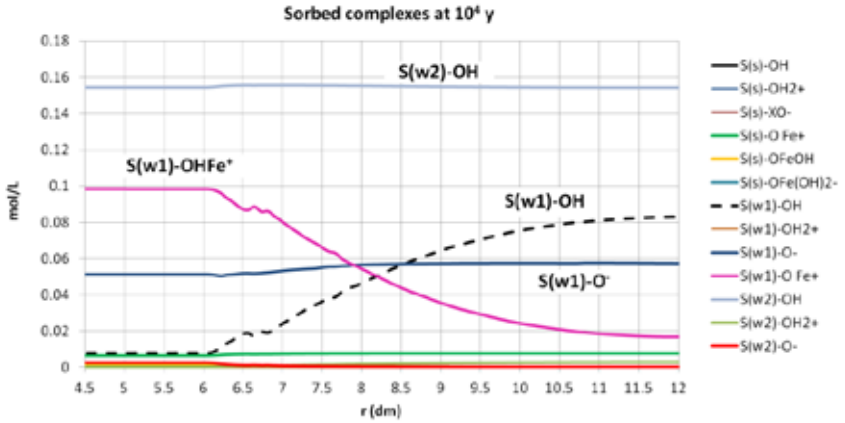

Fig. 6.58 Spatial distribution of the concentrations of the sorbed species in the bentonite at 10^4 years computed with the reference scenario and the sensitivity run with a corrosion rate dependent on the chemical conditions

The precipitation of the corrosion products is significantly sensitive to the dependence of the corrosion rate on the chemical conditions. Magnetite and siderite precipitation in the sensitivity run at 10^4 years is significantly lower than that of the reference scenario. After 1 Ma, magnetite and siderite precipitation is significantly lower than that of the reference scenario near the canister, but it takes place in the entire bentonite buffer showing small concentrations (Fig. 6.59 and Fig. 6.60).

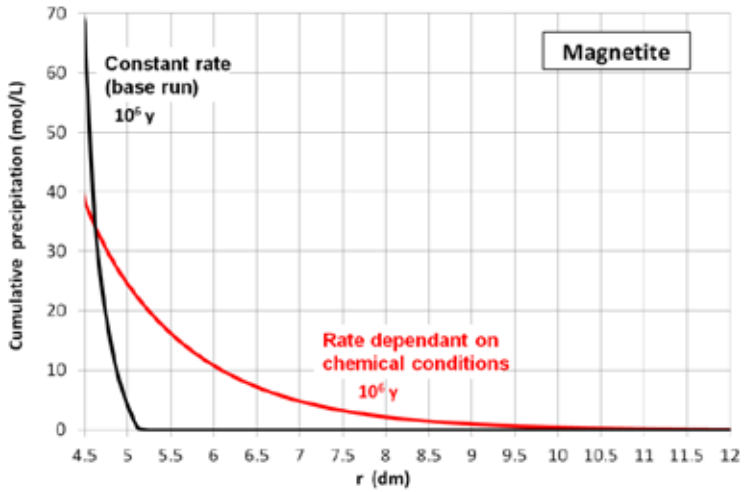

Fig. 6.59 Spatial distribution of the concentration of cumulative precipitated magnetite in the bentonite at t = 1 Ma computed with the reference scenario and the sensitivity run with a corrosion rate dependent on the chemical conditions

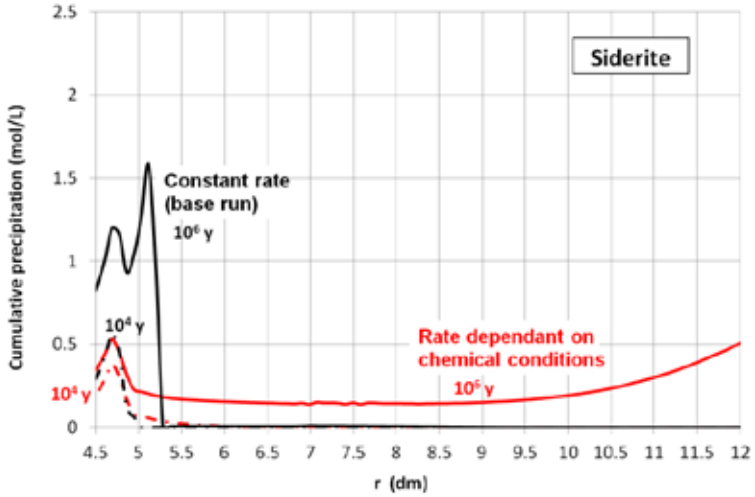

Fig. 6.60 Spatial distribution of the concentration of cumulative precipitated siderite in the bentonite at t = 1 Ma computed with the reference scenario and the sensitivity run with a corrosion rate dependent on the chemical conditions

Figure 6.61 presents the spatial distribution of the changes in bentonite porosity at selected times due to mineral dissolution/precipitation for the reference scenario and the sensitivity run which accounts for the dependence of the corrosion rate on the chemical conditions. The reduction of the porosity affects a thickness of bentonite of about 45 cm. However, the thickness of bentonite significantly altered (50% of reduction) is of 14 cm.

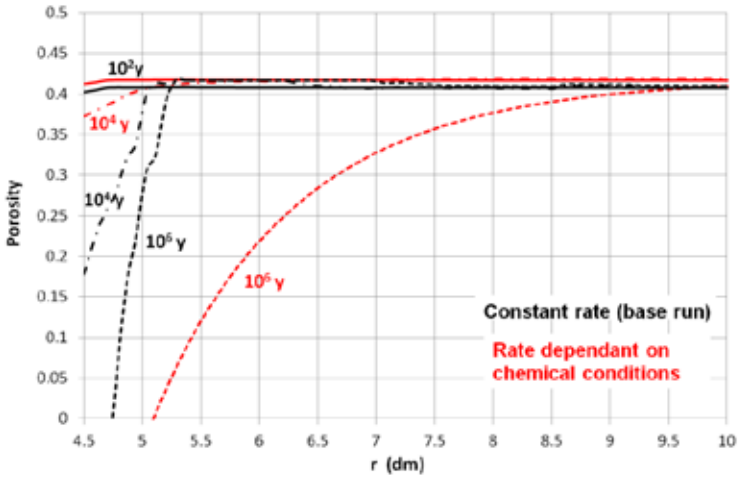

Fig. 6.61 Spatial distribution of the bentonite porosity at selected times which changes due to mineral dissolution/precipitation for the reference scenario and the sensitivity which accounts for the dependence of the corrosion rate on the chemical conditions

Finally, the reduction of the corrosion rate leads to small $H_2(g)$ pressures because dissolved hydrogen can diffuse at a rate similar to its generation after 10^3 years (Fig. 6.62).

It can be concluded that the dependence of the corrosion rate on the chemical conditions (pH, Eh, Fe concentration) leads to significant changes in the long-term geochemical evolution of the repository. The thickness of the bentonite zone affected by the corrosion products is larger than that for the reference scenario.

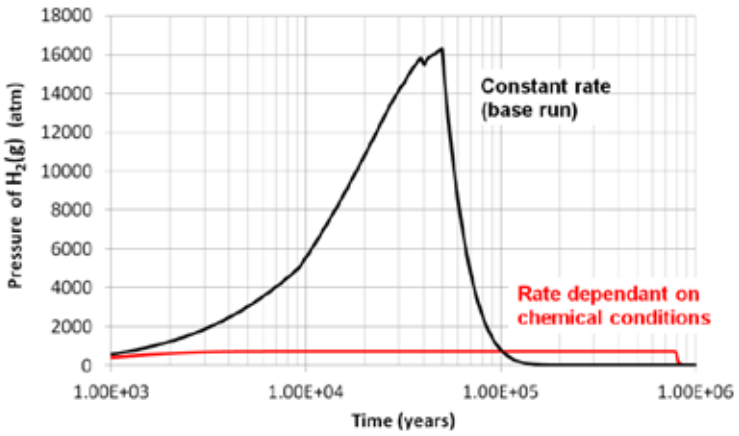

Fig. 6.62 Time evolution of the hydrogen partial pressure in the bentonite for the reference scenario and the sensitivity run which accounts for the dependence of the corrosion rate on the chemical conditions

Accounting for kinetically controlled magnetite precipitation

The THC model results of the laboratory corrosion tests indicate that the migration of corrosion products should be modelled by using a kinetically-controlled magnetite precipitation rate (Samper *et al.*, 2012; 2014). The reference scenario assumes that magnetite precipitation takes place at equilibrium. The uncertainty caused by this assumption is evaluated by performing simulations of the long-term geochemical evolution of the buffer which accounts for kinetic-controlled magnetite precipitation.

The magnetite is assumed to precipitate according to the following kinetic law proposed by De Windt and Torres (2009)

$$r_m = k_m (W_m^{\theta.1} - 1) \qquad (6.17)$$

with exponents θ = 0.1 and μ = 1. The reactive surface area, σ, has been calibrated with data of the corrosion laboratory experiments performed in the framework of the PEBS project. A value of 100 m^2/L has been derived.

Convergence problems were found in the long-term simulation of this scenario for a reactive surface of 100 m^2/L. Model results were then obtained for the following reactive surface areas: σ = 1 and 10 m^2/L. Model results are very sensitive to changes in the magnetite reactive surface area.

Figure 6.63 shows computed cumulative precipitation of magnetite at 10^5 years for the reference scenario, which assumes magnetite at equilibrium, and the two sensitivity runs accounting for kinetically-controlled magnetite precipitation. The penetration of magnetite into the bentonite and, therefore, the zone of bentonite affected by porosity reduction decreases significantly when magnetite kinetics is considered. The larger the reactive surface area, the thinner the zone of bentonite affected by canister corrosion (Fig. 6.64).

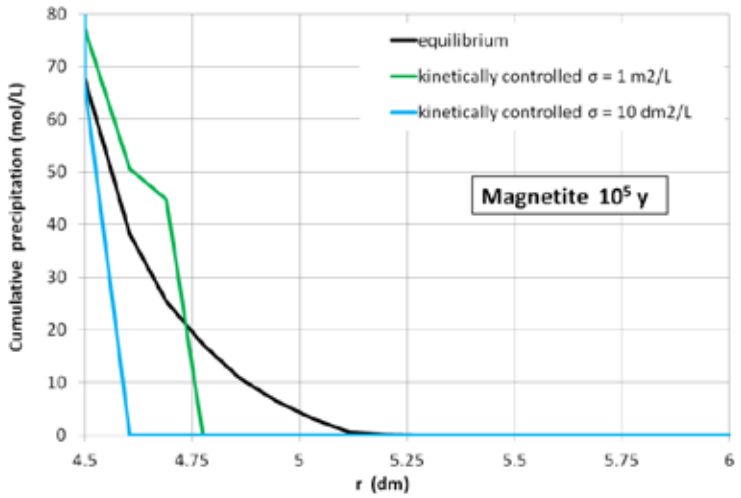

Fig. 6.63 Computed cumulative precipitation of magnetite at 105 years for the reference scenario (magnetite at equilibrium) and the two sensitivity runs accounting for kinetically-controlled magnetite precipitation

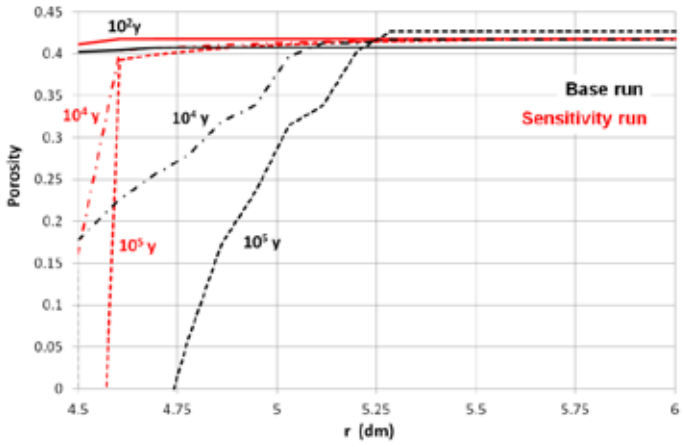

Fig. 6.64 Spatial distribution of the changes in bentonite porosity at selected times due to mineral dissolution/precipitation for the reference scenario (magnetite at equilibrium) the sensitivity run accounting for kinetically-controlled magnetite precipitation with σ = 10 m2/L

Accounting for smectite dissolution and neoformation of zeolites

Some geochemical reactions such as smectite dissolution are commonly disregarded in short to medium-term geochemical models (e.g. lab and in-situ tests) because they are considered not relevant in the short term. However, smectite dissolution could be relevant for the long-term geochemical evolution of the EBS. Savage *et al.* (2010) studied the potential contribution of the smectite hydrolysis to the long-term geochemical processes in a KBS-3 bentonite buffer. They concluded that smectite dissolution may be significant for the future geochemical state of a buffer, but the time-scale of this process is too long for experimental verification. They also suggested the importance of further studies through field observation of natural clay-water systems that have evolved over long time scales.

The long-term relevance of kinetically-controlled smectite dissolution and its influence on the thickness of altered bentonite was evaluated with a sensitivity run.

This sensitivity run requires accounting for silica and Al^{3+} aqueous complexes in the geochemical model. It was necessary to add Al^{3+} as a primary species. Its initial concentration in the bentonite and the granite porewater was taken equal to 10^{-8} mol/L and $1.85 \cdot 10^{-8}$ mol/L, respectively (Enresa, 2001). The primary species, $SiO_{2(aq)}$, was already considered in the reference model. Relevant silica and Al^{3+} aqueous complexes were identified from speciation runs performed for bentonite and granite porewaters with EQ3/6 (Wolery, 1992). The homogeneous chemical reactions added to the geochemical model and their equilibrium constants for aqueous complexes are listed in Tab. 6.6.

Tab. 6.6 Additional silica and Al3+ aqueous complexes added to the reference geochemical model and their equilibrium constants at 25 ºC (Wolery, 1992)

Reaction	Log K (25°C)
$Al(OH)_2^+ + 2H^+ \rightleftharpoons Al^{3+} + 2H_2O$	10.0991
$Al(OH)_{3(aq)} + 3H^+ \rightleftharpoons Al^{3+} + 3H_2O$	16.1577
$Al(OH)_4^- + 4H^+ \rightleftharpoons Al^{3+} + 4H_2O$	22.1477
$Al(OH)^{2+} + H^+ \rightleftharpoons Al^{3+} + H_2O$	5.0114
$NaH_3SiO_4(aq) + H^+ \rightleftharpoons Na^+ + SiO_2(aq) + 2H_2O$	8.6616
$H_6(H_2SiO_4)_4^{2-} + 2H^+ \rightleftharpoons 4SiO_2(aq) + 8H_2O$	13.4464

The initial volume fraction of smectite is assumed equal to the total mineral volume minus the volume occupied by quartz and calcite. It is equal 0.57. The chemical formulation of the FEBEX-montmorillonite experimentally derived by Fernández *et al.* (2009) is taken for smectite (see Tab. 6.7). The log K for smectite dissolution is equal to 6.26 at 25 ºC. Smectite dissolution is kinetically-controlled according to the kinetic law proposed by Rozalen *et al.* (2008):

$$r_m = 10^{-14.37} + 10^{-12.30}\left(H^+\right)^{0.40} + 10^{-13.05}\left(OH^-\right)^{0.27} \qquad (6.18)$$

were r_m is the dissolution/precipitation rate in mol/m^2/s which includes three terms. The first term is constant term. The second term depends on proton activity [H^+] while the third term depends on hydroxyl activity [OH^-]. Therefore, the dissolution rate depends on pH. On the other hand, the reactive surface area is considered equal to 1 m^2/L and the molar volume is equal to 134.88 cm^3/mol (Fernández *et al.*, 2009).

The dissolved Al^{3+} concentration released by smectite dissolution may precipitate as a secondary Al mineral phase. Analcime is ncluded in the geochemical system. Analcime is a zeolite which is not initially present in the bentonite, but it is allowed to precipitate. The considered chemical formulation of analcime and the log K value at 25º C are listed in Tab. 6.7 (Savage *et al.*, 2010; Wilkin and Barnes, 1998). Analcime precipitation is kinetically-controlled according to Savage *et al.* (2010):

$$r_m = 10^{-13.9}\left(W_m - 1\right) \qquad (6.19)$$

where r_m (mol/m^2/s) is the kinetic rate which depends on the ratio between the ion activity product and the equilibrium constant, Ω_m. The reactive surface area of analcime is equal to 0.01 m^2/L (Fernández *et al.*, 2009; Savage *et al.*, 1999) and the molar volume is equal to 97.1 cm^3/mol (Fernández *et al.*, 2009).

Accounting for kinetically-controlled smectite dissolution is prone to numerical convergence problems. A 1 Ma simulation tracks a week.

Tab. 6.7 Dissolution/precipitation reaction included to the reference geochemical model and their equilibrium constants at 25ºC

	Reaction	Log K (25°C)
Smectite (Fernandez *et al.*, 2009)	$K_{0.055}Na_{0.135}Ca_{0.125}Mg_{0.1}(Al_{1.545}Mg_{0.425})\cdot(Si_{3.86}Al_{0.145})O_{10}(OH)_2 + 6.56H^+ \rightleftharpoons 0.135Na^+ + 0.055K^+ + 0.125Ca^{2+} + 0.525Mg^{2+} + 1.69Al^{3+} + 3.86SiO_2(aq) + 4.82H_2O$	6.26
Analcime (Savage *et al.*, 2010)	$NaAlSi_2O_6\cdot H_2O + 4H^+ \rightleftharpoons Na^+ + Al^{3+} + 2SiO_2(aq) + 3H_2O$	6.7833

Smectite dissolves and analcime precipitates in the entire bentonite barrier after 10^4 years in very small concentrations (Fig. 6.65). Figure 6.66 shows the spatial distribution of precipitated/dissolved smectite and analcime at the end of the sensitivity run. After 1 Ma, only 0.2% of the smectite (in volume) is dissolved. Therefore, smectite dissolution is not a relevant reaction in the long-term geochemical evolution of the repository.

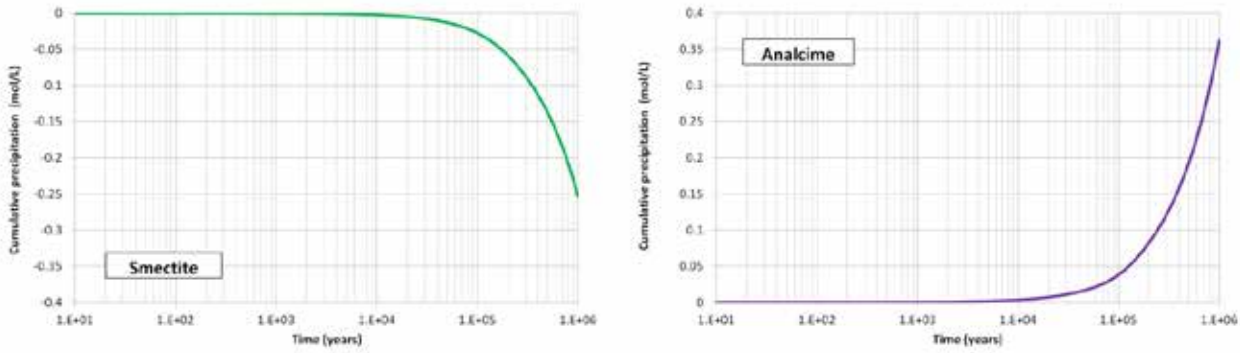

Fig. 6.65 Time evolution of cumulative precipitation/dissolution of smectite (right) and analcime (left) in the bentonite at r = 4.6 dm for the sensitivity run accounting for kinetically-controlled smectite dissolution and precipitation of analcime

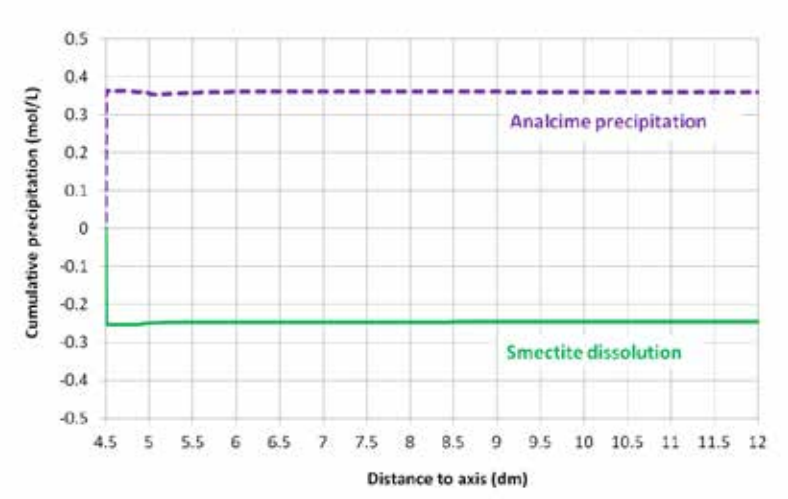

Fig. 6.66 Spatial distribution of computed cumulative precipitation/dissolution of smectite and analcime at 106 years for the sensitivity run accounting for kinetically-controlled smectite dissolution and analcime precipitation

The concentrations of the dissolved species are not sensitive to smectite dissolution and analcime precipitation for $t < 10^5$ years. Afterwards, very slight changes are due to mineral precipitation/dissolution. The computed pH in the sensitivity run shows a larger decrease than that of the reference scenario after $2 \cdot 10^5$ years, when relevance of smectite dissolution and analcime precipitation increases (Fig. 6.67).

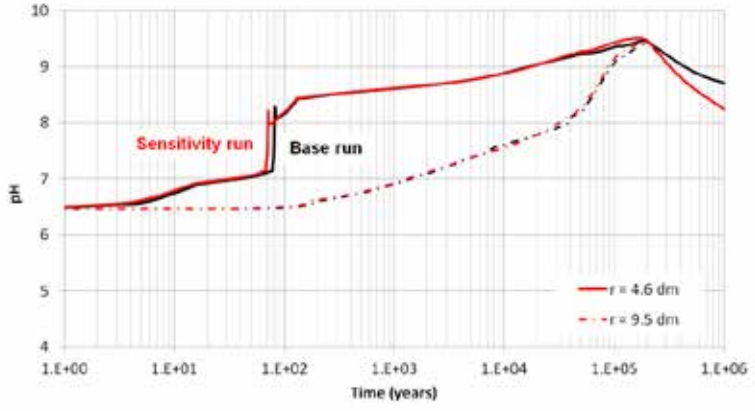

Fig. 6.67 Time evolution of computed pH at r = 4.6 dm and r = 9.5 dm for the reference scenario and the sensitivity run accounting for kinetically-controlled smectite dissolution and precipitation of analcime

On the other hand, the precipitation of the corrosion products is sensitive to smectite and analcime dissolution/precipitation. Figure 6.68 presents the spatial distribution of computed cumulative precipitation of magnetite and siderite at the end of the simulation

(1 Ma) for the reference scenario and the sensitivity run accounting for kinetically-controlled smectite dissolution and analcime precipitation. The penetration of corrosion products into the bentonite is 3 cm lower than that of the reference scenario.

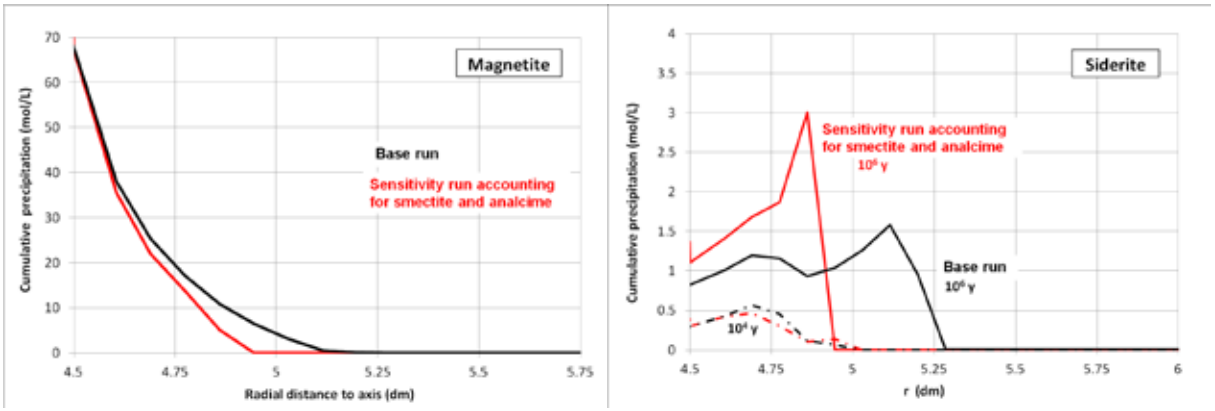

Fig. 6.68 Spatial distribution of computed cumulative precipitation of magnetite at 106 years (left) and siderite at 104 and 106 years (right) for the reference scenario and the sensitivity run accounting for kinetically-controlled smectite dissolution and analcime precipitation

Smectite and analcime dissolution/precipitation affect also the precipitation of other mineral phases such as calcite and quartz (Fig. 6.69). The penetration of calcite precipitation into bentonite is 3 cm lower than that of the reference scenario. Quartz slightly dissolves in the bentonite where corrosion products and calcite precipitates.

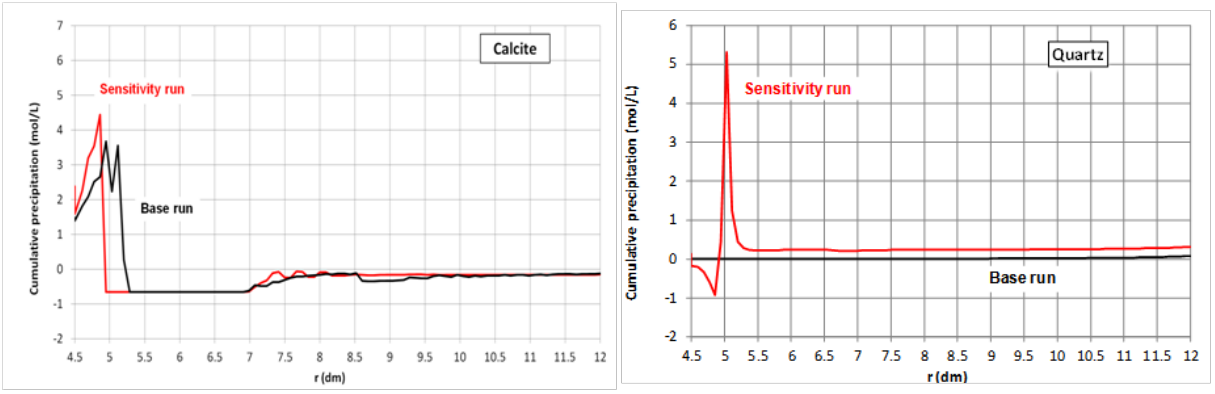

Fig. 6.69 Spatial distribution of computed cumulative precipitation/dissolution of calcite (left) and quartz (right) at 106 years for the reference scenario and the sensitivity run accounting for kinetically-controlled smectite dissolution and analcime precipitation

Figure 6.70 shows the spatial distribution of the bentonite porosity at selected times which changes due to mineral dissolution/precipitation computed with the reference scenario and the sensitivity run which accounts for kinetically-controlled smectite dissolution and analcime precipitation. The thickness of the bentonite zone affected by the porosity reduction decreases slightly in the sensitivity run.

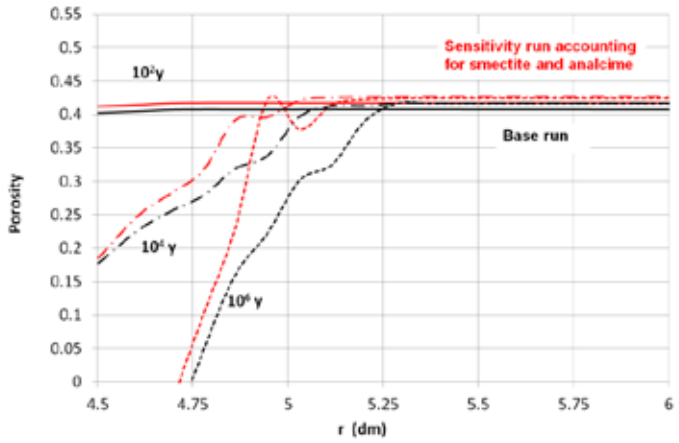

Fig. 6.70 Spatial distribution of the bentonite porosity at selected times which changes due to mineral dissolution/precipitation for the reference scenario and the sensitivity run accounting for kinetically-controlled smectite dissolution and analcime precipitation

Accounting for smectite dissolution and neoformation of zeolites and Fe-clay minerals

An additional sensitivity run was performed which considers the neoformation of cronstedite (Fe-phyllosilicate) in addition to the dissolution of smectite and the precipitation of analcime. Cronstedite is assumed at equilibrium. The chemical reaction of cronstedite and its log K value at 25 ºC are listed in Tab. 6.8 (Savage *et al.*, 2010).

Tab. 6.8 Dissolution/precipitation reaction of cronstedite and its equilibrium constants at 25 ºC (Savage et al., 2010)

	Reaction	Log K (25°C)
Cronstedite	$Fe_2Fe_2SiO_5(OH)_4 + 10H^+ \rightleftharpoons 2Fe^{2+} + 2Fe^{3+} + SiO_2(aq) + 7H_2O$	16.2603

Cronstedite precipitates near the canister/bentonite interface reducing slightly the precipitation of analcime (Fig. 6.71). The thickness of the bentonite zone where cronstedite precipitates is equal to 9 cm. Smectite dissolution/precipitation is not significantly influenced by the precipitation of cronstedite.

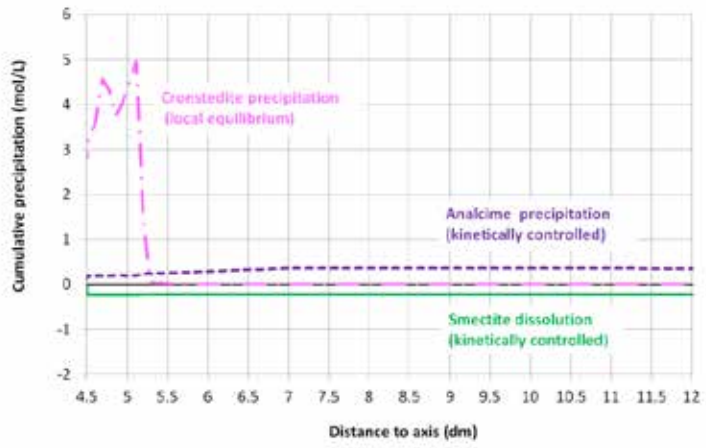

Fig. 6.71 Spatial distribution of computed cumulative precipitation/dissolution of smectite, analcime and cronstedite at 106 years for the sensitivity run accounting for kinetically-controlled smectite dissolution and analcime precipitation and cronstedite precipitation at local equilibrium

The precipitation of the corrosion products is influenced by cronstedite precipitation. Figure 6.72 shows the spatial distribution of computed cumulative precipitation of magnetite at the end of the simulation (1 Ma) for (1) the reference scenario, (2) the sensitivity run which accounts for kinetically-controlled smectite dissolution and analcime precipitation and (3) the sensitivity run which also accounts for cronstedite precipitation. Siderite precipitation during the earliest 10^5 years is similar to that for the base run. However, the precipitated siderite dissolves afterwards, coinciding with a fast decrease of the pH, and there is not siderite left at the end of simulation. The penetration of corrosion products in the sensitivity run is in the range of that of the reference scenario.

Figure 6.73 presents the spatial distribution of the bentonite porosity at selected times which changes due to mineral dissolution/precipitation for the reference scenario and the sensitivity run which accounts for smectite dissolution and analcime and cronstedite precipitation. The thickness of bentonite affected by the porosity reduction is in the range of that of the reference scenario.

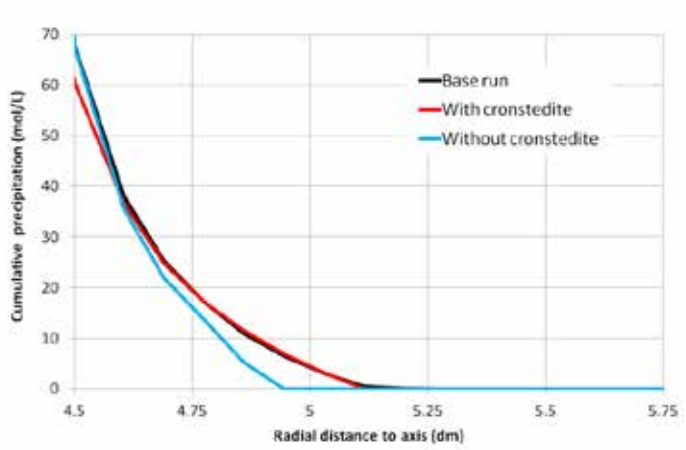

Fig. 6.72 Spatial distribution of computed cumulative precipitation of magnetite at 106 years for the reference scenario (base run), the sensitivity run which accounts for kinetically-controlled smectite dissolution and analcime precipitation and the sensitivity run which also accounts for cronstedite precipitation

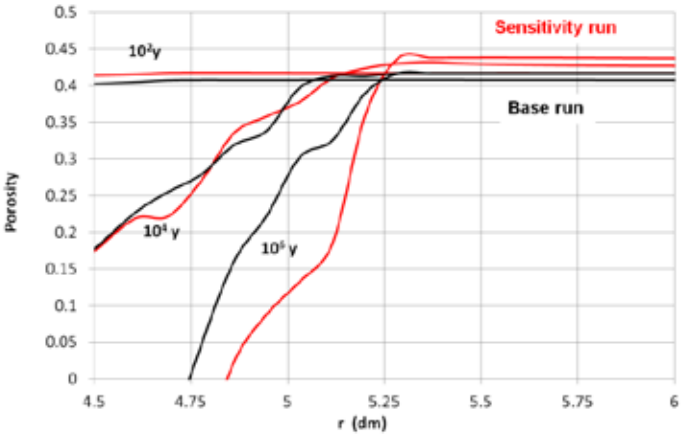

Fig. 6.73 Spatial distribution of the bentonite porosity at selected times which changes due to mineral dissolution/precipitation for the reference scenario (base run) and the sensitivity run which accounts for smectite dissolution and analcime and cronstedite precipitation

6.1.8.3 Influence of geometric simplifications

Geometric simplifications lead to deviations in the numerical predictions of the long-term geochemical evolution of the EBS.

The 1D axisymmetric model of an individual disposal cell of the reference scenario neglects the canister border effects. The influence of this simplification has been evaluated by comparing the results of the 1D axisymmetric model of the reference scenario with the 2D axisymmetric model of Case 4.3 presented in Section 6.3. There are no significant differences between the results of the 1D and 2D models in terms of the geochemical trends, the penetration of the corrosion products into the bentonite and the thickness of bentonite affected by the porosity reduction.

The 1D model of the reference scenario accounts for the canister and the bentonite, but does not consider the granitic rock. Water flow through the granite was simulated with a prescribed water flux of granite water at the outer element of the model, which washes the bentonite/granite interface. For the most part, the results of the 1D model are similar to those of the 2D axisymmetric model, which accounts for the excavation damaged zone and the granite in its domain and accounts for the flow and solute transport through them.

The 1D and 2D models assume that the disposal galleries can be analyzed independently. Since the geochemical perturbations caused by the corrosion products extend into the granitic rock formation a distance of 12 m which is smaller than the separation between galleries, it can be concluded that the assumption of analyzing each disposal gallery independently is valid.

6.1.9 Recommendations for future research

Future research should be devoted to implement the following model improvements:

1. Considering different types of waters: internal, external and free waters;
2. Allowing for different effective diffusion coefficients for each chemical species;
3. Allowing for the dynamic update of bentonite porosity and accounting for pore clogging;
4. Allowing for the canister void space to have properties other than those of the bentonite;
5. Taking into account kinetic magnetite precipitation with the experimentally calibrated value of the specific surface area;

6. Accounting for the neoformation of an appropriated set of kinetically-controlled secondary mineral phases among Fe-phylosilicates (chlorite, berthierine), Fe-rich smectite (saponite), zeolites (phillipsite, chabazite, merlionite) and corrosion products;

7. Considering inhomogeneous corrosion.

6.1.10 Comparison of UDC numerical results against those of other models of the interactions of iron and bentonite

The numerical results of the UDC models of the interactions of iron and bentonite have been compared to the results reported by Bildstein *et al.* (2006), Wersin *et al.* (2007), Savage *et al.* (2010) and Marty *et al.* (2010).

Savage (2012) describes how iron-bentonite interactions and the effects of corrosion products on the bentonite were first identified by Nagra in the mid 1980's. Andra and JAEA performed experiments and modelling studies in the late 1990's. In the middle of the last decade Posiva and SKB followed with reviews and experiments as part of their KBS-3H research programme. Some of these experiments have been interpreted using coupled THC models (Montes-H *et al.*, 2005; Bildstein *et al.*, 2006; Hunter *et al.*, 2007; Wersin *et al.*, 2007; Samper *et al.*, 2008a; Savage *et al.*, 2010; Marty *et al.*, 2010; Lu *et al.*, 2011).

Bildstein *et al.* (2006) modelled the interaction of the canister with the bentonite and the clay formation in the French reference system with a 1D purely diffusive model under full saturation conditions. The model accounts for a 7 cm thick stainless steel canister, an 80 cm thick MX-80 bentonite-based EBS, and a 10 m long geological barrier of clay host rock. The reaction-transport code CRUNCH was used to investigate the iron-clay interactions at 50 ºC over 10.000 years. A constant corrosion of 4.3 µm/y was considered. The potential corrosion products included iron oxides and hydroxides, iron carbonates, and iron-rich smectite and serpentine minerals (Fe-phyllosilicates). The porosity was updated according to the net volume balance of dissolved and precipitated minerals. The model considered a gap at the interface between the EBS and the clayey formation. They performed calculations for two systems, i.e., one containing a bentonite-based EBS and another one without EBS, since both options were considered for the disposal of different types of waste packages. Their results for the system involving bentonite show that pH at the bentonite-container interface increases progressively

from 7.7 to a 10.5 after 5.000 years. At this time, pore clogging takes place at this location. When porosity vanishes, the pH increases to values around 11. High values of pH were obtained because no iron hydroxide minerals precipitate while the oxidation of Fe by water produces H^+ and OH^- ions. The Ca-montmorillonite and Na-montmorillonite tend to dissolve in the EBS at both the interfaces with the canister and the argillite, whereas illite remains stable. In this system the corrosion products and interactions with clay were essentially located in the cell representing the canister. The corrosion products include magnetite (35%) and cronstedtite (40%, an iron-rich serpentine). The precipitation of chamosite and siderite are less than 1%. Porosity clogging occurs in the cell containing the iron after 5.000 years in the case with EBS and after 16.000 years in the case without EBS. Clogging is due to the precipitation of magnetite and cronstedtite, and to a lesser extent, of chamosite and siderite. The different timing is due to the fast precipitation of cronstedtite in the EBS. Porosity is also increasing inside the EBS and the argillite. In the case with EBS, the increase of porosity at the interface with the canister (+6%) affects around 10 cm of bentonite and is due to the dissolution of the initial Na-montmorillonite and Ca-montmorillonite in the EBS which is not compensated by the precipitation of other minerals. In the argillite, a front develops and reaches 4 m depth into the system after 5.000 years, featuring a +5% porosity increase with the complete dissolution of Ca-montmorillonite and Na-montmorillonite, and the dissolution of 5% of illite. These minerals are partly replaced by minerals incorporating iron (up to 12% of cronstedtite, 2% of chamosite, and 2% low-Fe smectite, 0.5% of siderite) and calcium (up to 10% of scolecite, a Ca-zeolite). Behind this first front, a small amount of Mg-saponite (0.1%) also precipitates. Overall, the results of UDC calculations share many features of the results of Bildstein *et al.* (2006). Magnetite is the main corrosion product while siderite precipitation is much lower than magnetite precipitation. The reduction of bentonite porosity due to mineral precipitation near the canister/bentonite interface could result in the clogging of the bentonite pores. The bentonite thickness affected by porosity reduction increases with time and it is of ~7 cm after 1Ma. Cronstedtite precipitates near the canister/bentonite interface.

Wersin *et al.* (2007) studied the impact of iron components released from the corrosion process on the bentonite buffer (MX-80) within the KBS-3H concept using the Olkiluoto site in Finland as a test case. At the front end, a constant concentration boundary condition, corresponding to the porewater in equilibrium with the corroded steel supercontainer, is imposed. At the back end closed boundary conditions are assumed. They performed reactive transport simulations using CrunchFlow with a 1D diffusion model con-

sidering site-specific geochemical data from Olkiluoto, iron corrosion, cation exchange, protonation/deprotonation and Fe(II) surface complexation and mineral dissolution/precipitation including thermodynamic and kinetic clay minerals. A general conclusion from this modelling study is that the extent of the bentonite zone transformed to non-swelling material is likely to remain spatially limited (a few centimetres) for very long times. UDC calculations agree with the general conclusion of the results of Wersin *et al.* (2007).

Savage *et al.* (2010) reported a model of the iron-bentonite interactions based in natural analogues. They claim that the studies of the natural systems suggest that the sequence of the alteration of the clay by Fe-rich fluids may proceed via an Ostwald step sequence. They used the code QPAC which was modified to incorporate nucleation, growth, precursor cannibalisation, and Ostwald ripening to address the issues of the slow growth of the bentonite alteration products. They modelled iron corrosion (corrosion rate of ~2 μm/year) and the alteration of MX-80 bentonite in a typical EBS environment. Their model neglected protonation-deprotonation reactions at clay edge sites and cation exchange reactions. They considered two model cases; one with fixed reactive surface areas for secondary minerals; and one with time-dependent variation of the surface areas of secondary minerals. Simulations with fixed mineral surface areas show that berthierine dominates the Fe-bearing minerals, with siderite replacing it for t > 10.000 years. Further away from the iron canister, berthierine continues to precipitate in the clay as the Fe^{2+} ions penetrate deeper into the bentonite with time. Large amounts of dolomite also appear, due to the relatively high concentrations of calcium in the host rock groundwater and the release of Mg^{2+} ions from the dissolving Ca-montmorillonite. This, along with the growth of iron-bearing minerals, results in complete pore blocking near the canister and causes the simulation to end prematurely. The pH of the bentonite pore fluids shows a rapid decrease, such that after 10 years pH decreases from ~10.4 to a value between 6 and 7, the precise value depending upon the location within the bentonite. This pH buffering is due to silicate precipitation reactions. Porosity blocking due to mineral precipitation also leads to a slowing of the steel corrosion rate. The simulations with time-dependent mineral surface areas show the following sequence: magnetite-cronstedtite-berthierine-chlorite. The evolution of the secondary minerals is somewhat different to that predicted by the fixed surface area model. Near to the corroding canister, at first magnetite is the dominant Fe-bearing mineral; this is followed by cronstedtite, which dominates between ~0.04 years and 500 years. Berthierine is again present throughout, but in reduced quantities compared with

the fixed surface area model; after 500 years cronstedtite dissolves away and berthierine is the dominant Fe-bearing mineral. Eventually, after about 5.000 years, chlorite grows in, using the berthierine surface growth sites rather than nucleating directly. Further into the clay, there is much less Fe-based mineral precipitation than in the fixed surface area case, with only small amounts of berthierine present. The evolution of pH with time is similar to the fixed surface area case, such that pH decreases rapidly over 1-10 years from 10.4 to 6–7. The results of the UDC model cannot be compared directly to those of Savage *et al.* (2010) because the UDC model considers neither the Ostwald step nor the time-dependent variation of surface areas of secondary minerals.

Marty *et al.* (2010) performed a model of the long-term alteration of the engineered bentonite barrier in an underground radioactive waste repository. The study was focused on the possible feedback effects of geochemical reactions on the transport properties (porosity and diffusion) of a compacted MX-80 bentonite. The system was modelled in reducing conditions by using the KIRMAT code. The model considers a 1 m thick buffer of MX-80 bentonite which is in contact on one side with a geological fluid (Callovo-Oxfordian groundwater at 25 ºC) diffusing into the engineered barrier. The calculations assumed a constant temperature of 100 ºC in order to estimate a maximum thermal effect on the mineralogy of the engineered barrier. By considering the temperature and the long-term evolution of the system, the mineralogical transformations were considered as being more important than the surface complexation and cation exchange reactions. As a consequence, these reactions were neglected in the model. After 100.000 years of simulated mass transport-reaction, the model predicted mineralogical modifications of the EBS in contact with the geological interacting fluid and with Fe^{2+} ions provided by the corrosion of the steel overpacks. According to the degree of smectite transformations the mineralogical modifications of the MX-80 bentonite until 100.000 years showed three distinct zones: (1) The first zone results from the mass transport of the geological groundwater through MX-80 bentonite. The resulting alteration front corresponds to a strong illitization of the montmorillonite together with the precipitation of quartz, saponite and vermiculite. (2) In the middle of the EBS, the volume of montmorillonite remains quite constant. The saponitization and the illitization processes can be distinguished in lower proportions as minor phase. (3) The third alteration front is constituted by significant precipitations of Fe(II)Al-chlorite, Fe(II)-saponite and magnetite in contact with the steel overpack. The precipitation of these phases decreases significantly the porosity of the EBS. Marty *et al.* (2010) concluded that only the outer parts of the simulated system are significantly affected. The dissolu-

tion of the montmorillonite contained in the MX-80 bentonite is mainly observed in the zone influenced by the groundwater mass transport and partly in a zone adjacent to the container. Despite the neo-formation of illite, vermiculite, saponite and magnetite detected in the barrier, the predicted evolution of the porosity is limited in the main part of the EBS and the porosity even tends to decrease in the perturbed outer zones. A porosity clogging near the steel overpack significantly decreases molecular diffusion. As a feedback effect, the influence of the iron corrosion on the EBS mineralogy then decreases as a function of time due to the reduction of the bentonite porosity. The long term transformation of the bentonite should have only a minor influence on the amount of montmorillonite. In the modelling, more than 60% of the initial montmorillonite is preserved after 100.000 years, and additional swelling minerals such as vermiculite and saponites are formed. Marty *et al.* (2010) recognize that the calculation may overestimate the transformation rate of the minerals because they assumed a fixed maximum temperature of 100 °C throughout the simulation time. The UDC model is more realistic because it takes into account the time variability of temperature for the geochemical simulation.

As a summary, the conclusions of the simulations performed by UDC within the PEBS project are consistent for the most part with those reported by others for similar systems. In some cases, however, there are marked differences in the geochemical systems and the hypotheses used by the modelling teams. This is especially the case for the simulation of Savage *et al.* (2010).

6.2 Study of the concrete/bentonite interface

6.2.1 General description

The evaluation of the long-term geochemical evolution of the engineered barrier system of a high-level radioactive waste repository requires the use of reactive transport models. Here we present a numerical model of non-isothermal unsaturated/saturated water flow and multicomponent reactive solute transport in a HLW repository in clay according to the Spanish Reference Concept (Enresa, 2004). This model has been constructed by extending and improving the model performed by UDC within the NFPRO Project which is reported by Yang et al. (2008). The model of 2008 focused on the interactions of the bentonite buffer, the concrete liner and the clay formation. The

updated model performed within the PEBS Project considers simultaneously the interactions of corrosion products and bentonite and the interactions of the bentonite buffer, the concrete liner and the clay formation. The reactive transport model has been improved also by:

- Considering kinetic smectite dissolution
- Considering the precipitation of secondary mineral phases
- Updating the bentonite selectivity coefficients
- Taking into account proton and iron sorption by surface complexation on three types of protolysis sites

6.2.2 Geometry

The model corresponds to a HLW radioactive waste repository in clay according to the Spanish Reference Concept (Enresa, 2004). The model accounts for a bentonite buffer having a thickness of 0.75 m, a 0.3 m thick concrete liner and the clay formation. The model extends to a total radial distance of 25 m (Fig. 6.74).

Axial symmetry is assumed for heat and transport processes. The axis of the gallery is the axis of symmetry. Similar to the previous model of Yang *et al.* (2008), the updated model considers a unit longitudinal length (1 dm) of the axis of the gallery.

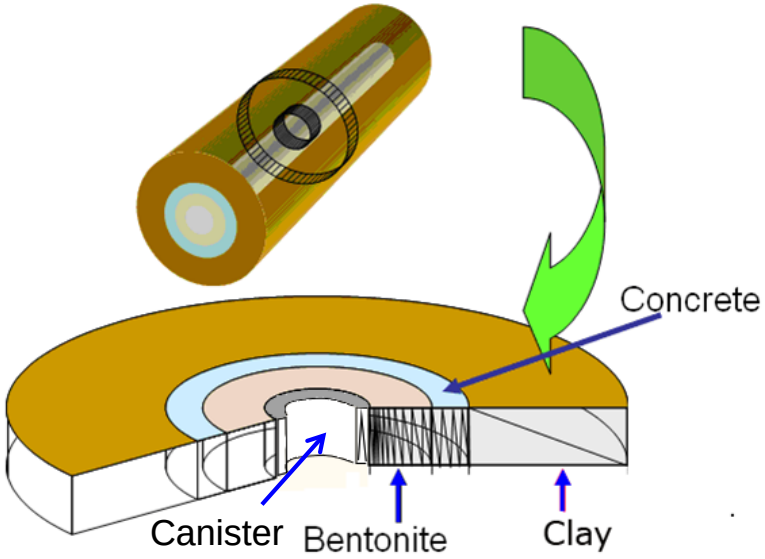

Fig. 6.74 Scheme of the multibarrirer system of a HLW repository in clay according to the Spanish Reference Concept (Enresa, 2004)

6.2.3 Process classes (T, H, M, C) and coupling

Initially, the bentonite buffer is unsaturated with a gravimetric water content of 14%. Water flow is negligible once the bentonite buffer is saturated. Then, solute transport occurs entirely by molecular diffusion.

Clay pore water infiltrates into the concrete, then interacts with the concrete liner and produces a hyperalkaline pore water which then diffuses into the bentonite. The high pH fluid interacts with the bentonite minerals as it diffuses and triggers the dissolution of the primary minerals and the precipitation of secondary minerals in the bentonite and the concrete.

The model was run for two stages. The first stage corresponds to the saturation of the bentonite buffer and the second one goes from bentonite saturation to t = 1 Ma. In the first stage of bentonite saturation, the model accounts only for the bentonite buffer and the concrete. The pore fluid from the host rock (clay formation) is taken as a boundary water which flows into the concrete.

The model results of the first stage are taken as initial conditions for the model of the second stage (Fig. 6.75). In the second stage (geochemical evolution after saturation of

bentonite), the clay formation is included in the model domain. This is reasonable because: 1) The time to saturate the bentonite is very short (on the order of a few decades) compared to the total simulation time of 1 Ma; and 2) The pore water mainly flows from the clay formation through the concrete to the bentonite and controls the solute transport in the system during the first stage. Therefore, the diffusion of the hyperalkaline pore water into the clay formation during the first stage can be disregarded.

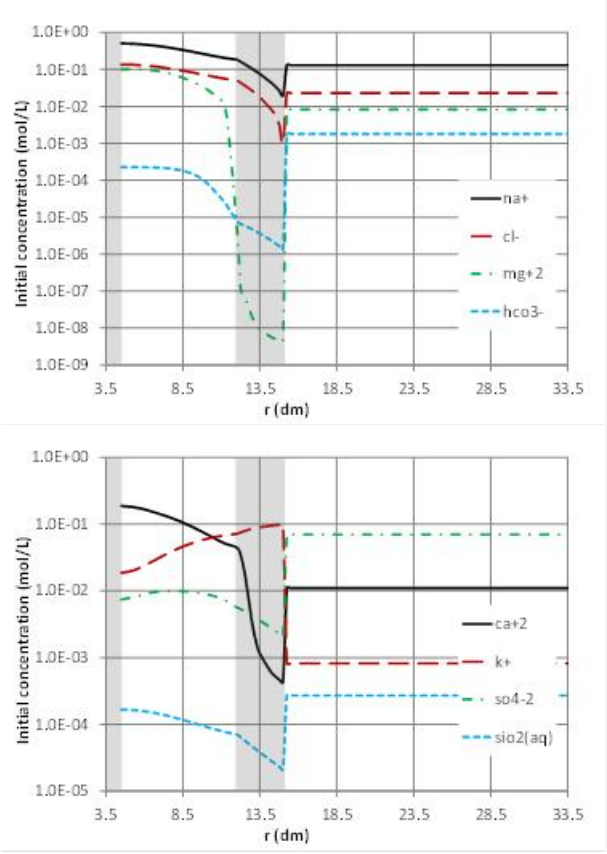

Fig. 6.75 Spatial distribution of the total dissolved concentrations of the major components at the end of the first stage (once the bentonite is fully saturated) of the numerical model of the canister, the bentonite barrier, the concrete liner and the clay formation

The model accounts for homogenous aqueous complexation reactions, dissolution/precipitation of minerals and cation exchange reactions.

Several hypotheses have been considered for mineral dissolution/precipitation. Similar to the previous model, in the first modelling stages, these reactions were assumed to proceed at local equilibrium. Later, mineral kinetics was considered.

The model is non-isothermal and takes into account the temperature dependence of the reaction constants.

6.2.4 Considered processes

In the first stage of bentonite saturation, water flows from the clay formation through the concrete to the bentonite and controls the solute transport in the system during the first stage. Water flow is negligible once the bentonite buffer is saturated (second stage) and, therefore, solute transport occurs entirely by molecular diffusion.

The model is nonisothermal. It accounts for the thermal field in across the bentonite barrier by prescribing a time-varying temperature function at the inner boundary to simulate the cooling of the radioactive waste and solving the heat transport. The computed temperatures are used for updating the temperature–dependant chemical parameters such as the equilibrium constants and the activity coefficients.

The chemical system is defined in terms of the following primary species: H_2O, H^+, Ca^{2+}, Mg^{2+}, Na^+, K^+, Cl^-, SO_4^{2-}, HCO_3^- and $SiO_2(aq)$ in the base run. $O_2(aq)$, Fe^{2+} and Al^{3+} were included in the updated and improved models.

The model considers the following initial minerals in the bentonite: calcite, gypsum and quartz initially. The initial phases in the concrete include tobermorite, portlandite, brucite and calcite. Tobermorite and gyrolite are used to simulate calcium silicate hydrate (CSH) phases. Finally, the following mineral phases were considered to be present initially in the clay formation: calcite, gypsum, quartz, and dolomite (Enresa, 2004).

The reference model accounts for homogeneous reactions (acid-base, aqueous complexation and redox reactions) and heterogeneous reactions such as mineral dissolution/precipitation of calcite, dolomite, gypsum, quartz, portlandite, brucite, sepiolite, tobermorite and gyrolite. The following mineral phases were added in the updated and improved models: magnetite, siderite, goethite, ettringite, smectite, analcime and Mg-saponite. The most advanced model simulation runs considers the kinetic dissolution of smectite and the precipitation of analcime. A constant corrosion rate is considered in the updated model for the canister.

The model accounts also for cation exchange reactions involving Na^+, Ca^{2+}, Mg^{2+}, K^+, H^+ and Fe^{2+}. Cation exchange was modelled with the Gaines-Thomas convention. Surface complexation reactions were considered in the bentonite. They were modelled with a triple sorption site model similar to that of Bradbury and Baeyens (1997; 2005).

6.2.5 Input data and data sources

Figure 6.76 shows the time functions of temperature used to simulate the heat transport in the numerical model of the canister, the bentonite barrier, the concrete liner and the clay formation. These functions were imposed at the canister, the bentonite-concrete interface (r = 1.2 m) and in the outer boundary (r = 25 m). The temperature in the canister is about 98 ºC until t = 10 years. Then, the temperature decreases to 45 ºC after 10,000 years. The final temperature is 19.7 ºC at 1Ma. The evolution of the temperature in the bentonite-concrete interface is similar. However, the maximum temperature is 75.8 ºC and then it decreases to 19.7 ºC. The average temperature of the external node at 25 m, the in clay, is 25 ºC.

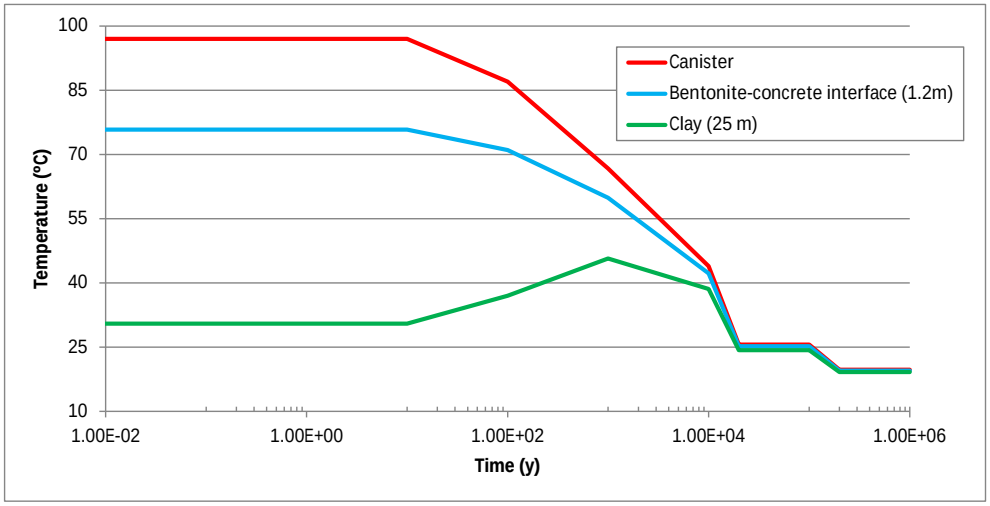

Fig. 6.76 Time functions of temperature used to simulate the heat transport in the numerical model of the canister, the bentonite barrier, the concrete liner and the clay formation

Table 6.9 lists the thermal and hydrodynamic parameters for each material.

Table 6.10 shows the components, the aqueous complexes, the minerals and the exchanged cations considered in the updated geochemical model.

Tab. 6.9 Thermohydrodinamic parameters of the numerical model for the study of the interactions of the canister, the bentonite barrier, the concrete liner and the clay formation

Parameter	Carbon steel canister (assumed)	Bentonite barrier	Concrete liner	Clay formation
Hydraulic conductivity (m/s)	$2.75 \cdot 10^{-14}$	$2.75 \cdot 10^{-14}$	$3.39 \cdot 10^{-12}$	$4.19 \cdot 10^{-12}$
Initial porosity	0.407	0.407	0.085	0.37
Effective diffusion coefficient (m^2/s)	$4.08 \cdot 10^{-11}$	$4.08 \cdot 10^{-11}$	$8.56 \cdot 10^{-12}$	$5.01 \cdot 10^{-11}$
Solid density (kg/m^3)	2750	2700	2513	2778
Specific heat capacity (cal/g^{o}C)	0.114	0.202	0.328	0.267

Tab. 6.10 Components, aqueous complexes, minerals and exchanged cations considered in the hydrogeochemical model. Thermodynamic data were taken from the reformatted EQ3NR database (Wolery, 1992)

Components	H_2O, H^+, Ca^{2+}, Mg^{2+}, Na^+, K^+, Cl^-, SO_4^{2-}, HCO_3^-, O_2(aq), Fe^{2+}, Al^{3+} and SiO_2(aq)
Aqueous complexes	OH^-, CO_3^{2-}, $CaCO_3$(aq), $CaHCO_3^+$, $CaSO_4$(aq), $CaOH^+$, $CaCl^+$, $CaCl_2$(aq), $Ca(H_3SiO_4)_2$(aq), CaH_2SiO_4(aq), $CaH_3SiO_4^+$(aq), $MgCO_3$(aq), $MgHCO_3^+$, $MgSO_4$(aq), $MgCl^+$, $MgOH^+$, $Mg(OH)_4^{4+}$, MgH_2SiO_4(aq), $MgH_3SiO_4^+$, $Mg(H_3SiO_4)$(aq), NaOH(aq), NaCl(aq), $NaCO_3^-$, $NaHCO_3$(aq), $NaH_3SiO_4^+$(aq), $NaHSiO_3$(aq), CO_2(aq), KOH(aq), KSO_4^-, $KHSO_4^-$, $NaSO_4^-$, HS^-, $H_3SiO_4^-$, $H_2SiO_4^2$, $HSiO_3^-$, $H_4(H_2SiO_4)_4^{4-}$, $H_3SiO_3^-$, $H_6(H_2SiO_4)_4^{2-}$, HCl(aq), HSO_4^-, $Al(OH)_4^-$, $Al(OH)_3$(aq), $Al(OH)_2^+$, $AlOH^{2+}$, H_2(aq), $Fe(OH)_2^+$, $Fe(OH)_2$(aq), $Fe(OH)_3$(aq), $Fe(OH)_4$, Fe^{3+},$FeCO_3$(aq), $FeHCO^{3+}$, $FeCl^+$, $FeCl^{2+}$, $FeOH^+$, $FeOH^{2+}$, $Fe(SO_4)_2^-$, $FeSO_4$(aq)
Minerals	calcite, gypsum/anhydrite, cristobalite, quartz, portlandite, brucite, ettringite, sepiolite, C0.8SH, C1.8SH, magnetite, siderite, goethite, smectite, analcime, Mg-saponite, cronstedite
Exchanged cations	$Ca^{2+,}$ Mg^{2+}, Na^+, K^+, H^+ and Fe^{2+}

The initial pore water chemical compositions in the bentonite barrier, the concrete liner and the clay formation are listed in Tab. 6.11 (Enresa, 2004). The initial porewater of the canister is assumed to be the same as that of the bentonite pore water.

Tab. 6.11 Initial porewater composition (mol/L) the bentonite barrier, the concrete liner and the clay formation (Enresa, 2004)

Species	Bentonite barrier	Concrete liner	Clay formation
pH	7.462	13.25	7.54
Cl^-	$1.30 \cdot 10^{-1}$	-	$2.30 \cdot 10^{-2}$
HCO_3^-	$2.70 \cdot 10^{-2}$	-	$1.80 \cdot 10^{-3}$
SO_4^{2-}	$1.62 \cdot 10^{-2}$	$2.00 \cdot 10^{-3}$	$7.00 \cdot 10^{-2}$
Na^+	$5.93 \cdot 10^{-1}$	$1.60 \cdot 10^{-2}$	$1.30 \cdot 10^{-1}$
K^+	$4.27 \cdot 10^{-3}$	$1.00 \cdot 10^{-1}$	$8.20 \cdot 10^{-4}$
Mg^{2+}	$1.60 \cdot 10^{-1}$	$4.10 \cdot 10^{-9}$	$8.20 \cdot 10^{-3}$
Ca^{2+}	$2.02 \cdot 10^{-1}$	$1.10 \cdot 10^{-2}$	$1.10 \cdot 10^{-2}$
$SiO_{2(aq)}$	$1.93 \cdot 10^{-4}$	$2.00 \cdot 10^{-5}$	$2.70 \cdot 10^{-4}$

Table 6.12 lists the initial mineral volume fractions in the canister, the bentonite, the concrete and the clay for the updated model. The canister is treated as a porous material made of 100% metallic iron, Fe(s). The bentonite contains initially 0.36% of calcite, 1.19% of quartz, 0.083% of gypsum and 57% of smectite The concrete liner contains initially 0.1% of calcite, 1% of brucite, 16.5% of portlandite, 36.6% of tobermorite and 55% of unreactive quartz. The clay is composed of calcite (11.3%), gypsum (1.2%), quartz (2.4%) and dolomite (2.4%). The remaining mineral phases are assumed unreactive.

Tab. 6.12 Initial mineral volume fractions (%) in the bentonite, concrete and clay (Enresa, 2004)

Canister		Bentonite		Concrete		Clay	
Fe(s)	100	Calcite	0.36	Calcite	0.1	Calcite	11.3
		Gypsum	0.083	Brucite	1.0	Gypsum	1.2
		Quartz	1.19	Portlandite	16.5	Quartz	2.4
		Smectite	57.0	Tobermorite	36.6	Dolomite	2.4

Carbon-steel canister corrosion is modelled by using a kinetic formulation in a manner similar to mineral dissolution. The corrosion rate is 2 μm/y (Samper *et al.*, 2013).

Table 6.13 shows the mineral dissolution/precipitation reactions and their equilibrium constants.

Tab. 6.13 Mineral dissolution/precipitation reactions and equilibrium constants at 25, 60 and 100ºC (Wolery, 1992)

Mineral	**Reaction**	**$logK_{25}$**	**$logK_{60}$**	**$logK_{100}$**
Brucite	$Mg(OH)_2$ Û $Mg^{2+} + 2H_2O - 2H^+$	16.30	14.27	12.45
Calcite	$CaCO_3 + H^+$ Û $Ca^{2+} + HCO_3^-$	1.85	1.33	0.77
Gyrolite	$Ca_2Si_3O_8{:}2.5H_2O + 4H^+$ Û $2Ca^{2+} + 3SiO_{2(aq)} + 4.5H_2O$	22.91	21.17	19.40
Tobermorite	$Ca_5Si_6O_{17}{:}10.5H_2O + 10H^+$ Û $5Ca^{2+} + 6SiO_{2(aq)} + 15.5H_2O$	63.84	59.26	54.89
Quartz	$SiO_{2(s)}$ Û $SiO_{2(aq)}$	–4.00	–3.47	–3.08
Dolomite	$CaMg(CO_3)_2 + 2H^+$ Û $Ca^{2+} + Mg^{2+} + 2HCO_3^-$	4.06	2.65	1.21
Portlandite	$Ca(OH)_2 + 2H^+$ Û $Ca^{2+} + 2H_2O$	22.55	20.20	18.06
Sepiolite	$Mg_4Si_6O_{15}(OH)_2{:}6H_2O + 8H^+$ Û $4Mg^{2+} + 6SiO_2(aq) + 11H_2O$	30.44	27.17	23.90
Gypsum	$CaSO_4{:}2H2O$ Û $Ca^{2+} + SO_4^{2-} + 2H_2O$	–4.48	–4.61	–4.90
Ettringite	$Ca_6Al_2(SO_4)_3(OH)_{12}{:}26H_2O + 12H^+$ Û $2Al^{3+} + 3SO_4^{2-} + 6Ca^{2+} + 38H_2O$	60.81	54.70	50.27
Magnetite	$Fe_3O_4 + 8H^+$ Û $Fe^{2+} + 2Fe^{3+}$ $4H_2O$	10.47	6.44	2.69
Siderite	$FeCO_3 + H^+$ Û $Fe^{2+} + HCO_3^-$	-0.19	-0.83	-1.49
Goethite	$FeO(OH) + 2H^+$ Û $Fe^{2+} + 1.5H_2O + 0.25O_2$ (aq)	0.53	-0.60	-2.60
Smectite	$K_{0.055}Na_{0.135}Ca_{0.125}Mg_{0.1}(Al_{1.545}Mg_{0.425})(Si_{3.86}A_{l0.145})O_{10}(OH)_2$+ $6.56H^+$ Û $0.135Na^+ + 0.055K^+ + 0.125\ Ca^{2+} + 0.525Mg^{2+} + 1.69\ Al^{3+} + 3.86SiO_{2(aq)} + 4.28H_2O$	6.26	6.26	6.26
Analcime	$Na_{0.96}Al_{0.96}Si_{2.04}O_6{:}H_2O + 4H^+$ Û $Al^{3+} + Na^+ + 2SiO_{2(aq)} + 3H_2O$	6.78	3.96	2.57
Mg-saponite	$Mg_{3.165}Al_{0.33}Si_{3.67}O_{10}(OH)_2 + 7.32H^+$ Û $0.33Al^{3+} + 3.165Mg^{2+} + 3.67SiO_{2(aq)} + 4.66H_2O$	25.97	21.88	17.91

Inasmuch as the dissolution of smectite under alkaline ambient conditions could be relevant, the updated model considers the dissolution of smectite and the precipitation of

secondary clay minerals. Smectite dissolution in alkaline conditions is simulated with the following kinetic rate law proposed by Huertas *et al.* (2001):

$$R = e^{\frac{-Ea}{RT}} K_{25} a^{n}_{(OH^-)} S \qquad (6.20)$$

where *Ea* is the activation energy which is equal to 22.7 KJ/mol, *R* is the gas constant, *T* is the temperature (K), K_{25} is the kinetic rate constant which equals $-2 \cdot 10^{-13}$ mol/s/m^2, $a^{n}_{(OH^-)}$ is a catalytic effect of the OH^- which has an exponent n equal to 0.5. The smectite specific surface, σ is assumed equal to 100 dm^2/L. The kinetic law depends on the pH and the temperature. The smectite dissolution will increase with increasing pH and increasing temperature. The precipitation of analcime is assumed to proceed at equilibrium.

The model accounts also for cation exchange reactions involving Na^+, Ca^{2+}, Mg^{2+}, K^+, H^+ and Fe^{2+}. Cation exchange was modelled with the Gaines-Thomas convention. The cation exchange reactions and their associated selectivity coefficients are listed in Tab. 6.14. The selectivity coefficients of cation exchange in the bentonite were recalibrated during the PEBS Project in order to reproduce the measured concentrations of exchanged cations (Tab. 6.15). These calibrated selectivities were used in the updated model.

Tab. 6.14 Cation exchange reactions and their associated selectivity coefficients

Cation exchange reaction	**$K_{Na\text{-}cation}$**
$Na^+ + X\text{-}K \hat{U} K^+ + X\text{-}Na$	0.1456
$Na^+ + 0.5\ X_2\text{-}Ca \hat{U} 0.5\ Ca^{2+} + X\text{-}Na$	0.3265
$Na^+ + 0.5\ X_2\text{-}Mg \hat{U} 0.5\ Mg^{2+} + X\text{-}Na$	0.3766
$Na^+ + 0.5\ X_2\text{-}Fe \hat{U} 0.5\ Fe^{2+} + X\text{-}Na$	0.5
$Na^+ + X\text{-}H \hat{U} H^+ + X\text{-}Na$	$3.16 \cdot 10^{-5}$

Surface complexation reactions in the bentonite are modelled with a triple sorption site model similar to that of Bradbury and Baeyens (1997; 2005). The updated model accounts for surface complexation reactions of H^+ and Fe^{2+}. Surface complexation reactions take place at the following three types of protolysis sites: S^SOH, $S^{W1}OH$ and

$S^{W2}OH$. Table 6.16 shows the types of sorption sites, capacity, reactions of the complex and the equilibrium constant for 25 ºC.

Tab. 6.15 Selectivities of cation exchange reactions in the bentonite

Exchanged cation	Selectivities of the previous model (Enresa, 2004) $K_{Na\text{-}cation}$	Selectivities of the updated model $K_{Na\text{-}cation}$
K^+	0.094	0.138
Ca^{2+}	0.279	0.2924
Mg^{2+}	0.306	0.2881
Fe^{2+}	-	0.5
H^+	$3.16\cdot10^{-5}$	$3.16\cdot10^{-5}$

Tab. 6.16 Thermodynamic data for surface complexation reactions in the bentonite corresponding to the triple site model of Bradbury and Baeyens (2005) at 25ºC

Type of site	Site capacity (mol/kg)	Surface complex	Reaction	Log K_{25}
S^S OH	$7.8\cdot10^{-3}$	$S^SOH_2^+$	º S^SOH^{2+} Û º $S^SOH + H^+$	-4.5
		S^SO^-	º $S^SO^- + H^+$ Û º S^SOH	7.9
		S^SOFe^+	º S^SOFe^+ Û º $S^SOH + Fe^{2+} - H^+$	0.6
		S^SOFeOH	º S^SOFeOH Û º $S^SOH + Fe^{2+} - 2H^+ + H_2O$	10.0
		$S^SOFe(OH)_2^-$	º $S^SOFe(OH)_2^-$ Û º $S^SOH + Fe^{2+} - 3H^+ + 2H_2O$	20.0
$S^{w1}OH$	$1.57\cdot10^{-1}$	$S^{w1}OH_2^+$	º $S^{W1}OH^{2+}$ Û º $S^{W1}OH + H^+$	-4.5
		$S^{w1}O^-$	º $S^{W1}O^- + H^+$Û º $S^{W1}OH$	7.9
		$S^{w1}OFe^+$	º $S^{w1}OFe^+$ Û º $S^{W1}OH + Fe^{2+} - H^+$	3.3
$S^{w2}OH$	$1.57\cdot10^{-1}$	$S^{w2}OH_2^+$	º $S^{W2}OH^{2+}$ Û º $S^{W2}OH + H^+$	-6.0
		$S^{w2}O^-$	º $S^{W2}O^- + H^+$Û º $S^{W2}OH$	-10.5

6.2.6 Numerical model and computer code

The model domain was discretized with a 1-D axisymmetric grid with 30 nodes in the bentonite, 20 in the concrete and 100 in the clay (Fig. 6.77). The model domain includes 3 material zones: the bentonite buffer, the concrete liner and the clay formation with a total length of 25 m. Simulations were run for 1 Ma.

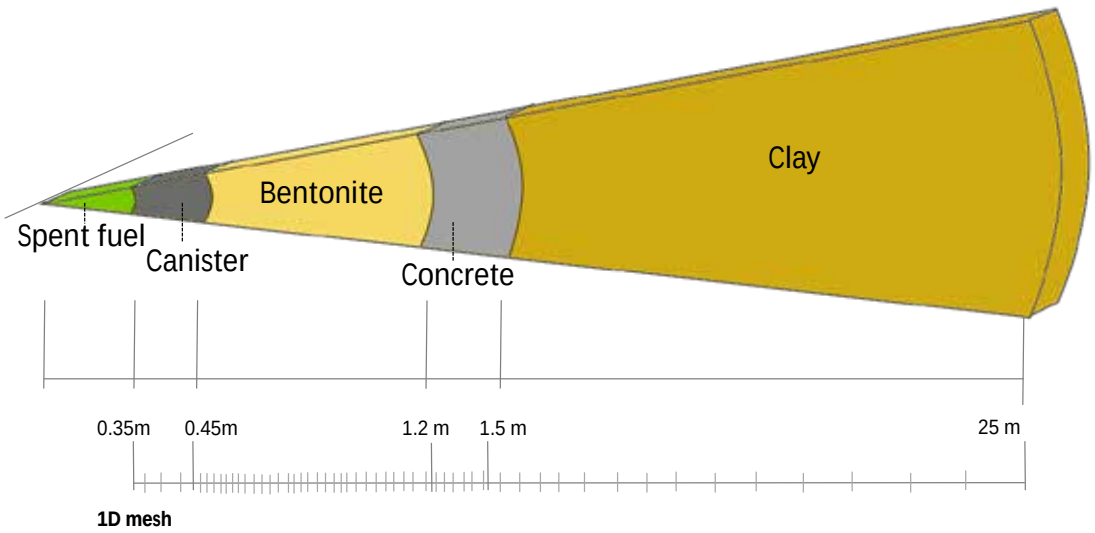

Fig. 6.77 1-D finite element grid which accounts for the canister, the bentonite barrier, the concrete liner and the clay formation

The hydrogeochemical calculations of the interactions of the corrosion products, the bentonite and the concrete have been performed with CORE^{2D}V4 (Samper et al., 2003; 2011). This code solves transient saturated and unsaturated water flow, heat transport and multicomponent reactive solute transport under both local chemical equilibrium and kinetic conditions in heterogeneous and anisotropic media (Section 6.1.6).

6.2.7 Description of model results

6.2.7.1 Previous model

This section presents the main results of the previous model (Yang *et al.*, 2008). Figure 6.78 shows the spatial distribution of the computed pH at several times. In this figure t = 0 represents the pH distribution in the bentonite, the concrete and the clay after the bentonite is saturated. The pH in the concrete increases first due to the dissolution

of portlandite. Then, it reaches a maximum value around 10,000 years and then slowly decreases after 40,000 years when portlandite is completely exhausted. The pH in the bentonite increases due to the penetration of the hyperalkaline plume from the concrete. However, the precipitation of calcite, brucite and sepiolite buffers the hyper alkaline plume. The pH reaches a maximum value around 10,000 years and then decreases to 9.5 after 1 Ma. The hyperalkaline plume slowly penetrates into the clay formation. The front of the hyper alkaline plume penetrates a radial distance of 0.7 m into the clay formation after 1 Ma.

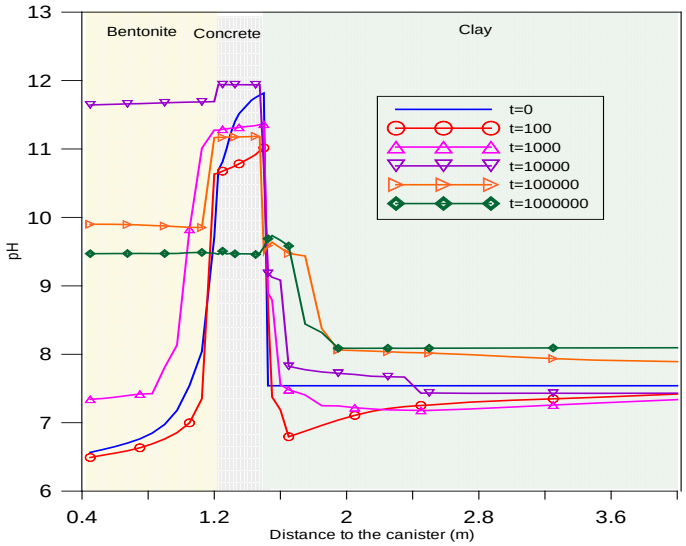

Fig. 6.78 Spatial distribution of the computed pH at selected times with the previous model

Figure 6.79 shows the time evolution of the total dissolved concentrations of the major chemical components in the bentonite near to the bentonite-concrete interface (r = 1.125 m). Dissolved concentrations decrease after 100 years, reaching minimum values at a time ranging from 2,000 to 10,000 years. This is due to: 1) The diffusion from the bentonite into the concrete because the initial concentrations of the major ions in the concrete are lower than those of the ions in the bentonite; and 2) The mineral precipitation caused by the penetration of the alkaline plume from concrete. The precipitation of calcite leads to a decrease in the concentrations of calcium and bicarbonate. The concentrations of calcium and bicarbonate in the bentonite at 2,000 years are almost 10 times smaller than their initial values. The sharp decrease of the concentration of dissolved magnesium, from its initial concentration (0.01 mol/L) to $2 \cdot 10^{-7}$ mol/L at 10,000 years, is mainly caused by the precipitation of sepiolite and brucite.

The concentrations of dissolved Ca^{2+}, Na^{+}, HCO_3^{-}, SO_4^{2-} and Cl^{-} in the bentonite reach slowly steady values after 10,000 years. It is worth noting that after 40,000 years, the concentration of dissolved Mg^{2+} increases rapidly due to the dissolution of the brucite which had previously precipitated in the bentonite. The concentration of K^{+} in the bentonite increases slightly before 100 years due to the diffusion from the concrete where the pore water has a higher concentration of K^{+} than in the bentonite. After 100 years, the concentration of K^{+} in the bentonite pore water decreases because the pore water in the clay has a very low concentration of K^{+}.

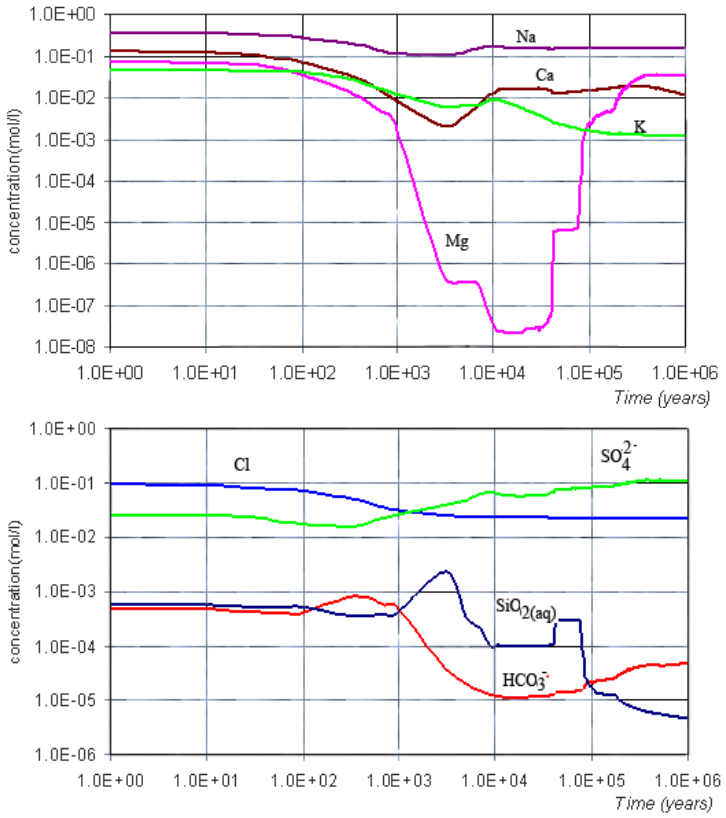

Fig. 6.79 Computed time evolution of concentrations of major ions near the bentonite-concrete interface, r = 1.125 m with the previous model

Figure 6.80 shows the cumulative amount of mineral computed at r = 1.125 m (bentonite) and r = 1.35 m (concrete). Brucite precipitates in the bentonite during 0 < t < 200,000 years. Gypsum precipitates until 300,000 years and then dissolves until it is exhausted. Quartz dissolves rapidly and then remains at equilibrium with the bentonite pore water. Calcite precipitates during 1 Ma. Sepiolite precipitates slightly for t < 200,000 years, and then remains at equilibrium with the bentonite pore water.

Portlandite is exhausted in the concrete after 40,000 years, and then tobermorite starts dissolving. Gypsum and calcite precipitate at a much smaller rate due to portlandite dissolution. Gypsum precipitates as long as portlandite dissolves until it is exhausted, but calcite does not because tobermorite starts dissolving. The precipitation of sepiolite after 60,000 years is caused also by the dissolution of tobermorite. Sepiolite stops precipitating when tobermorite is exhausted. It should be noted that the cumulative amount of calcite and gypsum in concrete is much greater than that in the bentonite.

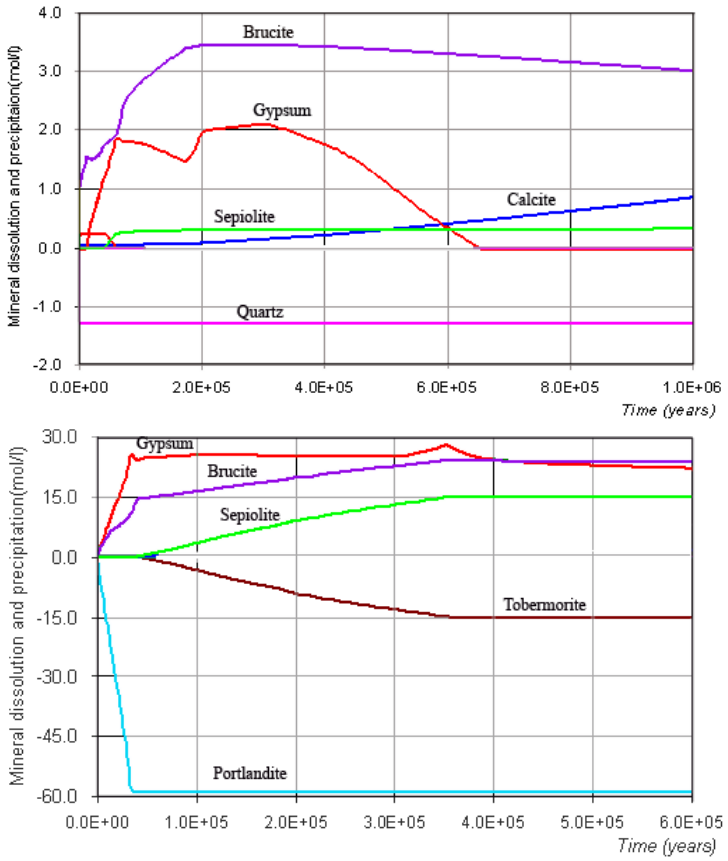

Fig. 6.80 Cumulative amount of mineral dissolution/precipitation (negative for dissolution) computed with the previous model: near the bentonite-concrete interface, r = 1.125 m (top), and at a point located in the middle of concrete liner (bottom)

Figure 6.81 shows the time evolution of the concentrations of exchanged cations in the bentonite computed with the previous model. Cation exchange plays a relevant role after several thousand years. It is after this time when exchanged Ca^{2+} concentration increases until a value near to 60 meq/100 g at 10^5 years. During this period of time Ca^{2+} replaces Mg^{2+} and K^+ in the exchanger. After 10^5 years Ca^{2+} is replaced by Mg^{2+} and released from solid phase to aqueous solution.

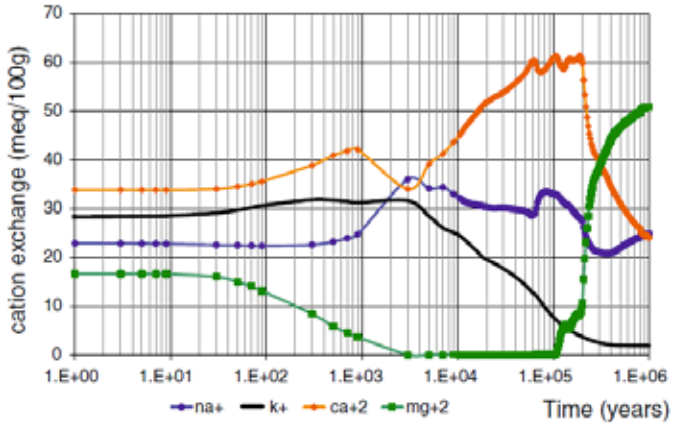

Fig. 6.81 Computed time evolution of the concentrations of the exchanged cations in the bentonite with the previous model

The pore water interacts strongly with the mineral phases and therefore the changes in porosity are important. Fig. 6.82 shows the time evolution of the changes in porosity at several locations. In the clay near the concrete-clay interface (r =1.525 m), porosity decreases from 0.37 to 0.18 after 10,000 years. Later, it keeps decreasing slowly to 0.16. Changes in porosity in the clay far from concrete-clay interface are negligible.

The porosity of bentonite decreases from its initial value of 0.407 to 0.3 during the first 200,000 years due to the precipitation of brucite and gypsum. After that, it increases slowly up to a value of 0.35.

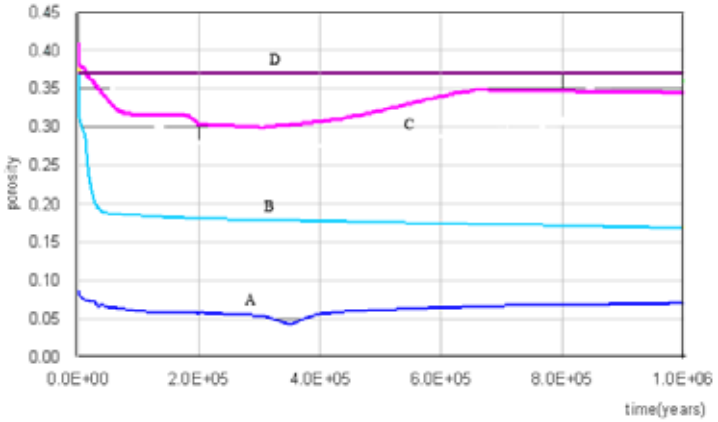

Fig. 6.82 Computed time evolution of the porosity in the bentonite (r = 0.525 m and r = 1.125 m), the concrete (r = 1.35 m) and the clay formation (r = 1.525 m and r = 13.5 m) in previous model

6.2.7.2 Updated model

The updated model considers simultaneously the interactions of corrosion products and bentonite, the interactions of the bentonite buffer, and the interactions of the concrete liner and the clay formation. The reactive transport model has been improved also by:

- Considering the kinetics of smectite dissolution
- Considering the precipitation of secondary mineral phases
- Updating the bentonite selectivity coefficients
- Taking into account proton and iron sorption by surface complexation on three types of protolysis sites

Figure 6.83 shows the time evolution of the pH computed with the updated model. The pH increases in the canister due to iron corrosion.

In the bentonite the pH decreases from its initial value because tobermorite and brucite precipitate slightly in the bentonite at 100 years. After 100 years, the pH increases and reaches the maximum at t = 10,000 years. All the bentonite is affected by the pH plume, from pH = 8.5 at the canister-bentonite interface and pH = 11.8 at the concrete-bentonite interface.

The pH in the concrete increases to 11 due to the dissolution of tobermorite. After 100 years, the pH increases in the concrete. The maximum is reached at 10,000 years. The pH in the concrete reaches 11.8 due to the simultaneous dissolution of portlandite and tobermorite. Then, it decreases after 20,000 years when the portlandite is exhausted. It decreases even more sharply after t = 100,000 when tobermorite is exhausted.

The pH front (pH > 7) penetrates 2.5 cm into the clay formation at 100 years. The pH in the clay formation is larger than 7.5 in the first 10 cm from the concrete. The clay formation is affected by the dissolution of dolomite which increases the pH with time at a value of 8 after 1Ma. The pH front (pH>8) penetrates 95 cm into clay.

The pH is equal to 9.4 in the canister, bentonite and concrete in at 1 Ma.

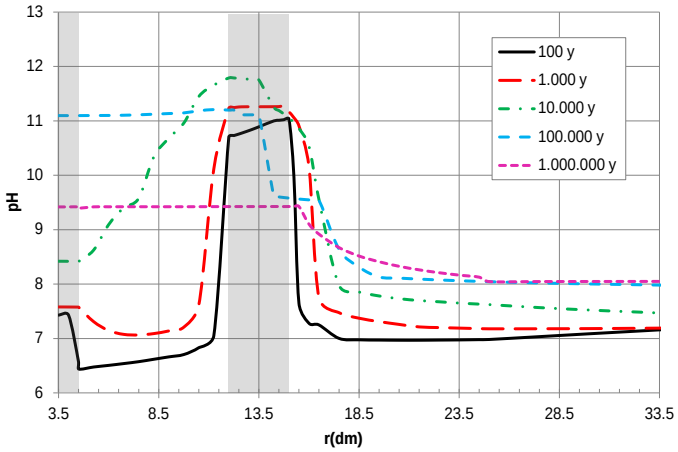

Fig. 6.83 Spatial distribution of the computed pH with the updated model at selected times

Figure 6.84, Fig. 6.85 and Fig. 6.86 show the computed evolution of the concentrations of the dissolved species in the bentonite near the bentonite-concrete interface (r = 1.125 m), in the concrete (r = 1.35 m) and in the clay formation near the concrete-clay interface (r = 1.525 m). The concentrations of the dissolved species in the bentonite decrease from t = 0 until t = 1,000 years due mainly to the solute diffusion from the bentonite into the concrete. The concentrations of dissolved of Na^+, K^+, HCO_3^-, SO_4^{2-} and Cl^- reach steady values after 1,000 years.

The precipitation of calcite and tobermorite at early times causes the decrease in the concentration of Ca^{2+} after 100 years.

The concentration of dissolved Mg^{2+} is affected by the precipitation of brucite in the bentonite near the concrete-bentonite interface. The concentration of dissolved Fe^{2+} decreases due to magnetite precipitation near the canister-bentonite interface. The strong decrease of the Fe^{2+} concentration at t = 100,000 years is associated with the previous increase of the concentration of the iron sorbed in the strong sorption sites.

The concentration of dissolved Al^{3+} in the bentonite increases due to the dissolution of the smectite. The dissolution of quartz causes the increase of dissolved silica which induces the precipitation of tobermorite initially and sepiolite afterwards near the bentonite-concrete interface.

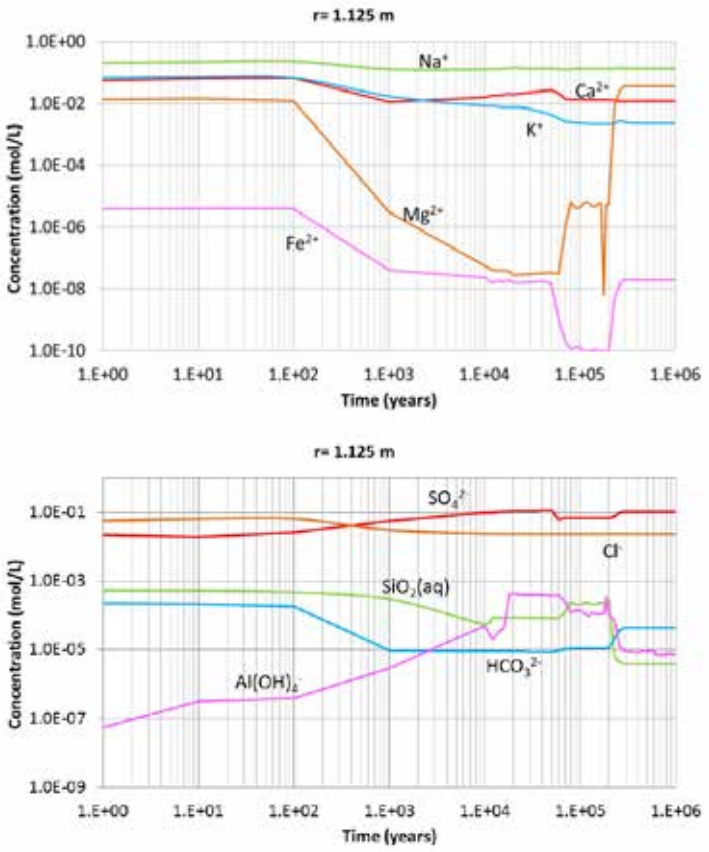

Fig. 6.84 Computed time evolution of the concentrations of the dissolved species at a point within the bentonite buffer close to the bentonite-concrete interface (r = 1.125) with the updated model

The concentrations of dissolved Na^+, K^+, Ca^{2+}, HCO_3^-, SO_4^{2-}, SiO_2 (aq) and Cl^- remain nearly stable in the concrete. The concentration of dissolved Mg^{2+} in the concrete increases after 65,000 years due to the diffusion from the bentonite, where the concentration of dissolved Mg^{2+} increases. Aluminium increases with time due to diffusion from bentonite.

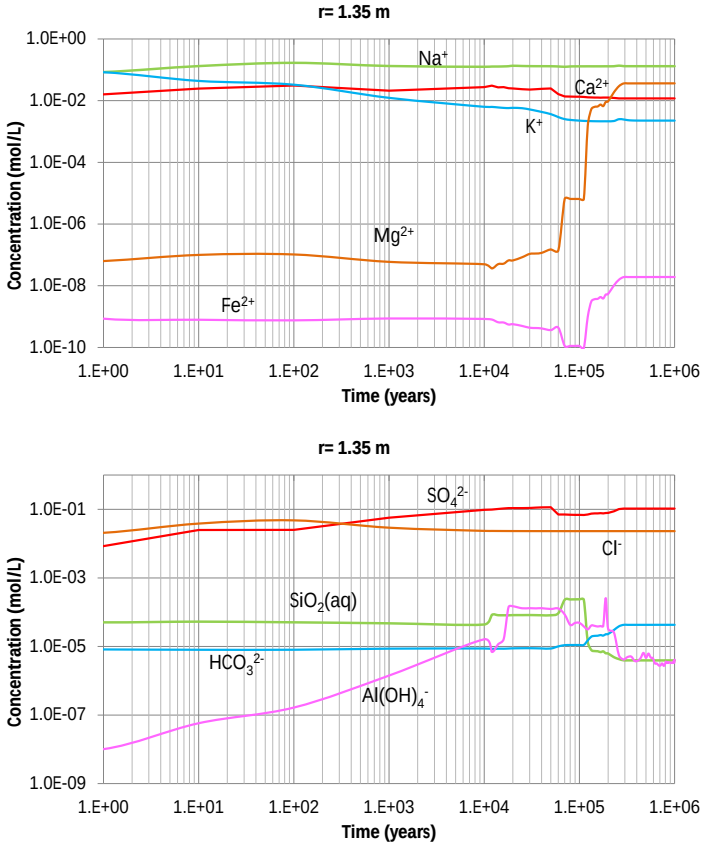

Fig. 6.85 Computed time evolution of the concentrations of the dissolved species at a point within the concrete buffer (r = 1.35 m) with the updated model

The concentrations of dissolved Na^+, K^+, Ca^{2+}, HCO_3^-, SO_4^{2-} and Cl^- at the clay-concrete interface remain stable and equal to the initial dissolved concentrations in the clay. The concentration of dissolved Mg^{2+} in the concrete-clay interface decreases after 100 years due to the precipitation of sepiolite and brucite in the clay-concrete interface. The concentration of dissolved Al^{3+} increases with time due to the Al^{3+} diffusion from the bentonite. The concentration of dissolved silica decreases with time at the clay-concrete interface due to sepiolite precipitation.

Figure 6.87 shows the cumulative precipitation of magnetite and siderite at the canister-bentonite interface. Magnetite precipitates after 1,000 years in the canister and at the interface reaching a maximum of 28 mol/L at 40,000 years. Siderite precipitates initially at a rate much lower than that of magnetite. Later, siderite dissolves. The penetration of the corrosion products into the bentonite is smaller than the penetration in the bentonite in a repository in granite.

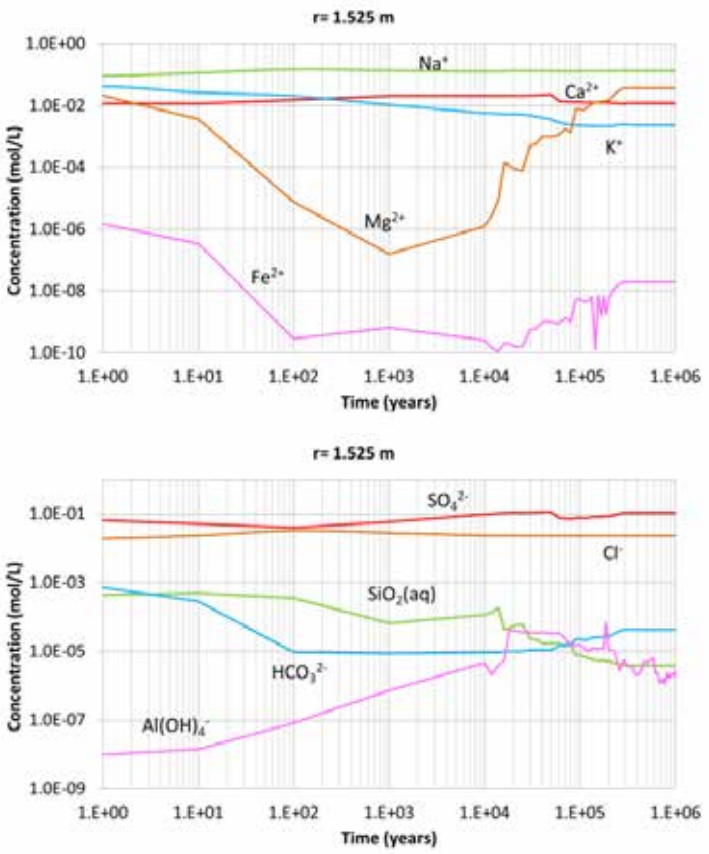

Fig. 6.86 Computed time evolution of the concentrations of the dissolved species at a point in the clay formation close to the clay-concrete interface (r = 1.525 m) with the updated model

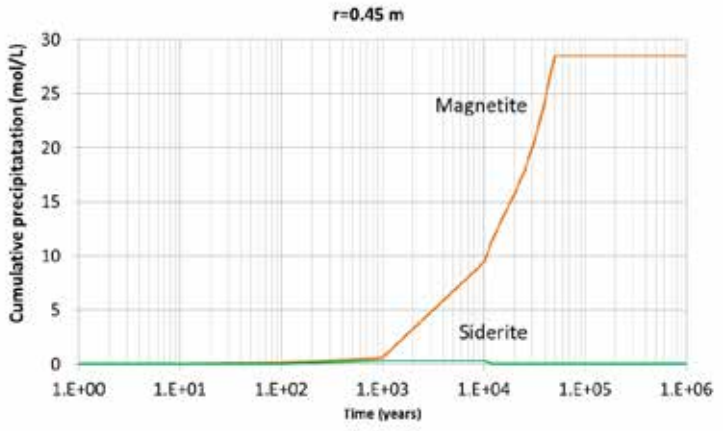

Fig. 6.87 Cumulative amount of magnetite and siderite precipitation computed at the canister-bentonite interface (r = 0.45 m) with the updated model

Figure 6.88 shows the time evolution of the concentration of the cumulative mineral precipitation/dissolution in the bentonite near the concrete-bentonite interface (r = 1.125 m). Brucite precipitates at the bentonite-concrete interface after 1,000 years. Sepiolite precipitates after 100 years. Its precipitation rate is much higher after t = 200,000 years when the dissolution of tobermorite increases the concentration of dissolved silica.

Gypsum precipitates after 200,000 years due to the temperature decrease. Quartz dissolves until 1,000 years and then silica remains at equilibrium with the pore water. Calcite precipitates in the bentonite during all the simulation time.

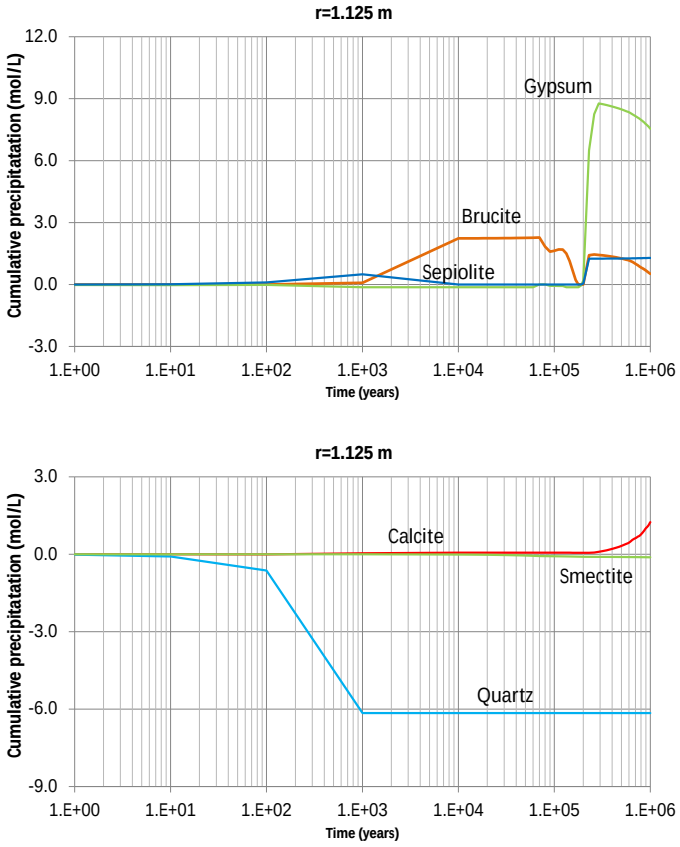

Fig. 6.88 Cumulative amount of mineral dissolution/precipitation (negative for dissolution) computed at a point within the bentonite buffer close to bentonite-concrete interface (r = 1.125 m) with the updated model

Figure 6.89 shows the computed cumulative dissolution of the smectite in the bentonite. Smectite dissolves throughout the bentonite, but its dissolution rate is highest near the concrete interface due to the high pH. Analcime precipitation is clearly linked to the dissolution of smectite. The front of analcime precipitation penetrates into the clay after 10,000 years.

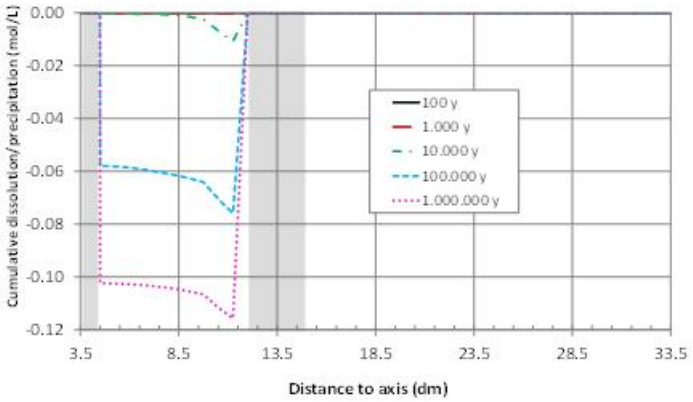

Fig. 6.89 Spatial distribution of the cumulative amount of smectite dissolution at selected times computed with the updated model

Figure 6.90 shows the time evolution of the concentration of cumulative mineral precipitation/dissolution in the concrete (r = 1.35 m). Portlandite dissolution is largest near the concrete-bentonite interface. The dissolution of portlandite stops after 20,000 years. Some small quantities of tobermorite precipitate at the bentonite-concrete and clay-concrete interfaces. Tobermorite starts dissolving in the concrete after t = 100,000 years. The dissolution of portlandite and tobermorite lead to the precipitation of gypsum, sepiolite and brucite in the concrete.

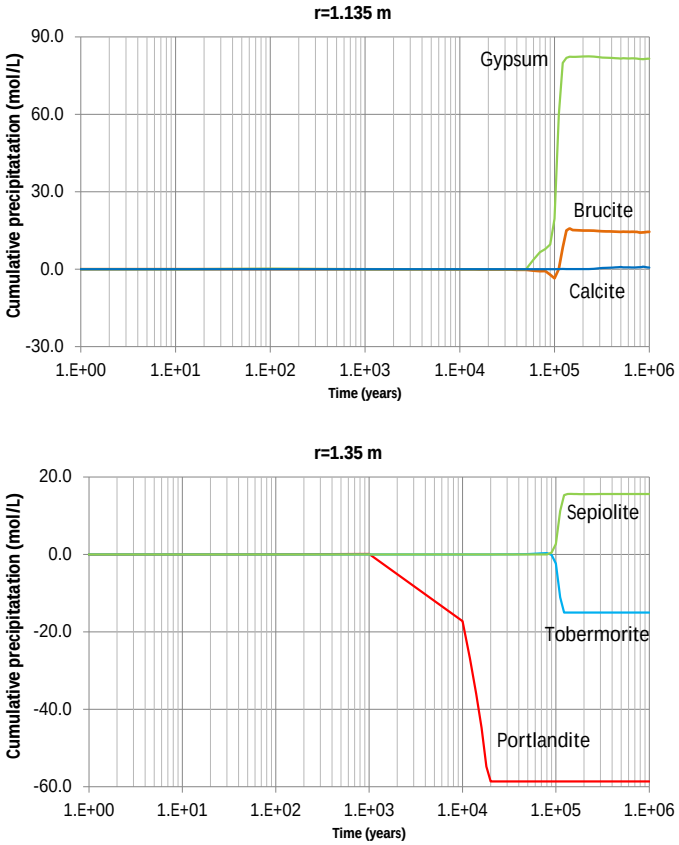

Fig. 6.90 Cumulative amount of mineral dissolution/precipitation (negative for dissolution) computed at a point within the concrete buffer (r = 1.35 m) with the updated model

Figure 6.91 shows the time evolution of the computed concentration of mineral precipitation/dissolution at the clay-concrete interface. Quartz and dolomite dissolve in the clay formation while calcite precipitates. Brucite, sepiolite and gypsum precipitate in the clay-concrete interface after t = 10,000 years.

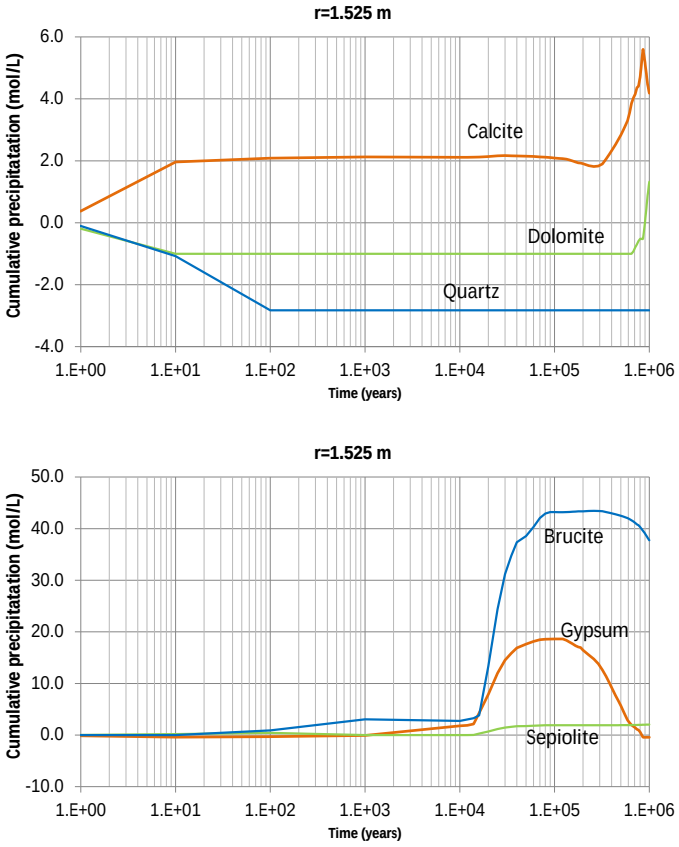

Fig. 6.91 Computed concentrations of cumulative mineral dissolution/precipitation (negative for dissolution) at a point of the clay formation located near the clay-concrete interface (r = 1.525 m) with the updated model

Figure 6.92 shows the time evolution of the porosity caused by mineral precipitation/dissolution. Pore clogging is predicted at the canister interface (r = 0.45 m) due to magnetite precipitation. The porosity decreases in the bentonite (r = 1.125 m) due to tobermorite precipitation for t < 200,000 years. After 200,000 years, tobermorite dissolves. However, brucite, calcite and gypsum precipitate and the porosity reduces to 0.08.The porosity of the concrete increases due to portlandite dissolution. At t = 100,000 years gypsum and sepiolite precipitate in the concrete and the porosity reduces to zero in the concrete. At the clay-concrete interface the porosity reduces to zero at 20,000 years due to the simultaneous precipitation of gypsum, sepiolite and brucite. The porosity of the clay at r = 13.5 m is not affected by mineral dissolution/precipitation reactions.

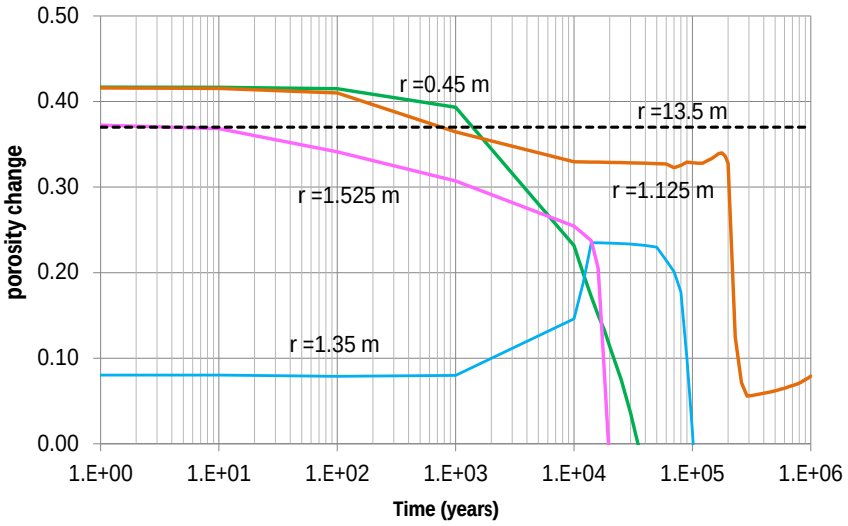

Fig. 6.92 Computed time evolution of the porosity at the bentonite-canister interface (r = 0.45 m), at the bentonite-concrete interface (r = 1.125 m), in the concrete (r = 1.35 m), at the clay-concrete interface (r = 1.525 m) and in the clay formation (r = 13.5 m) with the updated model

Figure 6.93 shows the mineral volume fractions and pH computed with the updated model at some selected times. It can be seen the dissolution of the iron of the canister (dark red curve) and the progressive precipitation of magnetite (light red curve) in the canister and at the bentonite-concrete interface. The quarz volume fraction decreases in the bentonite and in the clay (yellow). The tobermorite volume fraction (dark blue) increases in the bentonite at early times and decrease with time in the concrete. The portlandite volume fraction dissolves in the concrete (green). Gypsum replenishes the voids left by the dissolution of portlandite. Tobermorite dissolution causes the precipitation of sepiolite. After 1 Ma sepiolite, gypsum and brucite occupy the volume fraction previously occupied by portlandite and tobermorite. The volume fraction of dolomite decreases with time and causes the precipitation of brucite and sepiolite at the interface clay-concrete. In this interface, dolomite and sepiolite precipitate at 1 Ma and the, in therefore the porosity of the clay reduces.

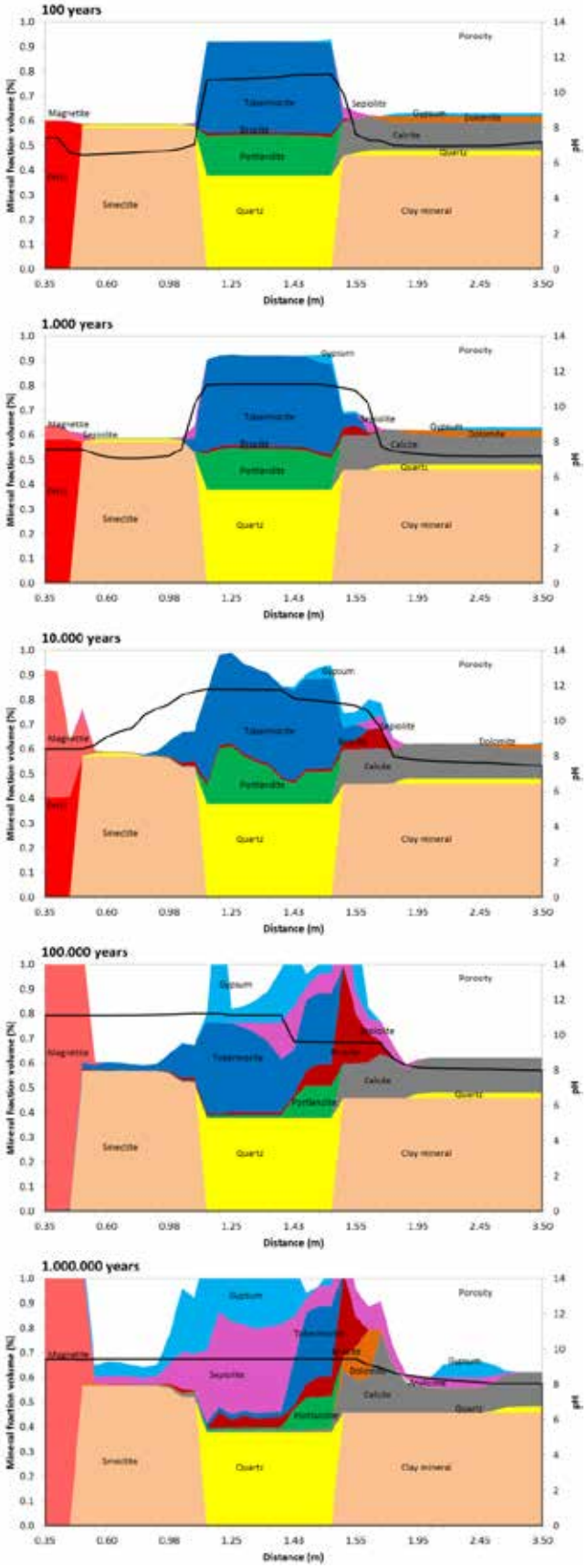

Fig. 6.93 Plots of mineral volume fractions and pH computed with the updated model at some selected times

Figure 6.94 shows the evolution of the concentrations of the exchange cations. The concentration of the exchanged K^+ decreases with time after t = 100 years at the bentonite-concrete interface while that of Ca^{2+} increases steadily until it reaches a maximum after 40,000 years. Later, the concentration of Ca^{2+} decreases sharply and stabilizes at a value of 20 meq/100 g. The computed trend of the concentration of Mg^{2+} is opposite to that of Ca^{2+} decreases. The concentration of Mg^{2+}decreases initially and becomes negligible at t = 1,000 years. It remains very small until 150,000 years. Later it increases sharply and stabilizes at a value of 56 meq/100 g. The concentration of the exchanged iron is small.

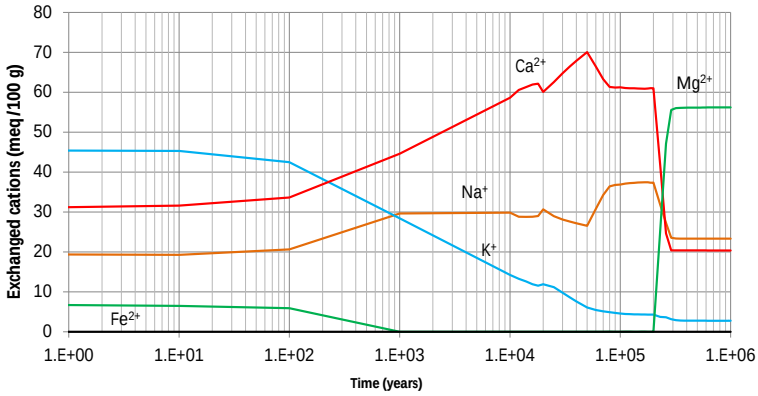

Fig. 6.94 Computed time evolution of the concentrations of the exchanged cations at the bentonite-concrete interface with the updated model at the bentonite-concrete interface (r = 1.125 m)

Figure 6.95 shows the time evolution of the concentrations of the sorbed species on strong, weak 1 and weak 2 sites computed with the updated model at the bentonite-concrete interface (r = 1.125 m). The concentration of S^sOFe^+ is the most important species in the strong sites until t = 1,000 years. Later, the concentration of S^sOFe^+ decreases and that of S^sO^- increases. $S^{w1}O^-$ is the major sorbed species in the weak 1 sites. Iron sorption is not relevant in the weak sites. The most important species in the weak 2 sites are $S^{w2}O^-$ and $S^{w2}OH^-$ which exchange each other with time. The spatial evolution of the sorbed species shows that the major species at 1Ma are $S^{w1}O^-$, $S^{w2}O^-$ and $S^{w2}OH^-$. They present a uniform distribution (Fig. 6.96).

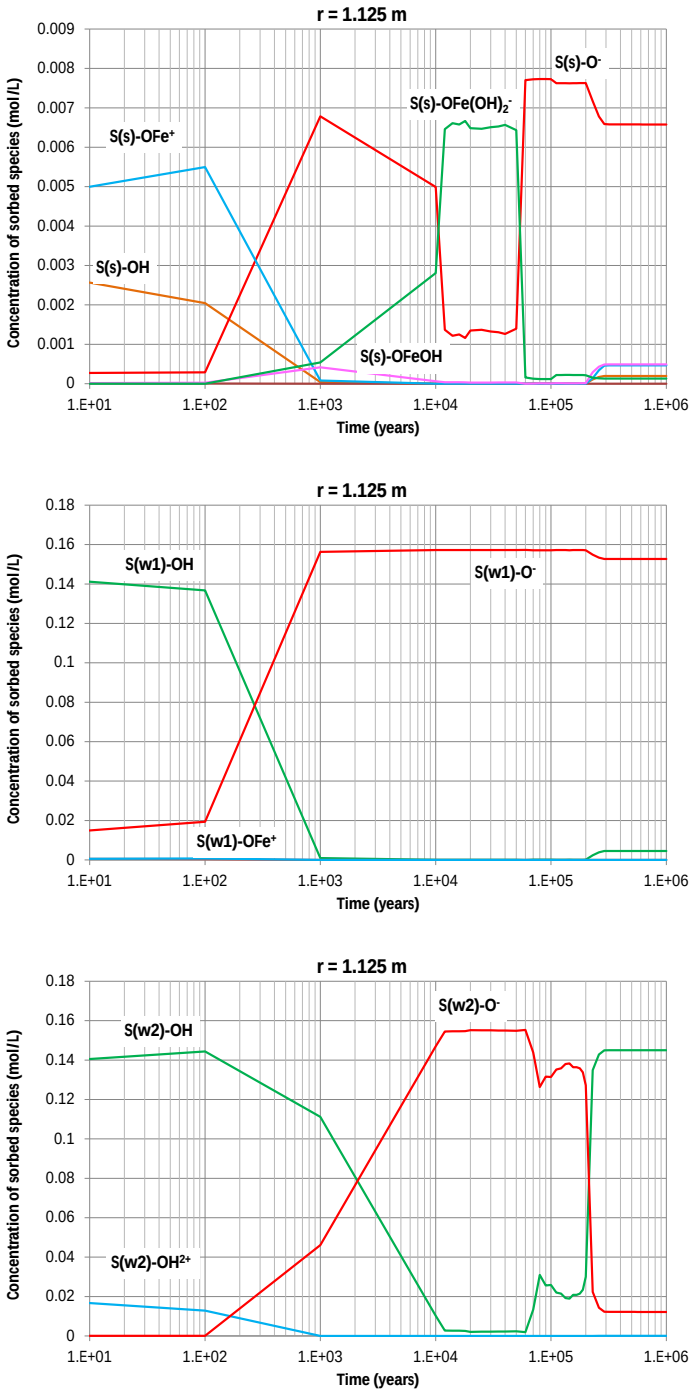

Fig. 6.95 Time evolution of the concentrations of the sorbed species on strong, weak 1 and weak 2 sites computed with the updated model

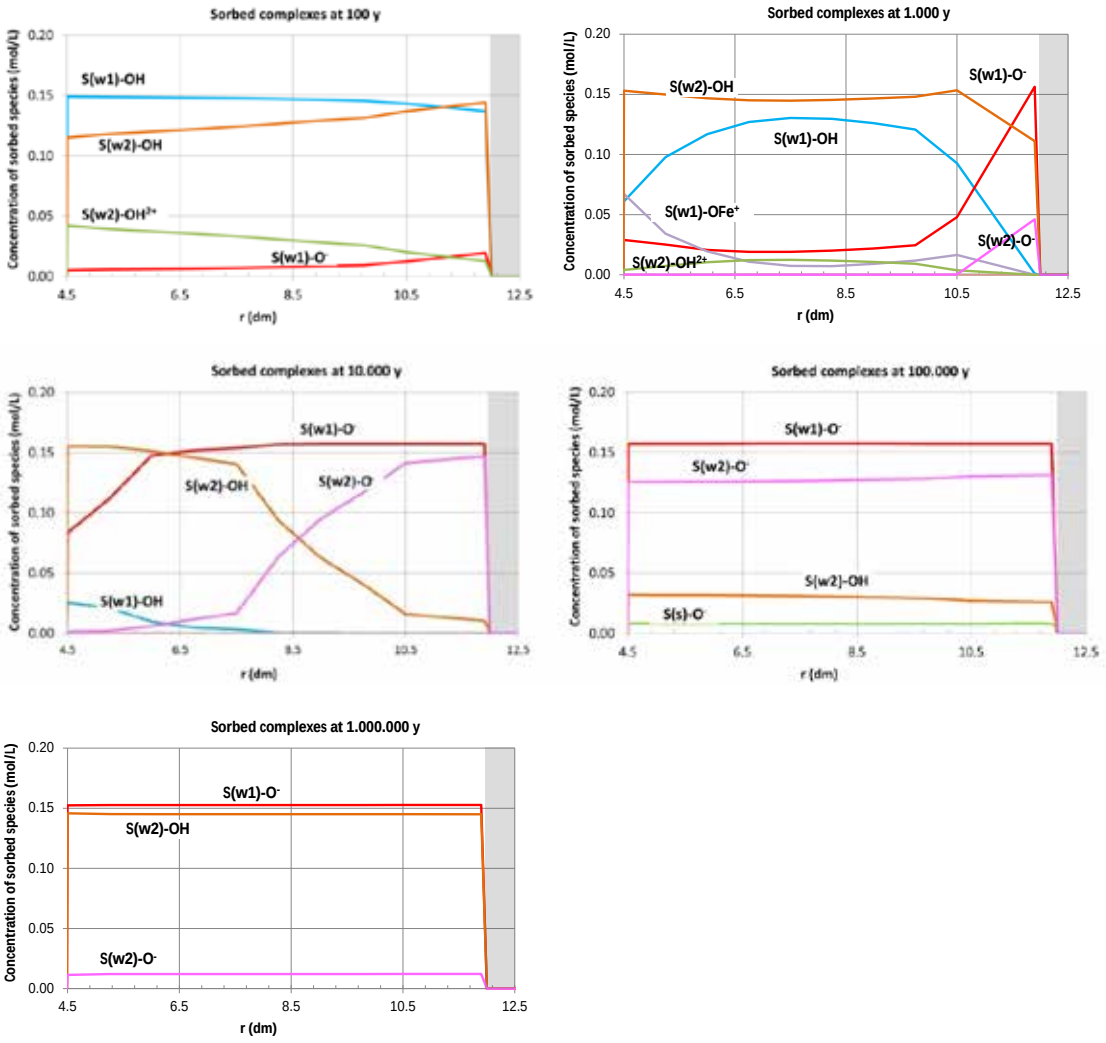

Fig. 6.96 Spatial distribution of the concentrations of the sorbed species on strong, weak 1 and weak 2 sites computed with the updated model at several times

6.2.7.3 Conclusions of the updated model

The updated model considers simultaneously the interactions of corrosion products and bentonite, the interactions of the bentonite buffer, and the interactions of the concrete liner and the clay formation. In addition, the updated model considers the kinetics of smectite dissolution, the precipitation of secondary mineral phases, takes into account proton and iron sorption by surface complexation on three types of protolysis sites and uses the calibrated values of the bentonite selectivity coefficients.

The pH front affects the entire bentonite buffer after t = 10,000 years and penetrates 0.95 m in the clay formation after 100,000 years. Table 6.17 lists the values of the penetration depths of the pH front in the bentonite and in the clay at other selected times.

Tab. 6.17 Penetration depths of the hyperalkaline pH fronts into the bentonite and the clay formation at selected times

Time (years)	pH penetration in the bentonite (pH > 7.5) (cm)	pH penetration in the clay (pH > 8) (cm)
100	-	3
1,000	15	10
10,000	75 (all bentonite)	25
100,000	75 (all bentonite)	95
1,000,000	75 (all bentonite)	95

Table 6.18 lists the values of the thickness of bentonite and clay affected by the reduction of the porosity. The following porosity reductions are considered: 15%, 50% and 100% (clogging). The values of the thickness are provided at the following interfaces: bentonite-canister, bentonite-concrete and clay-concrete. The reduction of the porosity due to mineral precipitation is not relevant until t = 10,000 years. The model predicts pore clogging at the bentonite-canister interface with a thickness of 1 cm after 1 Ma. Pore clogging is also predicted at the bentonite-concrete interface with a thickness of 2.5 cm after 1 Ma. The pore clogging is predicted to affect 5 cm after 100,000 years at the concrete-clay interface.

Tab. 6.18 Values of the thickness of bentonite and clay affected by the reduction of the porosity. The following porosity reductions are considered: 15%, 50% and 100% (clogging). Values are provided at the following interfaces: bentonite-canister, bentonite-concrete and clay-concrete

Time (years)	Affected thickness (cm)								
	Bentonite-canister interface			**Bentonite-concrete interface**			**Clay-concrete interface**		
	Porosity reduction > 15%	Porosity reduction > 50%	**Pore clogging**	Porosity reduction > 15%	Porosity reduction > 50%	**Pore clogging**	Porosity reduction > 15%	Porosity reduction > 50%	**Pore clogging**
1,000	0	0	0	0	0	0	5	0	0
10,000	1	1	0	15	0	0	15	0	0
100,000	1	1	1	15	0	0	15	10	5
1,000,000	1	1	1	22.5	15	2.5	25	12.5	2.5

Figure 6.97 shows the computed spatial distribution of the porosity at t = 10,000 years. The zone where the porosity reduces by 15% at the bentonite-canister interface is a few cm thick. At the bentonite-concrete and clay-concrete interfaces the thickness is approximately equal to 15 cm.

Figure 6.98 shows the computed spatial distribution of the porosity at t = 100,000 years. Pore clogging is computed in a 1 cm thick zone at the bentonite-concrete interface and in a 5 cm zone at the clay-concrete interface. The zone where the porosity reduces by 15% at the bentonite-concrete and clay-concrete interfaces is 15 cm thick.

Figure 6.99 shows the computed spatial distribution of the porosity at t = 1Ma. Pore clogging is computed in a 1 cm thick zone at the bentonite-concrete interface and in a 2.5 cm zone at the clay-concrete interface. The zone where the porosity reduces by 50% at the bentonite-concrete interface is 15 cm thick and at the clay-concrete interface is 12.5 cm thick. The zone where the porosity reduces by 15% at the bentonite-concrete interface is 22.5 cm thick. At this time, pore clogging affects all the concrete.

The clay-concrete interface affected by a pore reducing larger than 15% is 25 cm. The zone where the porosity reduces by 15% at the concrete-clay interface is 25 cm thick.

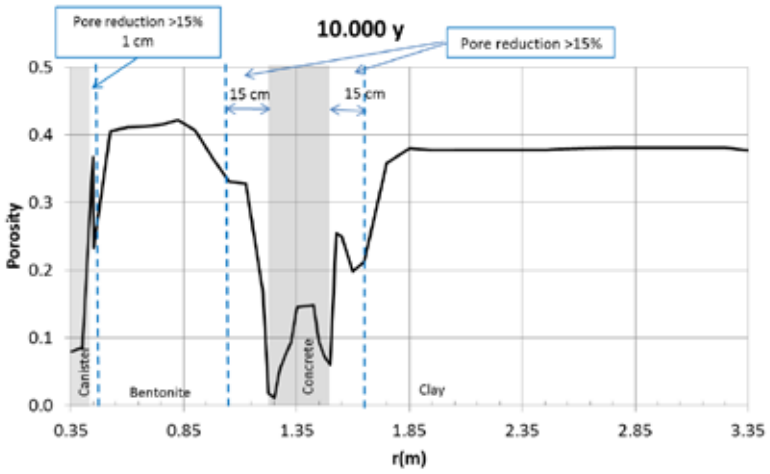

Fig. 6.97 Spatial distribution of the computed porosity at 10.000 years. Porosity changes due to mineral dissolution/precipitation reactions Blue lines indicate the zones where the porosity reduction is higher than 15%

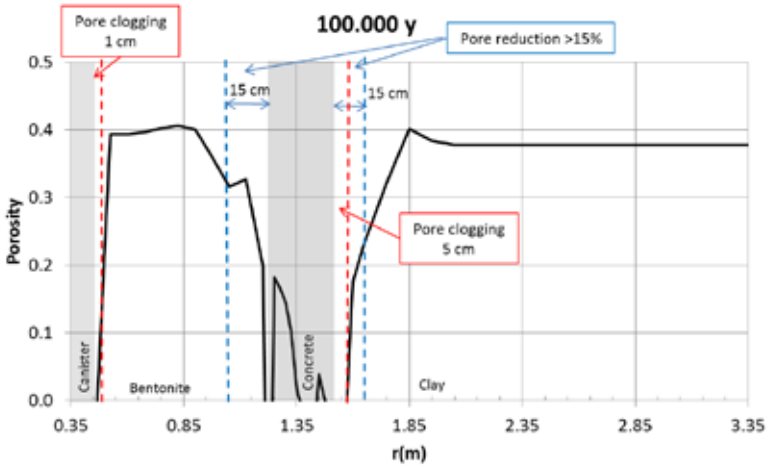

Fig. 6.98 Spatial distribution of the computed porosity at 100.000 years. Porosity changes due to mineral dissolution/precipitation reactions Blue lines indicate the zones where the porosity reduction is higher than 15%. The red line indicates the zone where the zones with pore clogging

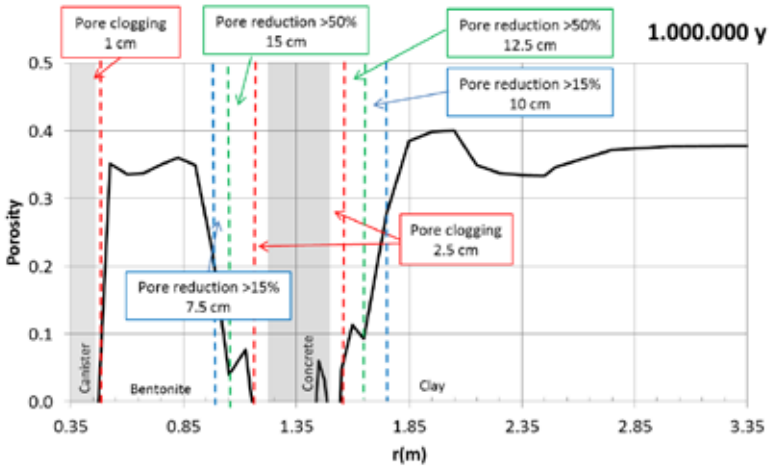

Fig. 6.99 Spatial distribution of the computed porosity at t = 1Ma. Porosity changes due to mineral dissolution/precipitation reactions. The blue lines indicate the zones where the porosity reduction is higher than 15%. The green lines indicate the zones where the porosity reduction is higher than 50%.The red line indicates the zone where the zones with pore clogging

The time evolution of the pH computed with the updated and the previous models is generally similar. The pH is slightly different in the bentonite due to canister corrosion and smectite dissolution. The maximum pH reaches nearly 12 in the concrete in both models. The final pH in the bentonite and concrete is equal to 9.5 for the previous and updated models. The penetration of the pH into clay for the updated model (0.95 m) is slightly larger than for the previous model (0.70 m). The time evolution of the concentration of most dissolved species and exchanged cations are similar for the previous and updated models, except for the concentration of the dissolved Fe^{2+} which is affected by magnetite precipitation and surface complexation.

The general patterns of the mineral dissolution/precipitation of the previous model are similar to those of the updated model. However, there are differences due to canister corrosion, the smectite dissolution and the role of surface complexation. Portlandite and tobermorite dissolve in the concrete. Brucite, gypsum and sepiolite precipitate in the concrete and at the bentonite-concrete and clay-concrete interfaces. The major differences are in the brucite, sepiolite and gypsum precipitation. The cumulative precipitation of gypsum and sepiolite in the updated model is larger than those of the previous model whereas the brucite precipitation at the bentonite-concrete interface in the updated model is lower than in the previous model. The major difference in the concrete

is the gypsum precipitation. Gypsum precipitation in the updated model is larger than in the previous model. The most relevant difference between the previous and the updated models is the porosity change. The updated model predicts more intense alterations in the bentonite and in the clay.

6.2.8 Impact of uncertainties and simplifications

The numerical predictions of the long term geochemical conditions of the EBS presented in the previous section have uncertainties due to uncertainties in the model processes and parameters. Next, we report the model results for the following parameters and processes:

1. Sensitivity to the selectivity coefficients
2. Sensitivity to the smectite dissolution
3. Sensitivity to the surface complexation
4. Sensitivity to ettringite dissolution in the concrete
5. Sensitivity to saponite precipitation

6.2.8.1 Uncertainty in material parameters

The first sensitivity run was performed to evaluate the sensitivity of model predictions to the selectivity coefficients. The values of the sensitivities of the previous and updated models are listed in Tab. 6.15. The run with the selectivities of the previous model is denoted Ksel1 and the run with the calibrated selectivities of the updated model is denoted Ksel2.

The concentration of the aqueous species, pH and the minerals in the concrete and clay are not sensitive to the selectivity coefficients. The computed concentrations of dissolved Mg^{2+}, SiO_2(aq) and Ca^{2+} with the updated model (run Ksel2) are slight. They are only relevant until t = 10,000 years. Later, both runs give identical results. Figure 6.100 shows the time evolution of the concentration of the exchanged cations at r = 1.125 m (bentonite-concrete interface). The concentrations of the exchanged Ca^{2+}, Mg^{2+} and Na^{+} computed with the updated model are larger than those of the previous

model. The concentration of the exchanged K^+ computed with the updated model is lower than that of the previous model.

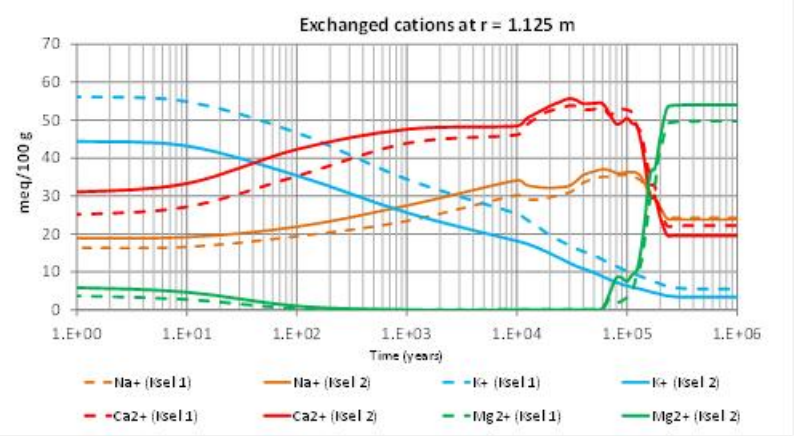

Fig. 6.100 Computed time evolution of the concentrations of the exchanged cations in the bentonite at r = 1.125 m for the previous (Ksel1) and the updated (Ksel2) models

6.2.8.2 Conceptual uncertainties in processes: influence of simplifications and neglecting processes

Sensitivity to smectite dissolution

Smectite dissolution could be relevant in hyperalkaline conditions (Huertas et al. 2001). For this reason, smectite dissolution was included in the updated model. The relevance of smectite dissolution was evaluated with a sensitivity run in which smectite dissolution and the associated secondary minerals precipitation (analcime) were disregarded. In the sensitivity run, smectite was considered as no a nonreacting mineral and analcime precipitation was disabled. The results computed with the sensitivity run are similar to those of the updated model, except for some differences.

Figure 6.101 shows the spatial distribution of the pH at 100, 1,000, 10,000 and 100,000 years computed with the updated model and the sensitivity run. The pH evolution is similar for both models. The major differences occur at t = 100,000 years. Figure 6.102 shows the spatial distribution of the pH at t = 1 Ma computed with the updated model and the sensitivity run. The pH in the sensitivity run is slightly lower than that of the updated model in the canister and in the bentonite. The penetration of the pH front (pH > 8.5) in the clay in the sensitivity run is 25 cm, clearly smaller than that of the updated model (95 cm).

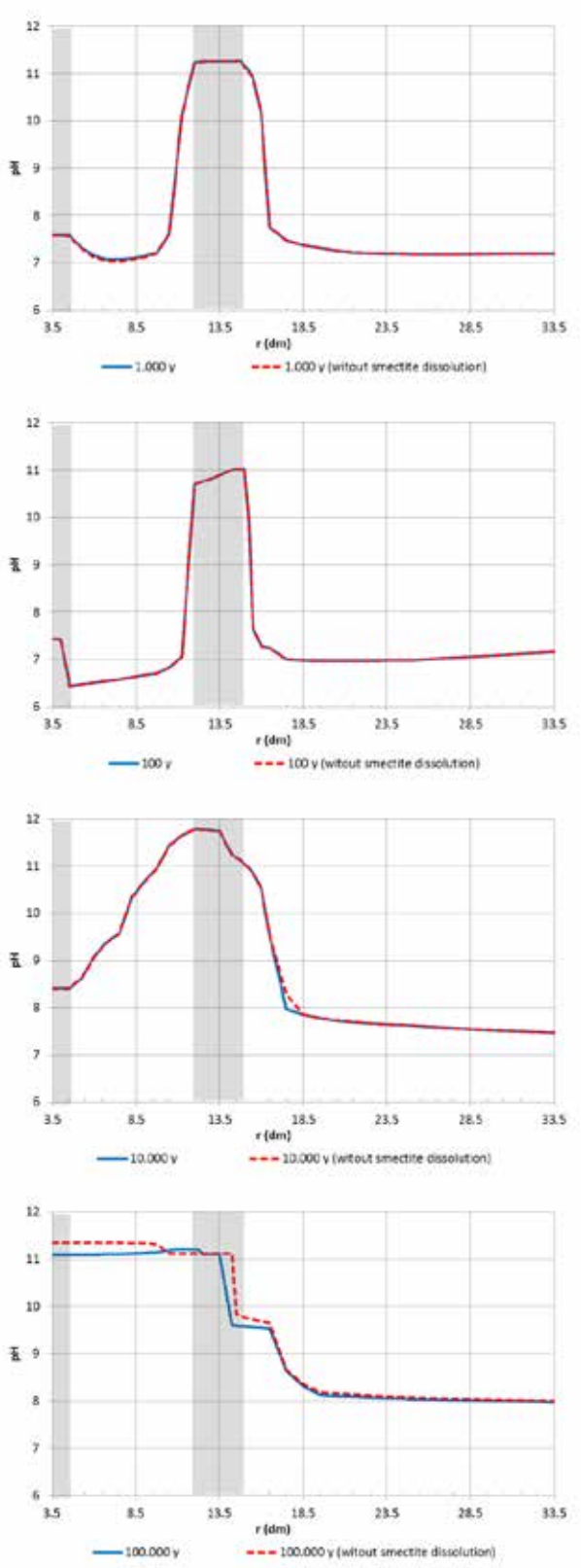

Fig. 6.101 Spatial distribution of the pH at 100, 1,000, 10,000 and 100,000 years computed with the updated model (blue line) and the sensitivity run without smectite dissolution (red discontinuous line)

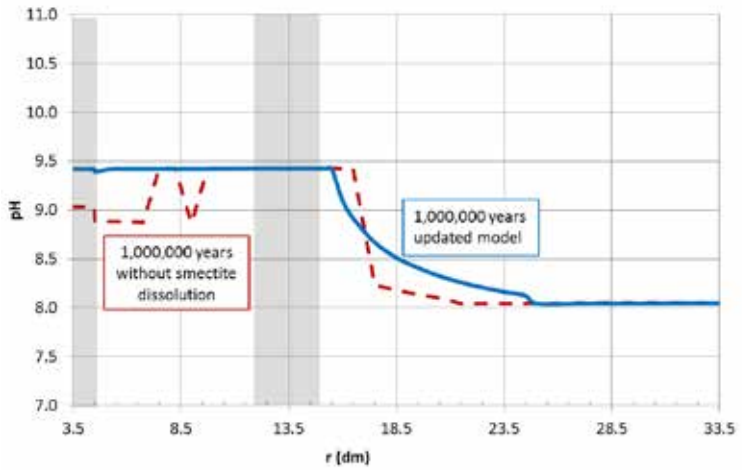

Fig. 6.102 Spatial distribution of the pH at 1 Ma computed with the updated model (blue line) and the sensitivity run without smectite dissolution (red discontinuous line)

Figure 6.103 shows the computed concentrations of the dissolved species at the bentonite-concrete interface (r = 1.125 m) with the updated model and the sensitivity run. In general, the results are similar in both model runs. The curves of magnesium show some small differences, which are related to due to differences in brucite precipitation. The concentration of the exchanged cations and sorbed species are similar for the sensitivity run and the updated model (not shown here).

Figure 6.104 and Fig. 6.105 show the cumulative mineral precipitation/dissolution at the bentonite-concrete interface and in the concrete, respectively. The concentrations of precipitated/dissolved brucite and gypsum show the largest differences. Brucite precipitation in the sensitivity run is much higher than that in the updated model at the bentonite-concrete interface. In the concrete, brucite precipitation in the sensitivity run is also higher than in the updated model. The precipitation of gypsum, however, shows an opposite trend because gypsum precipitation in the sensitivity run is lower than in the updated model.

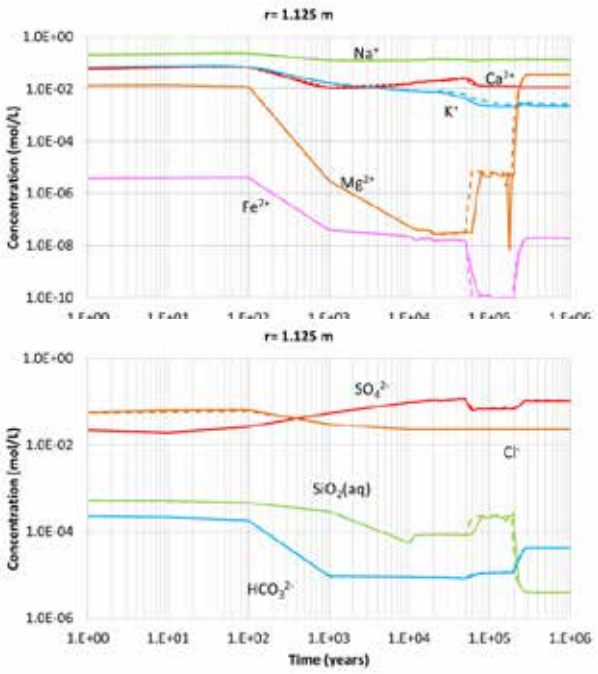

Fig. 6.103 Computed time evolution of the concentrations of the dissolved ions at the bentonite-concrete interface (r = 1.125 m) with the updated model (straight lines) and the sensitivity run (discontinuous lines)

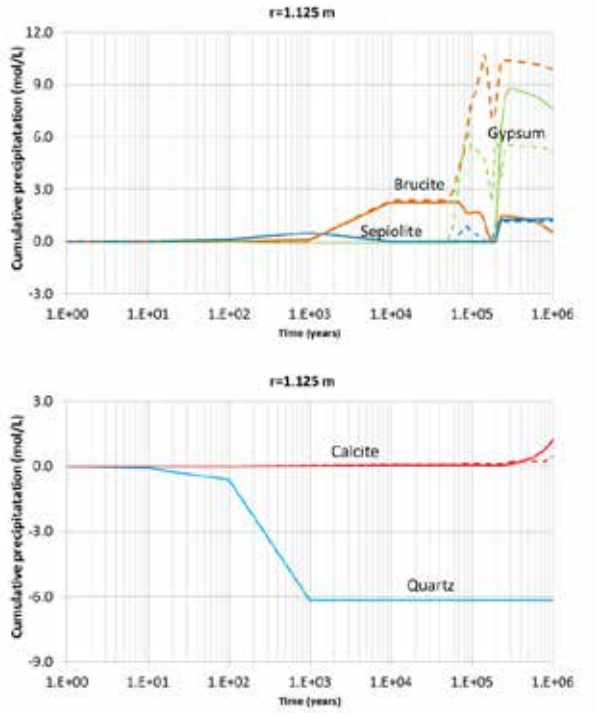

Fig. 6.104 Computed cumulative mineral precipitation/dissolution at the bentonite-concrete interface (r = 1.125 m) with the updated model (straight lines) and the sensitivity run (discontinuous lines)

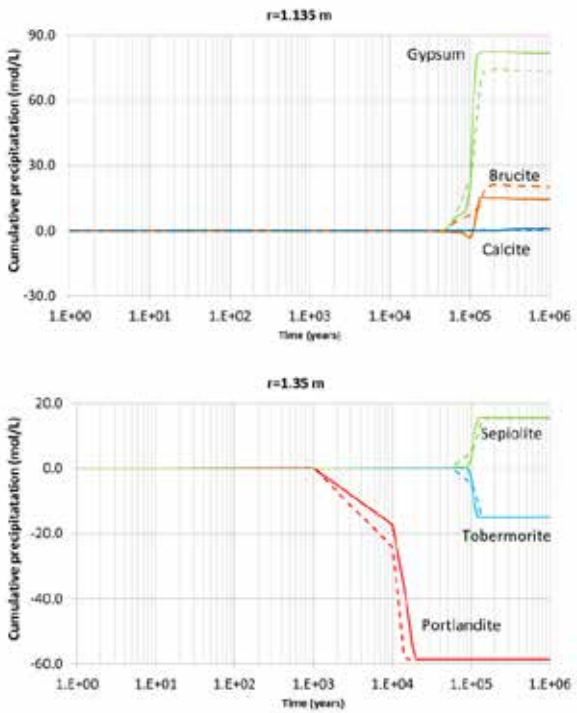

Fig. 6.105 Computed cumulative mineral precipitation/dissolution at the concrete (r = 1.35 m) with the updated model (straight lines) and the sensitivity run (discontinuous lines)

Figure 6.106 shows the spatial distribution of the mineral volume fractions and pH computed with the updated model and the sensitivity run at t = 1 Ma. The largest differences in mineral precipitation occur at the bentonite-concrete and clay-concrete interfaces. The brucite volume fraction in the sensitivity run is larger than that in the updated model at the bentonite-concrete and clay-concrete interfaces. The computed gypsum volume fractions in the sensitivity run are slightly lower than those of the updated model. Dolomite and calcite precipitation in the sensitivity run is smaller than the updated model.

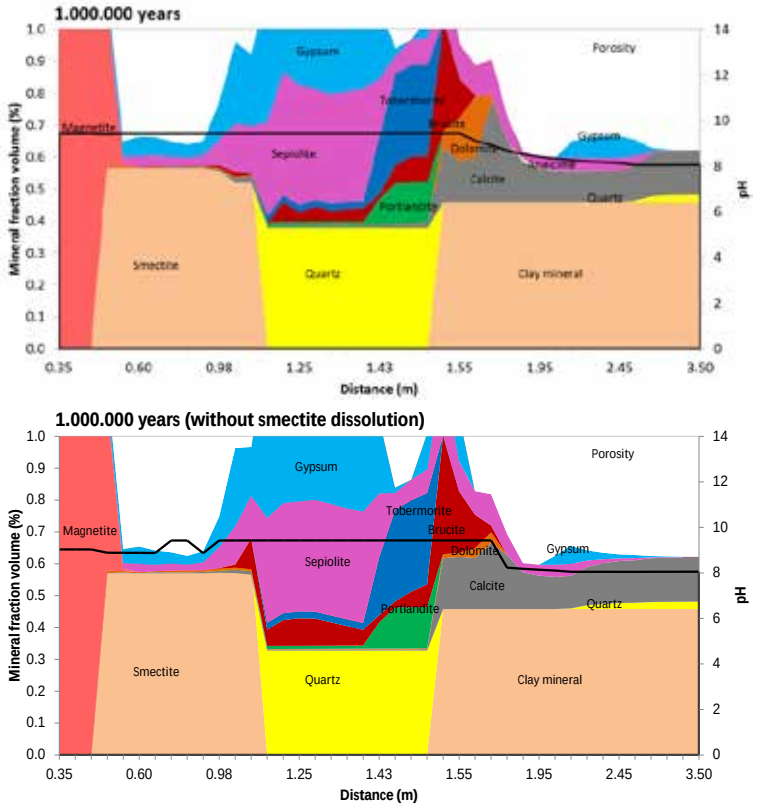

Fig. 6.106 Computed mineral volume fractions and pH at t = 1 Ma with the updated model (top) and the sensitivity run (bottom)

Figure 6.107 shows the computed time evolution of the porosity which changes due to mineral dissolution/precipitation. The computed porosities at the bentonite-canister interface (r = 0.45 m), the concrete (r = 1.35 m) and at the bentonite-concrete interface (r = 1.525 m) with the updated model and the sensitivity run show similar trends. The porosity at the bentonite-concrete interface computed with the updated model is smaller than that of the sensitivity run due to brucite precipitation during 50,000 < t < 300,000 years. However, at t = 1 Ma, the computed porosity is the same in both runs.

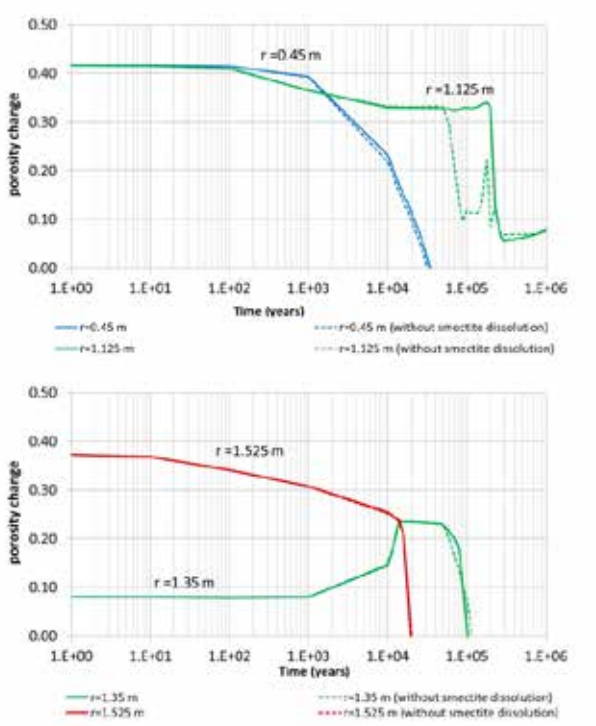

Fig. 6.107 Computed time evolution of the porosity at the bentonite-canister interface (r = 0.45 m), the bentonite-concrete interface (r = 1.125 m), in the concrete (r = 1.35 m), at the clay-concrete interface (r = 1.525 m) and in the clay formation (r = 13.5 m) with the updated model (lines) and the sensitivity run (discontinuous lines)

Sensitivity to surface complexation reactions

The relevance of surface complexation reactions was evaluated with a sensitivity run in which surface complexation reactions were disregarded. Similar to the previous model, the sensitivity run accounts for H^+ exchange.

Figure 6.108 shows the spatial distribution of the computed pH at several times with the updated model and the sensitivity run. The computed evolution of the pH of the sensitivity run shows some small differences in the bentonite compared to the updated model.

Figure 6.109 shows the spatial distribution of the pH at t = 1 Ma computed with the updated model and the sensitivity run. The pH is nearly the same in both runs. The penetration of the pH front (pH > 8.5) in the clay is not sensitive to surface complexation reactions.

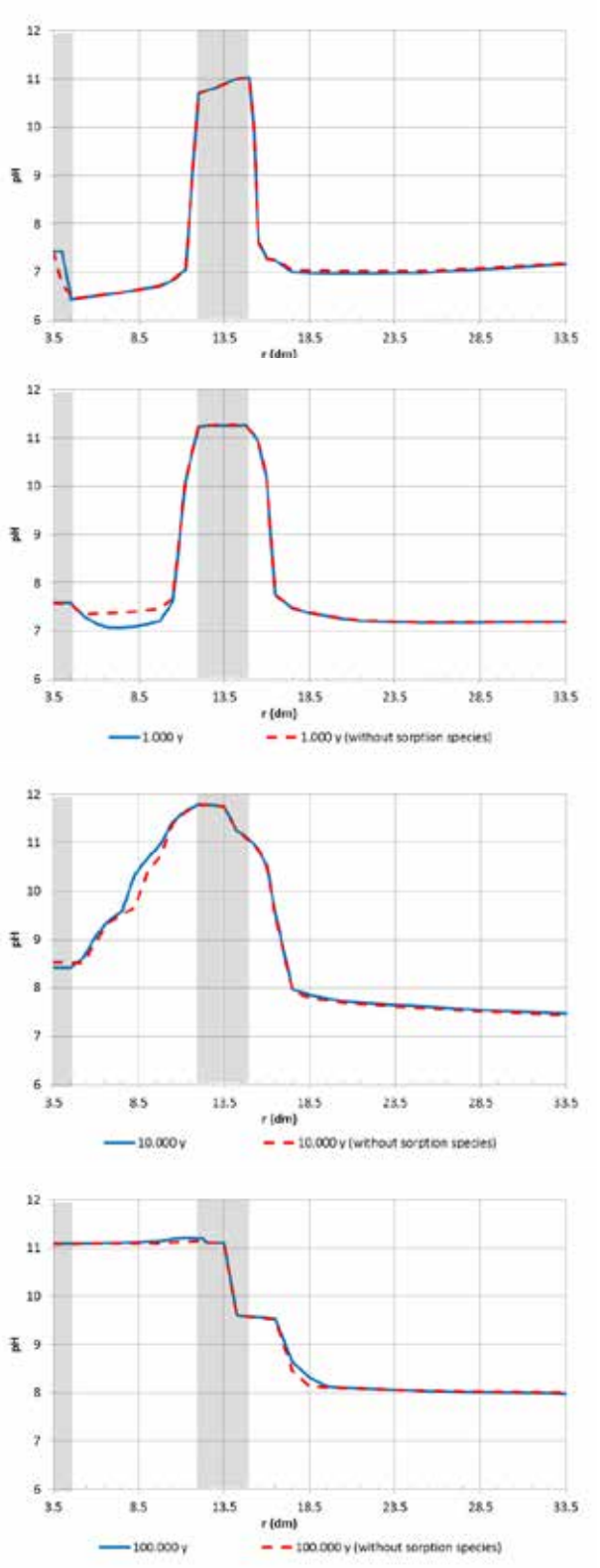

Fig. 6.108 Spatial distribution of the pH at 100, 1,000, 10,000 and 100,000 years computed with the updated model (blue line) and the sensitivity run without surface complexation reactions (red discontinuous line)

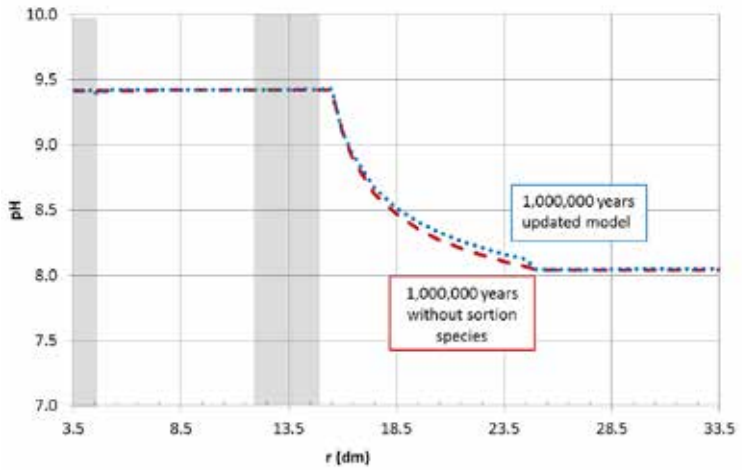

Fig. 6.109 Computed pH at t = 1 Ma for the updated and the sensitivity run (without surface complexation)

Figure 6.110 shows the computed concentrations of the dissolved species at the bentonite-concrete interface (r = 1.125 m) with the updated model and the sensitivity run. In general, the results are similar in both model runs. The curves of magnesium show some small differences, which are related to due to differences in brucite precipitation. The magnesium concentration in the sensitivity run decreases more rapidly than in the updated model around t = 200,000 years.

Figure 6.111 shows the time evolution of the precipitation of magnetite at the canister-bentonite interface with the updated model and the sensitivity run. Magnetite precipitation in the sensitivity run which neglects H^+ and Fe^{2+} sorption is larger than that of the updated model. Clearly, magnetite precipitation and Fe^{2+} sorption on surface sites compete for dissolved iron.

Figure 6.112 shows the cumulative mineral precipitation/dissolution at the bentonite-concrete interface (r = 1.125 m). In general, the computed concentrations of the mineral precipitation/dissolution are similar in the sensitivity run and the updated model. Gypsum and brucite precipitation show some small differences. Gypsum precipitation in the sensitivity run is lower than in the updated model while brucite precipitation is slightly higher than that of the updated model.

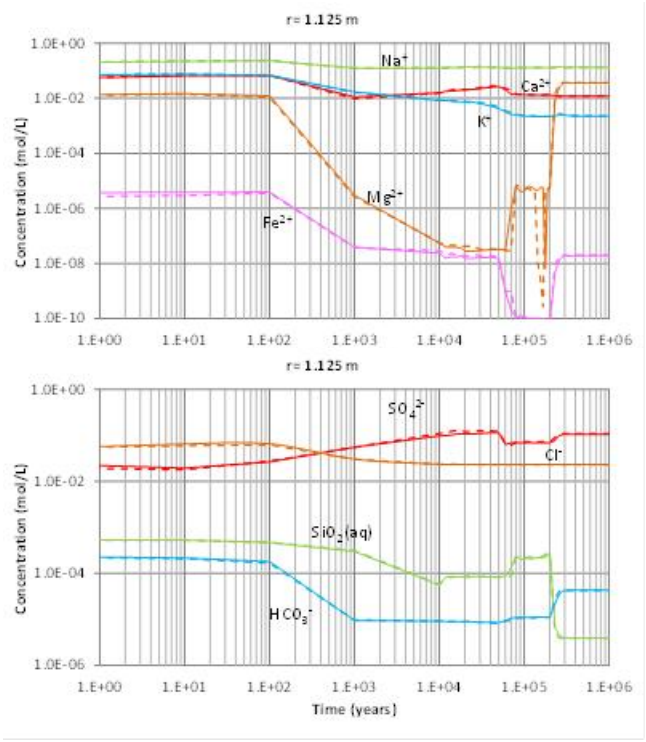

Fig. 6.110 Computed time evolution of the concentrations of the dissolved species at the bentonite-concrete interface (r = 1.125 m) with the updated model (straight lines) and the sensitivity run (discontinuous lines)

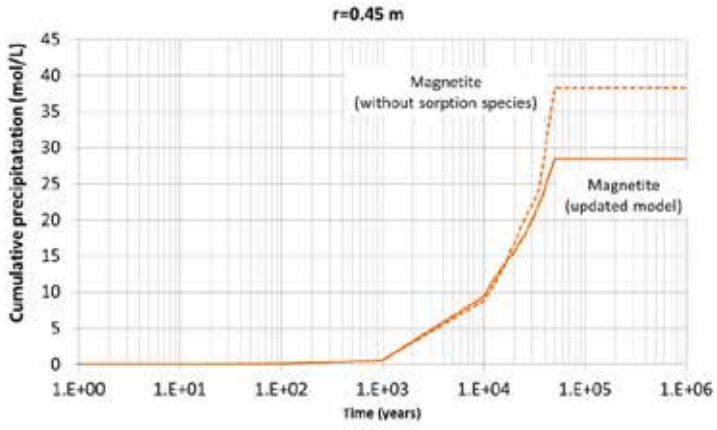

Fig. 6.111 Computed cumulative precipitation of magnetite with the updated model (line) and the sensitivity run (discontinuous line)

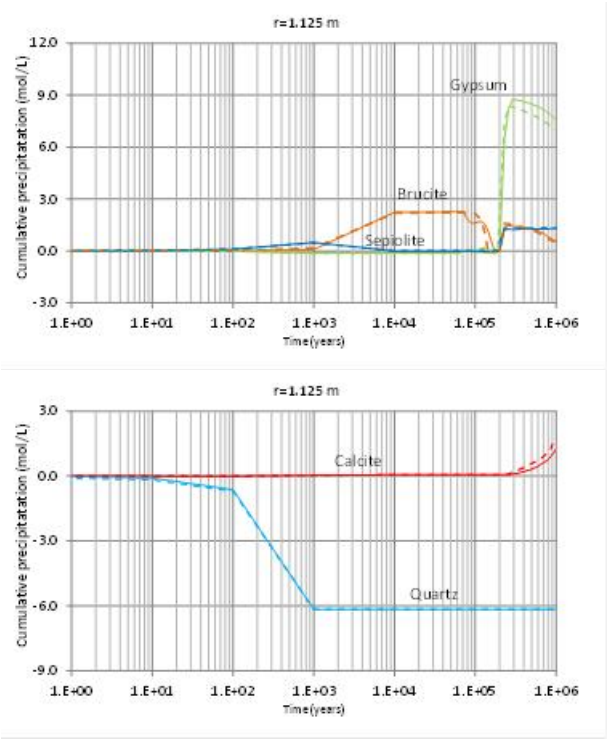

Fig. 6.112 Computed cumulative mineral precipitation/dissolution at the bentonite-concrete interface (r = 1.125 m) with the updated model (straight lines) and the sensitivity run (discontinuous lines)

Figure 6.113 shows the spatial distribution of the mineral volume fractions and pH computed with the updated model and the sensitivity run at t = 1 Ma. It can be seen that both runs provide similar results.

Figure 6.114 shows the computed time evolution of the porosity. The porosity changes are nearly the same for the updated model and the sensitivity run at the bentonite-canister, bentonite-concrete, and clay-concrete interfaces.

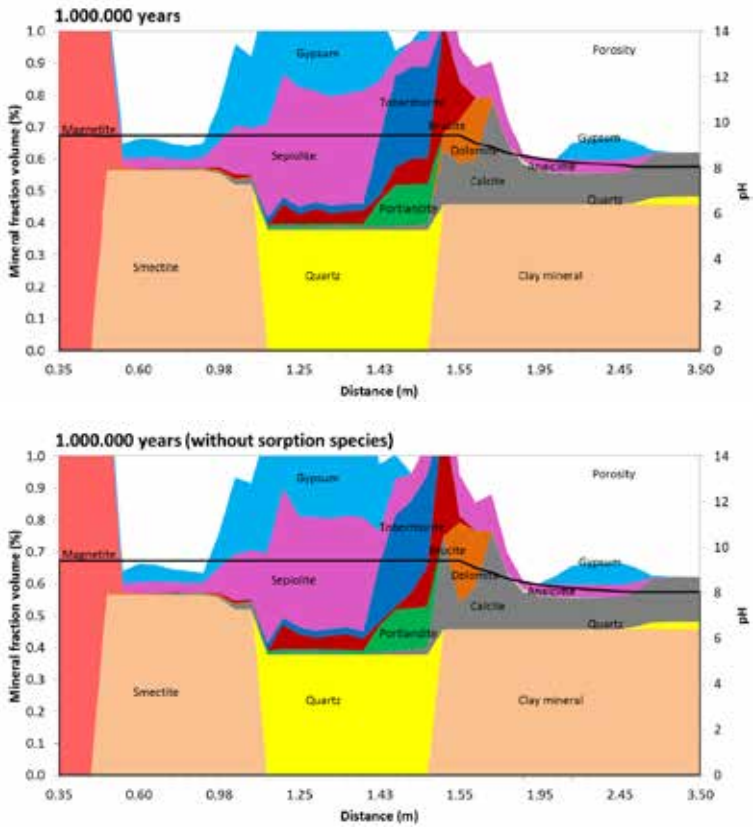

Fig. 6.113 Computed mineral volume fraction and pH at t = 1 Ma with the updated model (top) and the sensitivity run (bottom)

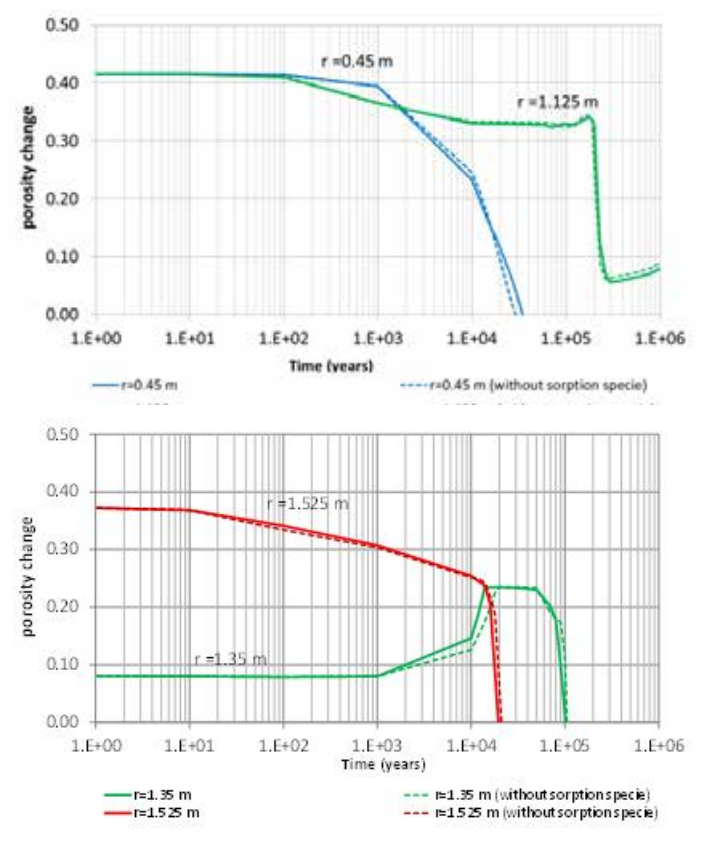

Fig. 6.114 Computed time evolution of the porosity at the bentonite-canister interface (r = 0.45 m), the bentonite-concrete interface (r = 1.125 m), in the concrete (r = 1.35 m), at the clay-concrete interface (r = 1.525 m) and in the clay formation (r = 13.5 m) with the updated model (lines) and the sensitivity run (discontinuous lines)

Sensitivity to smectite dissolution and surface complexation

The effects of different chemical reactions on the overall geochemical evolution of the EBS may add, counteract or be independent. For this reason, in this section we explore the sensitivity of the model results to the combination of surface complexation sorption and smectite dissolution. An additional sensitivity run was performed by dropping simultaneously surface complexation reactions and smectite dissolution from the updated model.

Figure 6.115 shows the spatial distribution of the pH at 100, 1,000, 10,000 and 100,000 years computed with the updated model and the sensitivity run. The pH evolution is similar for both models and similar to the surface complexation sensitivity run. The time evolution of the pH in the bentonite is more sensitivity to the surface complexation re-

actions than to smectite dissolution. However, the final pH at t = 1 Ma is more sensitivity to smectite dissolution than to the surface complexation reactions.

By neglecting simultaneously the surface complexation reactions and the smectite dissolution, the penetration of the pH front into the clay formation at t = 1 Ma decreases and the bentonite zone affected by the hyperalkaline plume is greatly reduced (Fig. 6.116). The pH in the bentonite zone nearest the canister is 8.7 in the sensitivity run. This value is lower that the value of the updated model (9.5). The pH front (pH > 8.0) penetrates into the clay formation only 30 cm, instead of the 95 cm of the updated model.

Figure 6.117 shows the computed concentrations of the dissolved species at the bentonite-concrete interface (r = 1.125 m) with the updated model and the sensitivity run. In general, the results are similar in both runs. There are some small differences in the magnesium and sulphate curves which are due to slight differences in the precipitation of gypsum and brucite.

Figure 6.118 shows the cumulative mineral precipitation/dissolution at the bentonite-concrete interface. Calcite precipitation in the sensitivity run is slightly smaller than that of the updated model.

Figure 6.119 shows the computed cumulative precipitation of magnetite at the canister-bentonite interface. The magnetite precipitation in the sensitivity run is slightly larger than that of the updated model. However, the differences in this sensitivity run are smaller than those of the sensitivity run in which only the surface complexation reactions are neglected. It can be concluded that magnetite precipitation is sensitivity to surface complexation reactions.

Figure 6.120 shows the spatial distribution of the mineral volume fractions and pH computed with the updated model and the sensitivity run at t = 1 Ma. The largest differences correspond to dolomite precipitation at the clay formation.

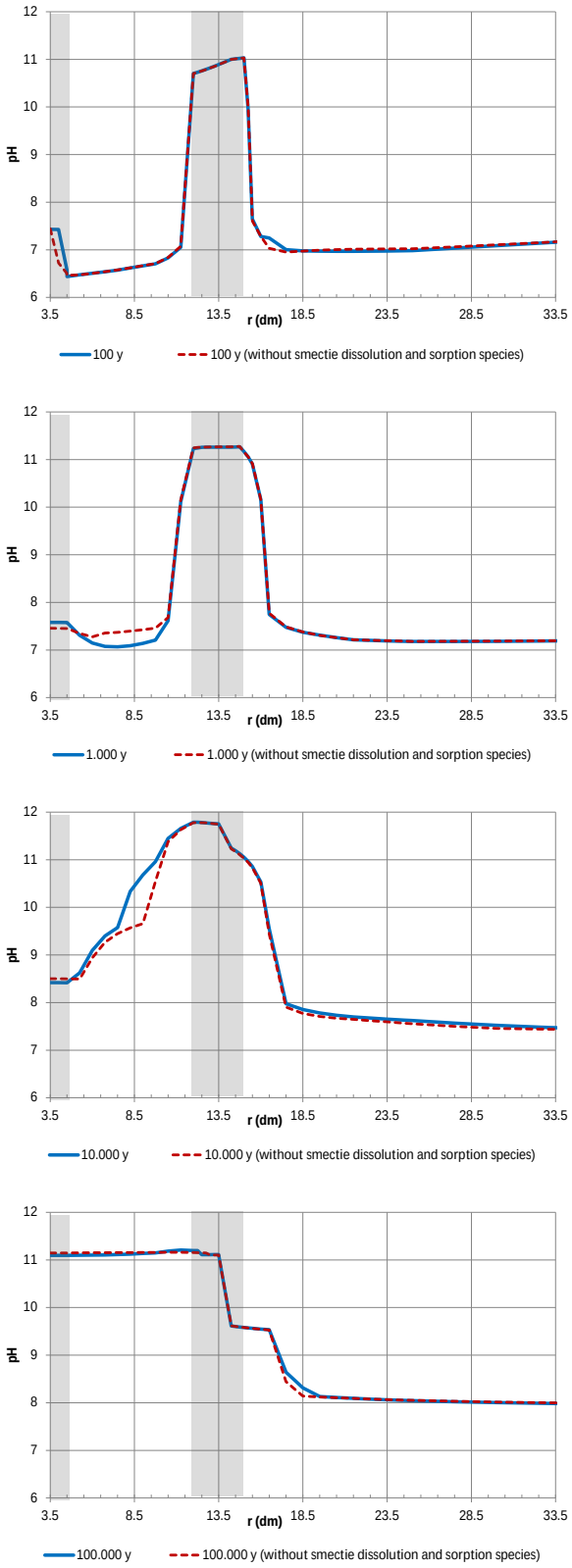

Fig. 6.115 Spatial distribution of the pH at 100, 1,000, 10,000 and 100,000 years computed with the updated model (blue line) and the sensitivity run without surface complexation reactions and smectite dissolution (red discontinuous line)

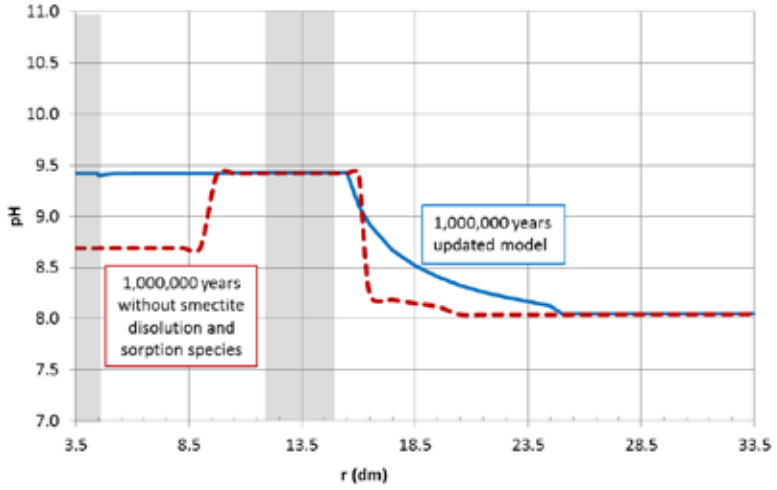

Fig. 6.116 Spatial distribution of the pH at 1 Ma computed with the updated model (blue line) and the sensitivity run without surface complexation reactions and smectite dissolution (red discontinuous line)

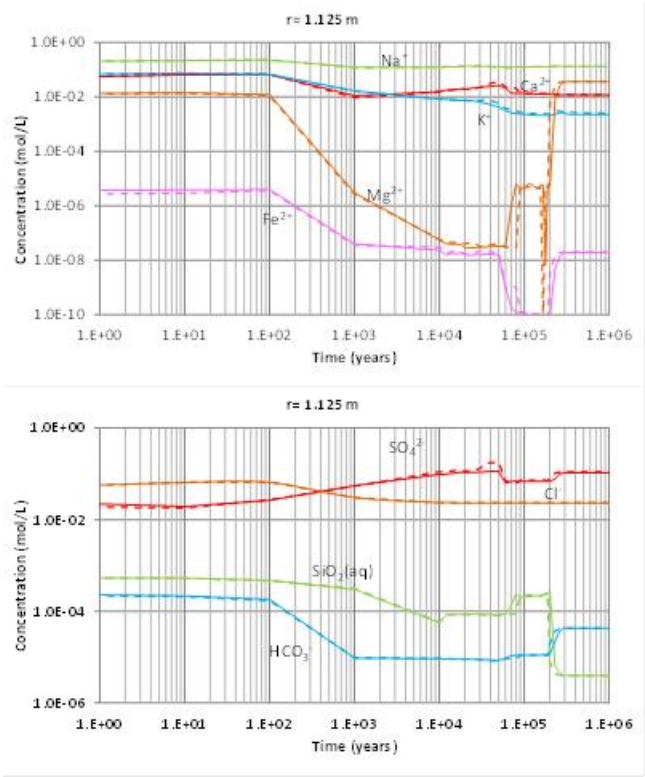

Fig. 6.117 Computed time evolution of the concentrations of the dissolved ions at the bentonite-concrete interface (r = 1.125 m) with the updated model (straight lines) and the sensitivity run (discontinuous lines)

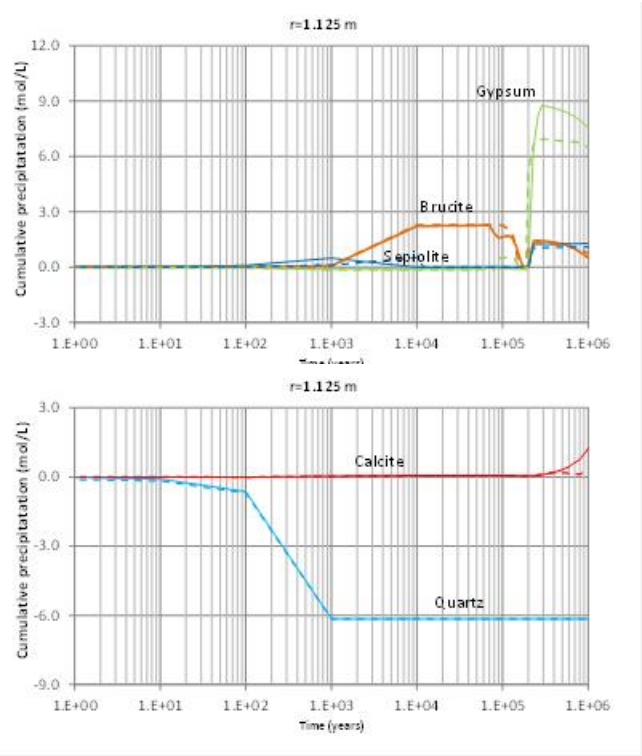

Fig. 6.118 Computed cumulative mineral precipitation/dissolution at the bentonite-concrete interface (r = 1.125 m) with the updated model (straight lines) and the sensitivity run (discontinuous lines)

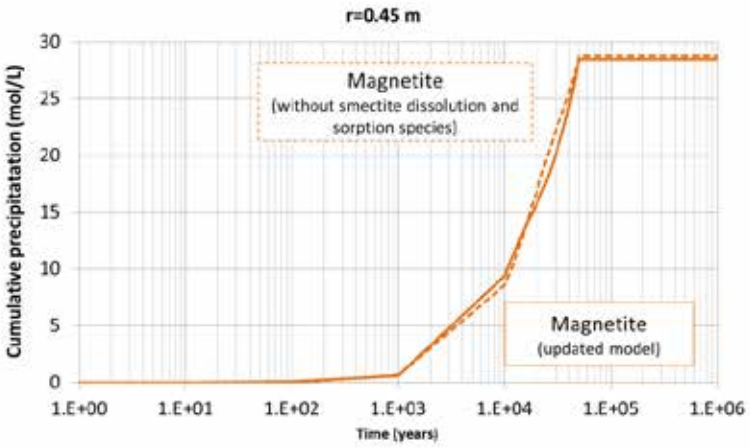

Fig. 6.119 Computed cumulative precipitation of magnetite with the updated model (straight line) and the sensitivity run (discontinuous line)

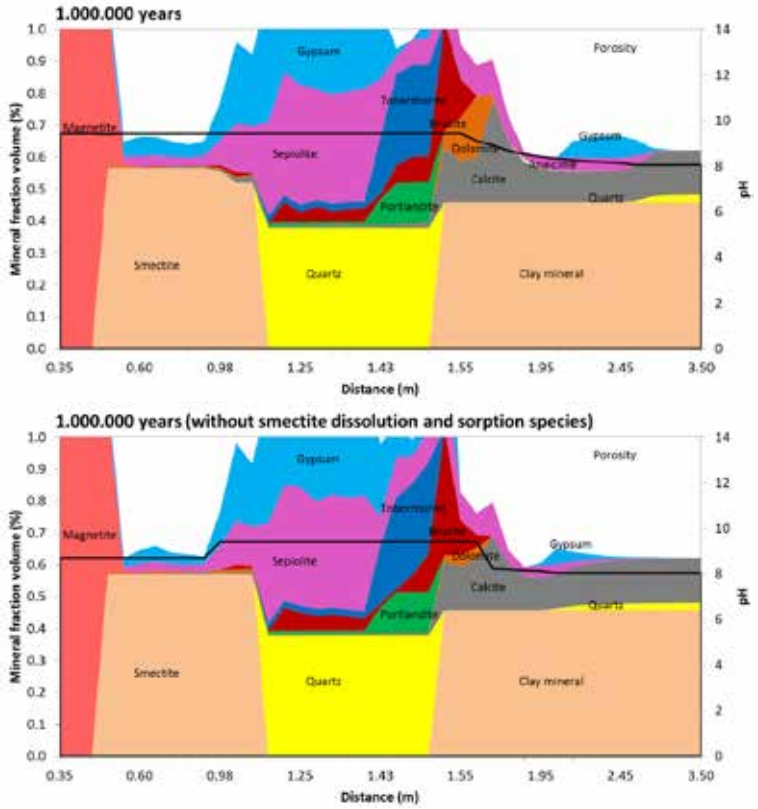

Fig. 6.120 Computed mineral volume fractions and pH at t = 1 Ma with the updated model (top) and the sensitivity run (bottom)

Figure 6.121 shows the computed time evolution of the porosity which changes due to mineral dissolution/precipitation. The porosity changes are slightly similar for the sensitivity run and the updated model because mineral precipitation/dissolution is similar in both runs. It can be noticed that the porosity at the bentonite-concrete interface reduces to 0.13 in the sensitivity run, instead to 0.08 in the updated model. This difference is due to gypsum precipitation, which in the sensitivity run is smaller than that in the updated model.

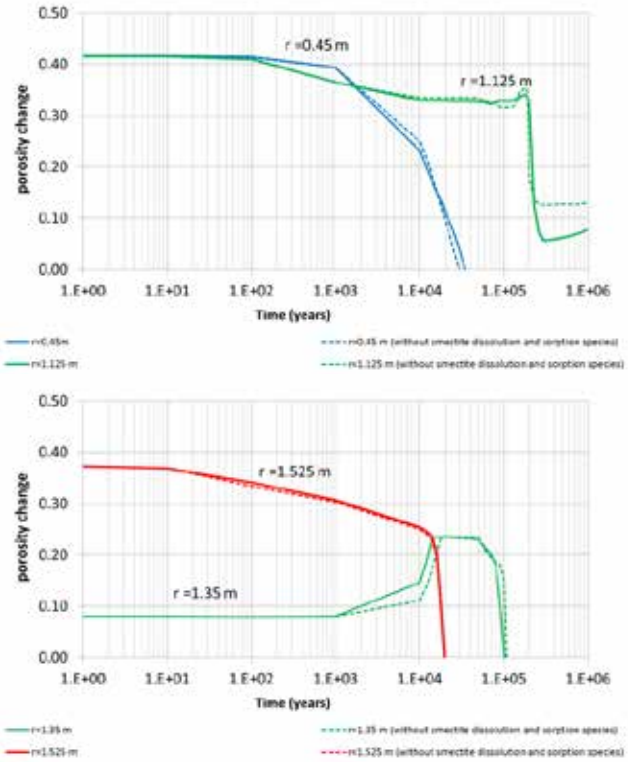

Fig. 6.121 Computed time evolution of the porosity at the bentonite-canister interface (r = 0.45 m), the bentonite-concrete interface (r = 1.125 m), in the concrete (r = 1.35 m), at the clay-concrete interface (r = 1.525 m) and in the clay formation (r = 13.5 m) with the updated model (lines) and the sensitivity run (discontinuous lines)

Sensitivity to ettringite dissolution in the concrete

The dissolution of the ettringite could be an important chemical reaction during concrete degradation. This sensitivity run addresses the relevance of the dissolution of ettringite in the concrete. To avoid convergence problems, the sensitivity run was performed based on the previous sensitivity run without smectite dissolution and surface complexation.

An initial mineral volume fraction of 5% of ettringite was considered in the concrete. Ettringite dissolution was assumed at chemical equilibrium.

Figure 6.122 shows the spatial distribution of the pH at 100, 1,000, 10,000 and 100,000 years computed with the updated model and the sensitivity run. The pH evolution is similar for the updated model and the sensitivity run with ettringite dissolution and with-

out esmectite dissolution and surface complexation. The time evolution of the pH is not sensitive to the ettringite dissolution in the concrete.

Figure 6.123 shows the spatial distribution of the pH at t = 1 Ma computed with the updated model and the sensitivity run. The pH of the sensitivity run without smectite dissolution and surface complexation is slightly different to the pH of the updated model. The pH front (pH > 8.7) penetrates 30 cm into the bentonite. The penetration of the pH front (pH > 8.0) in the clay in the sensitivity run is 30 cm, clearly smaller than that of the updated model (95 cm).

Figure 6.124 shows the computed concentrations of the dissolved species at the bentonite-concrete interface (r = 1.125 m) with the updated model and the sensitivity run. The results of both model runs are similar. The curves of magnesium and sulphate show some small differences, which are related to due to differences in brucite, sepiolite and gypsum precipitation.

Figure 6.125 shows the cumulative mineral precipitation/dissolution at the bentonite-concrete interface. The computed results show similar trends. However, there are some differences in gypsum and brucite. The cumulative precipitation of these minerals in the sensitivity run is larger than in the updated model. The same behaviour can be seen in the concrete (Fig. 6.126).

Figure 6.127 shows the spatial distribution of the mineral volume fractions and pH computed with the updated model and the sensitivity run at t = 1 Ma. Ettringite dissolves in the concrete after 100,000 years. Ettringite has not dissolved entirely after at 1 Ma. The main effects of the presence of ettringite occur in the concrete and at the bentonite-concrete and the clay-concrete interfaces. The dissolution of the ettringite increases the concentration of dissolved sulphate in the concrete pore water. This leads to an additional precipitation of gypsum. In fact, gypsum precipitation in the sensitivity run in the concrete and at the bentonite-concrete interface is larger than in the updated model. The volume fractions of the rest of the minerals do not show significant differences.

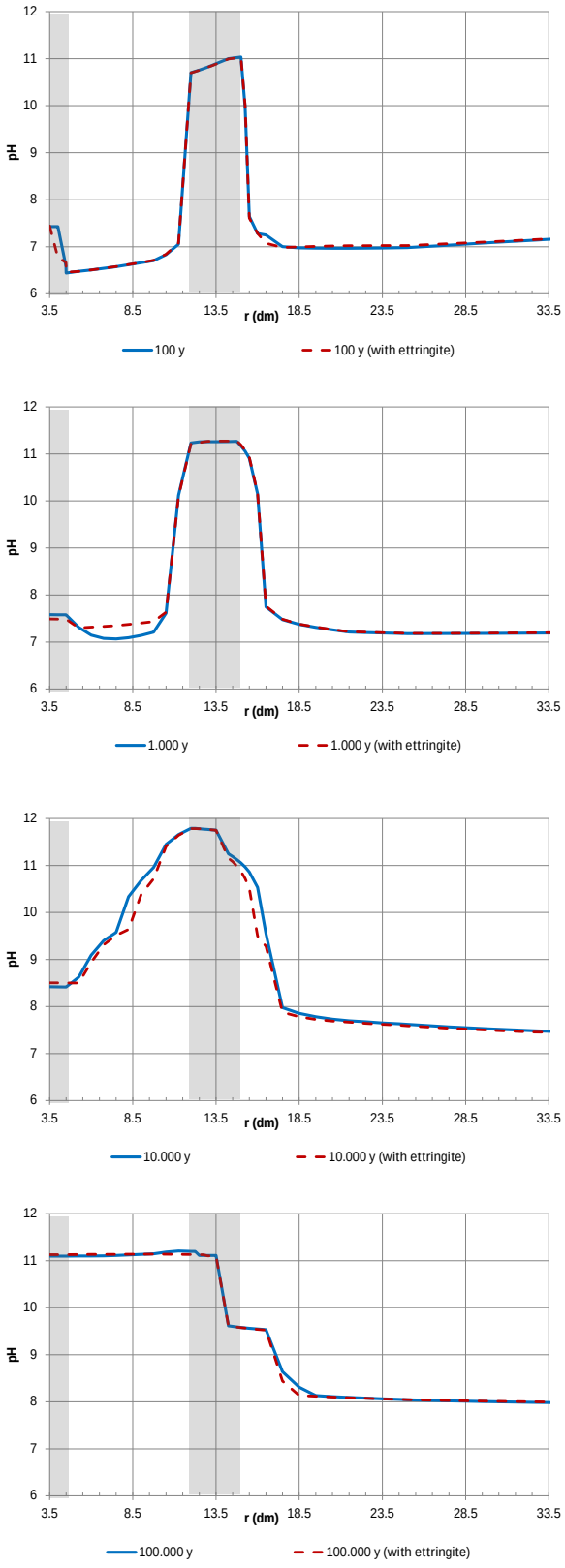

Fig. 6.122 Spatial distribution of the pH at 100, 1,000, 10,000 and 100,000 years computed with the updated model (blue line) and the sensitivity run with ettringite dissolution (red discontinuous line)

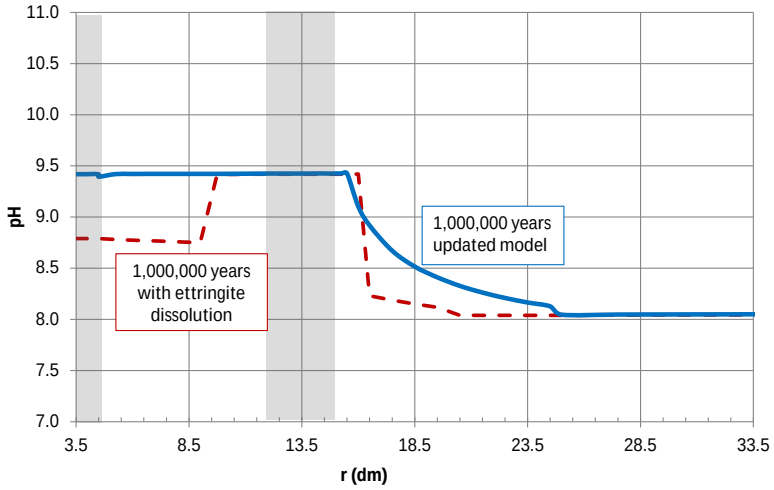

Fig. 6.123 Spatial distribution of the pH at 1 Ma computed with the updated model (blue line) and the sensitivity run with ettringite dissolution (red discontinuous line)

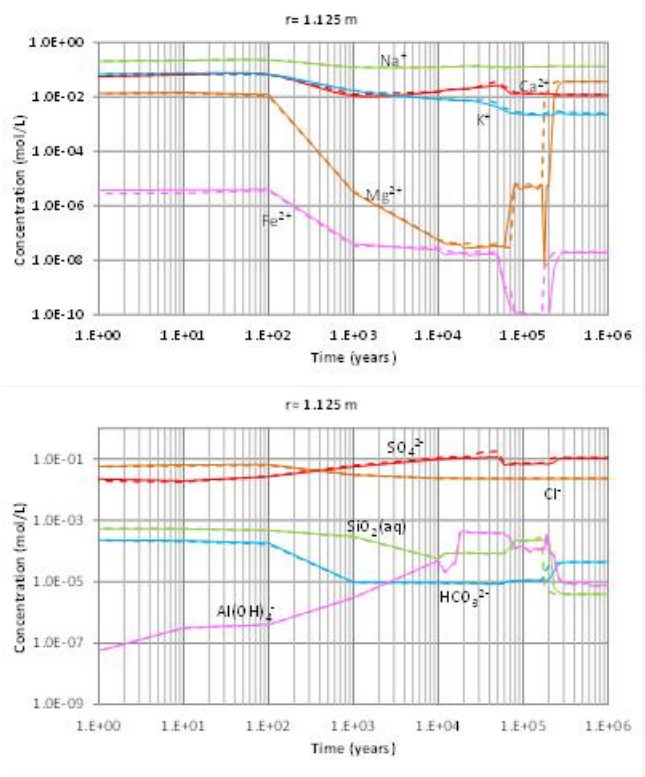

Fig. 6.124 Computed time evolution of the concentrations of the dissolved ions at the bentonite-concrete interface (r = 1.125 m) with the updated model (straight lines) and the sensitivity run (discontinuous lines)

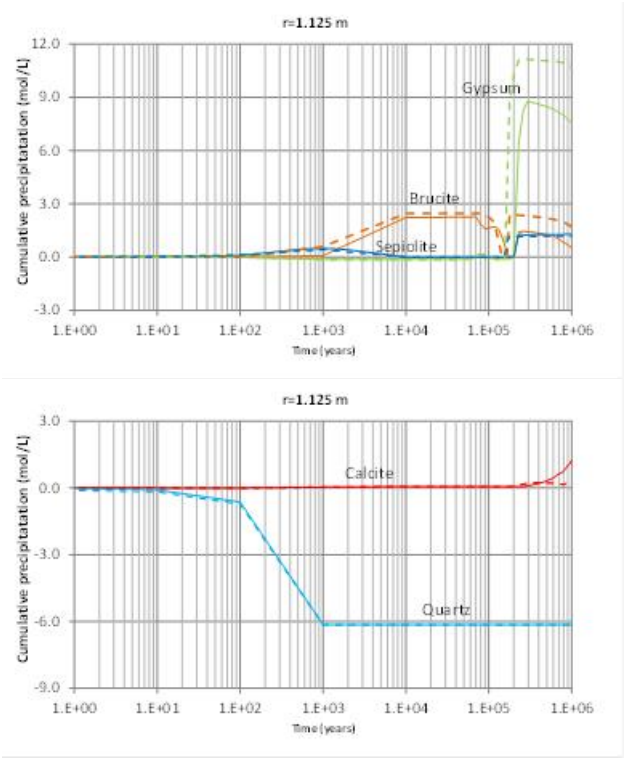

Fig. 6.125 Computed cumulative mineral precipitation/dissolution at the bentonite-concrete interface (r = 1.125 m) with the updated model (straight lines) and the sensitivity run (discontinuous lines)

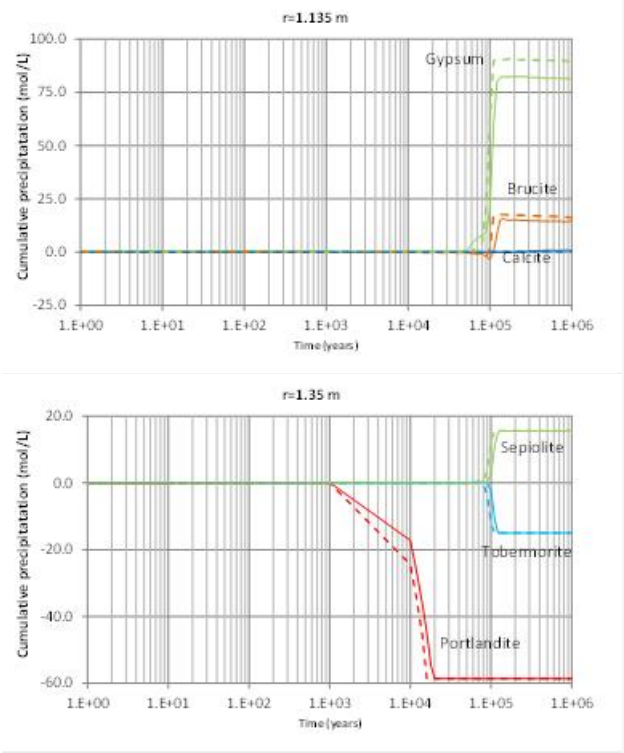

Fig. 6.126 Computed cumulative mineral precipitation/dissolution at the concrete (r = 1.35 m) with the updated model (straight lines) and the sensitivity run (discontinuous lines)

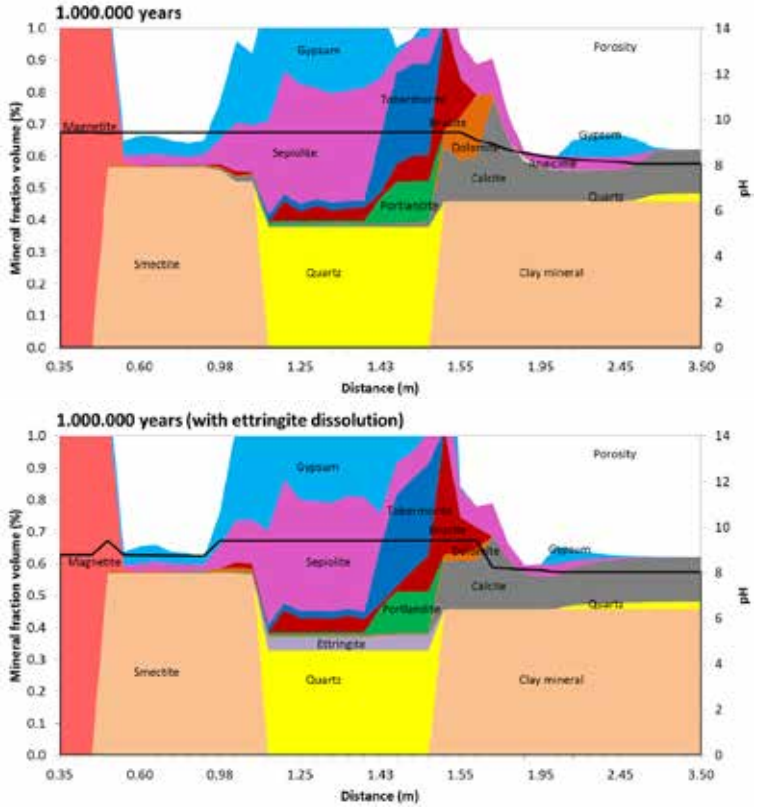

Fig. 6.127 Computed mineral volume fractions and pH at t = 1 Ma with the updated model (top) and the sensitivity run (bottom)

Figure 6.128 shows the computed time evolution of the porosity which changes due to mineral dissolution/precipitation. It can be seen the pore clogging in the bentonite-concrete interface at 200,000 years. The porosity at the bentonite-canister interface (r = 0.45 m), at the the concrete (r = 1.35 m) and at the clay-concrete interface (r = 1.525 m) of the sensitivity run is similar to that of the updated model. The precipitation of gypsum causes the clogging of the pores at the bentonite-concrete interface.

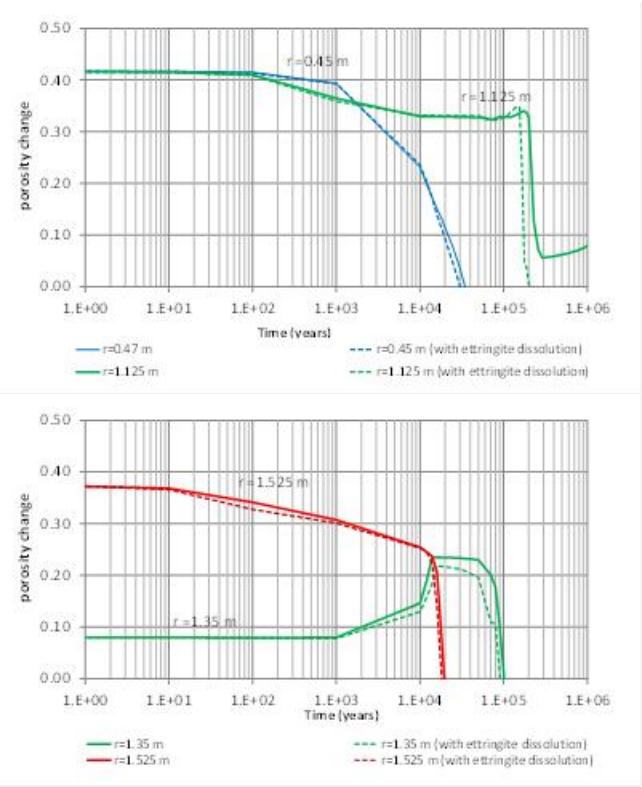

Fig. 6.128 Computed time evolution of the porosity at the bentonite-canister interface (r = 0.45 m), the bentonite-concrete interface (r = 1.125 m), in the concrete (r = 1.35 m), at the clay-concrete interface (r = 1.525 m) and in the clay formation (r = 13.5 m) with the updated model (lines) and the sensitivity run (discontinuous lines)

Sensitivity to Mg-saponite precipitation

The sensitivity run includes Mg-saponite precipitation. Mg-saponite could be an important secondary mineral in the bentonite. The following kinectic rate law was used (Fernández et al., 2009):

$$R = e^{\frac{-Ea}{RT}} K_{25} (\Omega - 1)^{s} \qquad (6.21)$$

where Ω is the ratio between the ionic activity product and the equilibrium constant, Ea is the activation energy which is equal to 41.86 KJ/mol, R is the gas constant, T is the temperature, K_{25} in the kinetic constant rate which is equal of $10 \cdot 10^{-10}$ mol/s/m^2, and σ is the mineral specific surface. The numerical modelling of Mg-saponite precipitation is prone to convergence problems. Therefore, the reference specific surface of Mg-saponite was decreased from 100 mol/m^{2}s (Fernández et al., 2009) to 10^{-10} mol/m^{2}s.

Surface complexation reactions were not considered in the bentonite in this sensitivity run.

Figure 6.129 shows the spatial distribution of the pH at 100, 1,000, 10,000 and 100,000 years computed with the updated model and the sensitivity run. The pH in the sensitivity run is slightly larger than that of the updated model due to the precipitation of the secondary mineral.

Figure 6.130 shows the spatial distribution of the pH at t = 1 Ma computed with the updated model and the sensitivity run. The pH at the bentonite-concrete interface in the sensitivity run is slightly larger than the pH of the updated model due to the Mg-saponite precipitation. The pH in the clay in the sensitivity run is 8.4 instead of 8.2 for the updated model because of calcite precipitation.

Figure 6.131 shows the computed concentrations of the dissolved species at the bentonite-concrete interface (r = 1.125 m) with the updated model and the sensitivity run. In general, the results are similar in both model runs. The remarkable discrepancy is the concentration of specie. The concentration of dissolved aluminium in the sensitivity run is slightly smaller than that of the updated model. This difference is due to Mg-saponite precipitation.

Figure 6.132 shows the cumulative magnetite precipitation at the bentonite-canister interface. The magnetite precipitation in the sensitivity run is slightly smaller than in the updated model.

Figure 6.133 shows the cumulative smectite dissolution in the bentonite. Mg-saponite precipitation leads to a reduction of smectite dissolution compared to the updated model.

Figure 6.134 shows the cumulative mineral precipitation/dissolution at the bentonite-concrete interface. The concentrations of precipitated/dissolved are similar in both models except for calcite dissolution after 200,000 years.

Figure 6.135 show the cumulative mineral precipitation/dissolution at the clay-concrete interface. Calcite dissolves after 200,000 years and precipitates as dolomite in the sensitivity run. Brucite precipitation in the sensitivity run is smaller than in the updated model.

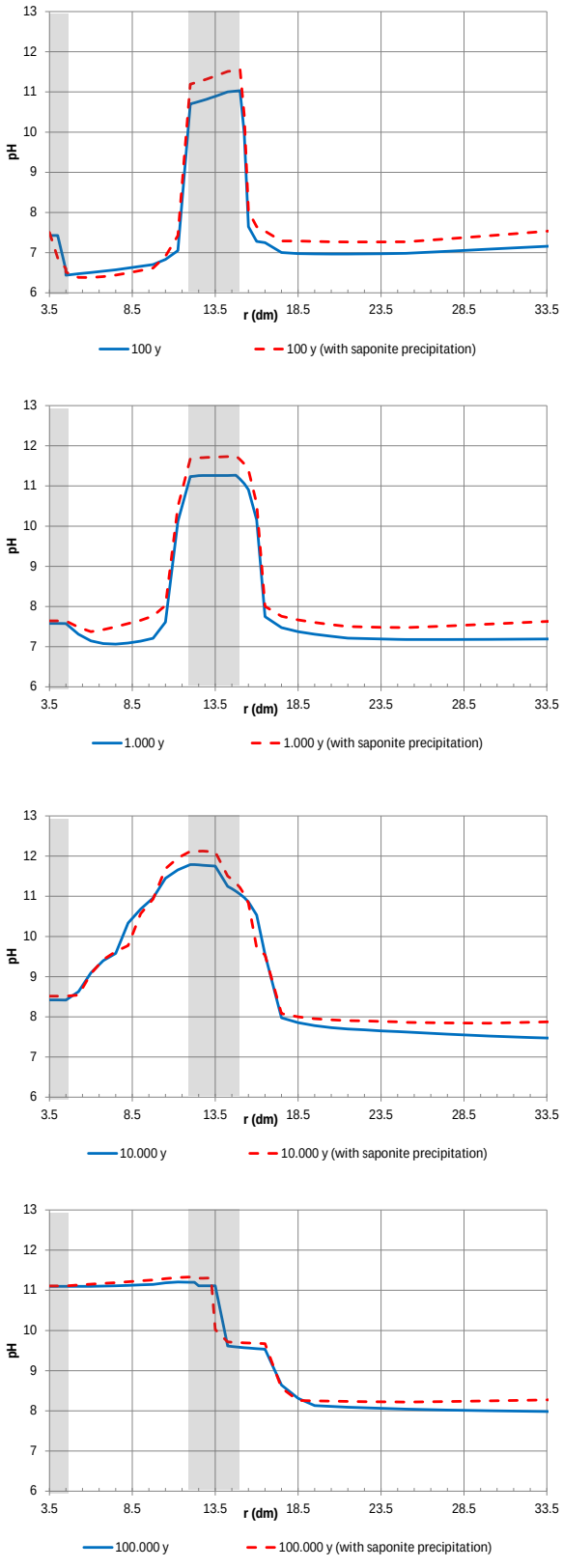

Fig. 6.129 Spatial distribution of the pH at 100, 1,000, 10,000 and 100,000 years computed with the updated model (blue line) and the sensitivity run with Mg-saponite precipitation (red discontinuous line)

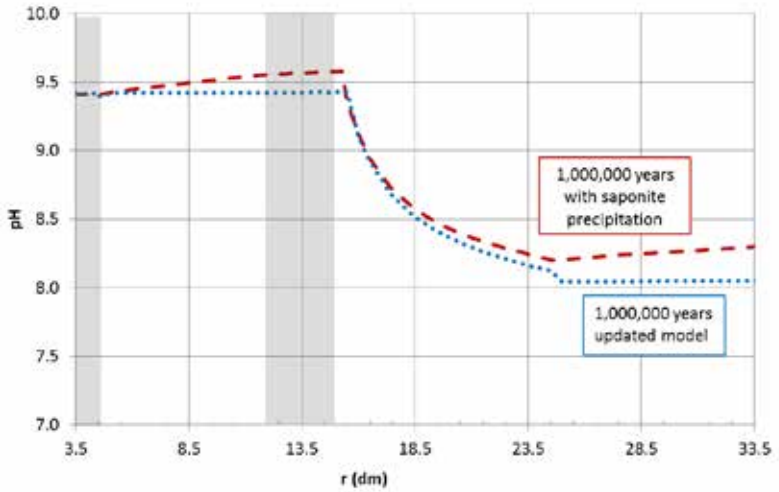

Fig. 6.130 Spatial distribution of the pH at 1 Ma computed with the updated model (blue line) and the sensitivity run with Mg-saponite precipitation (red discontinuous line)

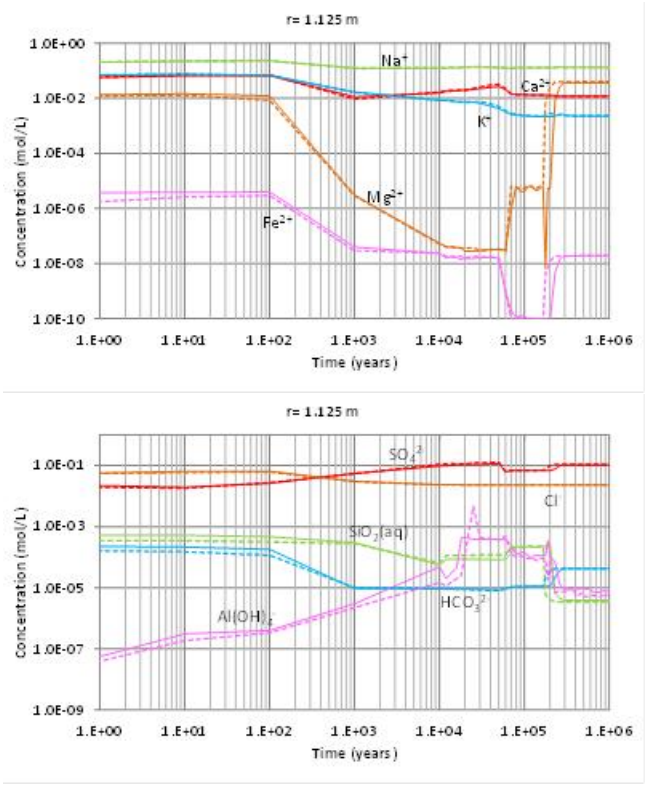

Fig. 6.131 Computed time evolution of the concentrations of the dissolved ions at the bentonite-concrete interface (r = 1.125 m) with the updated model (straight lines) and the sensitivity run (discontinuous lines)

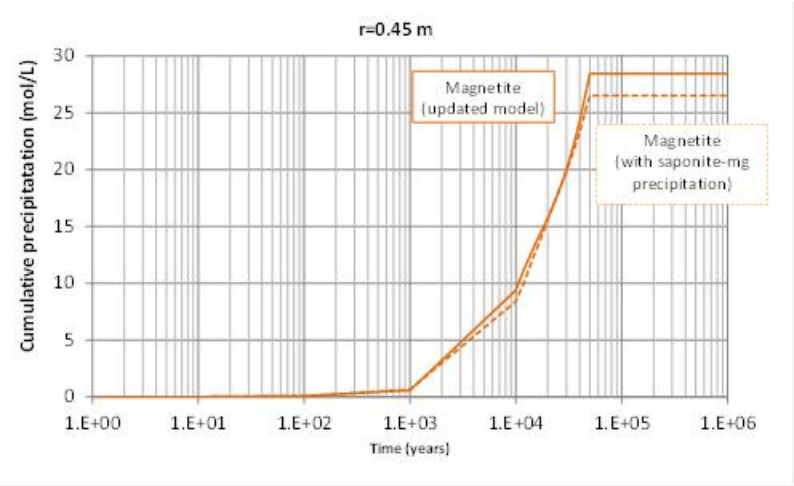

Fig. 6.132 Computed cumulative precipitation of magnetite with the updated model (straight line) and the sensitivity run (discontinuous line)

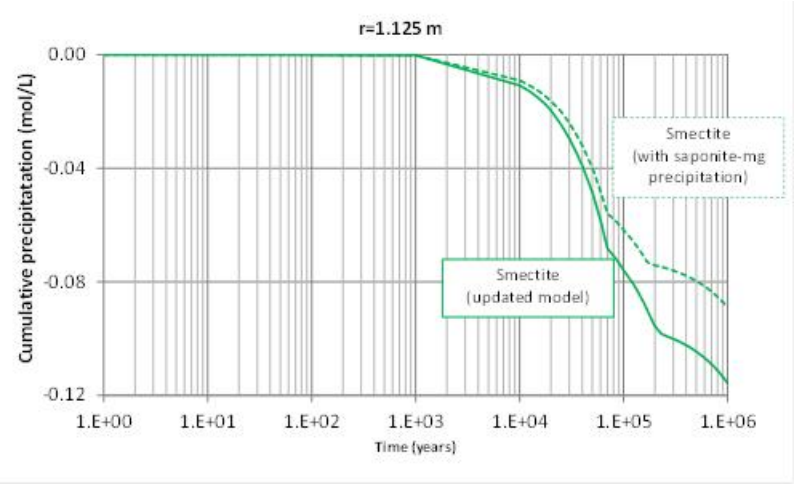

Fig. 6.133 Time evolution of the cumulative dissolution of smectite in the bentonite computed with the updated model (line) and the sensitivity run with Mg-saponite precipitation (discontinuous line)

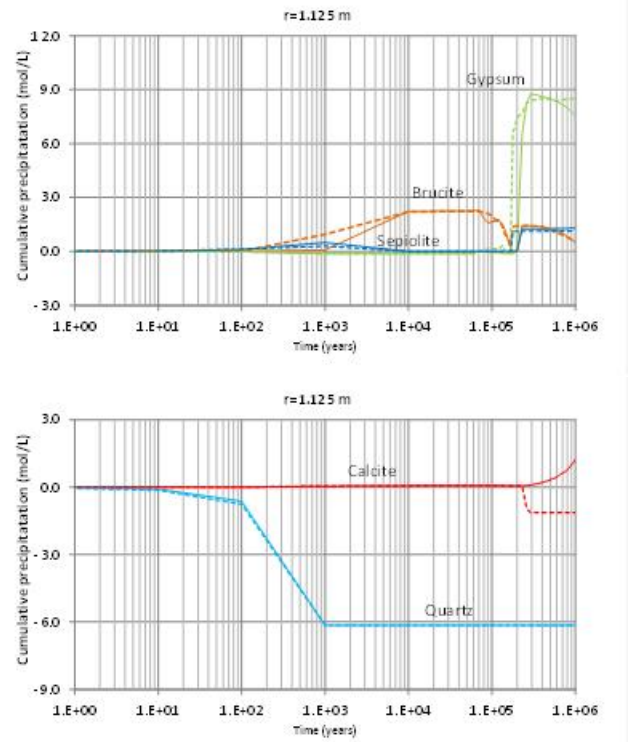

Fig. 6.134 Computed cumulative mineral precipitation/dissolution at the bentonite-concrete interface (r = 1.125 m) with the updated model (straight lines) and the sensitivity run (discontinuous lines)

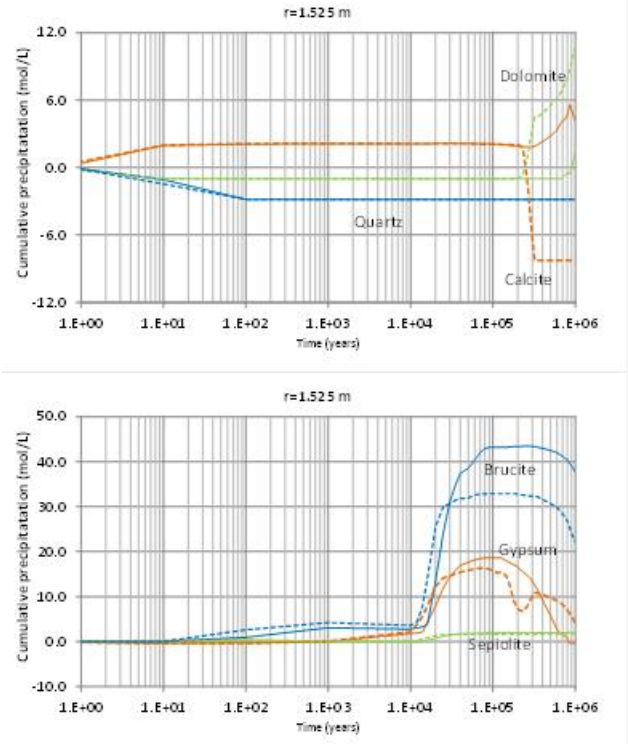

Fig. 6.135 Computed cumulative mineral precipitation/dissolution at the concrete-clay interface (r = 1.525 m) with the updated model (straight lines) and the sensitivity run (discontinuous lines)

Figure 6.136 shows the spatial distribution of the mineral volume fractions and pH computed with the updated model and the sensitivity run at t = 1 Ma. Small amounts of Mg-saponite precipitate in the bentonite in response to smectite dissolution. Mg-saponite precipitation leads to the increase of pH and the dissolution of the calcite at the clay-concrete and bentonite-concrete interfaces. Dolomite precipitates and occupies the voids created by calcite dissolution. Sepiolite and brucite precipitation in the sensitivity run is smaller than that of the updated model at the clay-concrete interface due dolomite precipitation.

The changes in the porosity in both runs are similar (Fig. 6.137).

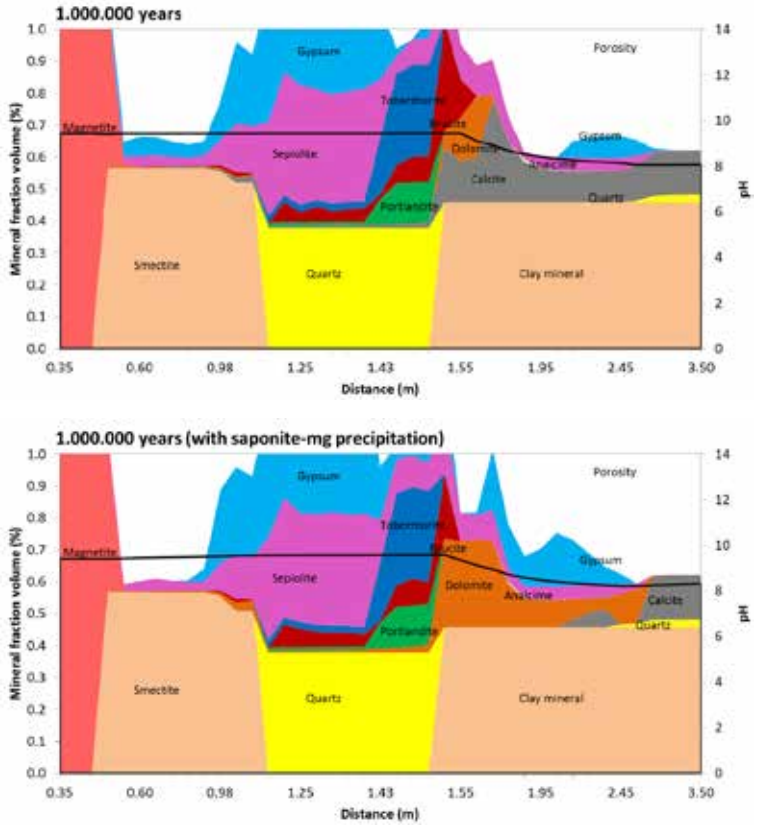

Fig. 6.136 Computed mineral volume fractions and pH at t = 1 Ma with the updated model (top) and the sensitivity run (bottom)

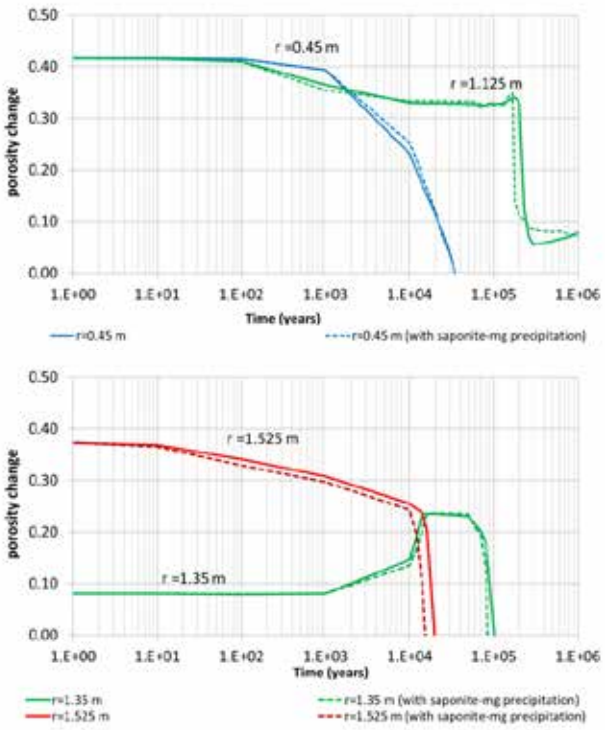

Fig. 6.137 Computed time evolution of the porosity at the bentonite-canister interface (r = 0.45 m), the bentonite-concrete interface (r = 1.125 m), in the concrete (r = 1.35 m), at the clay-concrete interface (r = 1.525 m) and in the clay formation (r = 13.5 m) with the updated model (lines) and the sensitivity run (discontinuous lines)

6.2.8.3 Conclusions

The concentrations of exchanged cations are sensitive to the cation selectivity coefficients. These coefficients affect slightly the geochemical evolution of the system for the first 10,000 years. Then, the geochemical variables are not sensitive to the selectivities.

The pH time evolution is not very sensitive to the surface complexation reactions and smectite dissolution. However, the final pH distribution is more sensitive to smectite dissolution. The concentrations of the dissolved species are not sensitive to the surface complexation and smectite dissolution. Magnetite precipitation is sensitive to the surface complexation.

Gypsum and brucite precipitation in the bentonite and the concrete is sensitive to the dissolution of the ettringite in the concrete which may causes the pore clogging in the bentonite-concrete interfaces at 200,000 years.

The Mg-saponite precipitation causes more precipitation of dolomite in the clay-concrete interface and the pore closes faster than in the updated model.

6.2.8.4 Influence in geometric simplifications

The non-isothermal water flow and multicomponent reactive solute transport numerical model of the EBS of a HLW repository in clay presented in this report assumes that the flow and the transport processes exhibit axial symmetry. This assumption should be valid except near the edges of the canisters. The detailed analysis of these border effects would require the use of 2D axisymmetric models. However, it is believed that the results of the 2D axisymmetric models will not differ a lot from those of the 1D axisymmetric models presented here.

Another geometric assumption of our models is that disposal galleries can be analyzed independently. Since the geochemical perturbations caused by the corrosion products and the concrete liner extend into the clay formation a distance smaller than the separation between galleries, this assumption can be accepted as valid.

6.2.9 Conclusions

A non-isothermal water flow and multicomponent reactive solute transport numerical model of the EBS of a HLW repository in clay according to the Spanish Reference Concept has been presented.

Mineral dissolution/precipitation is especially strong in the concrete. Kinetically-controlled smectite dissolution, using the the rate from Sánchez et al. (2006), leads to analcime precipitation. Model results indicate that smectite dissolution in the presence of an OPC concrete liner in a repository in clay is about 4 times more relevant than in the case of the repository in granite.

Magnetite precipitates near the canister. The thickness of the altered zone at the canister-bentonite interface in the presence of the high pH plume is 4 cm. This is half of the thickness of the altered zone for a repository in granite.

The pH in the concrete increases due to portlandite dissolution. It also increases in the bentonite due to the penetration of the hyperalkaline plume from concrete. The precipitation of calcite, brucite and sepiolite buffers the hyperalkaline plume. The high pH plume extends throughout the bentonite and causes mineral precipitation, changes in the composition of the exchanged cations and a reduction of the porosity of the bentonite. The pH is about 11 after 100000 years and later decreases to 9.5. The hyperalkaline plume from the concrete penetrates 1 m into the clay host rock after 1 Ma.

Numerical models predict pore clogging in a 4 cm thick zone near the canister, 5 cm in the concrete-bentonite interface and 5 cm in the clay-concrete interface. Changes in porosity caused by mineral dissolution precipitation are significant throughout the bentonite and in a narrow band (25 cm) of the host rock.

6.2.10 Comparison of UDC numerical results with those reported by others for the interactions of concrete and bentonite

The numerical results of the UDC models of the interactions of concrete with bentonite and clays and the effects of the hyperalkaline plumes generated by concrete on engineered and geological barriers have been compared to the results reported by Shao et al. (2013), Kosakowski and Berner (2013) and Berner et al. (2013).

Shao et al. (2013) performed reactive transport simulations of the Maqarin marl rock natural analogue for 500 years with a 1D model by using the OpenGeoSys-GEM code. Their results show pore clogging in the marl rock exposed to the hyperalkine plume in a band of 5 to 10 mm due to the precipitation of ettringite and CSH phases. According to the UDC numerical model, the pores of the clay rock formation become clogged after 20,000 years.

Kosakowski and Berner (2013) presented numerical reactive transport calculations to evaluate the geochemical evolution at cement/clay interfaces for different transport scenarios through several Swiss clay rocks for a time span of 2,000 years. Their calculations show that the effects of geochemical gradients between concrete and clay ma-

terials are very similar for all investigated host rocks. The mineralogical changes at the material interfaces are restricted to narrow zones for all host rocks. The extent of strong pH increase in the host rocks is limited. The calculations show massive porosity changes due to precipitation/dissolution of mineral phases near the interface, in line with other reported transport calculations on cement/clay interactions. They concluded that the degradation of concrete materials will be limited to narrow zones. The porosity reduction will be restricted to very narrow zones. The clogging of the pore space leads to a strong reduction of diffusive fluxes across the interface, which essentially stops the geochemical alteration processes and significantly slows down mass transport across the interface. However, connecting the evaluated temporal porosity evolution to realistic and true times is very difficult. The calculations of UDC share most of the features of the results of Kosakowski and Berner (2013) such as narrow alterations zones with pore clogging.

Berner et al. (2013) presented the simulations of the interactions of a MX-bentonite buffer with a low-pH concrete and the Opalinus Clay. Calculations were performed for 30000 years by using the OpenGeoSys-GEM code. Their results show that the thickness of the zone containing significant mineralogical alterations is at most a few tens of cm in both the bentonite and the Opalinus Clay adjacent to the liner. The precipitation of minerals causes a reduction in the porosity near the bentonite–concrete and concrete–Opalinus Clay interfaces. The effect is more pronounced and faster at the concrete liner–Opalinus Clay interface. The simulations reveal that significant pH changes (i.e. pH > 9) in the bentonite and the Opalinus Clay are limited to zones less than 10 cm thick after 30000 years. UDC calculations share also many of the results of Berner et al. (2013). The zone of the bentonite affected by clogging is 15 cm while clogging affects 10 cm of the clay formation. Similar to Berner et al. (2013), UDC results show that smectite dissolution is very small (less than 0.2% after 1Ma). The model of Berner et al. (2013) predicts that the pH is around 8 after 100000 years and the pH front in the clay formation reaches about 10 cm. The UDC model predicts a pH of 11 at t = 100000 years and a pH of 8 after 1 M years. The front of high pH penetrates 14.5 cm after 1 Ma. This discrepancy in pH predictions is due to the fact that Berner et al. (2013) considered a low-pH concrete while UDC considered OPC.

6.3 Long term evolution in a granite repository

6.3.1 General description

Section 6.1 presented a 1D axisymmetric numerical model of the long-term geochemical evolution of a spent-fuel carbon-steel canister repository in granite. The 1D model neglects the canister border effects and takes into account the groundwater flow through the granite in a simplified manner. Here, a 2D axisymmetric numerical model of the long-term geochemical evolution is presented. The model considers the carbon-steel canister, the bentonite, the excavation disturbed zone (EDZ) and the granite. The 2D model is more realistic than the 1D model because it accounts for the canister border effects and the flow and solute reactive transport in the EDZ and in the granite.

6.3.2 Geometry

The geometry of the model corresponds to an individual disposal cell according to the Spanish reference concept of a spent-fuel carbon-steel canister repository in granite (Enresa, 2000a; 2000b; 2004; 2006).

A 2D axisymmetric model domain is considered with a radial distance of 25 m. The domain includes the canister, the bentonite, the EDZ and several meters of rock (Fig. 6.138). The canisters are 4.5 m long and have an outer radius of 0.45 m. The outer radius of the bentonite barrier is 1.2 m. The spacing between canisters is filled with bentonite. The thickness of the EDZ is equal to 0.2 m. All the materials are assumed homogeneous and isotropic.

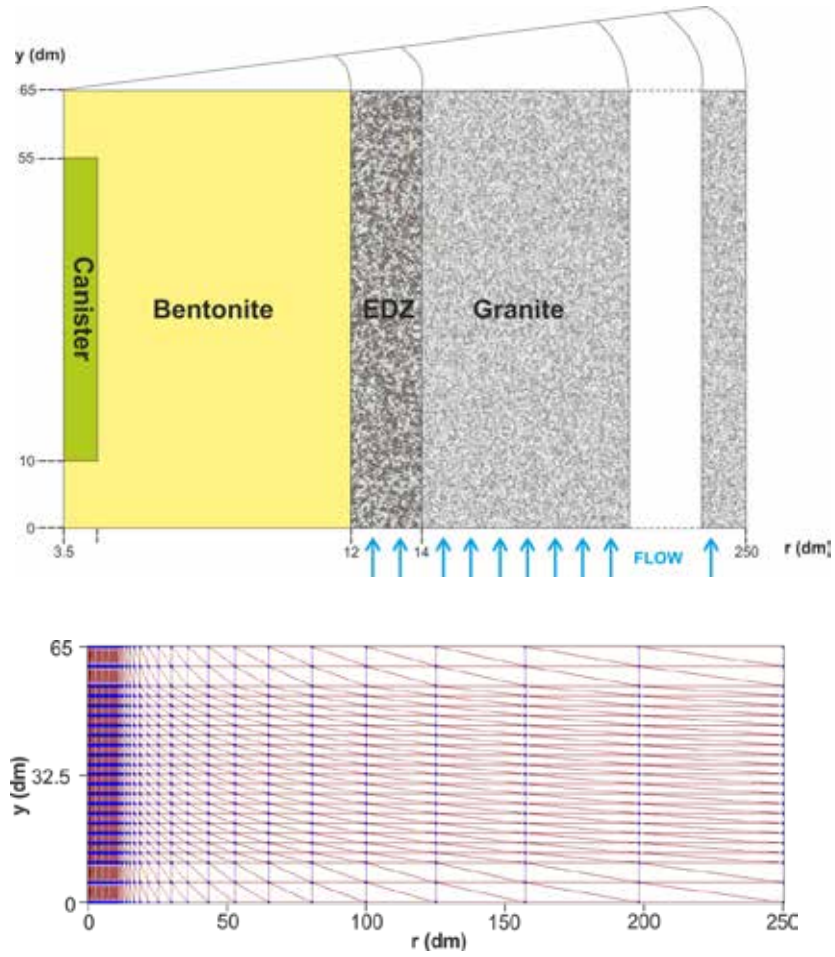

Fig. 6.138 Sketch of the model domain for the 2D axi-symmetric model of a disposal cell and finite element mesh (length units in dm)

6.3.3 Process classes (T, H, M, C) and coupling

The simulation of the long-term evolution of a high-level waste repository is not a blind extension of the models developed for experiments to different space and time scales. It requires a careful assessment of the key long-term processes and their coupling.

Mechanical effects of the drilling of the disposal drifts in the granitic rock lead to the formation of the EDZ and a partial desaturation of the granite near the drift surface. The rock is soon resaturated once the disposal cell is closed. There is a first phase in the long-term evolution of the EDZ and granite around a disposal cell in which THM processes are relevant. This time period, shorter than 1000 years, coincides with the resaturation of the bentonite barrier and the time in which thermal gradients are the most

important. Saturation and thermal gradients are driving forces for physical and chemical processes in the bentonite but also in the EDZ and granite. When long-term evolution analysis is extended until 10^5 or 10^6 years, THM processes will be of minor importance.

Chemical reactions induced by the diffusion of solutes from the bentonite into the rock are influenced by water flow through the EDZ and the granite and may take place at all temporal scales in the near field of a disposal cell. Mineral dissolution and precipitation in the EDZ and the granite may result in changes in parameters such as porosity, permeability and sorption.

6.3.4 Considered processes

The model assumes that the entire domain is initially water-saturated. In this stage (after fully resaturation), mechanical effects are neglected.

The 2D axis-symmetric model accounts for flow through the EDZ and the granite by assuming that groundwater flow is parallel to the gallery axis. The hydraulic conductivity of bentonite is much lower than that of granite. Therefore, the water flow through the bentonite can be neglected.

Solute diffusion is the main transport mechanism in the engineered barrier. The canister is assumed to have the same transport properties as the bentonite.

The geochemical model is similar to that of the 1D axisymmetric model. A constant corrosion rate of 2 μm/year is assumed. The system considers 6 mineral in the bentonite and the granite: calcite, gypsum, quartz, magnetite, siderite and goethite. The initial volume fractions of calcite and quartz in the bentonite, the EDZ and the granite are similar to those reported in Samper *et al.* (2008a). Gypsum, magnetite, siderite and goethite are minerals which are not initially present in the system, but are allowed to precipitate. Similar to the 1D model, the changes in porosity caused by mineral dissolution/precipitation are disregarded. Surface complexation and cation exchange are only considered in bentonite. All the reactions, except for canister corrosion, are assumed at equilibrium.

The simulation starts after the thermal pulse has dissipated. Therefore, the model is isothermal and all the reactions are modeled at a constant temperature of 25 ºC.

The model considers a single phase and therefore the hydrogen produced by canister corrosion is assumed to dissolve and diffuse in the liquid phase. The model disregards gas migration in the bentonite and the mechanical effects of high gas pressures which could be relieved by temporary cracks in the bentonite.

6.3.5 Input data and data sources

6.3.5.1 Flow and transport

Flow and transport parameters are similar to those reported by Samper *et al.* (2008a; 2011). The hydraulic conductivity of the granite is $8.72 \cdot 10^{-12}$ m/s. The hydraulic conductivity of the EDZ is an order of magnitude larger than that of granite. The hydraulic conductivity of bentonite is extremely low ($6 \cdot 10^{-14}$ m/s) and equal to that used in the 1D model. All dissolved chemical species are assumed to have the same effective diffusion: $4.07 \cdot 10^{-11}$ m^2/s in the bentonite and $5.02 \cdot 10^{-14}$ m^2/s in the EDZ and the granite. The porosity is assumed to be constant and equal to 0.407 for the bentonite and 0.005 for the EDZ and the granite.

Water flow through the granite and the EDZ is simulated with a prescribed water flux of granite water parallel to the axis. Hydraulic head is fixed at a value H_1 at the bottom boundary (y = 0) and H_2 at the top boundary (y = 6.5 m), where $H_1 > H_2$. The values of H_1 and H_2 were calibrated in order to obtain a flow through the EDZ and the granite such that the diffusion of a conservative species through bentonite is similar to the solute diffusion computed with the 1D axisymmetric model.

6.3.5.2 Geochemical model

The chemical system coincides with that of the 1D model. The initial chemical composition of bentonite porewater is taken from Samper *et al.* (2008a). The porewater composition is equilibrated with respect to calcite, quartz, surface complexation and cation exchange. The initial porewater in the canister is assumed to have the same chemical composition as that in the bentonite. The initial chemical composition of the porewater

in the granite and the EDZ and that of the inflow water at the boundaries is a granitic porewater also taken from Samper *et al.* (2008a), which coincides with that of the boundary water of the 1D model. The initial volume fractions of calcite and quartz in the bentonite, the EDZ and the granite are similar to those reported in Samper *et al.* (2008a). They coincided with those considered in the 1D model for bentonite. Cation exchange and surface complexation are only considered in the bentonite.

6.3.5.3 Canister corrosion

Similar to the 1D model, the corrosion of carbon-steel is assumed to be constant and equal to 2 μm/year. The canister is treated as a porous material made of 100% metallic iron, Fe(s).

6.3.6 Numerical model and computer code

The model domain has been discretized with a finite element mesh of 1035 nodes and 1936 elements (Fig. 6.138). Grid size decreases near the canister. Simulations were carried out at a constant temperature of 25°C for 1 Ma by using 30000 time steps.

Water flow is steady state and parallel to the disposal gallery (Fig. 6.139). The following head values were assigned at the boundary nodes to ensure a flow through the EDZ and the granite so that the diffusion of a conservative species through the bentonite is similar to that of the bentonite/granite interface in the 1D axisymmetric model: H_1 = 11 dm and H_2 = 0 dm at the bottom and top boundary of the domain, respectively. These conditions produce a flow rate of 0.8 L/y through the EDZ and 4.4 L/y through the granite.

The long-term simulation of the geochemical evolution of a spent-fuel carbon-steel canister repository in granite has been performed with CORE^{2D} (Samper *et al.*, 2003; 2011), a code for transient saturated and unsaturated water flow, heat transport and multicomponent reactive solute transport under both local chemical equilibrium and kinetic conditions in heterogeneous and anisotropic media.

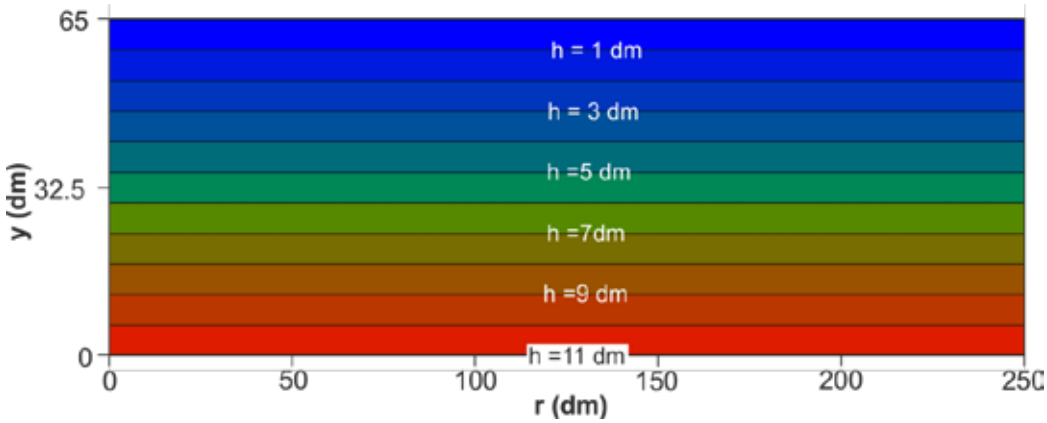

Fig. 6.139 Computed hydraulic head distribution for the 2D axysimmetric model

6.3.7 Results description

Figure 6.140 shows the contour plot of the computed concentrations of a conservative species, Cl^-, at 10^2 and 10^4 years. The conservative species diffuses from the bentonite into the granite. The contour lines of Cl^- concentration are affected by water flow through EDZ and granite. It should be noticed they are almost parallel to each other. Therefore, the spatial distribution of chemical species can be analyzed along radii (lines of constant y). We selected the radius located at the middle of the canister, which corresponds to y = 3.5 m, to illustrate the time evolution of the concentrations.

Figure 6.141 shows the radial distribution of the computed concentration of Cl^- at selected times. Chloride diffuses from the bentonite into the granite. Cl^- concentrations decrease in the bentonite and increase in the granite, reaching a maximum penetration of 12.45 m after 10^4 years. Afterwards, the computed Cl^- concentration decreases also in the granite and recovers its initial value after approximately 10^5 years.

Dissolved cations such as Ca^{2+}, Mg^{2+}, Na^+ and K^+ show trends similar to those of a conservative species but they are also subjected to mineral dissolution/precipitation and cation exchange reactions.

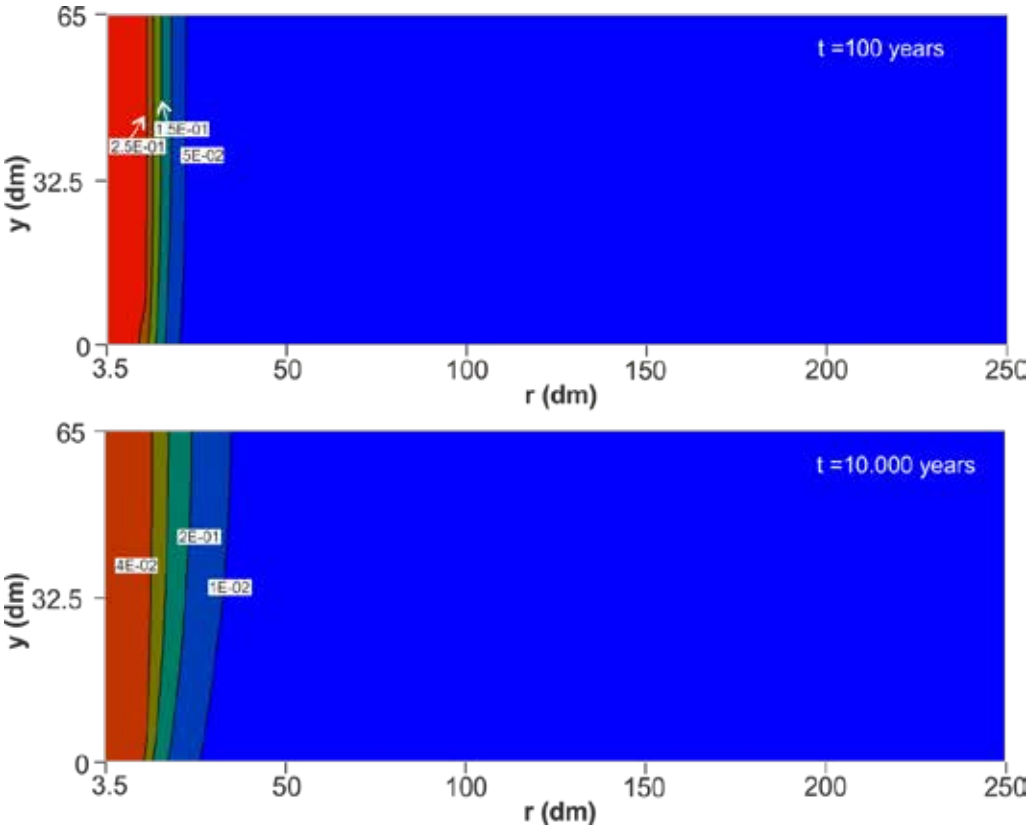

Fig. 6.140 Contour plots of the computed Cl- concentrations at 102 and 104 years. Notice that the contour labels are different in each plot

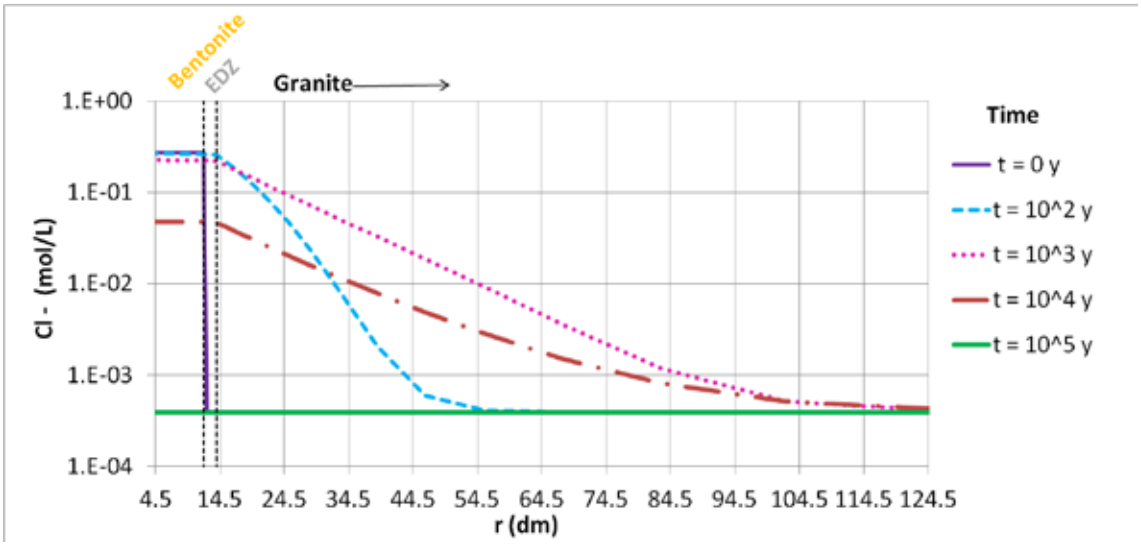

Fig. 6.141 Radial distribution of the computed Cl- concentration at selected times along y = 3.5 dm

Model results of canister corrosion and bentonite long-term evolution are almost similar to those computed with the 1D axisymmetric model. The general trends and the thickness of bentonite affected by the precipitation of corrosion products and the porosity

changes are similar. There are slight differences which are caused by the differences in the finite element mesh near the canister. The mesh of the 2D model is less refined than that of the 1D model.

Canister corrosion leads to a marked increase in pH and the concentration of dissolved Fe^{2+} in the bentonite around the canister. Figure 6.142 shows the radial distribution of the computed pH at selected times. The pH increases in the bentonite near the canister until it reaches a maximum value of 9.5 at around 10^5 years and later decreases steadily. The pH shows several fronts in the bentonite. A pH front takes place at about 100 years near the canister. A second pH front takes place between 10^4 and $5 \cdot 10^4$ years (see computed pH at 10^4 years in Fig. 6.142). Both fronts are similar to those identified in the 1D simulations and are related to the competition of Fe^{2+} and H^+ for the sorption sites.

The computed pH in the EDZ and granite increases from its initial value of 7.83 to 8.13 in the first time interval due to the equilibration of the porewater with the mineral phases. The computed pH near the bentonite-granite interface is lower than in the rest of the granite for $t < 5 \cdot 10^4$ years. Later, it becomes larger. The pH changes in the granite affect a granite zone of less than 9 m thickness.

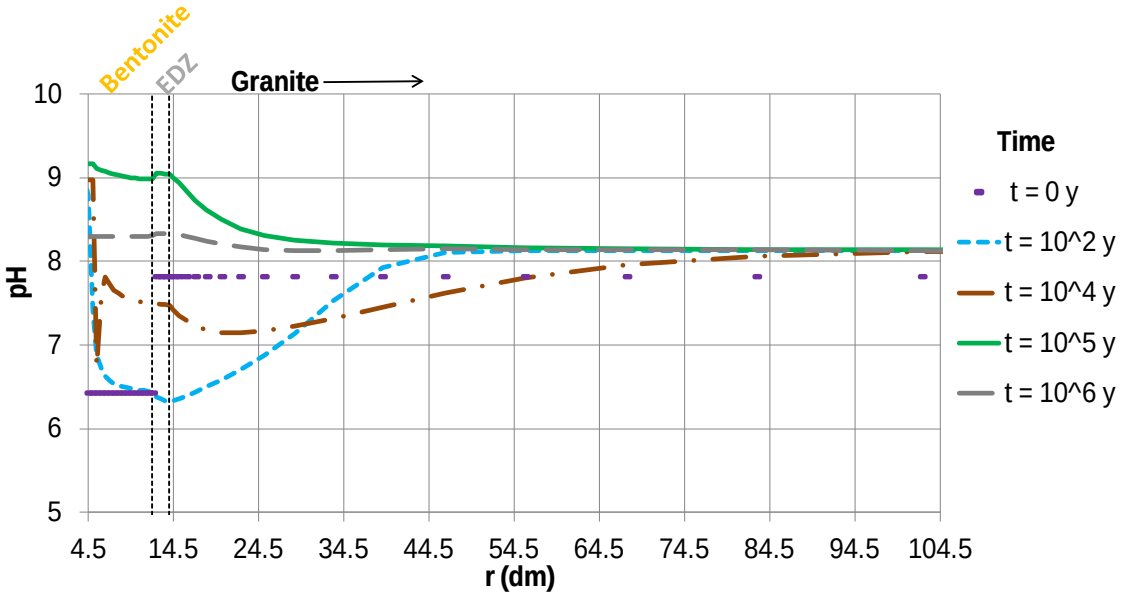

Fig. 6.142 Radial distribution of the computed pH at selected times along y = 3.5 dm

Similar to the 1D model, most of the released Fe^{2+} diffuses from the canister into the bentonite where it precipitates, sorbs by surface complexation and undergoes cation exchange. It mainly precipitates as magnetite. Siderite precipitation is much lower than magnetite precipitation due to the limited availability of dissolved bicarbonate. The precipitation of corrosion products progresses as Fe^{2+} diffuses into the bentonite a distance between 5 and 10 cm. Fe^{2+} sorption plays a relevant role in the geochemical evolution of bentonite because it influences the surface complexation and the pH. However, only a small part of the Fe^{2+} released by canister corrosion is sorbed or exchanged. Only a very small concentration of dissolved Fe^{2+} progresses through the bentonite and diffuses to the EDZ and granite (Fig. 6.143). The penetration of dissolved Fe^{2+} into the rock is lower than 0.5 m.

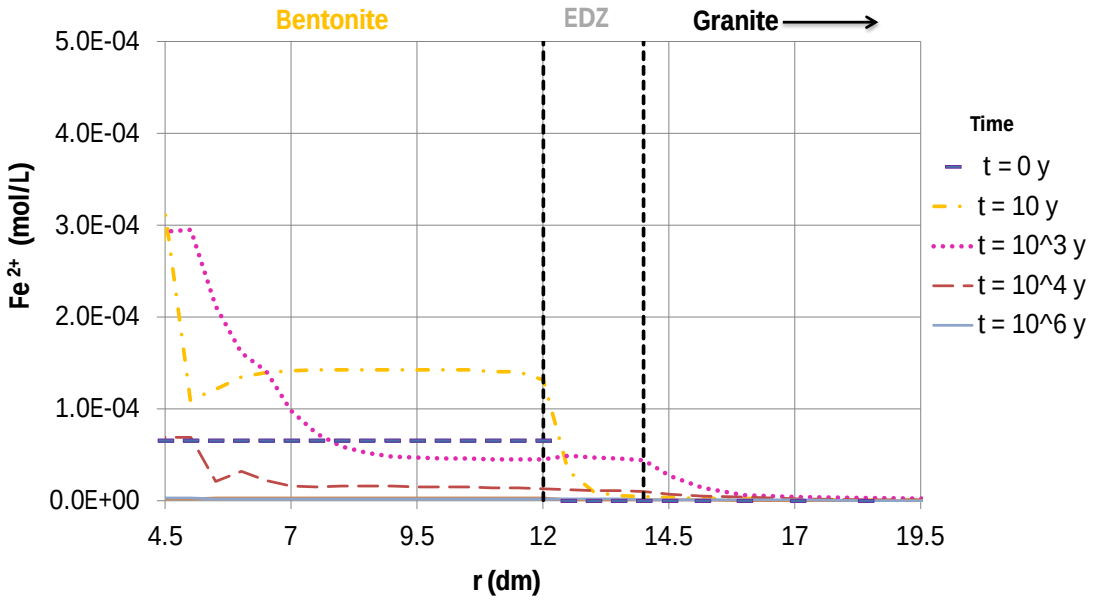

Fig. 6.143 Radial distribution of the computed Fe2+ concentration at selected times along y = 3.5 dm

The effects of mineral dissolution and precipitation on porosity have been evaluated. The porosity of the bentonite is greatly reduced due to the precipitation of corrosion products near the canister/bentonite interface which could result in clogging of the bentonite pores (Fig. 6.144). The bentonite thickness affected by porosity reduction increases with time and ranges from 5 to 10 cm after 1 Ma. Model predictions indicate that changes in porosity will be negligible (lower than 5%) in the rest of the buffer, the EDZ and the granite.

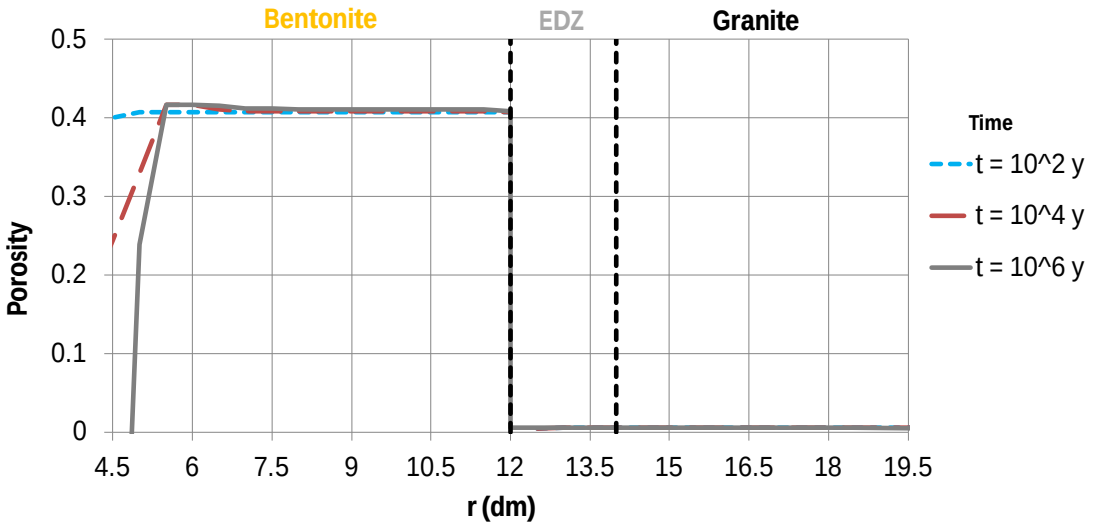

Fig. 6.144 Radial distribution of the computed porosity at selected times along y = 3.5 dm

6.3.8 Main conclusions

The main conclusions of the simulations performed with the 2D model include:

1. The results of the 2D model are similar to those of the 1D axisymmetric model. There are only slight differences in the computed geochemical trends, penetration of corrosion products into bentonite or thickness of bentonite affected by porosity reduction.

2. Dissolved species diffuse from the bentonite into the granite and are affected by water flow through EDZ and granite. Conservative species reach a maximum penetration into the granite of 12 m.

3. The bentonite thickness affected by the reduction of porosity increases with time and ranges from 5 to 10 cm after 1 Ma.

4. The changes in porosity in the the EDZ, the granite and the outermost zone of the bentonite buffer will be negligible.

7 Summary and Conclusions – Consequences for Long-Term Safety Considerations

Four long-term simulation cases representing actual repository concepts in clay or crystalline rock were defined and modelled, using constitutive models and parameters obtained in the frame of PEBS:

- Case 1 – Isothermal buffer evolution;
- Case 2 – Thermo-hydro-mechanical evolution of the buffer at temperatures up to 100 °C;
- Case 3 – Thermo-hydro-mechanical evolution of the buffer with temperatures temporarily exceeding 100 °C;
- Case 4 – Geochemical evolution at canister-bentonite and bentonite-concrete interfaces, including a long-term simulation of a repository in granite.

The results of the long-term simulations are input to Work Package 4, where they are evaluated in detail with respect to their impact on long-term safety considerations.

7.1 Case 1: Isothermal buffer evolution

For the numerical simulation of the long-term isothermal buffer evolution CIMNE extrapolated the Mont Terri EB experiment over a period of 100 years. A new double structure model was used for the simulation. In contrast to the other simulation cases, no thermal effects had to be considered, so that a pure hydro-mechanical formulation could be used.

The analysis of the EB experiment was continued until reaching a time of 100 years to examine the long-term behaviour of an engineered barrier under isothermal conditions. Since the barrier was in a state of saturation or near saturation at the end of the EB field test, few changes were computed in the extended analysis. Basically, the rock mass returned to the initial state before excavation and buffer emplacement, and the barrier naturally stayed saturated.

The most relevant observation is the fact that the degree of heterogeneity remained unchanged so the distribution of porosity (or dry density) observed at dismantling re-

mained frozen in time. It is likely that this conclusion is quite dependent on the degree of irreversibility implicit in the constitutive model of the barrier material. Although the constitutive model and parameters used have proved very adequate when modelling the observed behaviour of the test, it is conceivable that different constitutive models could lead to potentially different results. This is an issue that probably deserves more attention in the future. It should also be noted that no creep phenomena (i.e. deformation under constant effective stress) have been considered either in the buffer or in the rock. If creep is relevant over the long period considered, it would probably lead to a higher degree of homogenization. Creep is potentially an important phenomenon in long-term predictions and should be the subject of focused research.

7.2 Case 2: Buffer THM evolution up to 100 °C

This case is based on the Spanish disposal concept in granitic rock. The repository concept in granite considers the disposal of spent fuel in carbon steel canisters in long horizontal disposal drifts. Canisters are surrounded by high-density bentonite. Two case variants were considered, one being a long-term simulation with constant thermal output after reaching a maximum temperature of 100 °C, which is not realistic but included for reference, the other incorporating a realistic thermal output of the emplaced canisters.

CIMNE performed full THM long-term simulations of the two case variants over 1000 years of emplacement using CODE_BRIGHT with an axisymmetric geometry. For the bentonite buffer behaviour, three formulations were compared to each other:

- Reference analyses, using the conventional THM formulation (BBM)
- Analyses incorporating thermo-osmosis
- Analyses incorporating the evolution of micro-fabric by means of the new double structure constitutive law

TK Consult and NAGRA simulated the case variant with realistic thermal output using the code TOUGH2 with a TH formulation over 100 years. The geometric model was again axisymmetric and represented the centre of a disposal drift. An additional model representing the end of the drift was also investigated.

The parameters for the different materials were taken from the inverse modelling of the FEBEX experiment. With the inverse framework provided by the code iTOUGH2, also confidence intervals for the modelling results could be given. Beside the statistic parameter uncertainty and the geometry effect, an additional two conceptual uncertainties were investigated by alternative simulations, namely an increased initial fluid pressure in the rock of 5 MPa corresponding to 500 m depth below surface of the disposal drift and a lower initial saturation of the buffer.

When comparing the two case variants (constant temperature and heat decay), the patterns of the early transient results in the two variants are naturally very similar. The long-term predictions are of course quite different.

In CIMNE's simulations, temperatures reach a peak and start to fall after a few centuries in the heat decay variant. Temperatures have practically recovered to the initial values at the end of the analysis (1000 years). It should be stated, however, that long-term temperature predictions are sensitive to the particular geometry (axisymmetry) adopted that, at those times, may not be quite representative of the actual repository.

In the heat decay reference case (without thermo-osmosis or double structure of the buffer), full saturation of the barrier is achieved after approximately 8.5 years - a significantly shorter time than in the constant temperature analysis. Swelling pressure also fully develops over similar times. Observing the long-term results, it can be noted that, after achieving the maximum values, the stresses reduce somewhat, because of the contraction associated with temperature reduction.

The incorporation of thermo-osmosis changes significantly the hydration times of the barrier. In the constant temperature case it prevents full saturation indefinitely, but even in the heat decay analyses, full saturation is only achieved towards the end of the analysis (1000 years). Development of swelling pressure follows the progress of hydration, so the full final value is only achieved at the end of the analysis. Similarly, consideration of the micro-fabric evolution also delays full hydration (and full swelling pressure development) until the end of the analysis, i.e. 1000 years. As expected, temperature fields are affected very weakly by using the alternative hypotheses of the enhanced models.

The results correspond to a specific geometry and a single set of parameters. The parameters chosen have the only merit of providing a reasonable good representation of

the observed short-term transient behaviour but here they are applied to long-term calculations, so a significant uncertainty inevitably remains. Even modest variations of parameters can result in significant changes in predicted THM behaviour. A sensitivity study for the long-term situation would thus be quite valuable to assess the degree of uncertainty and the reliability of the reported results.

In contrast to CIMNE, TK Consult and NAGRA received confidence intervals for their results with respect to parameter uncertainty and also performed some alternative calculations with altered initial conditions. The simplification of disregarding mechanical effects, on the other hand, led to best-fit parameters that are not in all cases reflected by measurements (e.g., bentonite porosity).

In the reference case, full saturation of the buffer was predicted to be achieved after 15 to 20 years. With increased initial pressure this time was reduced to 5 to 8 years, while it was increased to above 20 years with lower initial water content of the buffer. This variant also led to slightly increased temperatures (4 °C maximum). The model considering the end of the emplacement drift showed slightly lower temperature at later times, which can be expected as a consequence of the additional axial heat flow component. The confidence bandwidth of results coming from the confidence intervals of the parameters was rather narrow as a consequence of small standard deviations of the parameters. On the whole, the results confirmed current knowledge regarding evolution of temperature and resaturation and showed the capability of the systematic error analysis to provide additional input to the assessment of modelling results.

Regarding maximum temperatures and time to full saturation of the buffer, the results of the different modelling teams for Case 2 show that the respective uncertainties are well bounded, when classical approaches are used. When enhanced models incorporating thermo-osmosis or micro-fabric evolution are used, the time to full saturation may be considerably increased. While the enhanced models are able to simulate the PEBS experiments in a more realistic way, it is not yet possible to decide which of the enhanced models (or which combination) is the most appropriate. Additionally, the parameters used still need more validation by long-term observations. It also has to be noted that the buffer develops sufficient swelling pressure and low permeability before reaching full saturation. Therefore, an increased hydration time is not necessarily problematic.

7.3 Case 3: Buffer THM evolution above 100 °C

Three teams (NAGRA, GRS and CIMNE) were involved in the simulation of this case, which is based on the Swiss reference concept of drift disposal. All teams simulated a disposal cell covering a single canister, making use of the obvious symmetry boundaries, and different additional simplifications.

NAGRA and GRS both used a three-dimensional model, giving a realistic geometrical representation of the repository cell, but reduced the complexity of the problem by performing thermal-hydraulic simulations, neglecting mechanical effects. NAGRA used TOUGH2 and simulated various cases in order to get an insight into modelling uncertainties: A reference case with the material parameters from the HE-E database and variants with reduced thermal conductivity of the buffer, reduced pore expansivity of the clay rock, altered hydraulic parameters of the bentonite blocks, the pellets, or the clay rock. GRS used CODE_BRIGHT and simulated the reference case. Due to very high calculation times (months), only an altered initial saturation profile of the rock was considered beside the reference case. An additional difference between NAGRA's and GRS' models was NAGRA's consideration of a 0.7 m wide excavation damaged zone (EDZ) with increased permeability in the rock.

CIMNE also used CODE_BRIGHT, but with full THM coupling and the simplification of a two-dimensional axisymmetric geometry. Since the heterogeneous buffer composition (bentonite blocks and pellets) cannot be represented in such a model, two variants were considered: a pure pellet buffer and a buffer where the canister is completely surrounded by blocks. Adjacent emplacement drifts had to be neglected due to the geometry. A 0.6 m wide EDZ was considered. Due to high calculation times, only the reference case using the database parameters with the conventional THM formulation could be simulated.

With respect to the temperature evolution, all three teams predicted the peak temperature to be reached after 5 – 6 years. The 3D-models of NAGRA and GRS came up with values of 141 °C and 145 °C, respectively, using the reference parameter values. After 130 – 185 years, the temperature dropped below 100 °C everywhere in the buffer. NAGRA's alternative variants using reduced thermal conductivities of the buffer resulted in peak temperatures of 152 °C. A change in the hydraulic parameters had no significant influence on the peak temperature. The temperature evolution in the clay rock is not visibly influenced by the buffer thermal conductivity.

CIMNE's 2D models considered the canister completely surrounded by bentonite pellets or by blocks, respectively. Due to the considerably higher initial thermal conductivity of the blocks, the peak temperature amounts to 165 °C for the pellet variant and to 115 °C for the block variant.

In the reference case, full saturation of the buffer was reached after 50 years (NAGRA), 27 years (GRS), 85 years (CIMNE pellet variant), or 56 years (CIMNE block variant). The low value for GRS may be due to the disregard of an EDZ or to the high calculated pore pressure. NAGRA's alternative variants showed that changing the buffer hydraulic parameters has only little influence, while decreasing the rock permeability prolonged the saturation time to 100 years.

NAGRA calculated a maximum pore pressure in the rock of 10 MPa, reached after about 100 years. In the GRS simulation, 10 MPa pore pressure are reached already after ten years, which is a reason for the lower saturation time of the buffer in this model. In contrast to the TH calculations of NAGRA and GRS, CIMNE considered different thermal expansion coefficients for the solid grains, the pore liquid, and the grain skeleton. This improvement has a direct effect on pore pressure evolution and leads to maximum pore pressures slightly below 8 MPa, reached after ten years at 15 m distance from the emplacement tunnel. It has, however, to be mentioned that, while this value is lower than those of the other simulations, CIMNE's model neglects additional parallel emplacement tunnels which will have an effect on pore pressure.

All in all, the different simulations of Case 3 led to comparable results. Where significant differences occurred, they could be explained by the different model assumptions and simplifications. The different models complemented one another, increasing confidence in the results.

The higher temperatures of Case 3 did not require any changes in the computer models. The high computational effort, however, inhibited the use of the enhanced models developed in PEBS and used for the Case 2.

7.4 Case 4: Geochemical evolution at interfaces

Significant advances in the geochemical modeling of the canister/bentonite and concrete/bentonite interfaces have been achieved within the PEBS project. However,

some uncertainties in geochemical reactions and parameters for modelling related to Case 4 have been identified, evaluated taking into account the impact on the repository long-term evolution and, in some cases, resolved (Deliverable 4.1).

Uncertainty in chemical reactions and parameters for modelling

Uncertainties in equilibrium constants and their dependence on temperature are judged to be insignificant. The uncertainties in $H_2(g)$ gas generation, diffusion and transport, and the formation of gaseous phases were addressed within the framework of other Euratom Projects such as FORGE.

A literature review was performed to evaluate the long-term relevance of the mechanical and chemical couplings induced by the corrosion products. The main conclusions of this review indicate that no expansion of the test cells was observed during the corrosion tests performed by Smart et al (2006a). The absence of the expansion was explained by the mechanical properties of the oxides. According to Smart *et al.* (2006b), natural analogues for anaerobic corrosion do not provide any experimental evidence for expansion caused by iron corrosion.

The remaining uncertainties include:

1. The identification of the secondary mineral phases that may form at the canister/bentonite and concrete/bentonite interfaces.
2. The kinetic data (rate laws, catalytic effects, rate constants, reactive surfaces).
3. The identification of chloride absorbing phases at cement and iron oxides.
4. The impact of the low porosity layer at the cement boundaries on bentonite hydration and on the spatial extent of the alkaline reaction plume.

These uncertainties influence the mineralogical alteration thickness. Sensitivity runs were performed to evaluate the dependence of the thickness of the altered zone near the canister-bentonite interface to several key parameters and processes including the corrosion rate, the water flow through the granite/bentonite, the dependence of corrosion on environmental conditions, the diffusion coefficient and the selectivities of the bentonite. The results show that this thickness is generally bounded within the predicted values of less than 10 to 12 cm.

Time-scale of some geochemical reactions

Some geochemical reactions such as smectite dissolution are commonly disregarded in short to medium-term geochemical models (e.g. lab and in-situ tests) because they are regarded not relevant in the short term. However, the long-term relevance of such reactions has to be ascertained.

Savage *et al.* (2010) studied the potential contribution of the smectite hydrolysis to the long-term geochemical processes in a KBS-3 bentonite buffer. They concluded that smectite dissolution may be significant for the future geochemical state of a buffer, but the time-scale of this process is too long for experimental verification. They also suggested the importance of further studies through field observation of natural clay-water systems that have evolved over long time scales.

UDC performed full geochemical calculations for repositories in granite and clay (Spanish Reference Concepts) using UDC codes by considering the kinetic dissolution of bentonite for one million years. Model simulations performed with and without kinetic smectite dissolution have been compared to test the relevance of this process. For a repository in granite the cumulative amount of smectite dissolution after 1 Ma is around 0.25 mol/L. This amounts to a decrease of bentonite mass lower than 0.2% after 1 Ma. The decrease in porosity of about 0.01 is compensated with the amount of precipitated analcime. Smectite dissolution has the beneficial effect of leading to a slight decrease (1 cm) of the thickness of the altered bentonite zone. Model results indicate that smectite dissolution in the presence of a concrete liner is about 4 times more relevant than in the case of the repository in granite).

As a conclusion, the long-term effect of the kinetic dissolution of smectite on bentonite porosity and on the thickness of altered bentonite is small for the EBS of repositories in granite and clay according to the Spanish reference concept.

Evaluation of uncertainties: Degree of alteration, properties and thicknesses of the altered zones

From a scientific perspective, the most relevant chemical processes involved in the interactions of corrosion products, bentonite and concrete have been identified, especially once the bentonite is fully saturated. For unsaturated conditions, the interactions are

more complex. However, most of the corrosion will take place under saturated anoxic conditions.

Several uncertainties were resolved or proven insignificant by the PEBS investigations:

1. The thermal transient does not have a significant effect on the overall geochemical evolution of the EBS.
2. Corrosion products have no traceable influence on the mechanical state of the buffer.
3. The effect of smectite dissolution on bentonite porosity and on the thickness of altered bentonite is negligible.

As a result of UDC's modelling in PEBS as well as other comparable studies, thicknesses of altered zones will generally be bounded within values of less than 10 to 12 cm.

Modelling chemical reactions, especially the dissolution and precipitation of mineral phases, requires knowledge of the nature of the reaction (thermodynamic equilibrium or kinetic control), the equilibrium constants and kinetic rate parameters (rate laws, rate constants and reactive surface areas). Available data from lab experiments are not enough to provide well-defined geochemical systems. Therefore, there are uncertainties some of which have been addressed and evaluated for the long-term simulations.

The remaining model uncertainties include:

1. The precipitation of secondary mineral phases at the concrete-bentonite interphase such as CSH, CASH, zeolites, and iron silicates.
2. The precipitation of the secondary mineral phases at the canister-bentonite interphase such as Fe-phyllosilicates and the reduction of Fe in the bentonite.
3. The rate laws, catalytic effects, rate constants and reactive surfaces of kinetic mineral dissolution/precipitation.
4. The clogging of the bentonite and clay pores. The precipitation of the minerals could form a low-porosity layer which could affect the hydration rate and the subsequent geochemical evolution of the system (Cuevas et al., 2014). Their nature is still unclear.

Further research is needed to improve the knowledge of the microstructure of the bentonite and the role of the adsorbed interlayered water. The use of dual porosity models and the update of the porosity due to chemical reactions could help resolve some of the uncertainties identified in the lab experiments.

Evaluation of uncertainties: Effect of alteration on overall buffer performance

The altered zone in the bentonite near the concrete exhibits altered mechanical and hydraulic properties. The alteration at the concrete-bentonite interface and on the iron-bentonite interface will have an effect on swelling pressure which, for now, cannot be quantified. As long as the altered zones are thin compared to the unchanged bentonite portion, it can be expected that the overall swelling pressure will not be critically impaired. From the modelling an upper boundary for the thickness of the altered zones is predicted; it is, however, important to further reduce the uncertainty in this prediction.

With regard to the effect of alteration on the hydraulic performance of buffer, one result of experiments and modelling is the pore clogging in the altered zones, which would in itself mean an improvement by permeability reduction, provided that a sufficient overall swelling pressure of the buffer is reached. The potential effect of pore clogging on the hydration rate could, on the other hand, mean a longer duration of the unsaturated state of the buffer with more complex conditions.

8 References

Berner, U., Kulik, D. A., Kosakowski, G. (2013). Geochemical impact of a low-pH cement liner on the near field of a repository for spent fuel and high-level radioactive waste. Physics and Chemistry of the Earth, 64, 46-56.

BENIPA (2003). Final Report of BENIPA Project: Bentonite Barriers in Integrated Performance Assessment. Final Technical Report EUR 21023.

Bildstein, O., Trotignon, L., Perronnet, M., Jullien, M. (2006). Modelling iron-clay interactions in deep geological disposal. Physics and Chemistry of the Earth 31, 618–625.

Bradbury, M.H., Baeyens, B. (1997). A mechanistic description of Ni and Zn sorption on Na-montmorillonite. Part II: Modelling. Journal of Contaminant Hydrology 27, 223-248.

Bradbury, M.H, Baeyens, B. (2002). Porewater chemistry in compacted re-saturated MX-80 bentonite: Physico-chemical characterisation and geochemical modelling. PSI Bericht 02-10, Villigen PSI and NTB 01-08, Nagra, Wettingen, Switzerland.

Bradbury, M.H., Baeyens, B. (2003). Porewater chemistry in compacted re-saturated MX-80 bentonite. Journal of Contaminant Hydrology 61, 329-338.

Bradbury, M.H., Baeyens, B. (2005). Modelling the sorption of Mn(II), Co(II), Ni(II), Zn(II), Cd(II), Eu(III), Am(III), Sn(IV), Th(IV), Np(V) and U(VI) on montmorillonite: Linear free energy relationships and estimates of surface binding constants for some selected heavy metals and actinides. Geochimica et Cosmochimica Acta 69, 875-892.

Czaikowski, O., Garitte, B., Gaus, I., Gens, A., Kuhlman, U., Wieczorek, K. (2012). Design and predictive modelling of the HE-E test. PEBS Deliverable D3.2-1. NAB 12-003. Nagra, Wettingen.

De Windt, L., Torres, E. (2009). Modélisation d'expériences en cellule reproduisant les conditions THC d'une alvéole de déchets HAVL. Rapport Technique Nº R201009LDEWI, Centre de Géoesciences, Ecole de Mines de Paris, Fontainebleau, France.

Drissi, S.H., Refait, Ph., Abdelmoula, M., Génin, J.M.R. (1995). The preparation and thermodynamic properties of Fe(II)–Fe(III) hydroxide carbonate (green rust 1); pourbaix diagram of iron in carbonate-containing aqueous media. Corrosion Science 37, 2025–2041.

Enresa (2000). Full-scale engineered barriers experiment for a deep geological repository in crystalline host rock FEBEX Project. EUR 19147 EN, European Commission.

Enresa (2001). Enresa 2000. Evaluación del comportamiento y de la seguridad de un almacenamiento de combustible gastado en una formación granítica. Enresa Informe 49-1PP-M-15-01. Madrid, 2001.

Enresa (2004). Evaluación del comportamiento y de la seguridad de un almacén geológico profundo de residuos radiactivos en arcilla. Clave: 49-1PP-M-A1-01. Enresa (In Spanish).

Enresa (2005). NF-PRO Project. Phenomenological description. Reference Concept (Spent Fuel–Carbon Steel Canister–Bentonite–Granite). Deliverable D5.1.1. Part 1.

Enresa (2006). FEBEX – Full-scale Engineered Barriers Experiment, Updated Final Report 1994-2004, publicación técnica 05-2/2006.

Fernández, A., Cuevas, J., Rivas, P. (2001). Pore water chemistry of the FEBEX bentonite. Materials Research Society Symposium Proceedings, 663, 573-588.

Fernández, A., Baeyens, B., Bradbury, M., Rivas, P. (2004). Analyses of the porewater chemical composition of a Spanish compacted bentonite used in a engineered barrier. Physics and Chemistry of the Earth 29, 105-118.

Fernández, A., Cuevas, J., Mäder, U.K. (2009). Modelling concrete interaction with a bentonite barrier. Eur. J. Mineral 21, 177-191.

Féron, D., Crusset, D., Gras, J.-M. (2008). Corrosion issues in nuclear waste disposal. Journal of Nuclear Materials, 379, 16–23.

Finsterle, S. (2007). iTOUGH2 User's Guide, LBNL-40040 Revised, Earth Sciences Division, Lawrence Berkeley National Laboratory, University of California, Berkeley, California, February 2007.

Finsterle, S. (2012). iTOUGH2 Command Reference, LBNL-40041 Revised, Earth Sciences Division, Lawrence Berkeley National Laboratory, University of California, Berkeley, California, March 2012.

Gaines, G.I., Thomas, H.C. (1953). Adsorption studies on clay minerals II. A formulation of the thermodynamics of exchange adsorption. Journal of Chemical Physics 21, 714–718.

Gaus, I., Garitte, B., Senger, R., Gens, A., Vasconcelos, R., Garçia-Siñeriz, J.-L.; Trick, T., Wieczorek, K., Czaikowski, O., Schuster, K., Mayor, J.C., Velasco, M., Kuhlmann, U., Villar, M.V. (2014): The HE-E Experiment: Lay-out, Interpretation and THM Modelling. Deliverable D2.2-11 and D3.2-2 of the PEBS Project.

Génin, J.R.M., Olowe, A.A., Refait, Ph., Simon, L. (1996). On the stoichiometry and Pourbaix diagram of Fe(II)–Fe(III) hydroxy-sulphate or sulphate containing green rust: 2. An electrochemical and Mössbauer spectroscopy study. Corrosion Science 38, 1751–1762.

Gens, A., Guimaraes L. Do N., Garcia-Molina, A., Alonso, E.E. (2002). "Factors controlling rock–clay buffer interaction in a radioactive waste repository". *Engineering Geology*, 64: 297-308.

Gens A, Sánchez M, Guimarães LDN, Alonso EE, Lloret A, Olivella S, Villar MV (2009). "A full-scale in situ heating test for high-level nuclear waste disposal: observations, analysis and interpretation". Geotechnique 2009; 59(4):377–399.

Gens, A., Sánchez, M. (2014). “Deliverable D3.5-2. Formulation of a model suitable for long term predictions”. PEBS project.

Gens, A., Vaunat, J., Garitte, B., Wileveau, Y. (2007). In situ behaviour of a stiff layered clay subject to thermal loading. Observations and interpretation. *Géotechnique* 57, Nº 2, 207-228.

Huertas, F.J., Caballero, E., Jiménez de Cisneros, C., Huertas, F. (2001). Kinetics of montmorillonite dissolution in granitic solutions. Applied Geochemistry, 16, 397-407.

Hunter, F., Bate, F., Heath, T., Hoch, A. (2007). Geochemical investigation of iron transport into bentonite as steel corrodes. SKB Technical Report TR-07-09.

JNC (2000). H12: Project to establish the scientific and technical basis for HLW disposal in Japan. Japan Nuclear Cycle Development Institute, Supporting Report 2, Repository Design and Engineering Technology.

Johnson, L.H., Niemeyer, M., Klubertanz, G., Siegel, P., Gribi, P. (2002) Calculations of the temperature evolution of a repository for spent fuel, vitrified high-level waste and intermediate level waste in Opalinus Clay. Nagra NTB 01-04.

King, F. (2008). Corrosion of carbon steel under anaerobic conditions in a repository for SF and HLW in Opalinus Clay, NAGRA Technical Report 08-12, October 2008.

Kosakowski, G., Berner, U. (2013). The evolution of clay rock/cement interfaces in a cementitious repository for low- and intermediate level radioactive waste. Physics and Chemistry of the Earth, 64, 65-86.

Kuhlmann, U. and I. Gaus (2014). Inverse Modeling of the FEBEX-in-situ test using iTOUGH2”. (Deliverable D3.3-1 of the PEBS project). Nagra NAB 14-20.

Lu, C., Samper, J., Fritz, B., Clement, A., Montenegro, L. (2011). Interactions of corrosion products and bentonite: An extended multicomponent reactive transport model, Physics and Chemistry of the Earth 36, 1661–1668, doi: 10.1016/j.pce.2011.07.013.

Lu, C., Samper, J., Cormenzana, J.L., Ma, H., Montenegro, L., Cuñado, M.A. (2012). Reactive transport model and apparent K_d of Ni in the near field of a HLW repository in granite. Computers and Geosciences 49, 256-266, doi: 10.1016/j.cageo.2012.06.003.

Ma, H. (2010). Reactive transport models in acid mine drainage and nuclear waste disposal, Ph.D. Dissertation, Universidad de A Coruña.

Marty, N.C.M, Fritz, B., Clément, A., Michau, N. (2010). Modelling the long term alteration of the engineered bentonite barrier in an underground radioactive waste repository. Applied Clay Science, 47, 82-90.

Miyata, S. (1983). Anion-exchange properties of hydrotalcite-like compounds. Clays and Clay Minerals 31, 305–311.

Molinero, J., Samper, J. (2006). Modeling of reactive solute transport in fracture zones of granitic bedrocks. Journal of contaminant Hydrology 82, 293-318.

Montes-H, G., Fritz, B., Clement, A., Michau, N. (2005). Modeling of transport and reaction in an engineered barrier for radioactive waste confinement. Applied Clay Science 29, 155-171.

Palacios, B., Rey, M., García-Sineríz, J.L. (2013). “D2.1-4. Engineered Barrier Emplacement Experiment in Opalinus clay: “EB” Experiment. As-built of dismantling operation”. PEBS project.

Pruess, K., C.Oldenburg, G.Moridis (2011). TOUGH2 User’s Guide, Version 2, LBNL-43134 (revised). Earth Sciences Division, Lawrence Berkeley National Laboratory, University of California, Berkeley, California, August 2011.

Refait, Ph., Drissi, S.H., Pytkiwicz, J., Génin, J.M.R. (1997). The anionic species competition in iron aqueous corrosion: role of various green rust compounds. Corrosion Science 39, 1699–1710.

Rozalén, M.L., Huertas, F.J., Brady, P.V., Cama, J., García-Palma, S., Linares, J. (2008). Experimental study of the effect of pH on the kinetics of montmorillonite dissolution at 25 ºC. Geochimica et Cosmochimica Acta 72, 4224-4253.

Samper, J., Yang, C., Montenegro, L. (2003). CORE^{2D} V4: a code for non-isothermal water flow and reactive solute transport. Users Manual. University of La Coruña, Spain.

Samper, J., Zheng, Montenegro, L. , Vázquez, A., Fernández, A.M., Rivas, P. (2005). Testing coupled thermo-hydro-geochemical models with geochemical data from FEBEX in situ test, En: Advances in Understanding Engineered Clay Barriers, Ed. E. Alonso and A. Ledesma Eds, Balkema Pub. ISBN 04 1536 5449, 565-576, 2005.

Samper, J., Vázquez, A., Montenegro, L. (2005b). Inverse hydrochemical modelling of aqueous extracts experiments for the estimation of FEBEX bentonite pore water chemistry. In: Alonso, E.E., Ledesma, A. (Eds.), Advances in Understanding Engineered Clay Barriers. A.A. Balkema Publishers, Leiden, The Netherlands, pp. 553-563.

Samper, J., Yang, Ch., Montenegro, L., Bonilla, M., Lu, C., Yang, Q., Zheng, L. (2007). Mass and energy balance and flux calculations for radionuclide release and geochemical evolution for SF carbon steel HLW repositories in clay and granite. NF-PRO project, Deliverable D5.1.13. University of A Coruña, Spain.

Samper, J., Lu, C., Montenegro, L. (2008a). Coupled hydrogeochemical calculations of the interactions of corrosion products and bentonite. Physics and Chemistry of the Earth 33, S306–S316, doi:10.1016/j.pce.2008.10.009.

Samper, J., Zheng, L., Fernández, A.M., Montenegro, L. (2008b). Inverse modeling of multicomponent reactive transport through single and dual porosity media. Journal of Contaminant Hydrology 98, 115–127.

Samper, J., Zheng, L., Montenegro, L., Fernández, A.M., Rivas, P. (2008c). Testing coupled thermo-hydro-chemical models of compacted bentonite after dismantling the FEBEX in situ test. Applied Geochemistry 23, 1186–1201, doi:10.1016/j.apgeochem.2007.11.010.

Samper, J., Xu, T., Yang, C. (2009). A sequential partly iterative approach for multicomponent reactive transport with CORE2D. Computational Geosciences. doi: 10.1007/s10596-008-9119-5.

Samper, J., Lu, C., Cormenzana, J.L., Ma, H., Montenegro, L., Cuñado, M.A. (2010). Testing Kd models of Cs+ in the near field of a HLW repository in granite with a reactive transport model. Physics and Chemistry of the Earth 35, 278–283, doi:10.1016/j.pce.2010.04.002.

Samper, J., Lu, C., Fritz, B., Clement, A., Montenegro, L. (2011). Interactions of corrosion products and bentonite: An extended multicomponent reactive transport model. Physics and Chemistry of the Earth, 36, 1661–1668, doi: 10.1016/j.bbr.2011.03.031.

Samper, J., Mon, A., Montenegro, L., Naves, A., Torres, E., Turrero, M.J. (2012). Coupled THC model of heating and hydration corrosion experiments with compacted bentonite. Proceedings of 5th International Meeting Clays in Natural and Engineered Barriers for Radioactive Waste Confinement, Montpellier (France), October 22-25, Poster AP/MCI/14.

Samper, J., Naves, A., Montenegro, L., Mon, A., Pisani, B. (2013). Report on long-term THC (m) predictions of a HLW repository in granite. Deliverable 3.5.3 of the PEBS Project.

Samper, J., Mon, A., Pisani, B., Montenegro, L., Naves A. (2014). Report on testing multiple-continua THC(m) models with laboratory and large-scale tests. Deliverable 3.4-1 of the PEBS Project.

Sánchez, M., Gens, A. (2014). “Deliverable D3.3-3. Modelling and interpretation of the FEBEX mock-up test and of the long-term THM tests”. PEBS project.

Savage, D., Rochelle, C., Mihara, M., Moore, Y., Milodowski, A., Bateman, K., Bailey, D. (1999). Dissolution of analcite under conditions of alkaline pH. Presented in: Proceedings of the 9th Annual V.M. Goldschmidt Conference.

Savage, D., Watson, C., Benbow, S., Wilson, J. (2010). Modelling iron/bentonite interactions. Applied Clay Science 47, 91-98.

Shao, H., Kosakowski, G., Berner, U., Kulik, D.A., Mäder, U., Kolditz, O. (2013). Reactive transport modeling of the clogging process at Maqarin natural analogue site. Physics and Chemistry of the Earth, 64, 21-31.

Smart, N.R., Rance, A.P., Fennell, P.A.H. (2006a). Expansion due to the anaerobic corrosion of iron. SKB Technical Report TR-06-41.

Smart, N.R., Rance, A.P., Carlson, L., Werme, L.O. (2006b). Further studies of the anaerobic corrosion of steel in bentonite. Material Research Society Symposium Proceedings 932, 813–820.

Taniguchi, N., Kawasaki, M., Kawakami, S., Kubota, M. (2004). Corrosion behaviour of carbon steel in contact with bentonite under anaerobic condition. In: Prediction of Long Term Corrosion in Nuclear Waste Systems Proceedings 2nd International Workshop, Nice, September 2004, p. 24–34.

Tournassat, C. (2003). Cations–clay interactions: The Fe(II) case. Application to the problematic of the French deep nuclear repository field concept. Ph.D. Dissert. Grenoble, France.

Vasconcelos, R., Pinyol, N., Alonso, E., Gens, A. (2014): Modeling and interpretation of the EB experiment hydration & Interpretation of the final state of the EB experiment barrier. Deliverable D3.1-1 and D3.1-2 of the PEBS Project.

Wersin, P., Birgersson, M., Olsson, S., Karnland, O., Snellman, M. (2007). Impact of corrosion-derived iron on the bentonite buffer within the KBS-3H disposal concept – the Olkiluoto site as case study. Posiva Report 2007-11.

Wilkin, R.T., Barnes, H.L. (1998). Solubility and stability of zaolites in aqueous solution: I. Analcime, Na-, and K-clinoptilolite. American Mineralogist 83, 746-761.

Wolery, T.J. (1992). EQ3/6, a software package for geochemical modeling of aqueous systems: Package overview and installation guide (version 7.0). Technical Report UCRL-MA-110662-Pt 1. Lawrence Livermore National Laboratory, CA, USA.

Xu, T., Samper, J., Ayora, C., Manzano, M., Custodio, E. (1999). Modeling of noniso-thermal multicomponent reactive transport in field scale porous media flow systems. Journal of Hydrology 214, 144–164.

Yang, C., Samper, J., Montenegro, L. (2008). A coupled non-isothermal reactive trans-port model for long-term geochemical evolution of a HLW repository in clay. Environmental Geology 53, 1627–1638, doi: 10.1007/s00254-007-0770-2.

Zheng, L., Samper, J. (2008). Coupled THMC model of FEBEX mock-up test. Physics and Chemistry of the Earth 33, S486–S498, doi:10.1016/j.pce.2008.10.023.

Zheng, L., Samper, J., Montenegro, L., Mayor J.C. (2008). Flow and reactive transport model of a ventilation experiment in Opalinus clay. Physics and Chemistry of the Earth 33, 1009-1018, doi: 10.1016/j.pce.2008.05.012

Zheng, L, Samper, J., Montenegro, L., Fernández, AM. (2010). A coupled THMC model of a heating and hydration laboratory experiment in unsaturated compacted FEBEX bentonite. Journal of Hydrology 386, 80-94, doi: 10.1016/j.jhydrol.2010.03.009.

Zheng, L., Samper, J., Montenegro, L. (2011) A coupled THC model of the FEBEX in situ test with bentonite swelling and chemical and thermal osmosis. Journal of Contaminant Hydrology 126, 45-60.

9 List of Figures

10 List of Tables